Development of Cold Gas Dynamic Spray Nozzle and Comparison of Oxidation Performance of Bond Coats for Aerospace Thermal Barrier Coatings at Temperatures of 1000°C and 1100°C

By

Jean-Michel Roy

Thesis submitted to the Department of Mechanical Engineering
in partial fulfillment of the requirements for the degree of
Master of Applied Science (Engineering)

University of Ottawa

Ottawa, Ontario, Canada

February 6th 2012

Abstract

The purpose of this research work was to develop a nozzle capable of depositing dense CoNiCrAlY coatings via cold gas dynamic spray (CGDS) as well as compare the oxidation performance of bond coats manufactured by CGDS, high-velocity oxy-fuel (HVOF) and air plasma spray (APS) at temperatures of 1000°C and 1100°C. The work was divided in two sections, the design and manufacturing of a CGDS nozzle with an optimal profile for the deposition of CoNiCrAlY powders and the comparison of the oxidation performance of CoNiCrAlY bond coats. Throughout this work, it was shown that the quality of coatings deposited via CGDS can be increased by the use of a nozzle of optimal profile and that early formation of protective α-Al_2O_3 due to an oxidation temperature of 1100°C as opposed to 1000°C is beneficial to the overall oxidation performance of CoNiCrAlY coatings.

Acknowledgements

I would like to thank my supervisor, Dr. Bertrand Jodoin for his guidance and help throughout my research. His rigorous methodology combined with the freedom he allowed to explore alternative ideas helped make this research project an enriching experience. Thanks for all those hours spent in the spraying room and those spent discussing our results!

I would also like to thank Dr. Mohammed Yandouzi for his help and training with the SEM as well as the numerous thought-provoking questions he asked throughout this work. Thank you for your help and for bringing your valuable input to all our discussions.

Thanks to Patrick Richer who completed the first part of this project. The knowledge and techniques you passed on to me were invaluable to the completion of this work.

I would like to thank the technicians from the machine shop of the department of Mechanical Engineering. Thank you James for providing great insight and dealing with all my nozzles, Leo for repairing every electronic gizmo that fails and John for your valuable input.

Thank you Nicole Mercier and Susan Rennie for dealing with all my purchase orders, my travel expense forms and all the other paperwork.

Special thanks go to Alexandre Bergeron and Pascal Gadoury. The numerous hours we spent studying for classes together and bounced ideas off each other were invaluable. Whenever I have a crazy idea, I know who to discuss it with!

Thank you to my lab mates: Jamil Assaad, Daniel MacDonald, Mathieu Bolduc, Jean-Louis Pelletier, Rubén Fernández, Patrick Trahan, Tyler Samson and Antoine Bacciochini as well as Hengyong Bu and Onur Meydanoglu.

Finally, a special thank you to my parents, family, friends and especially my girlfriend. You have all encouraged and supported me through the many hours of study and work.

Table of Contents

List of Tables

List of Figures

Chapter 1 - Introduction

1.1. Gas Turbines, Thermal Barrier Coatings and Thermal Spray

In order to meet demand for higher performance gas turbine engines, the trend has been to increase the turbine inlet temperature (TIT) [**1**]. While the effect of raising the TIT significantly increases the gas turbine performance according to thermodynamic modelling, the caveat is increased strain on the mechanical components of the hot sections. The hot sections of gas turbines are already considered to be one of the harshest operating environments for material systems. The elevated TIT poses significant engineering challenges including a reduction in material properties, elevated thermal stresses, intensive loading conditions, corrosion, oxidation, erosion and possibly foreign object damage. The increase in performance offered by raising the TIT is therefore often overshadowed by the lower turbine life expectancy leading to elevated maintenance and part replacement costs and by the higher risk of in-flight failure.

In an attempt to increase the TIT while maintaining adequate safety and acceptable maintenance costs, researchers and industry have employed different techniques to increase material properties and develop new technologies applicable to gas turbine components. These advances have lead to a significant increase in the TIT from approximately 675K in the first gas turbines (1903)[**1**] to temperatures over 1920K in modern high-performance engines (1993)[**2**] and to temperatures over 2255K reported for the state-of-the-art F135-PW engine (2011)[**3**] as can be seen in Figure 1.1.

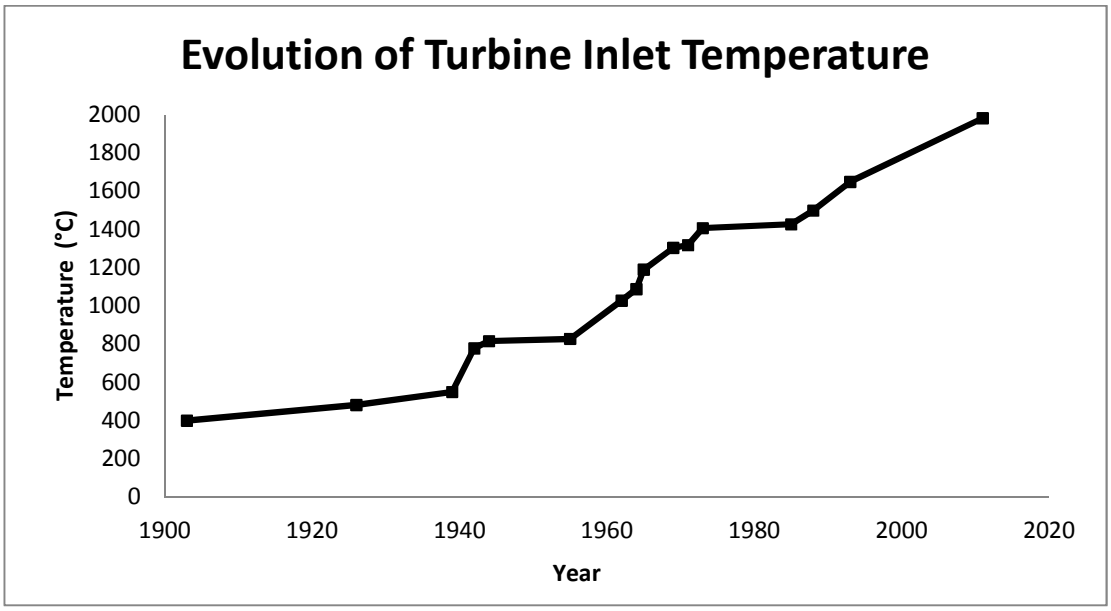

Figure 1.1: Evolution of gas turbine inlet temperature [1,2,3]

These elevated temperatures have been made possible due to the development of high-temperature resistant nickel-based superalloys and sophisticated cooling solutions. Advances in superalloy elemental composition coupled with the ability to grow directional grains and create single crystal components have increased the allowable temperatures for turbine components to over 1300K. Although much research has focused on increasing the allowable temperature for superalloys, further significant improvements seem unlikely considering these components are currently operating at 80-90% of their melting temperature[**3**]. Research is therefore mostly concentrating on methods of reducing the temperature of the superalloy components rather than pushing the limits of the superalloy properties.

One of the methods to keep the superalloy temperature at an acceptable level is the use of sophisticated cooling solutions. These solutions typically employ cooler air which was fed through the compressor section and bypass the combustor section. The flow is then used to cool the turbine blades in one or a combination of 5 solutions: convection cooling, impingement cooling, film cooling, full-coverage film cooling or transpiration cooling as shown in Figure 1.2[**4**].

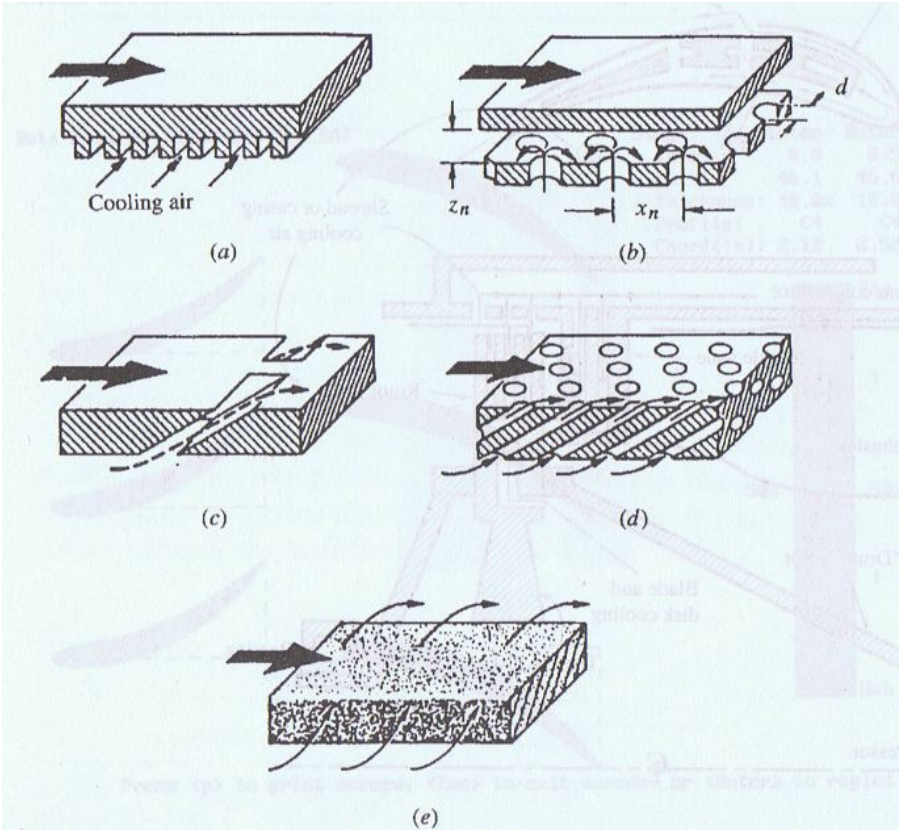

Figure 1.2: Cooling methods used in gas turbine blades showing (a) convection cooling, (b) impingement cooling, (c) film cooling, (d) full-coverage film cooling and (e) transpiration cooling [4]**.**

These solutions have been refined over the past 30 years using knowledge gathered in fluid dynamics and more recently with computational fluid dynamics (CFD). While these systems are capable of lowering the blade surface temperature by more than 400°C [**5**], there are some drawbacks. The air used in cooling the blade does not contribute to producing work in the turbine and there is therefore a reduction in engine efficiency. Furthermore, the requirements for the compressor section are increased to allow for the loss of air to the cooling solution. Further advances in blade configuration and design will reduce the significance of these drawbacks, especially with the possibility of analysis and refinements via CFD. The effectiveness of cooling however will likely progress slowly due to the maturity of theses cooling solutions and the drawbacks in diverting more air from the compressor section to further increase cooling.

Another method of keeping an acceptable superalloy temperature is the use of high-performance coatings. Coatings are thin layers of material (typically < 500μm) applied on

the surface of other materials in an attempt to increase specific material properties. A wide variety of coating materials and techniques have been developed to protect components from oxidation, corrosion, wear, impacts, temperature and other undesirable surface effects. Coatings have also been used for repair of damaged components, dimensional restoration, biomedical compatibility, anti-adhesive properties, abradable protection, sealing, increasing hardness and modification of electromagnetic and thermal conductivity[**6**,**7**]. Coatings are therefore suitable for many engineering environments and requirements while having a high degree of flexibility and potential for cost-savings over other material systems. These benefits have driven the global thermal spray market to an estimated value of €6 billion ($8.6 billion) in 2009[**7**]. It is expected that this industry will increase in the coming years as some of the products and technologies mature.

Coatings have been used in the aerospace industry since the 1960s when diffusion aluminide coatings were first applied to superalloy components in gas turbine engines [**5**]. These coatings were applied by a chemical reaction and the diffusion of metallic elements on the surface of the component. Further advances in coating deposition techniques were developed including physical vapour deposition and plasma spray in the 1980s. These new techniques enabled coatings to be deposited on the part without any mixing between the coating and the coated substrate and were called overlay coatings. A subset of overlay technologies that utilise thermal energy are classified as thermal spray processes and are depicted in Figure 1.3. Overlay coatings were a significant advantage since the composition of the substrate was unaffected by the coating and thus retained its mechanical properties. They were soon used on turbine blades due to better control of chemical composition, thickness and for their physical, chemical and mechanical properties [**5**].

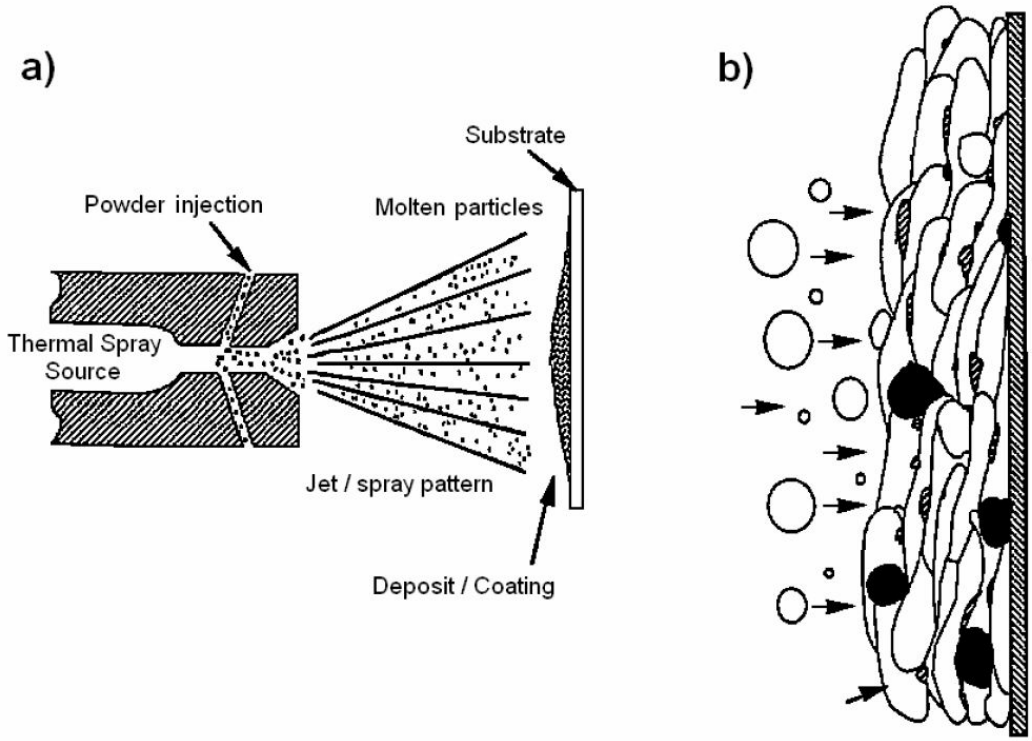

Figure 1.3: Schematic representation of a) thermal spray coating process and b) formation of a coating from the impact of particles on the substrate[8**]**

Overlay coatings are typically manufactured by thermal spray processes such as detonation spraying, high-velocity oxy-fuel (HVOF), plasma spraying, wire arc spraying and flame spraying. These processes typically manufacture coatings via deposition of molten droplets or semi-molten particles of the required material onto the substrate. The coating material is initially in the form of powder, wires or rods. This feedstock material is then melted by heat produced via a plasma jet, electric arc or flame obtained by combustion. The molten material is then propelled towards the substrate via a flow of gas. The gas velocity varies depending on the process and sophisticated nozzles are often used to obtain the desired gas velocity. Upon contact with the substrate, the molten particles flatten and rapidly solidify to form the desired coating. The thermal spraying process chosen depends on the type of material to be deposited which includes pure metals, alloys, ceramics, ceramic-metal-matrix composites, polymers and nanomaterials[**8**]. The development of overlay coatings was driven by two factors: thermal protection from the high temperature gas and protection from oxidation and hot corrosion, the effect of which is enhanced by the elevated temperatures.

In an effort to offer protection from these characteristics, a protective coating system called thermal barrier coating (TBC) was developed. These coating systems are composed of two layers that are deposited on the superalloy substrate. The outer layer is a ceramic top coat that provides thermal insulation while the inner layer is a metallic bond coat that protects the substrate from oxidation and hot corrosion and promotes bonding between the ceramic top coat and the substrate. A diagram of the layers of a typical TBC system is presented in Figure 1.4.

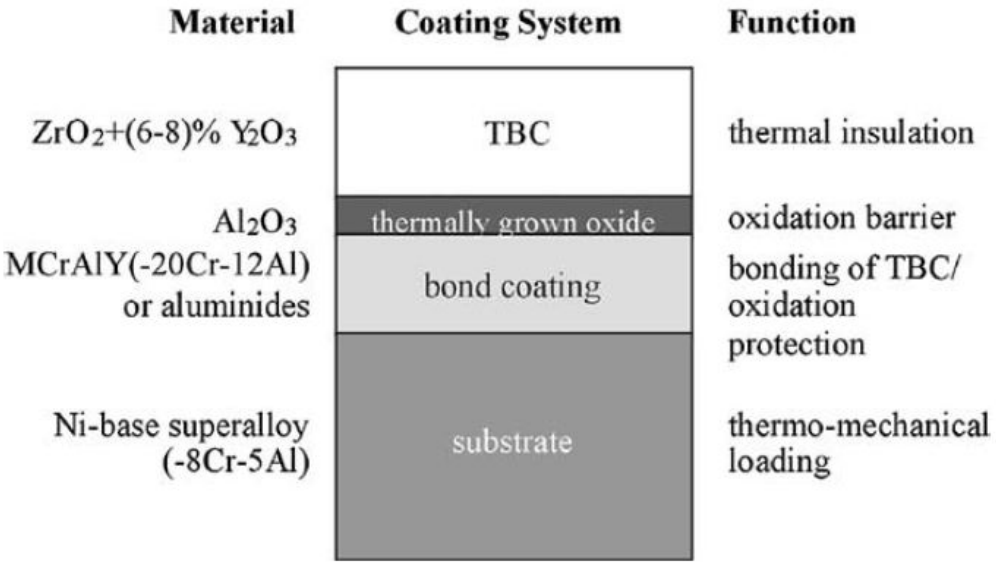

Figure 1.4: Diagram of typical TBC structure [9]

Although the ceramic top coat is a very good thermal insulator it offers little protection from oxidation or hot corrosion due to its porous nature. The bond coat not only protects the substrate from these phenomena but also reduces thermal stresses that would occur between the ceramic and the substrate due to their difference in thermal expansion coefficients. These TBC systems are considered the pinnacle of thermal protection in the aerospace industry and are the subject of numerous studies throughout the world. TBC systems are usually deposited via HVOF or plasma spray. In certain cases where only oxidation or hot corrosion resistance are required, only the bond coat may be applied and can adequately protect components in less hostile environments. The properties of these coatings are therefore extremely important in dictating the overall protection offered. The influence of TBC addition on the TIT is shown in Figure 1.5.

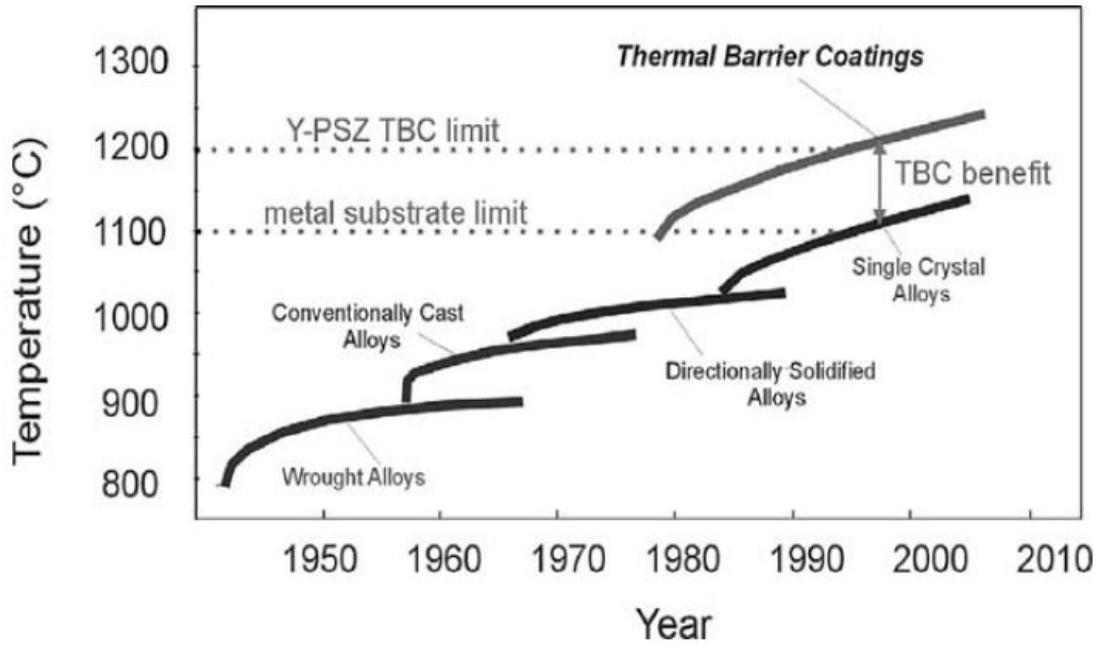

Figure 1.5: Evolution of turbine blade technology[9]

Although the properties of a coating are mostly dictated by its chemical composition, the deposition process can have a significant impact on its physical properties. It is generally favourable for the coating microstructure to be free of oxides, porosity and cracks in order to obtain the highest mechanical properties. However, thermal spraying processes inadvertently introduce these defects into the coating during deposition, especially when the coating deposition parameters are not optimal. The elevated temperatures required for deposition is the primary reason for the introduction of defects in coatings. The elevated process temperature affects the particles in-flight temperature, upon deposition and during cooling. Spraying in an air or oxygen-rich atmosphere can lead to the oxidation of particles both in-flight and upon deposition. The oxides formed in the coating lead to increased hardness, reduced ductility and reduced coating cohesion. The oxide particles can also become nucleation sites for additional oxides during the coating lifetime and are detrimental to the oxidation protection the coating may provide. The as-sprayed coating oxidation can be reduced by spraying in an inert atmosphere or in a low pressure or vacuum chamber but these methods can significantly increase costs to a level that becomes uneconomical. The elevated temperatures of thermal spraying can also lead to porosity and tensile residual stresses in the coating due to contraction upon cooling of the deposited particles. Grain

growth is another detrimental effect of the thermal spray processes high temperatures, in particular when dealing with nanocrystalline materials. In some applications, significant effort is made to obtain fine grains due its advantageous effect on the material properties. It is therefore important to consider the coating process and coating parameters in order to maintain the desired grain size, composition and microstructure which are carefully selected to obtain the best possible properties.

As was stated previously, the detrimental effects of current coating methods are mostly due to elevated temperature. This has lead to the development of a new kind of spraying process in which process temperature is low and velocity is high. In these processes, thermal energy used in conventional thermal spraying has been replaced by kinetic energy and called kinetic spraying.

Currently, the most widespread kinetic spraying process is called Cold Gas Dynamic Spraying (CGDS). This process makes use of a gas flow at supersonic velocities to accelerate powder particles at high velocities. The particles with enough kinetic energy then plastically deform upon impact and adhere to the substrate to form a coating[**10**]. Each material has a defined "critical velocity" below which deposition is limited or non-existent due to insufficient particle deformation. CGDS addresses one of the drawbacks of traditional thermal spray methods by employing temperatures low enough to prevent the melting of particles. This enables coatings to maintain the original powder microstructure with little grain growth. Oxidation of the coating material and thermal stresses are also reduced drastically. This gives CGDS the advantage of depositing coatings that are almost identical to the original feedstock powder and broadens the scope of coating capabilities.

The quality of bond coats in a TBC system is important to the protection offered and overall lifetime of the coating system. Defects introduced through the spraying process can be extremely detrimental to the bond coat behaviour especially during high-temperature oxidation. The growth of the oxide layer between the bond coat and the top coat leads to internal stresses and premature failure. Presence of oxides during the spraying process can accelerate the growth of this oxide layer. This fact increases the importance of the bond coat composition and deposition method to ensure a long TBC life. Current TBC deposition methods are unable to deposit extremely high-quality coatings free of defects. Due to this

fact, current TBC systems are mostly used to prolong the turbine blade life rather than increasing turbine operating temperature for more performance and efficiency. Although nanocrystalline bond coats have the capacity to increase the coating lifetime by having an increased oxidation resistance, current spraying techniques used by the industry (Plasma and HVOF) are not capable of effectively depositing these coatings. The Cold Gas Dynamic Spraying process however, is capable of depositing nanocrystalline coatings with very low oxide content which could be beneficial to TBC systems. Due to this fact, recent trends have modified the HVOF spraying parameters in order to approach the coating properties and bonding mechanisms of CGDS. It is therefore evident that in order to achieve high-quality coatings capable of sustaining increased TIT temperatures for prolonged periods, improvements in the thermal spray process and refinement of spray parameters must be achieved.

1.2. Motivation of Research and Objectives

The motivation for the present study is driven by the potential to obtain dense bond coats with low oxide content through the use of the CGDS process. Previous studies have shown that bond coat porosity and oxide content are two factors currently limiting bond coat performance and lifetime [**11**]. The improvement of bond coat quality is therefore primordial in obtaining higher performing TBC coatings and more powerful and efficient gas turbines.

Process parameters have a large influence on final coating properties and in the current CGDS systems these parameters are often far from optimal. The optimization of these parameters is necessary in order to obtain coatings that are both dense and free of oxides. Important parameters in CGDS systems include gas type, gas temperature, pressure, travel speed and the nozzle geometry. All of these parameters can be easily modified via system controls with the exception of the nozzle geometry. In order to change the nozzle geometry, a new nozzle must be designed, constructed and installed on the system. When keeping the same nozzle, an increase in gas temperature and pressure will increase particle velocity while a change in travel speed will modify coating thickness. Since these parameters are easily modified, it was decided to try and optimize the nozzle design for the required material. With

optimization of the parameters surrounding an optimal nozzle, the CGDS system should yield coatings that are dense and low in oxide content.

Upon completion of the design and manufacturing of an optimal nozzle, this work will concentrate on the high-temperature oxidation behaviour of free-standing bond coats without the presence of a superalloy substrate or of the ceramic top coat. This will allow for a thorough investigation of the influence of the deposition technique on the oxidation behaviour of the bond coat. The investigation of the oxidation behaviour is of high importance since it is one of the major causes of TBC failure and dictates bond coat performance and effectiveness. Bond coats are often subjected to pre-oxidation heat treatments prior to the deposition of the ceramic top coat. There is therefore significant benefit in determining what heat treatment will increase the performance of the bond coat. Although many studies evaluate TBC performance as a whole, numerous studies are directed specifically at evaluating bond coat oxidation behaviour due to its import role in dictating TBC performance. Furthermore, it is expected that the addition of a ceramic top coat will alter the thermo-mechanical behaviour of the TBC system during thermal cycling but it is not expected to influence the general trends found in bond coat-specific oxidation studies. The methods employed in this work have been shown to be a valid investigation method to assess bond coat oxidation performance in a high-temperature environment.

This work is part of a broader ongoing research project which aims to develop high-performance bond coats for TBC systems manufactured via the CGDS method. It is the continuation of a previous study in which the initial CGDS coating parameters, microstructure and certain oxidation parameters were investigated. This work will build-up on the previous study in an attempt to further improve and refine the previous results. In order to achieve this, the following specific studies will need to be performed:

a) Using CFD, design a CGDS nozzle able to deposit dense coatings with low oxide content at lower driving gas consumption.
b) Using CFD, analyse the effect of various driving gases mixtures, temperatures and pressures as well as nozzle stand-off distances.
c) Manufacture the nozzle designed, install it on the existing CGDS system and test its capability to deposit bond coats.

d) Evaluate the oxidation behaviour of the CGDS bond coats.
e) Compare the properties and performance of the CGDS bond coats with those manufactured by industrial thermal spray techniques such as plasma spraying and HVOF spraying.
f) Compare the performance of the bond coats in this study with those oxidized at a lower temperature, analysed in the previous study.

1.3. Outline of the Thesis

The content of this work has been divided into seven chapters.

Chapter 1 presents some general background information, certain research objectives and the motivation for conducting this research project.

Chapter 2 provides a review of the literature relevant to this research project. A detailed description of the thermal spray techniques considered in this study is present. Also included is a review of the gas dynamic theory relevant to the design of a CGDS nozzle. Finally, a review of TBC systems, bond coats oxidation performance and failure mechanisms is presented.

Chapter 3 describes the specific objectives of this research work in order to facilitate the understanding of the study direction for the design of a CGDS nozzle and the characterization of bond coat oxidation behaviour.

Chapter 4 provides relevant detail pertaining to the research approach, instrumentation and equipment used throughout this study. A description of the feedstock material will be included as well as a description of the material characterization techniques.

Chapter 5 presents the approach and methodology used in designing a CGDS nozzle, specifically the use of CFD. Information obtained from CFD including the effect of gas temperature, pressure and nozzle stand-off distance will be presented.

Chapter 6 the manufacturing technique of the CGDS nozzle designed will be presented. Data relating to the physical testing of the nozzle will also be included.

Chapter 7 presents the characterization of the CoNiCrAlY feedstock powders. Key features such as phase content and grain structure are presented.

Chapter 8 presents a characterization of the CoNiCrAlY coatings manufactured via CGDS, HVOF and APS. Specific details such as coating phase content, porosity and oxide content are presented and compared with the original feedstock powder to determine changes that may have occurred in the deposition process.

Chapter 9 reports the results obtained from the extensive oxidation experiments carried out on bond coat samples. These results are then compared with results of a previous study done at a lower temperature in order to compare oxide growth rates, oxide scale composition and oxide morphologies. Results from long-term oxidation and non-grinded samples are also presented to provide the reader with a more in-depth comparison of the various coating processes and oxidation temperatures.

The conclusion will summarize the findings of this study and present final remarks on the content of this thesis. Recommendations and suggestions for future work are also included.

Chapter 2 - Literature Review

This chapter contains a detailed review of the literature relevant to this research project. The chapter will begin with an overview of current thermal spray technologies and coating processes with emphasis on the processes used to manufacture TBC systems. Following this, a more detailed review of the CGDS system will be presented. Detailed information on CGDS nozzle designs including an overview of gas dynamics will be included. Finally, a review of TBC systems with a focus on oxidation performance and failure mechanisms will be presented.

2.1. Thermal spray processes

While the goal of every thermal spray process is to deposit a coating on a given surface, the means by which this is achieved varies. The different processes have therefore been historically classified into categories based on the method of heating the coating material. Although kinetic spraying does not heat the material it is considered to be a derivative of the thermal spray processes and included in this classification. The categories are therefore as follows: plasma spraying, electric arc spraying, combustion spraying, and kinetic spraying as shown in Figure 2.1.

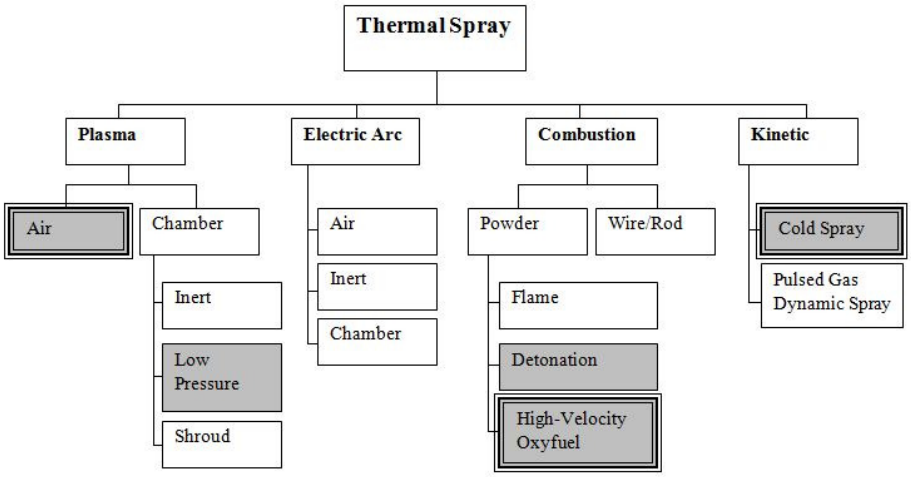

Figure 2.1: Classification of thermal spray processes (adapted from [8])

Each category features sub-categories which represent either evolutions or variations of their respective parent. The processes highlighted in gray in Figure 2.1, represent the thermal spray processes that are used to create TBCs and more specifically, those with a triple border are the processes of which bond coats are evaluated in this study. The following sections will describe each process in detail and include characteristics of the resulting coatings and microstructures.

2.1.1. Plasma Spraying

Plasma spraying is a technique that relies on heating a mixture of gases until it ionizes and is in a state known as plasma. The jet of high temperature plasma gas is then directed towards a substrate while feedstock material is injected in the stream to be deposited in either a molten or semi-molten state. In order to heat the gases, a heat source comprised of either a direct current electric arc or a radio frequency discharge is used. These methods are able to heat the gases to temperatures over 25000K [**6**] while temperatures of 8000K are sufficient to melt any material [**12**] at atmospheric pressure. Different carrier gases are used to form the plasma jet in order to control the heat transfer to the particles. This is an important spray parameter to ensure the particles are uniformly heated. Typical gases are mixtures of Ar, He, N_2 and H_2. The plasma flow is accelerated through a nozzle to reach high velocities. In some cases the nozzles are designed to accelerate the plasma to supersonic speed. Particles are injected into the plasma jet either at the exit of the nozzle or within the nozzle itself though the use of an inert carrier gas. A schematic of a typical plasma torch is shown in Figure 2.2.

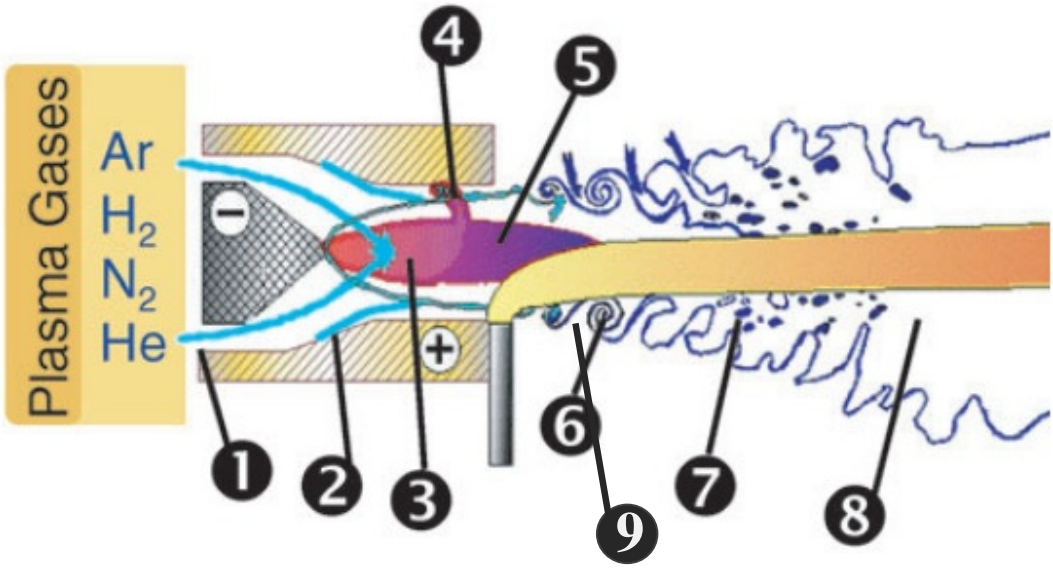

Figure 2.2: Schematic of a DC arc spray plasma torch. 1-plasma forming gas injection, 2-cold boundary layer, 3-Arc column, 4-connecting arc column, 5-plasma jet exiting nozzle, 6-large scale eddies, 7-surrounding atmosphere bubbles, 8-plasma plume, 9-powder injection. (Adapted from [12])

In an ideal scenario, the particles deposited by plasma spraying are fully melted, uniformly heated and achieve velocities as high as possible. In reality, this is very difficult to accomplish since increasing the particle residence time in the plasma jet in order to obtain uniform heating, also means a decrease in the particle velocities. The variation of particle sizes also increases complexity as small particles need to be fully melted even if their residence time in the plasma jet is much lower than the larger particles. In general, the plasma jet accelerates the particles to velocities between 10 and 600 m/s while the plasma jet itself can have velocities ranging from 600 to 2500 m/s[**12**]. In plasma spraying, the particles flatten and solidify upon impact to form a coating while some material is expelled and "splashes" onto other parts of the substrate due to the impact shockwave. The cooling rate of the particles is on the order of 10^7 to 10^8K/s [**12**]. In most cases, preparation of the substrate material via cleaning followed by grit blasting or water jet is mandatory for the adhesion of the coating. Once the particles have been in contact with the plasma jet and are at a high temperature, the surrounding atmosphere can react with the particles. To mitigate the effect this can have on coatings it is possible to locate plasma spraying equipment in a controlled atmosphere. Some of the variations of air plasma spray (APS) are called vacuum plasma spray (VPS) which is done in a vacuum or low pressure plasma spray (LPPS) which occurs at a lower pressure than ambient. Although these techniques reduce the amount of oxidation

and other detrimental effects, their purchase and operation costs has been estimated to be over one order of magnitude higher than conventional APS[**12**] and thus the use of such techniques is limited to a few high value added coatings.

Plasma spraying is suitable for the deposition of many materials including metals, alloys and high melting point ceramics and is considered the most versatile coating technique. Recent developments in plasma spraying have made it possible to spray nanocrystalline coatings through various techniques that limit particle melting. The plasma spraying technology continues to evolve especially with the advent of CFD which has helped researchers determining the complex interactions between the plasma jet and the powdered particles as well as the behaviour of the particles on impact. It is expected that the plasma spraying industry will continue to grow and improve as understanding of the effect of approximately 60 spray parameters and better models are developed to characterize the plasma jet and its effects on coating properties.

2.1.2. Combustion Spraying

Combustion spraying is a thermal spray process in which thermal and kinetic energy is generated by the combustion of fuel and used to accelerate feedstock material towards a substrate. The feedstock material is injected axially into the spray gun in the form of powders, wires or rods. The most notable combustion spraying technology is the D-Gun developed by Union Carbide (now Praxair Surface Technologies Inc.). In this process oxygen and acetylene are mixed and ignited increasing gas temperature from between 300 to 3600K depending on the gas mixture[**13**]. The supersonic detonation wave travels down a barrel at a pressure of 1.02MPa while accelerating particles towards the substrate [**13**]. The chamber is then purged using an inert gas and readied for another detonation. This detonation and purging cycle occurs at a frequency of 1-15Hz [**13**] although recent developments have reported up to 50Hz. The D-Gun is therefore considered an intermittent process as coating only occurs during a detonation and not through the entire cycle. A D-Gun schematic is presented in Figure 2.3. A similar non-intermittent process capable of elevated operating pressures was developed and known as high-velocity oxy-fuel (HVOF) spraying.

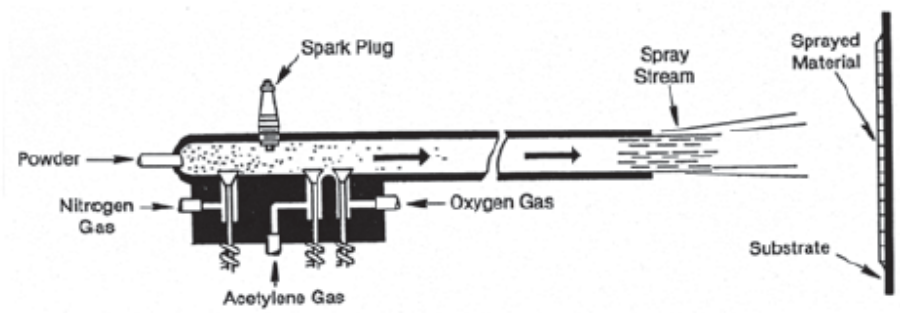

Figure 2.3: Schematic of cross-section view of a D-Gun [14]

HVOF improves on the D-Gun by making the process continuous and increasing operating pressures thus increasing particle velocity. Various HVOF configurations were developed to modify cooling method (air or water), combustion location (throat or chamber) and powder injection location (axial or radial). Different combustion gases such as hydrogen, propane, acetylene or kerosene can be used depending on the temperature and pressure required. HVOF systems are also equipped with a converging-diverging nozzle in order to accelerate the flow to supersonic velocities [**15**]. The hot gases are accelerated through this nozzle to velocities which can reach 1900m/s and temperatures of approximately 3300K[**13**]. The velocity of particles has been measured to range from 400m/s to 1050m/s and can reach a temperature of 2500K[**13**]. A schematic of an HVOF spray gun is depicted in Figure 2.4.

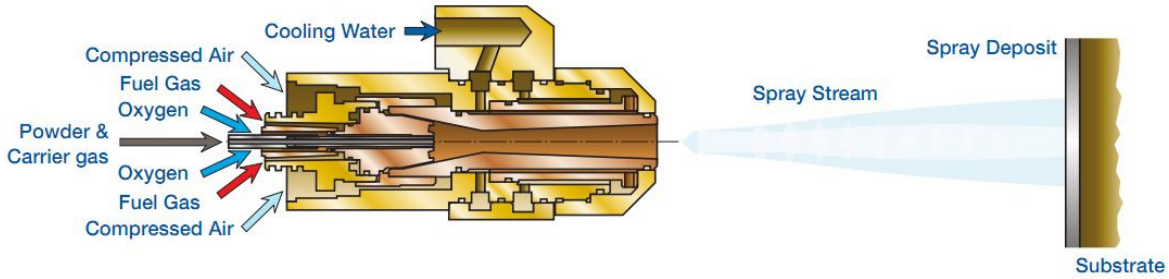

Figure 2.4: Schematic cross-section view of an HVOF spray gun [16]

Particles can be melted, partially melted or softened depending on the flame temperature, exposure time and particle size and composition. Increasing the nozzle length will increase both particle temperature and velocity as shown in Figure 2.5.

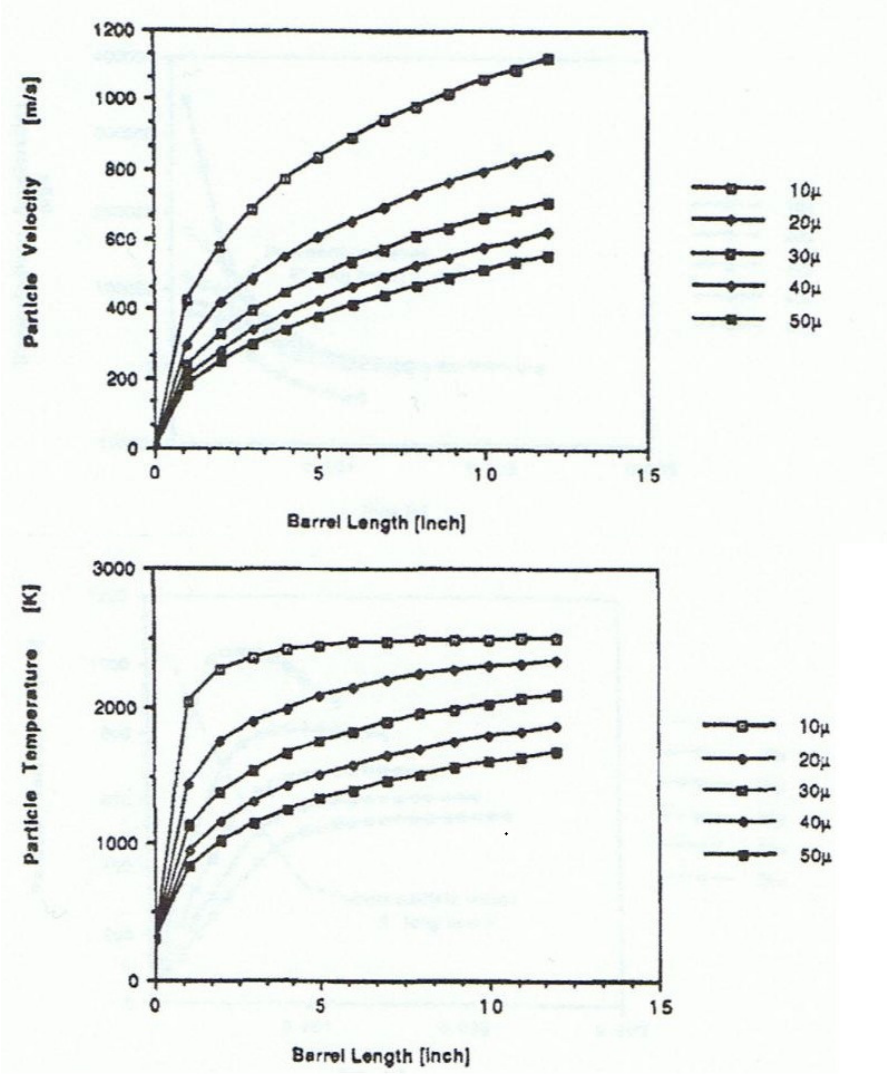

Figure 2.5: Effect of barrel length on particle velocity and particle temperature with respect to particle diameter (indicated on right) [13]

Unlike plasma spraying, HVOF can rely on lower temperatures and higher kinetic energies. The coating formation is therefore due to a combination of splat formation from melted particles and of plastic deformation upon impact with the substrate. Due to the lower temperatures involved in HVOF, the coatings usually do not exhibit as much oxidation or grain growth when compared with plasma spraying. The increase in particle velocities counters the loss in thermal energy and enables HVOF coatings to have very low porosity levels due to the plastic deformation. HVOF is currently used to deposit dense coatings composed of hard materials such as WC-Co and other metallic coatings including TBC bond

coats. However due to the lower process temperatures, HVOF is unsuitable for the deposition of high melting point ceramics.

2.1.3. Kinetic Spraying

The kinetic spraying processes rely on kinetic energy rather than thermal energy to produce coatings. Kinetic spray processes include kinetic powder deposition, kinetic spraying, high-velocity powder deposition and Cold Gas Dynamic Spraying (CGDS). Kinetic spraying processes were developed in order to solve problems relating to elevated temperatures in traditional coating methods. In these spray processes, the coatings are manufactured almost exclusively by kinetic energy and thus high particle velocities are required to compensate for the lack of thermal energy on impact. Particle velocities can be on the order of 200-1200m/s [**17**]. Although gas stagnation temperature can reach up to 1250K at the nozzle inlet [**18**,**19**], the expansion of the gas rapidly reduces its temperature downstream of the throat. The dwell time of the particles in the hot gases is also very short and limits their rise in temperature. The particle temperatures are therefore low enough to attribute coating formation solely to plastic deformation as a result of the high velocity impact. Due to the necessity for the coating particles to undergo a high degree of plastic deformation in order to adhere to the substrate, this coating method can only be employed with ductile materials. Brittle materials such as ceramics are incapable of deforming plastically and merely erode the surface. These brittle materials can be deposited if they are included in a ductile matrix to form a composite coating [**20**]. A more detailed description of the CGDS process is presented in Section 2.2.

2.1.4. Emerging Processes

Some processes have been developed throughout the years that are modifications or evolutions of existing technologies. One of these technologies is pulsed-gas dynamic spraying (PGDS) in which particles are accelerated towards the substrate through the use of shockwaves. As opposed to the DGun process, there is no combustion, rather the driving gases are selected to maximise the speed of sound much like in the case of CGDS process. In PGDS, both the driving gas and the feedstock powder particles are heated before being injected in a tube. A shockwave is then created using a valve located between the driving gas and the tube inlet. This shockwave accelerates and heats the powder particles until they

impact the substrate. The additional heat due to the shockwave combined with the pre-heating of the powder particles reduces the material critical velocity and thus lower impact velocities required for deposition[**21**]. Much like CGDS, this process maintains the material below its melting point however the velocities required for deposition are lower than in the CGDS process. This process is therefore a compromise between the high velocities of CGDS and the high particle temperatures of HVOF. This process has been demonstrated to successfully deposit materials such as Cu, Zn, Al, Al-12Si, amorphous Fe and nanocrystalline WC-15Co[**21**]. A schematic of the PGDS process is depicted in Figure 2.6.

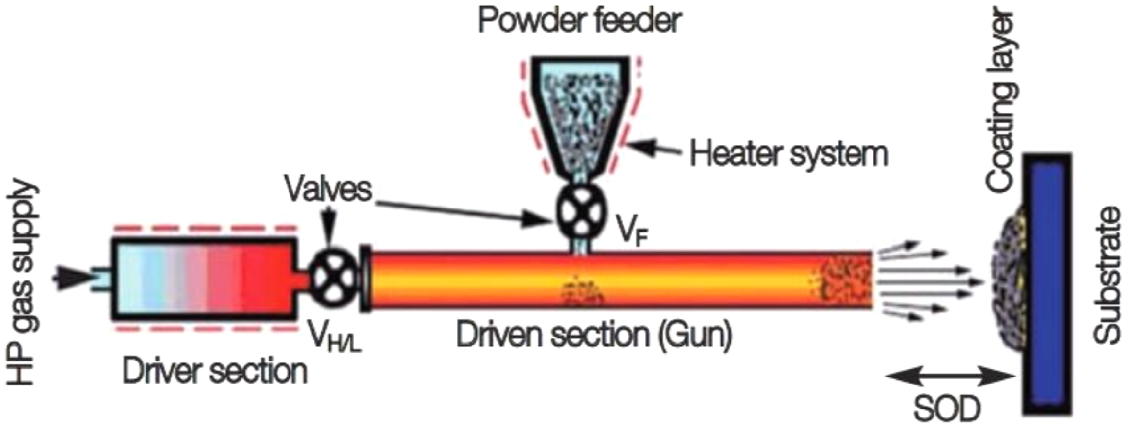

Figure 2.6: Schematic of PGDS process [22]

Another process which has evolved from HVOF is warm spraying. This process was developed in an attempt to reduce particle temperatures and increase particle velocities, becoming a compromise between CGDS and HVOF. By modifying the nozzle geometry and the driving gases, more of the energy transferred to the particles can be kinetic as opposed to thermal. The particle velocities can be maintained while their temperatures are reduced in an attempt to achieve higher coating qualities through reduced particle melting. This process has been able to lower HVOF particle temperatures while maintaining the same velocities and was successful in depositing titanium, metallic glass, cermet and plastics[**23**].

Finally, laser-assisted cold spray (LCS) has been explored in recent years. This process uses a conventional CGDS setup with non-heated gases and a laser of varying power to deposit particles. The CGDS system provides high particle velocities while the pulse laser system increases the thermal energy through heating of the substrate directly at the

deposition location. The heating of the substrate decreases its hardness and facilitates plastic deformation upon particle impact. Due to the lack of gas heating, the particle velocities achieved by this CGDS system are lower than in conventional cold spraying. The lower amount of kinetic energy is balanced by higher thermal energy provided by heating of the substrate. Since the laser pulses are focused specifically at the particle impact site, the amount of detrimental effects in the substrate due to heating are minimized. When coating a surface with multiple overlapping passes, the deposited coating is heated using the laser in order to allow for further coating deposition. This process once again attempts to bridge the gap between CGDS and HVOF. LCS has been demonstrated to have the ability to produce dense titanium coatings [**24**]. A schematic of the LCS process is depicted in Figure 2.7.

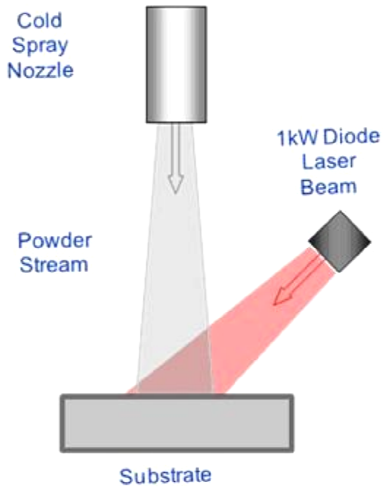

Figure 2.7: Schematic of the LCS deposition process [25]

2.1.5. Summary and Comparison of Thermal Spray Processes

The operating features such as particle temperature and particle velocity of the thermal spray processes discussed in this section are presented in Figure 2.8.

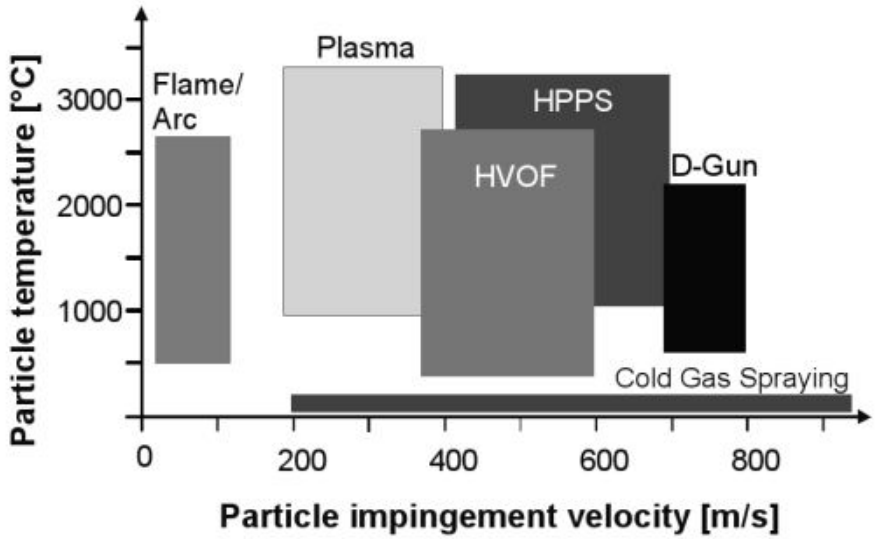

Figure 2.8: Comparison of ranges of particle velocities and particle temperatures for various thermal spray processes [26]

As can be seen in this figure, the plasma spray process has the highest particle temperature while having mid-range particle velocities. In contrast, kinetic spraying has very low particle temperatures and very high particle velocities. The combustion processes are somewhere in between with moderate temperatures and moderate to high particle velocities. Other processes discussed such as PGDS, warm spraying and LCS lie between the detonation processes and cold spray. Due to these differences, certain spray techniques are more suitable for the deposition of particular types of materials. The process temperatures and particle velocities for each process is outlined in Table 2-1.

Table 2-1: Characteristics of various thermal spray techniques [6,13,17,21,23,24]

Spray Technique	Process Temperature	Particle Temperature	Particle Velocity	Suitable Materials
Plasma	5000-25000K	1200-4500K	10-600m/s	Metals & ceramics
Detonation	600-3900K	Up to 2500K	400-1050m/s	Metals, cermets & low-melting point ceramics
Kinetic	300-1100K	Up to 900K	200-1200m/s	Metals
Emerging Techniques	900k-2500K	600K-1500K	250-800m/s	Metals, polymers & cermets

Due to the different particle temperatures and velocities of the various thermal spray processes, there are some differences between coating features and properties. Cross-sectional images of coatings produced by the APS, HVOF and CGDS coating processes are presented in Figure 2.9. Typical coating properties can be found in Table 2-2. These three processes were chosen for comparison as the oxidation performance of coatings produced by these methods will be analysed in the following sections.

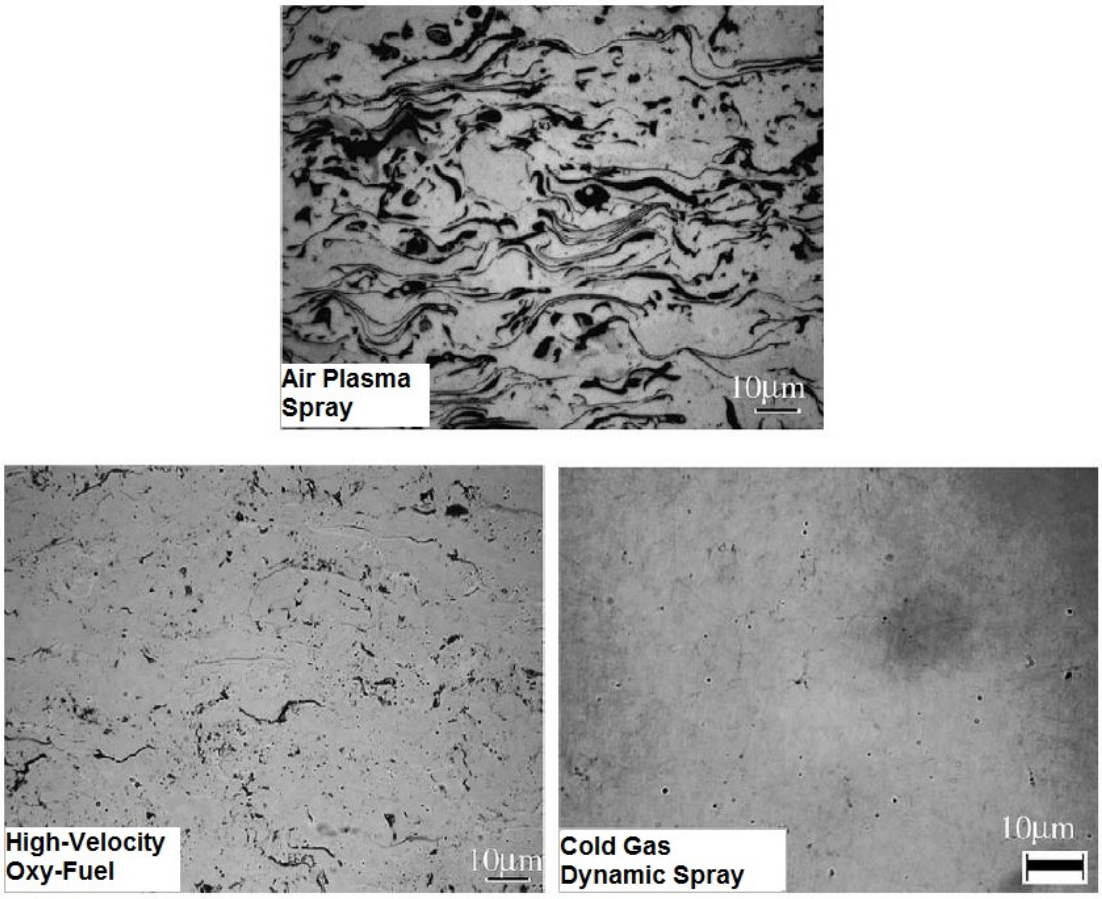

Figure 2.9: Cross-section images of Ni-Al alloy coatings manufactured by air plasma spray, high-velocity oxy-fuel and cold gas dynamic spray (adapted from [27])

Table 2-2: Typical characteristics of various thermal spray techniques [8,28,29]

Coating Property	APS	HVOF	CGDS
Porosity (%)	1-40	0.5-5	0.5-20
Oxide Content	Moderate-High	Moderate	Minimal
Residual Stresses	Tensile	Compressive	Compressive
Adhesion Strength (MPa)	10-45	Up to 80	20-70

All three coating processes are able to manufacture coatings with low porosity, with the APS coatings being more porous than the two others. Due to the elevated temperatures and melting of the particles in-flight, APS coatings have the most oxide content followed by HVOF. The low oxide content of the CGDS coatings is attributed to the inert atmosphere and low process temperatures. Coating processes with higher kinetic energy produce coatings with compressive residual stresses as is the case with HVOF and CGDS. These types of residual stresses generally improve mechanical properties. Coatings manufactured via HVOF and CGDS are expected to outperform APS while behaving similarly to one another.

2.2. Cold Gas Dynamic Spraying

This section will present a detailed review of the kinetic spray process known as Cold Gas Dynamic Spraying. The process historical background and overview will be presented including basic gas dynamic principles. Important process concepts will be discussed such as particle critical velocity, advantages, limitations, nozzle design considerations and an overview of bonding mechanisms.

2.2.1. Background

As with many scientific discoveries, the cold gas dynamic spraying process was discovered by accident in the mid-1980s at the Institute of Theoretical and Applied Mechanics of the Siberian division of the Russian Academy of Science in Novosibirsk. While conducting experiments in a supersonic wind tunnel to observe models subjected to two-phase flow (gas + solid tracer particles), it was observed that metallic particles injected into the flow were depositing on the leading edges of the models[**30**]. Using laser Doppler velocimetry (LDV),

the researchers determined that aluminum was depositing at a velocity of 400-450m/s while bronze particles were eroding the models [**30**]. The coating formation was attributed to the particle velocity and further experiments on this potential coating method were conducted. A system was designed that was able to accelerated aluminum particles up to velocities of 1200m/s in order to further investigate this build-up phenomenon. Several more experiments were conducted to test the deposition of other materials. Recognising this process had much potential, patent applications were filed and a US patent was issued in 1994[**10**] followed shortly by a European patent in 1995. Since the first patent was issued, research on the subject has increased and the number of patents has increased exponentially [**31**]. As of 2007, there have been 164 patents applications relating to the CGDS process worldwide [**31**]. Many commercial CGDS systems have been developed and are currently on the market and many in-house systems in laboratories are in use to further develop and perfect the CGDS technology[**31**].

2.2.2. Process overview

The CGDS process uses a high-pressure gas supply to generate the driving flow and accelerate powder particles. The gas used is typically helium or nitrogen and depends on the particle velocity requirements. Prior to entering the nozzle, the driving gas is heated to temperatures up to 1100K as a mean of increasing the gas velocities downstream. The flow is then directed through a converging-diverging (de-Laval) type nozzle to expand and accelerate to supersonic speeds. As the gas expands, its temperature is reduced while its velocity increases, in other words, thermal energy is converted into kinetic energy. It is therefore possible to increase the outlet velocities by increasing the initial gas temperature. The nozzle geometry also affects the outlet velocity by dictating the expansion ratio of the gas. A detailed analysis of the gas dynamics involved in CGDS can be found in the following section.

Powders are injected into the driving gas through the use of a second gas flow (carrier flow). This carrier flow is directed through a powder feeder where it entrains powder particles into the driving gas where they are accelerated to the required velocity. The powder injection point is usually located in one of these two different areas: axially prior to the nozzle throat or radially through a sidewall port in the nozzle, downstream of the throat.

While particles injected axially can theoretically achieve a slightly higher velocity due to their longer dwell time in the driving gas, these particles are heated to higher temperatures and can possibly clog the nozzle throat. High-pressure powder feeding equipment and gas flows also increase equipment costs. Radial injection downstream of the throat has the advantage of using lower pressure carrier gas and equipment but can suffer from lower particle velocities and the erosion of the nozzle. Erosion in the nozzle is caused by particles which impact the nozzle walls downstream of the injection point. In radially injected nozzles, the risk of this is increased due to the need for an initial particle radial velocity in order to enter into the driving gas stream. A schematic of a typical CGDS system is illustrated in Figure 2.10.

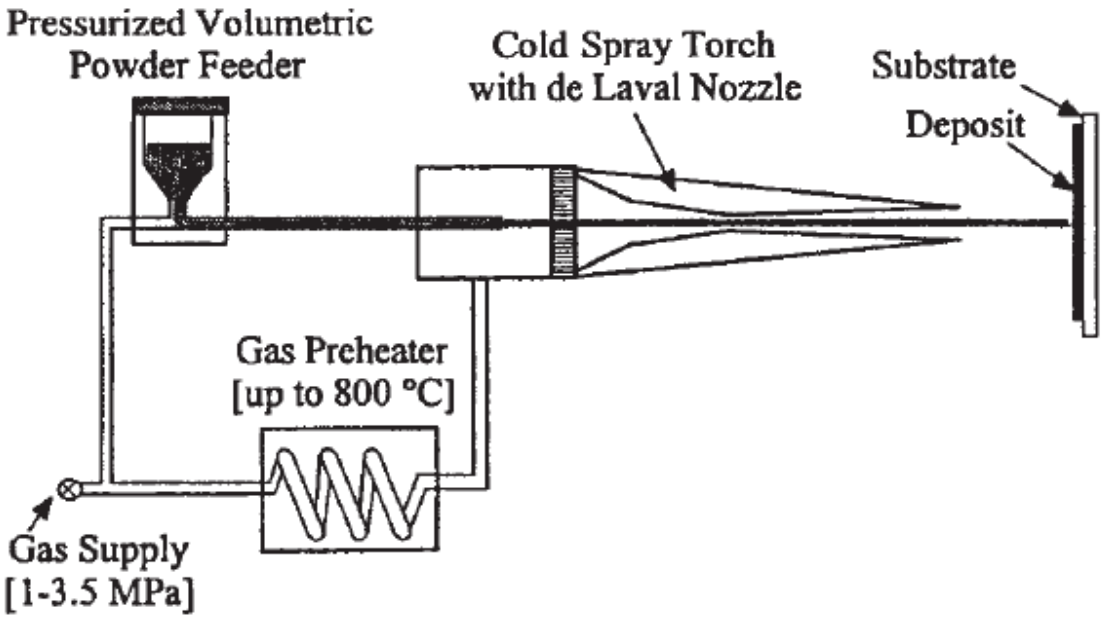

Figure 2.10: Diagram of a typical CGDS system [14]

2.2.3. Gas Dynamic Principles in CGDS

The current section will examine the fundamental gas dynamic principles relevant to the CGDS technique. The most important component of CGDS systems is the nozzle which is responsible for accelerating the driving gas to supersonic velocities. In order to properly design a nozzle for this task, proper understanding of compressible fluid mechanics is required. This section will introduce compressible flow concepts including flow through

variable area sections, gas stagnation properties, flow in a converging-diverging nozzle and important information relevant to nozzle design.

2.2.3.1. Relevant Assumptions for CGDS

The fluid mechanics of CGDS are complex and can be greatly simplified by using a few relevant assumptions. The CGDS process typically uses inert gases as the driving and carrier gases. It is therefore a valid assumption to assume these gases are calorically perfect. The flow is assumed to be in a steady-state, meaning there are no variations of flow conditions with respect to time. This would be the case in a commercial CGDS system where all parameters are monitored and controlled during the spray process. The flow is also assumed to be isentropic. Isentropic flows are both adiabatic and reversible, this means that no energy is added or removed from the flow and friction or viscous effects are ignored. In the case of CGDS, these assumptions are thought to be valid as the effects of friction and energy transfer from the system are minimal due to the very short nozzle length. Finally, the flow is assumed to be one-dimensional. This supposes that the flow and fluid properties are uniform throughout a given cross-section. Given that the flow properties vary greatly in the nozzle axial direction, the small variations in the radial direction are negligible. For example, pressure in the nozzle can vary from 4MPa to 100kPa (or 4000%) from the inlet to the outlet (axially) while variations in the radial direction are expected to be orders of magnitude lower. Although these simplifications will allow for the rapid calculation of gas properties throughout the CGDS nozzle, they induce some amount of error in the final result which is expected to be approximately 20%.

2.2.3.2. Introduction to Compressible Flows

Flows are considered compressible if a considerable change in density occurs when changing the pressure applied to the fluid. In liquids, this change in density is generally minute while in gases it can be quite considerable. When dealing with compressible flows, one has to consider that density may change. In order to analyse the effects of compressibility, we must consider the effect of a simple pressure wave travelling through a stagnant gas. It should be noted that pressure waves travel in a medium at the speed of sound for that specific medium. When the continuity and momentum equations are applied to both sides of the pressure wave, the following equations can be obtained [**32**]:

$$\frac{d\rho}{\rho} = \frac{du}{c} \tag{2.1}$$

$$c^2 = \left(\frac{dP}{d\rho}\right)_s \tag{2.2}$$

where ρ is the flow mass density, u is the flow velocity, c is the local speed of sound and P is the flow local static pressure. Equation 2.1 relates the change in density with the change in velocity with respect to the speed of sound. Equation 2.2 relates the speed of sound to the change in pressure with respect to density. According to this equation, the larger the speed of sound, the higher a pressure increase is required to change the density. Mediums in which the speed of sound is low are therefore more compressible than those that have a high speed of sound. When considering a perfect gas in an isentropic evolution, equation 2.2 can be simplified to:

$$c = \sqrt{kRT} \tag{2.3}$$

where k is the specific heat ratio, R is the specific gas constant and T is the local static temperature. The speed of sound of a gas is therefore dependent both on the gas type and on the static gas temperature. Using this equation, it is possible to compute the speed of sound for various gases which could be used in the cold spray process as outlined in Table 2-3.

Table 2-3: Speed of sound of various fluids at standard pressure and temperature

Fluid	Speed of Sound
Carbon Dioxide	269 m/s
Argon	322 m/s
Air	346 m/s
Nitrogen	351 m/s
Helium	1016 m/s
Hydrogen	1315 m/s

As can be seen from these values, Hydrogen and Helium have a very high speed of sound when compared to the other gases. They are therefore excellent candidates for use as driving gases in CGDS systems.

The Mach number is a non-dimensional number given by the ratio of the flow velocity with respect to the speed of sound, and is determined with the following equation:

$$M = \frac{u}{c} = \frac{u}{\sqrt{kRT}} \tag{2.4}$$

The Mach number is a very important property when considering compressibility effects in flows. When Mach numbers are low (M<0.3), the flow is considered incompressible and its density is mildly affected by changes in pressure. In the subsonic regime (0.3<M<1) compressibility effects are present and density is directly influenced by changes in pressure. A flow is said to be sonic if it is travelling exactly at the speed of sound (M=1) while it is considered supersonic when its velocity is greater than that of sound (M>1). In both of these cases the compressibility effects of the gases must be considered. The Mach number is therefore used extensively when characterizing compressible flows and their properties.

2.2.3.3. Flow Through a Variable Area Section

This section contains an analysis of flow through a variable area section for a one-dimensional, steady and isentropic flow. Three governing equations are considered to investigate this scenario: continuity, conservation of energy and Gibbs equation. Under these conditions, the equations can be combined to the following [**32**]:

$$\frac{du}{u}(1 - M^2) = -\frac{dA}{A} \tag{2.5}$$

$$dp(1 - M^2) = \rho u^2 \frac{dA}{A} \tag{2.6}$$

where *A* is the cross-sectional area. Equation 2.5 relates the change in velocity ($\frac{du}{u}$) to the change in area ($\frac{dA}{A}$) by the use of the Mach number while equation 2.6 is a relation to determine the change in pressure relating to a change in area. With these equations, the properties of a gas passing through a nozzle can be determined if the gas stagnation properties and the nozzle geometry are known. When dealing with subsonic (M<1) flows, a change in area is inversely proportional to the change in velocity. If passing through a diverging section, the flow decelerate while if it is passing through a converging section it will accelerate (left side of Figure 2.11). However, when dealing with supersonic flows (M>1) the change in area is proportional to the change in velocity. If passing through converging sections, the flow will decelerate while when passing through diverging sections

it will accelerate (right side of Figure 2.12). The tipping point is found at sonic velocities (M=1). The response of a flow to a specific geometry can be more clearly explained through the use of a graphical representation available in Figure 2.11.

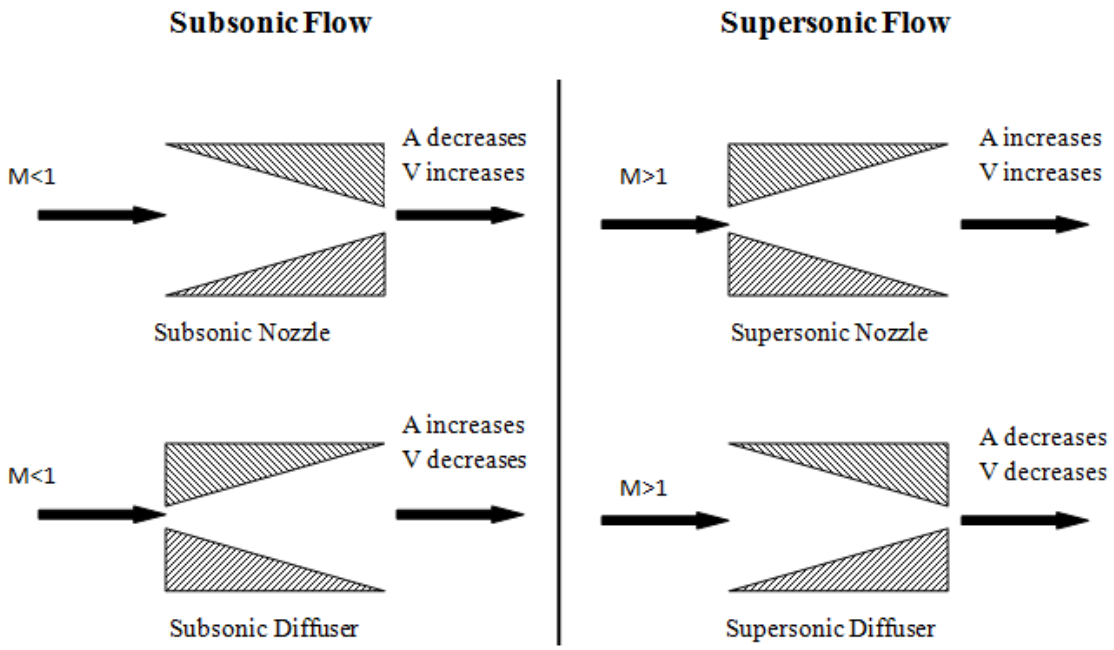

Figure 2.11: Representation of differences in flow behaviour for subsonic and supersonic flows in nozzles of variable area

With this flow behaviour in mind, the specific nozzle geometry required to accelerate the flow to supersonic velocities can be determined. The flow must first be accelerated to sonic conditions through the use of a converging nozzle. At this point, the flow is said to be choked, no further acceleration is possible through area reduction. Once this velocity is reached, further acceleration of the gas requires the use of a diverging nozzle. This type of nozzle is called a converging-diverging nozzle due to the geometry. A schematic of such a nozzle is presented in Figure 2.12.

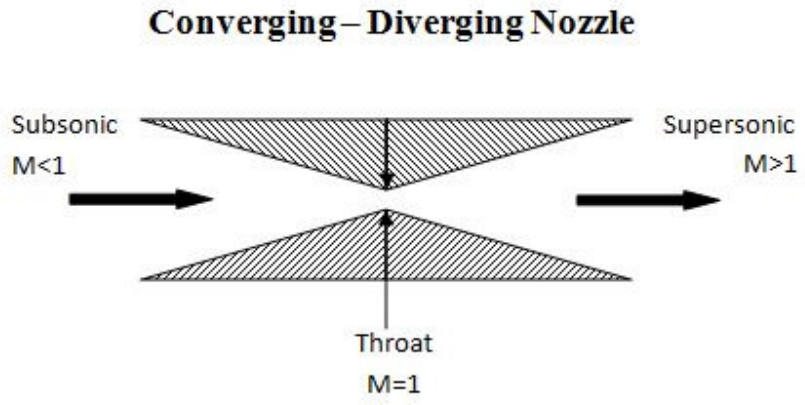

Figure 2.12: Schematic of converging-diverging nozzle required to accelerate a gas to supersonic velocities.

Although this nozzle geometry has the potential for accelerating the flow to supersonic velocities, this is not always the case. Low gas stagnation pressures will prevent the flow from reaching Mach 1 at the throat. The flow will therefore remain subsonic in the converging section and will never reach sonic or supersonic velocities. Other parameters can also have an influence on the fluid flow and will be discussed in the following section.

2.2.3.4. Definition of fluid stagnation properties

Fluid stagnation properties of a flow represent the properties that would be measured should the flow be decelerated isentropically to a velocity of zero. When considering the properties of a flow, it is simpler to refer to the stagnation properties which can be controlled and easily determined than the instantaneous properties at some point in the flow. As a gas passes through a converging-diverging nozzle, its pressure and temperature decrease while its velocity increases. These variations in temperature and pressure can be calculated for the general case of a calorically perfect gas that follows an isentropic expansion [**32**]:

$$\frac{T_0}{T} = 1 + \frac{k-1}{2}M^2 \tag{2.7}$$

$$\frac{P_0}{P} = \left(1 + \frac{k-1}{2}M^2\right)^{\frac{k}{k-1}} \tag{2.8}$$

where the stagnation properties are identified with the subscript $_0$. These equations are important in determining the properties of a flow given its current Mach number. Inversely, the Mach number can be determined knowing the current flow properties and the stagnation properties. The equations can also indicate what stagnation properties are required to reach a

certain Mach number. For example, if a flow of nitrogen ($k=1.4$) is to be accelerated to Mach 2, the discharge temperature will be reduced by 56% of the stagnation temperature and the stagnation pressure will need to be 7.8 times larger than the discharge pressure. The stagnation pressure must be carefully chosen in order to obtain a supersonic flow from a converging-diverging nozzle without inducing detrimental shockwaves. The following section will analyse flow through such a nozzle.

2.2.3.5. Compressible isentropic flow in converging-diverging nozzle

In order to analyse the flow through a converging-diverging nozzle, the pressure ratio must be varied. This pressure ratio is defined as the stagnation or inlet pressure P_0 divided by the back or exit pressure P_B. Seven different flow behaviours are identified in a converging-diverging nozzle by varying the back pressure and thus, changing the pressure ratio (Figure 2.13).

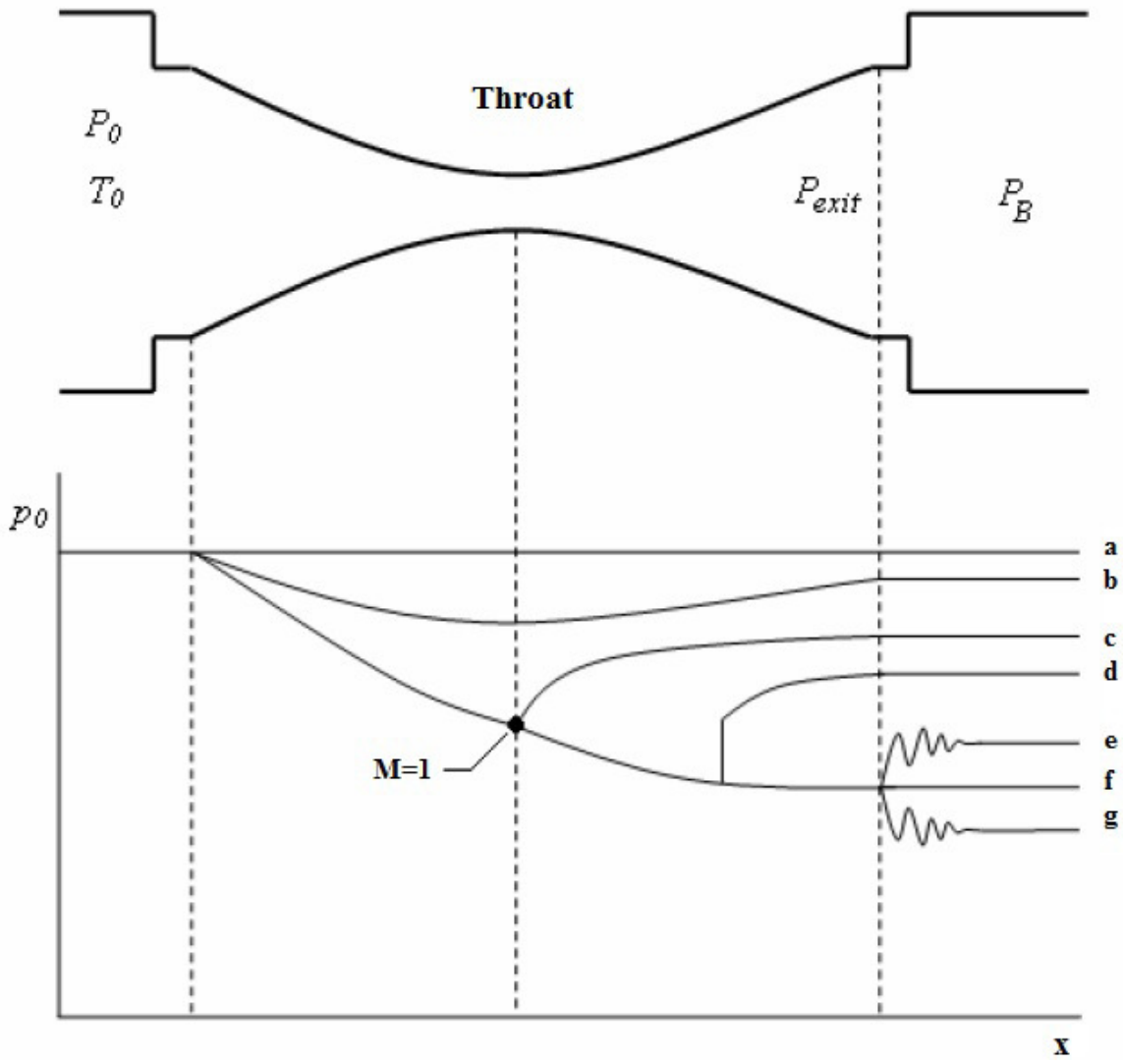

Figure 2.13: Flow behaviour in a converging-diverging nozzle as a function of the pressure ratio P_0/P_B (adapted from [33])

In case a) the back pressure is equal to the stagnation pressure ($P_0 = P_B$) and no flow is detected through the nozzle. When the back pressure is reduced, gas begins to flow through the nozzle. In case b), the pressure ratio is not significant enough to choke the flow (M<1) at the throat. The flow is therefore accelerated in the converging section and decelerated in the diverging section remaining at subsonic velocities and exiting the nozzle at a pressure equal to P_B. Further decreasing the back pressure will yield a pressure ratio large enough to choke the flow at the throat (M=1) but too low to increase velocity after the throat as is depicted in case c). The flow therefore decelerates in the diverging section and returns to an exit pressure of P_B. Reducing the back pressure, the flow is now choked and reaches

supersonic velocities for a portion of the diverging section. The pressure ratio is not high enough to accelerate the flow to the end of the nozzle and an abrupt deceleration of the flow is observed by the means of a shockwave inside the diverging section. The flow then reverts to subsonic velocities and exits the nozzle with a pressure equal to P_B as shown in case d). The remaining three cases e), f) and g) all have sufficient pressure ratios to achieve supersonic velocities at the end of the nozzle without experiencing shockwaves inside the nozzle. Case e) represents a case where the flow has been expanded in the nozzle to a pressure lower than the back pressure. To re-adjust itself to the ambient conditions at the exit of the nozzle (P_B), the flow increases pressure through the means of oblique shockwaves and expansion waves. This is a case of "over-expanded" nozzle flow. Case f) represents the ideal case where the flow reaches supersonic velocities and has a nozzle exit pressure equal to the back pressure. No shockwaves are formed and the pressure ratio is said to be matched to the nozzle geometry. This is a case of "ideally-expanded" nozzle flow. If the back pressure is further reduced, the flow continues to reach supersonic velocities much like the ideal case however, at the nozzle exit the flow is at a higher pressure than the back pressure represented by case g). To re-adjust to the correct pressure, the flow experiences a series of expansion waves and oblique shockwaves much like in the over-expanded case but in inverse order. This is a case of "under-expanded" nozzle flow.

A few interesting observations can be made, in cases c) through g). In these cases, the flow reaches sonic velocities at the throat, the conditions in the converging section are identical from case to case. This is due to the inability of the flow information of the downstream conditions to propagate past the throat. As the information is passed through infinitesimal pressure waves which travel at the speed of sound, they cannot propagate past the flow in the throat which travels at Mach 1. It is also apparent that CGDS nozzle designs should attempt to generate ideally-expanded flows as in case f). This case features no shockwaves to disturb the flow and slow down powdered particles [**34**]. Further analysis of CGDS design parameters are presented in the following section.

2.2.3.6. Design parameters of CGDS nozzles

Although the final flow characteristics are dependent on the gas stagnation properties, the physical geometry of the nozzle is one of the most important parameters when

accelerating flows to supersonic speeds. It is critical to understand the effect of the nozzle geometry, in order to obtain a design which will require attainable pressure ratios and be feasibly constructed. The most important parameter is the area ratio *A/A**, where *A** is the area at the throat and *A* is the area at the location of interest. To calculate the final gas Mach number, this location of interest is chosen as the exit of the nozzle. It is possible to relate the Mach number with the area ratio using the following equation [**32**]:

$$\frac{A}{A^*} = \frac{1}{M}\left[\left(\frac{2}{k+1}\right)\left(1+\frac{k-1}{2}M^2\right)\right]^{\frac{k+1}{2(k-1)}} \tag{2.9}$$

When solving equation 2.9 for a given area ratio, there are two possible solutions to the Mach number: subsonic or supersonic. The valid solution depends on the pressure ratio between the nozzle inlet and outlet. When substituting the Mach number of the supersonic case in equation 2.8, the stagnation pressure required to achieve supersonic flow can be determined.

Once the exit Mach ratio has been determined, it is possible to calculate the exit gas temperature by using equation 2.7. With the gas temperature it is then possible to calculate the speed of sound at this temperature using equation 2.3 and finally, the speed of the gas flow by using equation 2.4. This indicates that for a fixed geometry nozzle, the final gas flow velocity is dependent on the gas stagnation temperature. Increasing the gas stagnation temperature will therefore increase the local speed of sound and the gas velocity at the nozzle exit.

It is important to consider physical limitations in order to design a nozzle that is capable of operation with currently available materials and technology. Current systems are limited by gas temperatures and pressures. Since increasing gas stagnation temperature also increases exit velocity, it is favourable to increase the temperature as high as possible. The materials used for the nozzles must be able to resist these high temperatures without changing geometry due to thermal expansion. The temperature must also remain below the powder particle melting point in order to retain the beneficial effects of cold spray. The stagnation pressures also have an upper limit due to both material and safety constraints while the back pressure (typically atmospheric) is extremely costly to modify requiring a spray chamber with a controlled environment. Finally, the flow rate of gas can become a cost

issue especially when using helium as the driving gas. The mass flow rate should therefore be minimized to keep costs acceptable. The mass flow rate can be calculated by:

$$\dot{m} = \rho u A \tag{2.10}$$

When considering converging-diverging nozzles, the flow rate is most easily calculated using the throat as reference where the Mach number is known to be equal to 1. Using equations 2.5 and 2.8 into 2.10 and using the perfect gas law generates [**32**]:

$$\dot{m} = P_0 A^* \sqrt{\frac{k}{RT_0}\left(\frac{2}{k+1}\right)^{\frac{k+1}{k-1}}} \tag{2.11}$$

Equation 2.11 can be used to evaluate the mass flow rate at the throat based on throat area, the gas type and the gas stagnation properties. The mass flow rate is directly proportional to nozzle throat area and stagnation pressure. It is therefore important to know the limits of pressure and acceptable mass flow rates before determining the nozzle throat area and corresponding exit area.

Although the mass flow rate is an important consideration, recent developments may decrease the importance of this property. A recent study conducted at the National Research Council Canada evaluated a system designed for Helium recovery in Cold spray systems [**35**]. This system was able to recover up to 90% of the Helium during long-term spraying. This technology, although significantly increasing initial equipment costs, was estimated to reduce running costs to roughly the same as spraying with nitrogen (approximately 10 times reduction). For industrial applications where systems are used for extended periods of time, Helium recovery systems could provide significant savings.

Other considerations must be accounted for in the design of a CGDS nozzle. The analysis so far has considered isentropic flow behaviour. However, in reality some irreversibility occurs due to friction and viscous effects which can significantly change the flow behaviour. According to research conducted by Alkhimov *et al.* [**36**], boundary layers developed along nozzle walls can reduce the actual exit Mach number when compared to the isentropic approximation. The study evaluated the effect of varying the thickness-to-length ratio of the nozzles and obtained Mach numbers between 62% and 97% of the isentropic evolution. With high nozzle internal thickness-to-length ratios, very little disturbance is

observed due to the small boundary layer development in the shorter nozzles. As the ratio decreases, the longer nozzles allow boundary layers to evolve and negatively impact the flow. Another study conducted by Jodoin [**37**] investigated the effect of the exit Mach number on the shockwave created as the supersonic jet impinges the substrate. The bow shockwave is a result of the change of direction of the high-velocity gas due to the presence of the substrate. The shockwave reduces the gas velocity and increases its pressure and temperature. It can be observed to occur outside the nozzle, near the substrate surface. The shockwave was found to considerably slow down small and light particles and potentially reduce deposition efficiency. In order to limit the strength of the bow shock and therefore its effect on particles, recommendations were made pertaining to the maximum nozzle exit Mach number.

As seen previously (state the section) shockwaves can occur in the nozzle due to improper nozzle optimization. A technique used to reduce shockwave occurrence in the nozzle involves designing the nozzle profile to a specific geometry dictated by solving Euler equations via the method of characteristics (MOC). The Euler equations represent the conservation of mass, momentum and energy in a system with zero viscosity. The MOC is a method used to reduce partial differential equations to a set of ordinary differential equations. These ordinary differential equations can then be used to find a solution given initial conditions. When the Euler equations are solved using the MOC, discontinuities in the flow can be identified. At the discontinuity locations, weak compression or expansion waves are present. These waves propagate in the flow and can reflect off walls. Upon coalescence of multiple weaker waves stronger and detrimental shock waves are formed. To reduce the amount of shockwaves in the flow, it is possible to design the curvature of the wall to reflect the weak waves along the wall. A correctly designed wall curvature can reduce the likelihood of shockwaves forming in the flow and possible eliminate them completely. Nozzles designed using this method have been demonstrated to be more efficient at increasing particle velocities and scale better with increasing stagnation temperature compared with straight nozzles[**38**].

The most critical component of CGDS systems is the nozzle since it is the method by which the powdered particles are accelerated. Several studies have been directed towards

improving nozzle designs in an effort to reduce shockwaves and boundary layer effects while increasing particle velocities. The following section will review the physics behind the main function of the nozzle: particle acceleration.

2.2.3.7. Particle Acceleration

Powdered particles are accelerated in a nozzle due to the drag forces between the particles and the velocity flow surrounding it. The drag force F_D can be determined using the following equation [**32**]:

$$F_D = \frac{1}{2}\rho A_p (u - u_p)^2 C_D \tag{2.12}$$

Where ρ is the gas mass density, A_p is the projected area of the powder particle, u is the gas velocity, u_p is the particle velocity and C_D is the drag coefficient. From this equation it is apparent that the most important term is the relative velocity $(u\text{-}u_p)$ which is squared in the equation. This demonstrates the importance of achieving a high gas velocity through the use of a properly designed nozzle. Other parameters that influence the particle acceleration are the driving gas mass density, drag coefficient, the particle mass and its projected area. The driving gas density is dependent on the stagnation gas properties. Increasing the stagnation pressure will increase the gas density and therefore increase particle acceleration according to the perfect gas law. However, the perfect gas law also predicts a drop in density when temperature is increased. This decrease in density has little effect on particle acceleration when compared to the effect of increased gas velocity due to the increase in temperature. The drag coefficient is mostly dependent on the particle morphology and as such is very difficult to modify to gain any advantage. A study conducted by Jodoin *et al.*[**39**] observed that particles with an irregular morphology had a higher drag coefficient then particles with a spherical morphology. The mass can be included in the equation by combining it with Newton's second Law (F=ma):

$$a_p = \frac{\frac{1}{2}\rho A_p (u - u_p)^2 C_D}{m_p} \tag{2.13}$$

Where a_p is the acceleration of the particle and m_p is the particle mass. The correlation between particle projected area and particle mass can be calculated for spherical particles. Taking the particle projected area ($A_p = \pi\left(\frac{D_p}{2}\right)^2$) and dividing it by the mass of a particle

($m_p = \rho_p \frac{4}{3}\pi \left(\frac{D_p}{2}\right)^3$) where D_p is the particle diameter and ρ_p is the particle mass density we can obtain the following $\frac{A_p}{m_p} = \frac{3}{2\rho_p D_p}$. This result indicates that an increase in particle mass density or particle diameter will reduce its acceleration. Smaller particles are therefore favoured in the CGDS process for these reasons and heavier materials have been proven harder to accelerate.

Although some studies indicate that an increase in nozzle length will increase particle exit velocity due to an extended time in the driving flow [**40**], considerations for the boundary layer development must be taken [**36**]. In general however, CGDS systems use nozzles with long diverging sections. Although the gas dynamic principles of CGDS are complex, proper understanding of the effect of every variable is essential in ensuring optimal particle acceleration to reach the critical particle velocity required for bonding.

2.2.4. Critical Particle Velocity

It is not sufficient for particles to merely impact the substrate at any velocity in order to have a good material bonding. The material must have a certain minimum velocity to adhere or it will merely bounce off or erode the substrate. Many studies have been directed at determining the minimum velocity required for adhesion[**17**,**38**,**41**,**42**,**43**,**44**,**45**,**46**,**47**,**48**]. It was determined that the particle velocity at which deposition efficiency (DE) reaches 50% [**41**] (or in some cases when there is a noticeable increase in DE) has been dubbed the critical particle velocity. The deposition efficiency is defined as the ratio of mass deposited on the substrate over the mass of the total sprayed powder. Recent studies have also theorised a velocity beyond which the powder particles stop adhering to the substrate and begin eroding it [**17**,**47**]. This velocity has been named the erosion velocity. A diagram comparing the deposition efficiency with the particle velocity and associated particle deformation is available in Figure 2.14.

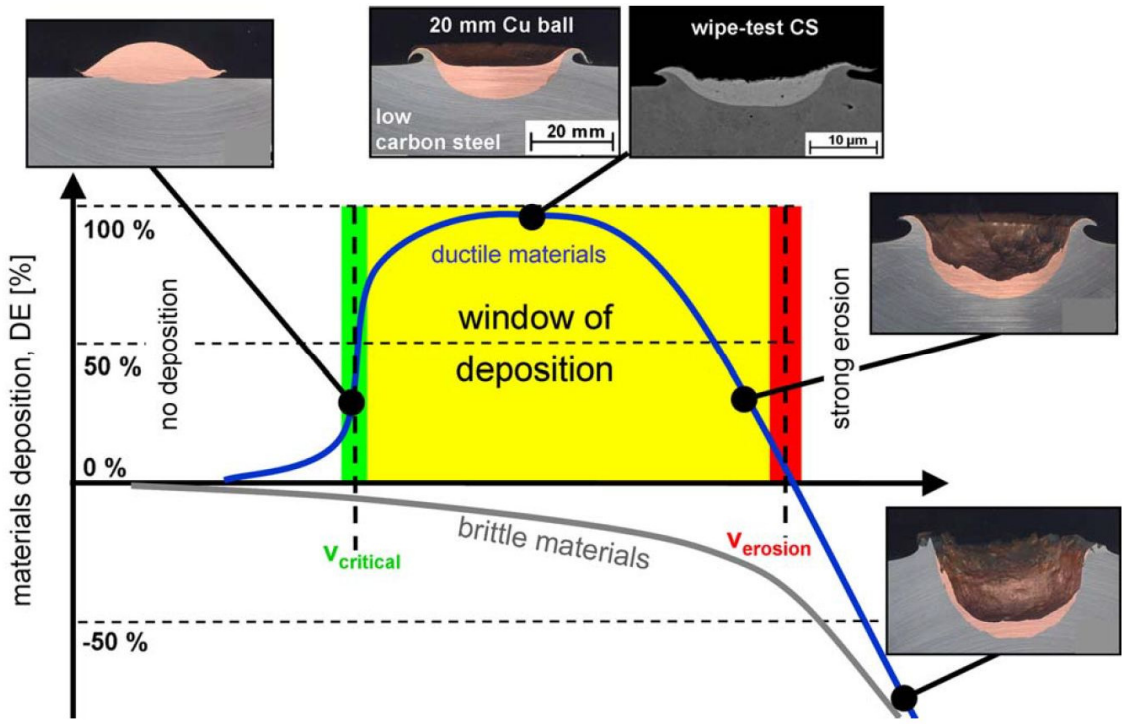

Figure 2.14: Deposition efficiency relative to particle velocity and associated cross-sectional images for large-scale kinetic processes [17].

As can be seen in Figure 2.14, the point at which the deposition efficiency starts to rise significantly is labelled the critical velocity. After this point, the DE continues to rise until it reaches a maximum. In theory, further increases in the particle velocities will reduce the DE until the substrate begins to erode. This has been demonstrated for large particles but has yet to be demonstrated for the CGDS process. Although this is a general trend in DE vs velocity, the actual velocities vary depending on material type[**17**,**48**], particle size[**42**,**47**], particle impact temperature[**44**,**45**], substrate material[**49**,**50**] and powder oxide content[**51**,**52**]. While all these properties have an effect on the critical velocity, the property that most affects it is the particle material type. Critical velocities are therefore typically given as a function of this property. Typical values for critical velocities of particles 20µm in diameter are presented in Table 2-4.

Table 2-4: Typical critical velocities for particles 20μm in diameter (Adapted from [17,48])

Material	Critical Velocity (m/s)
Aluminum	620-660
Titanium	700-890
Tin	160-180
Zinc	360-380
Stainless steel (316L)	700-750
Copper	460-500
Nickel	610-680
Tantalum	490-650
CoNiCrAlY	850-900

The large variation in critical velocities for different material types has been attributed to a difference in crystallographic structures, stiffness and density, melting temperature and mechanical strength [**48**]. Particle bonding occurs only when enough plastic deformation is achieved. Any property affecting the energy necessary for plastic deformation will also affect the critical velocity. Of particular interest for this study is the critical velocity of CoNiCrAlY, an alloy which is commonly used as the bond coat in TBCs. The high critical velocity, attributed to an elevated melting point and complex microstructure, makes this alloy extremely difficult to deposit requiring specially designed nozzles and in most cases, Helium as a process gas.

The temperature of particles at impact can significantly affect the critical velocity, a property which is taken advantage of in warm spraying and PGDS. Modelling work has been conducted by Schmidt *et al.*[**47**] which indicates that higher impact temperatures reduce particle critical velocity. However, increasing particle temperature is difficult due to the cooling effect of expanding the process gases in the converging-diverging nozzle. Pre-heating of powder may increase the powder temperature upon entry in the nozzle but these particles will be cooled during acceleration. Furthermore, the particle size will affect its heating and cooling rate and therefore its final impact temperature. A study conducted by Stoltenhoff *et al.*[**45**] modeled the nozzle exit temperature of copper particles of 15μm in diameter when cold-sprayed with varying gas stagnation temperature (axial injection). With

a gas stagnation temperature of 300K, the particle temperature was 200K, when raising the gas stagnation temperature to 800K, the particle temperature rose to 500K. While there is a definite heating of the copper particles, the temperature reached is much lower than the melting temperature of the material. Furthermore, increasing the gas stagnation temperature does not scale very well with the particle exit temperature. For any significant rise in particle temperature, the stagnation temperature would have to increase to levels higher than acceptable for current nozzle materials. The heat transfer to the particles could be raised by increasing the particle time spent in the hot region of the nozzle (for axial injection) but this would likely lead to more nozzle clogging issues. Heating of the particles through the use of a distinct powder heater (as is the case in PGDS) can also have a beneficial effect as was demonstrated by Schmidt *et al.*[**53**]. The powder pre-heating was only found to affect larger particles (with higher thermal capacity) while smaller particles would get quickly cooled by the cold process gases.

The modelling work done by Stoltenhoff *et al.* [**45**] also includes the effect of particle sizes, stagnation pressure and stand-off distance on particle velocity and particle temperature. According to their model, smaller particles had a lower nozzle exit velocity due to cooling in the nozzle diverging section. As particle size increases, the temperature increases due to the higher particle thermal capacity. Upon reaching a certain particle size, the heating section is insufficiently long to raise the particle temperature and a drop is observed. Stagnation pressure did not have an effect on particle temperature (but did raise particle velocity as expected) while an increase in stand-off distance slowly raised particle temperature and reduced particle velocity due to the presence of the bow shock which reduces gas velocity but increases gas temperature.

It has been reported that external oxidation of powdered particle increases its critical velocity. This has been used as an explanation for the relatively high critical velocity of aluminum [**42**]. It is thought that the velocity of the particles has to be high enough to break down the oxide film and plastically deform the particle. Another study conducted on copper, stainless steel and Monel particles oxidised to varying degrees has confirmed that the critical velocity increases with oxide content[**51**]. This was especially true for copper whose critical velocity was identified at 310m/s at 0.02% wt. oxide content and increased dramatically to

610m/s at 0.32% wt. oxide content[**51**]. As such, powders should be stored in an environment that prevents oxidation and used before they are significantly oxidised.

The substrate material can also have an influence on the critical velocity however this subject is controversial. Numerical modelling has indicated that harder substrate materials can affect the deformation mechanisms linked with particle bonding [**46**]. This finding was confirmed in a study by King *et al.* [**49**] which investigated the bonding mechanisms of particles impacting on different substrates. It was determined that harder substrates may not deform during particle impact and thus higher particle velocities are needed for successful bonding. However, further investigations by Yin *et al.*[**50**] concluded that once the first layer of material has been deposited, it essentially acts as the substrate. Particles will therefore impact with the previously deposited layer and deform it regardless of the underlying substrate (assuming the particles are above their critical velocity). It would appear that although the initial deposition of particles is affected by the substrate composition [**49**], once the initial layer of material is deposited, the difference from substrate to substrate has little or no effect [**50**].

For the CGDS process to function, particles must be accelerated above a critical velocity to properly deform and bond with the substrate. Although the critical velocity varies with material composition, particle size, particle temperature and oxide content, the bonding mechanism remains the same. The following section will seek to explain the bonding mechanisms involved in CGDS.

2.2.5. Bonding mechanisms

Although it is understood how to accelerate particles beyond the critical velocity in order to obtain coatings in the CGDS process, the actual bonding mechanisms are very complex phenomena. This section is dedicated to presenting the possible bonding mechanisms that occur during cold spraying.

Many studies have focused on the process involving bonding of particles to substrate and particles to particles in CGDS[**42**,**43**,**46**,**54**,**55**,**56**,**57**,**58**,**59**]. However, due to the complex and fast nature of the bonding process, there is no consensus on a single dominant bonding mechanism but rather a few dominant theories, all to be proven. In all cases, there is

agreement that high velocity impact of the particles onto the substrate leads to plastic deformation of both the particles and the substrate and dissipation of heat [**42**,**43**,**46**,**54**,**55**,**56**,**57**,**58**,**59**]. While some researchers believe that the amount of heat dissipated upon impact can cause local melting [**46**], others believe temperatures involved remain below the particle melting point [**42**,**43**,**55**,**56**]. These different views lead to different theories pertaining to the implicated bonding mechanism.

A theory proposed by Dykhuizen *et al.*[**55**] suggests that the bonding mechanisms found in cold spraying are very similar to those found in explosive welding. In explosive welding, metal plates are impacted at high velocities. Bonding is achieved through localized softening and solid-state jetting at the impact interface due to heat dissipation. These metal jets break up the surface oxides and provide clean and intimate contact between the two metals. This intimate contact between surfaces is necessary for good bonding. A photograph of the metal jetting is shown in Figure 2.15. Numerous modelling and experimental studies have demonstrated the formation of metal jets upon particle impact in the CGDS process. Many of these studies have also indicated that jetting occurred without the material reaching its melting temperature. A similar bonding mechanism without melting has also been suggested by Van Steenkiste *et al.*[**42**] where large pressures on impact cause localized plastic flow.

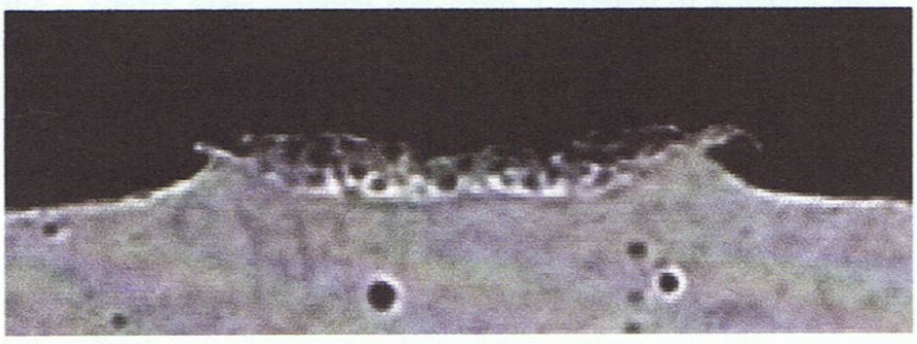

Figure 2.15: Cross section of a crater created by the impact of a 700m/s copper particle onto a stainless steel substrate showing evidence of material jetting. The crater was created using the CGDS process [55].

Modelling work by Grujicic *et al.* [**46**] was aimed at investigating jetting as a means of bonding in CGDS. The study showed that bonding via localized atomic diffusion was insignificant due to the very short period of high temperature at the jet interface. Similarly, bonding due to localized melting at the interface between the particles and substrate was

found to be of minimal importance. The suggested bonding mechanism was jetting in which severe plastic deformation leads to jets in the material. The jets formed by the impact of the particles with the substrate promote intimate and clean contact between the materials in which metallurgical bonding can occur. Along with the intimate contact, the formation of vortex-like regions due to the jetting further improves the bonding by increasing the contact area between materials and increases adhesion through mechanical interlocking. The presence of vortex-like roll-ups has also been observed in explosive welding. These roll-ups occur when two materials in a fluid-like state are subjected to a displacement parallel to their interface. Perturbations at the interface can result in a fluid flowing over the other with increasing intensity as displacement continues. A schematic of the evolution of roll-ups can be found in Figure 2.16 while an experimental observation of this phenomenon during CGDS can be found in Figure 2.17.

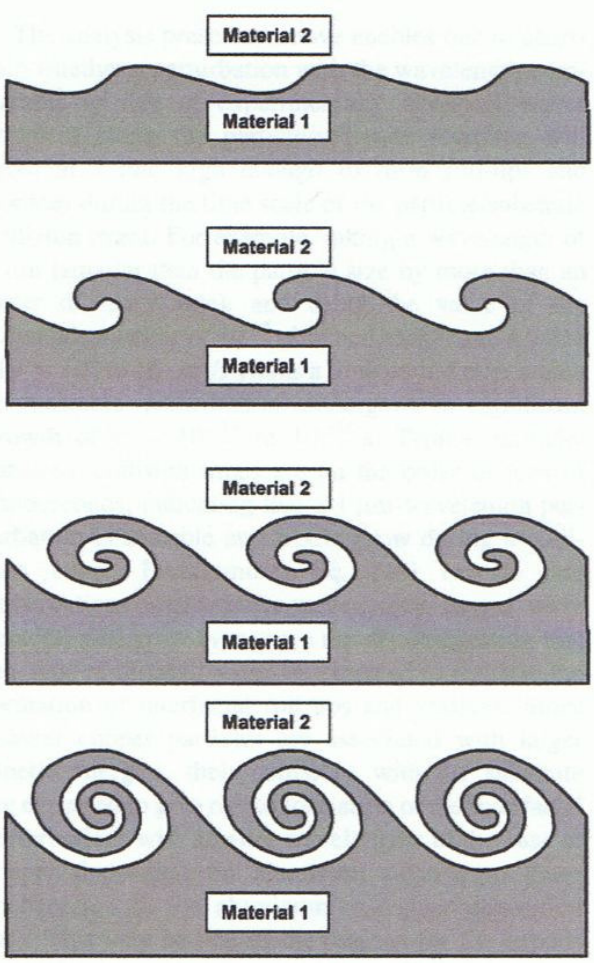

Figure 2.16: Schematic representation of the evolution of vortex-like roll-ups which can enhance bonding in CGDS [46]**.**

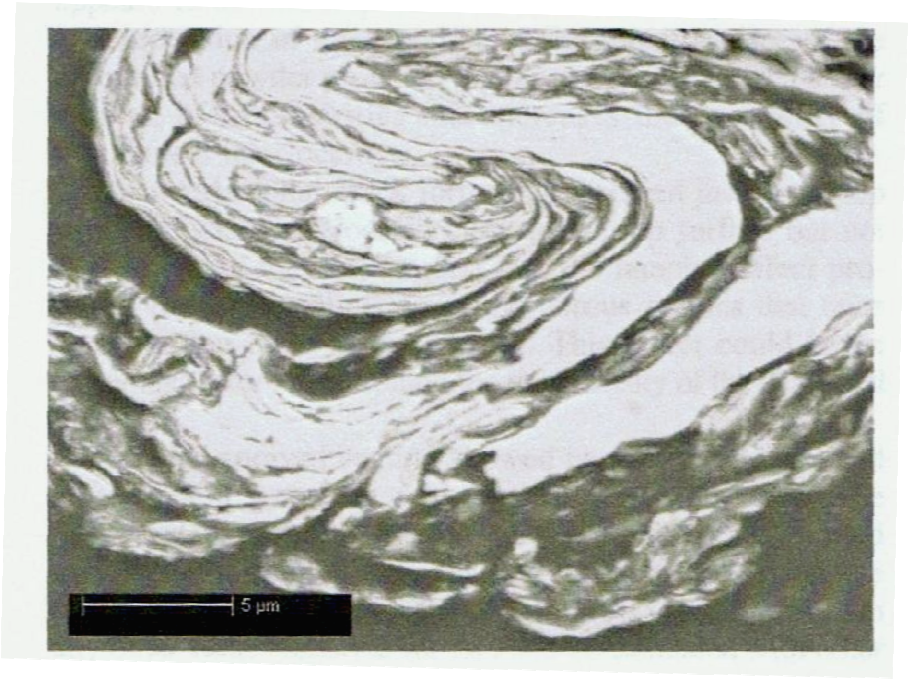

Figure 2.17: Evidence of roll-ups at the interface between the particle and the substrate of a CGDS coating[60**]**

Although some modelling work indicates that both the substrate and the impacted particles will experience jetting, a recent study by King *et al.*[**49**] in which Al and Cu was sprayed on a substrate of piezoelectric ceramic (PZT), as well as Al and Cu substrates has shown that jetting of both metals is not necessary for bonding. When spraying Al on PZT, it was observed that the ceramic substrate does not deform, while the Al particles show evidence of jetting as can be seen in Figure 2.18. During a second trial where Al was sprayed onto Cu, the softer Al particles showed evidence of jetting while the Cu substrate was plastically deformed without jetting. Finally, when Cu was sprayed onto Al it resulted in the Cu particles embedding themselves into the Al substrate. While the Cu particles were deformed, the Al substrate showed signs of melting due to the high kinetic energy impacts. No evidence of jetting was observed. According to this study, jetting of both substrate and particles is not necessary for proper bonding. It appears this effect is highly dependent on the hardness of the materials used for both the particles and the substrate. This seems to support the claim by Zhang *et al.*[**54**] who suggested that plastic deformation of the substrate is not a requirement for bonding.

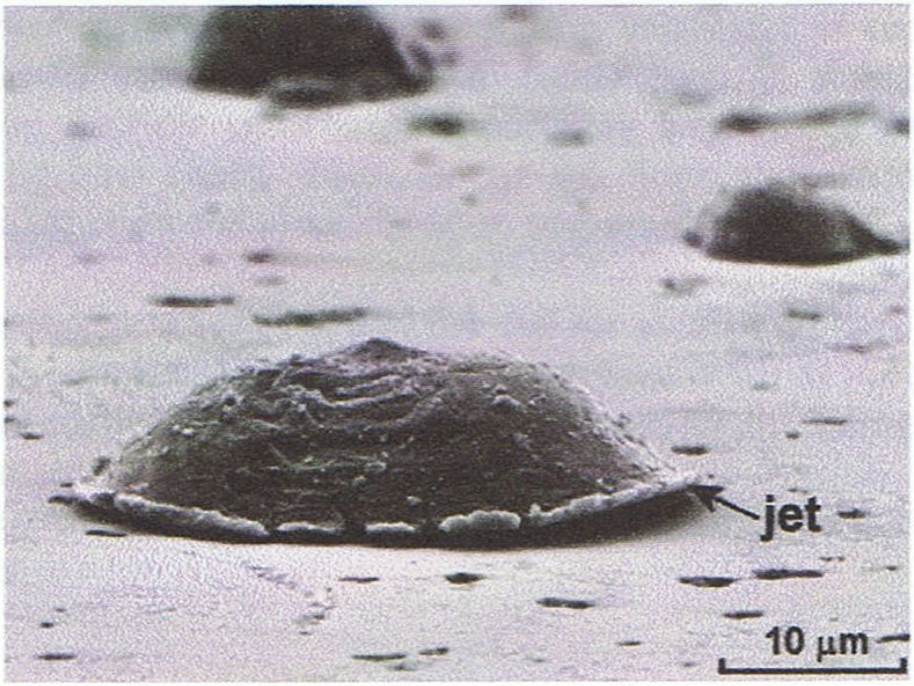

Figure 2.18: Evidence of jetting on Al particle bonded to ceramic substrate[59]**.**

Another suggested CGDS bonding mechanism is known as adiabatic shear instability. This mechanism was originally described by Wright [**61**] and was used by Assadi *et al.*[**43**] and Grujicic *et al.*[**56**] to explain the deformation mechanisms in particle to particle and particle to substrate bonding during the CGDS process. Adiabatic shear instability is based on the assumption that the material temperature increases adiabatically to a point where there is localized material softening. In the CGDS process, this localized melting occurs at the impact interface. The high strain rates present at this location due to the high velocity impact lead to shear instabilities and the material deformation mechanism becomes viscous as opposed to plastic. This theory rests on the assumption that the interactions at the interface can be considered adiabatic. The assumption of adiabatic evolution is a very good approximation of the material behaviour considering the very short contact and deformation times in which heat conduction can be neglected.

Numerical simulations performed by Assadi *et al.* [**43**] evaluated the impact behaviour of copper particles at various velocities and determined that at sufficiently high velocities, the material deformation is governed by adiabatic shear instability. The evolution of the strain, temperature and stress with respect to time of impacting copper particles from

this study is presented in Figure 2.19. The effect of raising the particle velocity from 550m/s to 580m/s has significant impact on these figures. It suggests that the velocity required for adiabatic shear instability is approximately 580m/s for copper particles which is very close to the experimentally determined critical velocity of such particles. It appears that adiabatic shear instability is therefore associated to the bonding of CGDS and linked with the particle critical velocity.

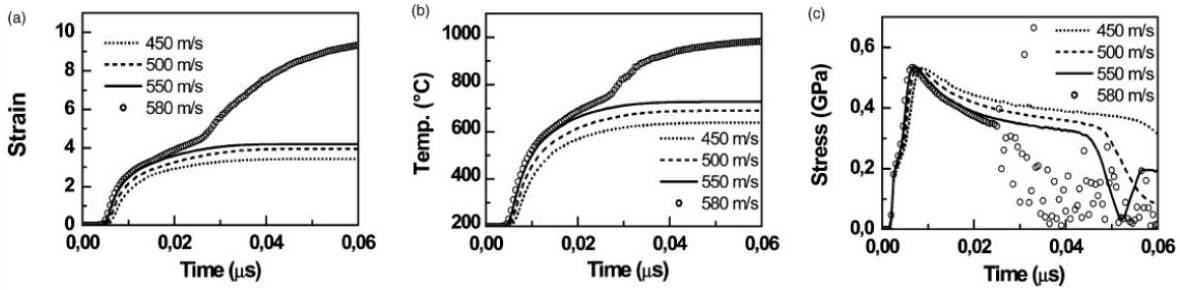

Figure 2.19: Evolution with respect to time of a) Strain, b) temperature and c) stress in the interface region of a particle at various velocities[43]**.**

Adiabatic shear instability has been identified as causing shear bands. These shear bands have been observed in many CGDS studies and support the theory of adiabatic shear instability as a bonding mechanism in CGDS [**47**,**62**,**63**]. Images demonstrating jetting and shear band formation due to adiabatic shear instability are presented in Figure 2.20 and Figure 2.21. These shear bands are thought to create intimate contact between surfaces and promote metallurgical bonding. Mechanical interlocking has also been attributed to jetting caused by adiabatic shear instability [**57**].

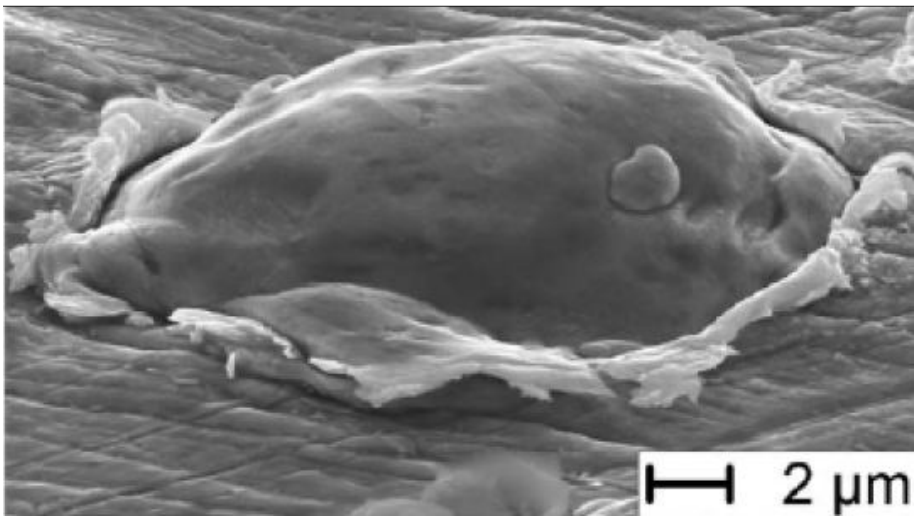

Figure 2.20: Copper particle showing the formation of jets around the impact surfaces (adapted from [43]).

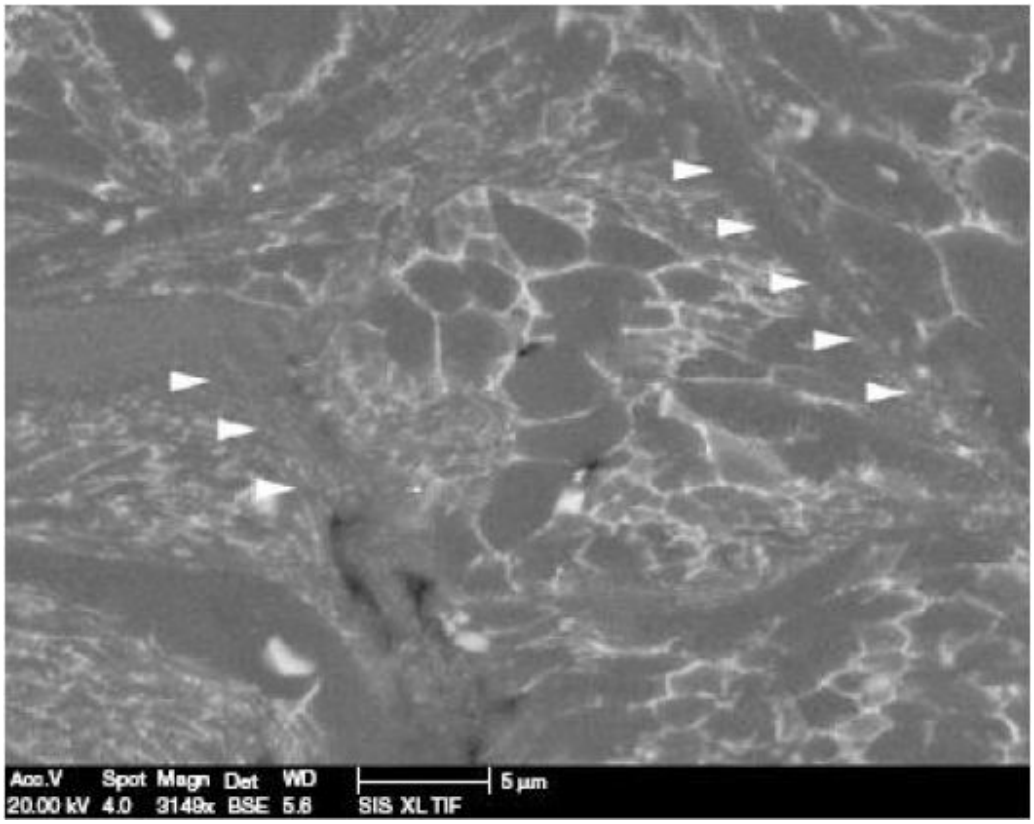

Figure 2.21: Evidence of shear bands (indicated by arrows) in the microstructure of an Al-alloy coating manufactured by CGDS [62].

Although many studies have focused on the bonding mechanisms present in CGDS, a consensus on a single mechanism has not yet been reached. The bonding mechanisms proposed include adhesion, mechanical interlocking and adiabatic shear band formation as

well as various combinations of mechanisms. The rapid evolution, small scale, high strain rates and varying material properties make modelling and experimental validation extremely difficult. As such, the exact method of bonding may not be determined until instrumentation and computer models are further refined.

2.2.6. Advantages and limitations

The CGDS process is capable of producing coatings made of a large variety of materials such as aluminum, copper, titanium and zinc, alloys and cermets in conventional, nanocrystalline and amorphous forms as well as metal-matrix composites [**20,39,42,52,57,60,63-70**]. Coatings deposited via CGDS can be relatively thick (up to 1 cm) and can be deposited in a single pass on thin (< 1 mm) or thick substrates without damaging the substrate material [**69**]. The CGDS process has been found suitable for free-forming and joining of materials [**71**,**72**] and has been used for the restoration and repair of damaged components and for corrosion protection as per U.S. military standard MIL-STD-3021[**73**].

Coatings manufactured by the CGDS process exhibit low porosity levels due to the high levels of plastic deformation required for adhesion. Plastic deformation of the particles flattens the material which can occupy voids in the coating. If there is insufficient plastic deformation, the particles will retain their spherical geometry and result in voids between particles. The porosity is further reduced by the subsequent impingement of particles on the deposited coating [**42**]. The subsequent particle impacts will deform the underlying particles increasing their plastic deformation and ability to fill voids. Coatings also exhibit a good adherence to the substrate due to the high amount of plastic deformation which can conform to irregular substrate surface profiles [**55**]. The hardness of coatings deposited via CGDS is higher than the original powder due to the cold working effect during particle deposition [**39**,**74**]. The coatings also exhibit better fatigue resistance than feedstock material due to the residual compressive stresses in the coating induced by the plastic deformation of the particles[**75**,**76**]. However, the most significant advantage of the CGDS process is the absence of significant heating of the powder particles. This feature enables the deposition of coatings with very low oxide content and prevents the powder microstructure from being affected during the spraying process [**10**,**60**,**64**,**67**]. This is especially interesting when the

use of nanocrystalline or oxidation sensitive coatings is required. These materials are easily affected by grain growth and oxidation induced by elevated temperatures and are therefore especially suitable for deposition via CGDS.

Not all materials are suitable for deposition via CGDS. Due to the material plastic deformation required for bonding, only materials that present some level of ductility can be deposited. It is possible to deposit brittle (ceramic) materials if they are embedded within a ductile matrix [**20**]. Other than material suitability, the CGDS process can also suffer from nozzle clogging when spraying at elevated temperatures for prolonged durations[**77**,**78**]. This can reduce the productivity of the process as the nozzle must be removed and cleaned or replaced before further spraying can take place. This problem may be overcome with further optimization of the nozzle and powder flow rate.

Productivity of the CGDS process can also be reduced due to the limitations of powder flow rate. While the nozzle accelerates the process gases, the injected powder causes some flow disturbance and reduces the energy of the gas through its own acceleration. If the powder flow rate is too high, its acceleration is therefore hindered and low particle velocities will result reducing coating quality [**79**]. The powder flow rate must therefore be carefully considered according to nozzle geometry and total available energy. Higher deposition rates require larger nozzles which in turn consume more process gases and more electrical energy to heat this gas. However in normal utilization, this should not be an issue as CGDS is capable of producing coatings over 1mm in thickness in a single pass, much thicker than other thermal spray techniques currently available. CGDS powder deposition rates have been reported to be as high as 10 lbs/h [**80**].

Studies of the microstructures of CGDS coatings have shown that there can be grain refinement in the coating and in some cases amorphization [**67**,**81**]. This indicates the coating microstructure can be altered by the severe plastic deformation present in the CGDS process. Although these studies indicate that the microstructure has been altered, the studied area was immediately at the impact sites. The coating microstructure away from the impact site (beyond a few nanometres) is not affected by the CGDS process. It is believed that the microstructural changes are due to severe plastic deformation caused by adiabatic shear

instability or the creation of shear bands. The presence of these changes is not thought to affect the overall coating performance.

2.2.7. Process Improvements

There are several areas in which the CGDS process can be improved. Firstly, some materials are currently difficult to deposit due to insufficient particle acceleration resulting in particle velocities below the material critical velocity. The evolution of heating systems capable of heating the driving gas to higher temperatures thereby increasing the particles velocities is an ongoing development process. The development of materials capable of coping with elevated temperatures of the heater and nozzle sections is also required for improvement of CGDS systems. Secondly, current CGDS nozzles are not optimised to take full advantage of the energy available for particle acceleration. The development of such nozzles must progress in order to reduce costs and increase process efficiency. Finally, the effect of process parameters such as the effect of nozzle stand-off distance [**82**], substrate heating [**83**], particle temperature, particle velocity and nozzle travel speed must be characterized and understood. The understanding of these parameters will only be achieved through the development of novel sensor systems capable of detecting both particle and gas temperatures and velocities [**84**,**85**,**86**] as well as extensive modelling work.

2.3. Powders for Thermal Spray Processes

Various routes have been developed to manufacture the powders used in thermal spray processes. As the final coating is formed using this powder, the powder manufacturing process is extremely important and will directly impact coating quality. Factors such as particle size distribution, particle shape and oxide contents can significantly affect the capability of the thermal spray process to produce a quality coating. This section will provide a brief overview of powder manufacturing and modification techniques.

2.3.1. Atomized Powders

Atomized powders are manufactured by atomizing a molten flow of metal through the use of an induction or arc furnace. The molten material is then accelerated to high velocities to form droplets of powder that are rapidly solidified in a medium of air, water or inert gas. In this process, it is important to control the particle shape, size distribution and oxidation

through careful control of the parameters and of the atomization environment. In particular, powders sensitive to oxidation must be solidified in an inert gas medium to limit the amount of oxidation that can occur in an air or water medium. Powders manufactured using the gas atomization process are spherical in nature while water atomized powders have an irregular rounded shape. Spherical particles are favourable as their temperature distribution and impact velocities are consistent and easier to predict. The use of inert gas however, significantly increases the manufacturing cost of the powder [**87**]. An image of inert gas atomized CoNiCrAlY powder is presented in Figure 2.22 while an image of water atomized Barium Fluoride-Calcium Fluoride is presented in Figure 2.23.

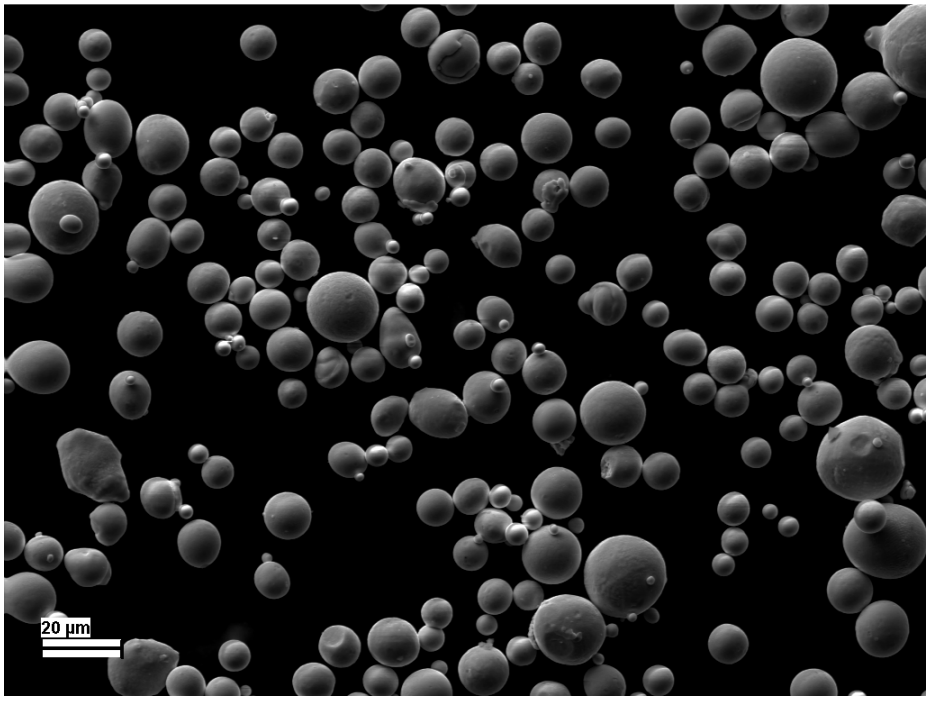

Figure 2.22: Image of inert gas atomized CoNiCrAlY powder

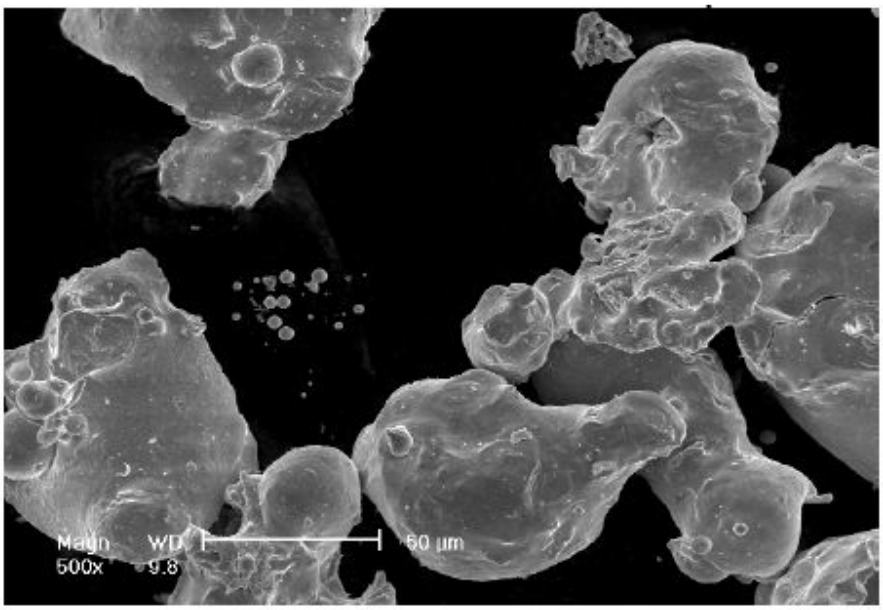

Figure 2.23: Image of water atomized Barium Fluoride-Calcium Fluoride [88]

2.3.2. Crushed Powders

This process is used exclusively for brittle materials, usually ceramics. The material is first mixed and melted before being cast. After cooling, the resulting block is crushed in order to obtain fragments of the desired size. The resulting powders are dense, blocky and angular [**87**].

2.3.3. Mechanical Alloying and Milling

Milling involves reducing powder particle sizes through the use of a barrel filled with grinding medium (usually steel balls). The milling process is usually conducted in the presence of a lubricant to reduce the wear and energy loss of the system. The process involves repeated welding, fracturing and re-welding of powdered particles to attain nanometre sized grains. The milling parameters must be carefully controlled to ensure the process manufactures the powder with the required size and morphology. In the milling process however, impurities can be found in the resulting powder due to degradation of the grinding medium or barrel casing and through oxidation of the powders. The addition of a coolant such as liquid nitrogen can create nanocrystalline particles and is known as cryomilling [**87**].

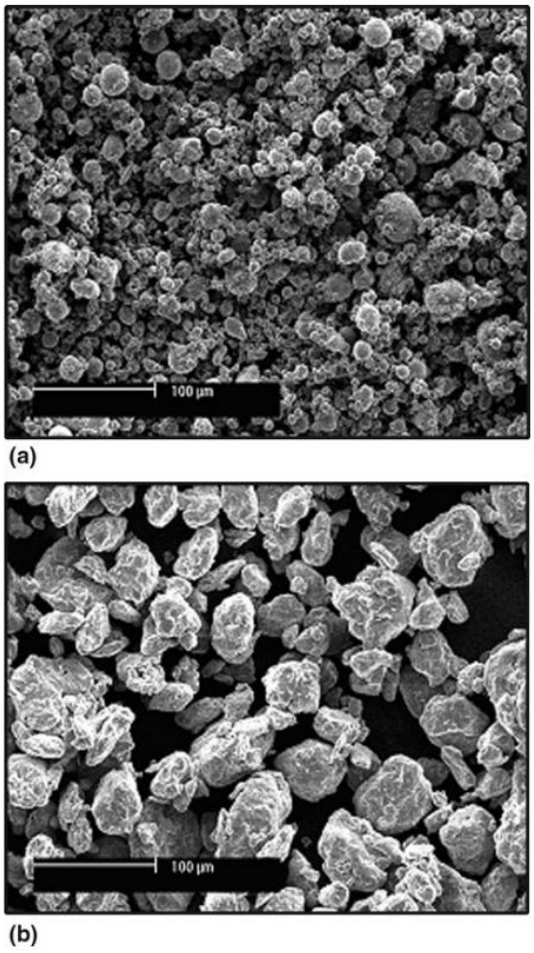

Figure 2.24: Image of a) as-received powder and b) cryomilled Al 5083 powder [87]

The non-spherical nature of cryomilled powders causes significant differences in its behaviour in the gas flow. Non-spherical particles generally have a higher drag coefficient and thus can achieve higher particle velocities. These increased velocities also reduce particle temperatures due to the lower residence time in the hot gases. The drag coefficient is however highly dependent on the particle orientation with respect to the flow. As such, certain particles reach much higher velocities than others and variations in the flow conditions can significantly affect these particles [**89**].

2.3.4. Powders Used in CGDS

The powders used in a thermal spray process can have a great influence on the final properties of the coating and the deposition efficiency of the process. In particular, CGDS requires particle sizes which are relatively small and which have a low oxide content. Small

particles are required to ensure they reach the material critical velocity. However they must be large enough to carry enough momentum through the bow shock and retain their velocity. The size of particles used in the CGDS process varies depending on material density but are typically in the 5μm-50μm range. It is also important to maintain a small particle size distribution. This ensures that all particles reach the critical velocity and are heated to approximately the same temperature during the spraying process to obtain a uniform coating quality.

As explained in the previous section, non-spherical particles create unpredictable coating qualities as the drag coefficient on the particle will vary depending on its orientation with the driving gas flow. A spherical morphology ensures the drag on the particles is identical irrespective of orientation creating much more predictable results.

Finally, oxide content in the powder can be detrimental to both the coating and also increases the critical velocity in CGDS. This increase in critical velocity increases manufacturing costs as operation pressures and temperatures must be increased to obtain a coating of equal quality than with powders with less oxide content.

2.4. Thermal Barrier Coatings

This section will present a detailed overview of thermal barrier coatings with specific attention to the bond coat components. Information relevant to the TBC structure, coating processing methods, failure mechanisms and suggested improvements of TBC coatings will be presented.

2.4.1. Overview

Thermal barrier coating systems have been mainly developed for use in gas turbines. They are used to protect hot components such as nozzle vanes and turbine blades in an attempt to increase engine life and performance. The TBC protection systems have two roles: provide thermal protection and protect against hot corrosion and oxidation. The hot gases encountered in the hot section of the gas turbine are near the melting point of the superalloy turbine blades. The TBC system thermally insulates the blade to ensure it is operating at an

acceptable temperature. These hot gases also contain oxygen and by-products of the combustion process which can combine with impurities in the intake air to form Na_2SO_4 [**90**]. If left unprotected at high temperatures, the superalloy blades will react with the oxygen and sodium sulphate and degrade quickly. No single coating material has been found able to cope with both these roles. TBC systems are therefore composed of two coating layers: the ceramic top layer thermally insulates the component, while the inner metallic layer protects it from oxidation and hot corrosion. Current ceramics used as top coats are capable of reducing the temperature up to 170°C across a coating of 150µm thickness [**91**]. A representation of the typical temperature gradient across a TBC system can be seen in Figure 2.25.

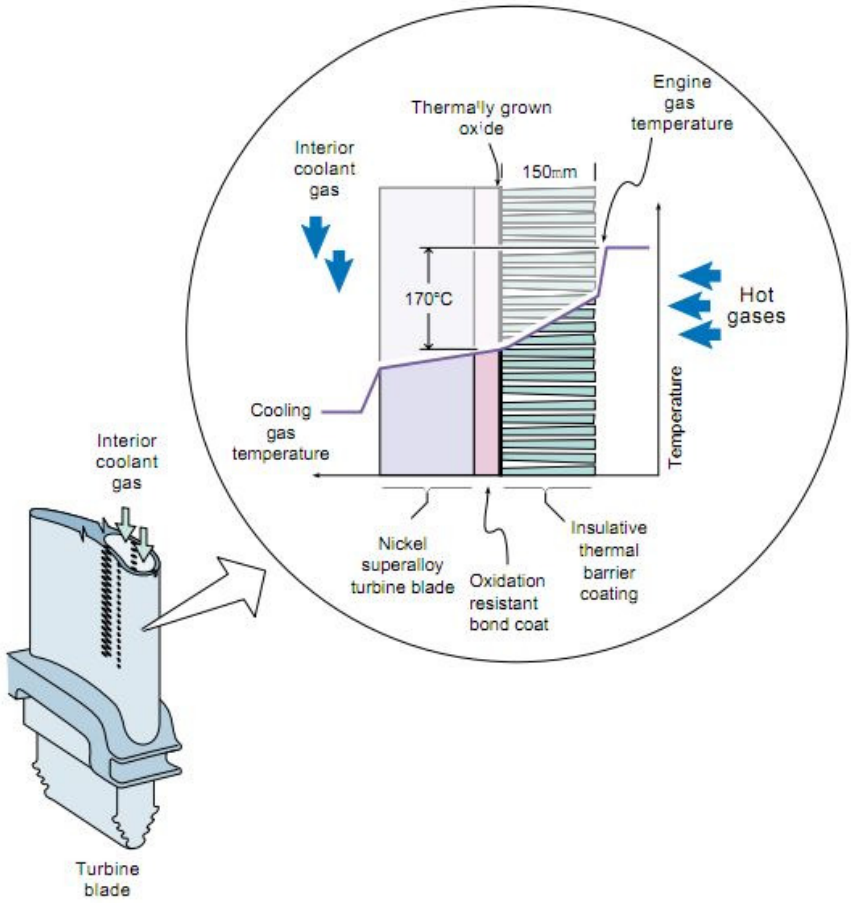

Figure 2.25: Schematic view of the temperature distribution across the cross-section of a TBC system applied to a turbine blade [91]**.**

While the ceramic top coat can effectively protect the turbine blade from elevated temperatures, it offers no real protection from oxidation or hot corrosion. Although the temperature drop inherently lowers the oxidation rate, the porous nature of the top coat is no hindrance to the inward diffusion of oxygen. The bond coat is therefore specifically designed to protect the components against oxidation and hot corrosion and to promote bonding between the superalloy substrate and the ceramic top coat. As the ceramic top coat has a low thermal expansion coefficient and the superalloy substrate has a higher thermal expansion coefficient significant stresses can develop during thermal cycling. The bond coat material must also have a coefficient of thermal expansion between that of the top coat and substrate in order to lower these thermal stresses and increase coating life.

2.4.2. TBC Composition

This section will present the structure and material composition of typical TBC systems in present-day operation. As was previously introduced, TBC systems are composed of two superimposed layers. However, in addition to the ceramic top coat and metallic bond coat, another layer is formed while in operation. Due to the exposure to high temperature oxygen, the metallic bond coat reacts and forms an oxide layer known as the thermally grown oxide (TGO). The TGO is formed between the top coat and bond coat and plays an important role in the performance of the TBC system. This section is divided in two subsections in order to provide specific details about the ceramic top coat as well as the metallic bond coat and the resulting thermally grown oxide.

2.4.2.1. Ceramic Top Coat

The ceramic top coat is designed to reduce the temperature of the turbine blade by having a low thermal conductivity. The top coat must maximize the drop in temperature across its thickness while remaining relatively thin (typically 150-250μm). Thicker top coats are used in some cases but lead to difficulties due to increased thermal stresses and decreased film cooling capability[**92**]. A thin top coat is required to keep dimensional tolerances. Ceramics are chosen for the top coat as they resist high temperatures and have very good insulating properties due to their low thermal conductivity. Top coats are typically composed of zirconia and more commonly, yttria-stabilized zirconia (YSZ) [**91**]. YSZ offers a low thermal conductivity of approximately 2.25W/mK (with 8 wt.% yttria) due to the low

thermal conductivity of zirconia and the phonon scattering defects from the addition of yttria[**93**]. A phonon is the name given to the vibrational motion in which the material crystal lattice vibrates at a certain frequency. The addition of yttria to the zirconia allows for phonon scattering. That is, the vibration frequency is slightly altered and the frequency mismatch of the yttria reduces the efficiency of thermal conductivity. As such, the concentration of yttria added to the zirconia has been shown to greatly affect the thermal conductivity of the ceramic while varying the applied temperature does not impact thermal conductivity significantly[**93**]. The typical concentration of yttria is between 6 to 8 wt.% in order to optimize spallation life[**94**]. YSZ also has a relatively high coefficient of thermal expansion (CTE) of 9.0×10^{-6} K^{-1} (at room temperature) when compared to other ceramics. A high CTE is important in order to reduce the stress between the top coat and the metallic bond coat during thermal cycling. Due to the elevated temperatures, a mismatch of CTE between the bond coat and the top coat can lead to large stresses at their interface and lead to premature failure. The ceramic top coat must therefore have the lowest possible thermal conductivity and the highest possible CTE to protect the underlying material while reducing stresses that can lead to failure. The ranges of CTE and thermal conductivity for various materials are presented in Figure 2.26 and indicate that YSZ is currently the most appropriate material for use as a top coat.

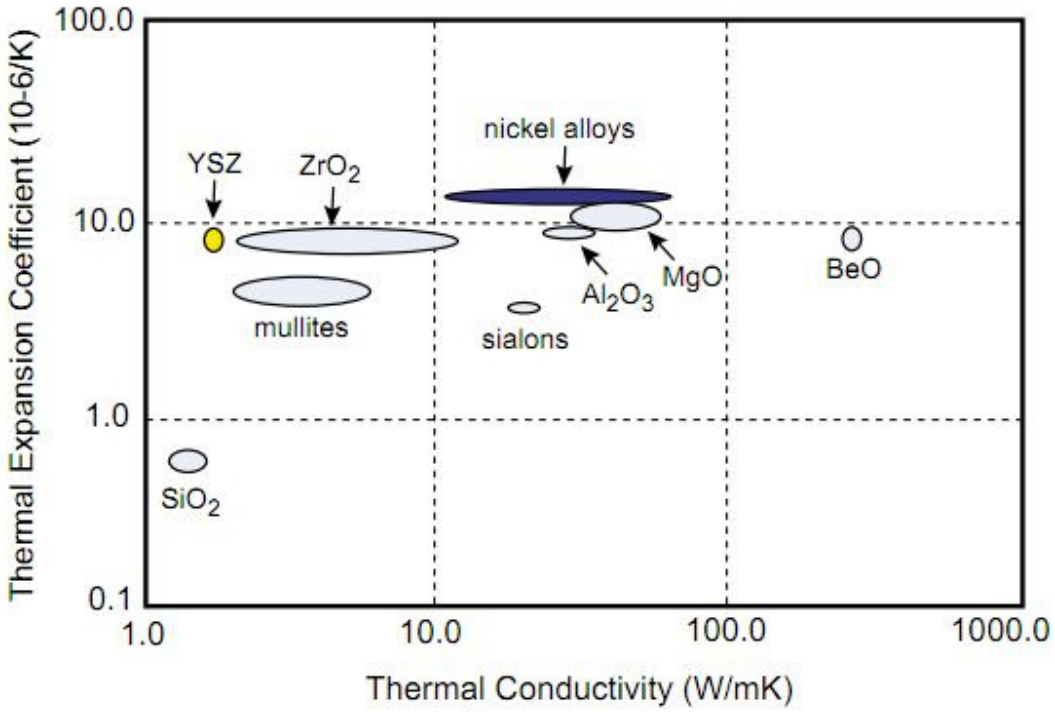

Figure 2.26: Thermal conductivity and thermal expansion coefficient of various material types [91]**.**

2.4.2.2. Metallic Bond Coat and Thermally Grown Oxide

The bond coat is arguably the most important component of the TBC systems due to its role in protecting the substrate from oxidation and hot corrosion and ensuring a good bonding with the ceramic top coat. The bond coat is a thin metallic coating which is typically 100-150μm thick. It is applied directly on the superalloy substrate prior to the application of the ceramic top coat. Bond coats can also be used without a top coat for the protection they offer against oxidation and hot corrosion as long as the temperature remains manageable. In a study by Li *et al.* [**95**] uncoated superalloy substrates were oxidized alongside substrates coated with a bond coat. The study found that the coated samples had 48% less mass gain when compared to the uncoated ones indicating the very good bond coat oxidation protection properties.

In order to insure a good adhesion between the ceramic top coat and the substrate superalloy, the bond coat CTE is carefully chosen to be between the CTE of the top coat and the substrate. The CTE of typical bond coats is approximately 13.5×10^{-6} K^{-1}[**5**]. A CTE

mismatch between the layers of the TBC system and/or the substrate can lead to spallation and significantly reduce the lifetime of the coating. In a study by He et al. [**96**], three substrates with varying CTEs were coated with a TBC and heated at 1100°C for 30 minutes before being cooled for 5 minutes to complete one thermal cycle. It was found that the substrate with the CTE most closely matching the CTE of the bond coat lasted much longer than the substrate that had the largest CTE mismatch (2512 cycles vs 652 cycles). It was concluded that the larger the mismatch in CTE, the faster the TBC system will fail.

The oxidation protection characteristics of the bond coat are optimised through the selection of its chemical composition. The bond coat reacts with high-temperature oxygen to form a thin oxide scale called the thermally grown oxide (TGO). The TGO protects the bond coat from further oxidation by limiting the amount of oxygen that can diffuse through to the bond coat. The favoured TGO composition is α-Al_2O_3 as it is slow growing, dense and uniform and restricts the diffusivity of oxygen across its thickness[**97**,**98**]. Bond coats compositions are therefore specifically selected to be rich in aluminum in order to form an alumina TGO in preference to other less optimal oxides and ensure a long coating life.

Two different types of bond coats currently exist, they are known as diffusion aluminide and MCrAlY. The diffusion aluminide bond coats consist of depositing a thin Al layer on the substrate and are typically manufactured using diffusion techniques such as pack cementation or chemical vapour deposition. Due to the Al diffusion into the nickel-based substrate superalloy, an intermetallic β-NiAl layer is formed near the surface. This intermetallic layer remains stable at high temperatures as can be seen in Figure 2.27. Upon exposure to high temperature oxygen, the β-NiAl layer reacts to form a TGO composed of protective alumina. Some of the Al in the β phase diffuses to the surface and reacts with oxygen and the β-phase near the surface reverts to γ'-Ni_3Al upon Al diffusion. A drawback of this bond coat type is the tendency for the Al to diffuse into the superalloy substrate leaving the γ'-Ni_3Al phase at the surface. This phase is less likely to form alumina when in contact with oxygen and can lead to premature failure due to oxidation of the substrate.

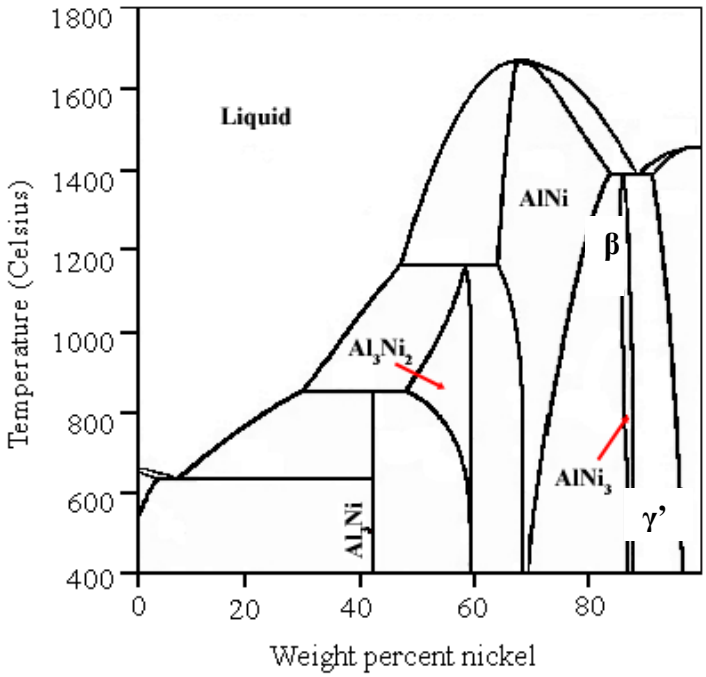

Figure 2.27: Ni-Al phase diagram

MCrAlY bond coats are manufactured with various thermal spray techniques. This gives a much better control of the material properties compared to diffusion aluminides although some defects are introduced during the deposition process. The increased control of material properties has lead to the use of complex alloys specifically designed for optimal bond coat performance. These alloys still contain Ni and Al in an effort to form an alumina TGO but other elements such as Cr, Co and Y have been included hence the name MCrAlY (where M can be Co, Ni or both). MCrAlY coatings typically have two phases, a face-centered-cubic (fcc) Ni/Co γ-matrix and a β-precipitate consisting of a body-centered-cubic (bcc) Ni-Al intermetallic [**5**]. An image of a typical MCrAlY coating can be found in Figure 2.28. The β-phase is Al-rich and is consumed during oxidation of the coating to form the TGO scale.

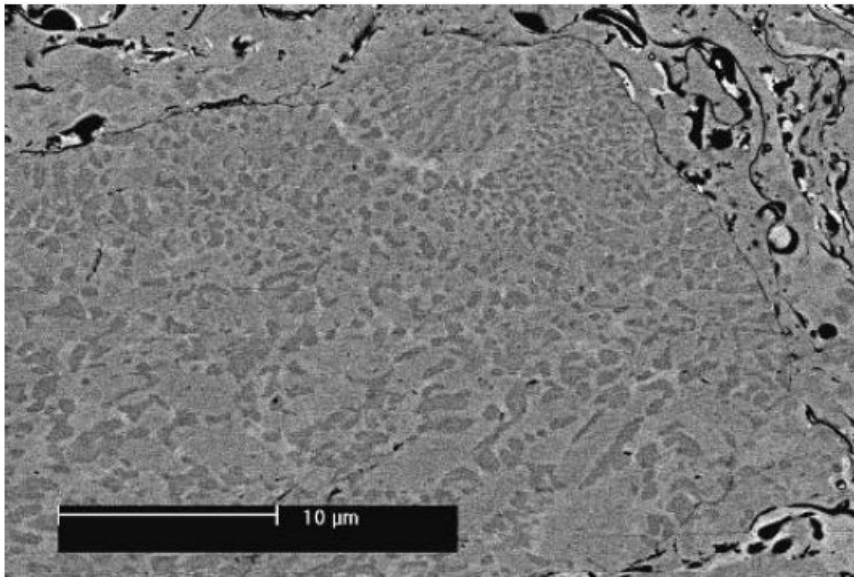

Figure 2.28: Typical two-phase structure of MCrAlY coating showing γ-matrix (light grey) and β-precipitates (dark grey) (adapted from [99]).

Bond coats of the MCrAlY type are typically used in modern TBCs over the diffusion aluminide type. The addition of Cr to the alloy has increased the corrosion resistance, particularly against hot corrosion [**100**] while the amount of Al remaining in the alloy is sufficient for oxidation resistance. The addition of a small amount of Y has been shown to increase the adhesion of the TGO scale to the bond coat surface. The addition of these elements has improved the corrosion and oxidation performance of bond coats. The level of protection offered by these coatings is summarised in Figure 2.29.

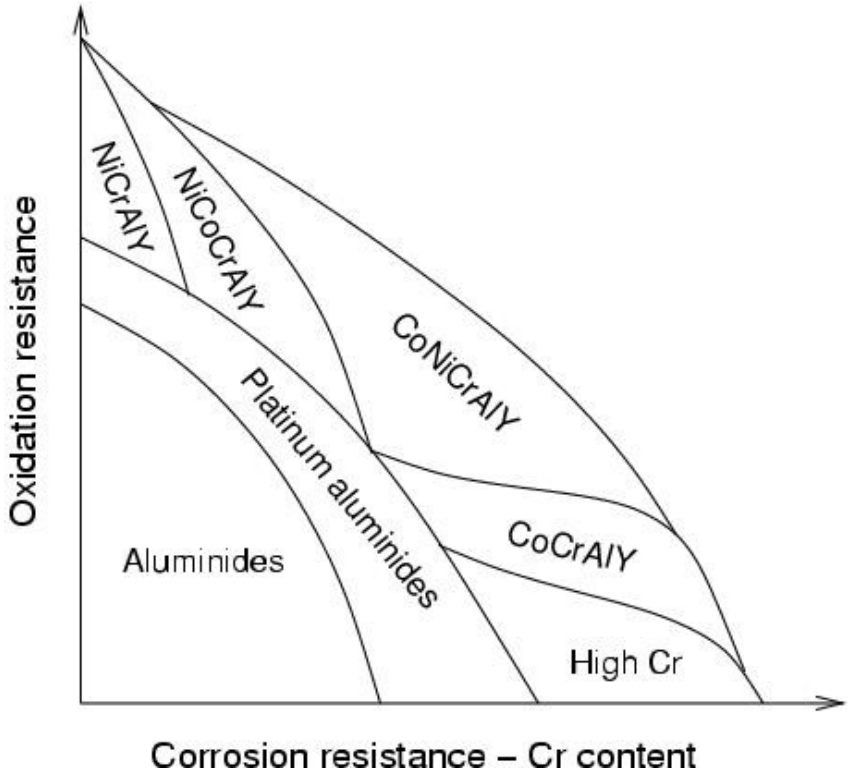

Figure 2.29: Relative protection levels against oxidation and corrosion for various bond coating materials [101]

As can be seen, the MCrAlY coatings offer better performance than the diffusion aluminides. This report focuses mainly on CoNiCrAlY coatings as they offer the best combination of protection from oxidation and hot corrosion. CoNiCrAlY coatings can be used both as bond coats in TBCs or as stand-alone corrosion protection.

2.4.3. Deposition Techniques and Associated Microstructural Features

Various deposition techniques are used to manufacture TBC systems, each resulting in coatings with unique microstructural features. The various techniques and their resulting coating microstructures will be discussed for the top coat and the bond coat separately due to the difference in material composition and deposition techniques.

2.4.3.1. Top Coat

The ceramic top coat is currently deposited by one of two techniques, plasma spraying or Electron Beam Physical Vapour Deposition (EB-PVD). The most popular of these techniques is plasma spraying as it is widely available and in use since the 1960s

[**102**,**103**,**104**] however top coats manufactured by EB-PVD can have a significant lifetime increase and are used in some components[**91**,**105**,**106**]. The difference of these two deposition techniques can be seen in Figure 2.30. The plasma spray method deposits a series of splats that are aligned parallel to the substrate while the EB-PVD method produces a coating with a columnar morphology.

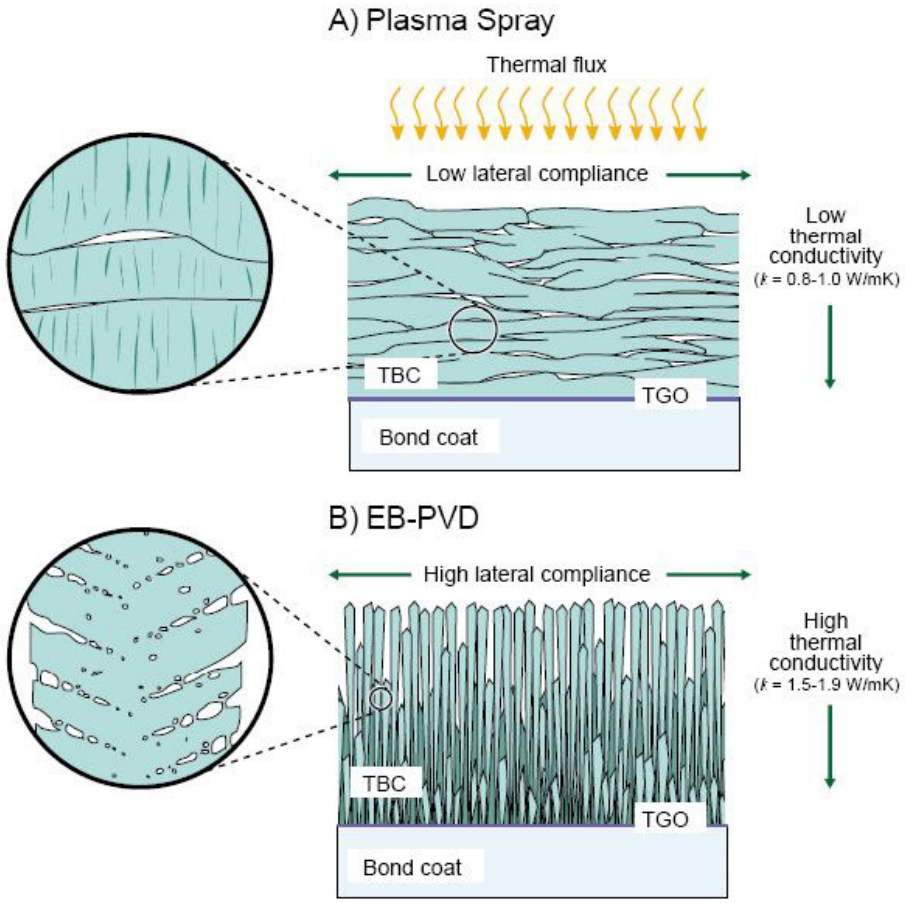

Figure 2.30: Ceramic top coat morphologies produced by Plasma spraying and EB-PVD coating process [91]

This difference in morphology leads to different mechanical properties. Plasma sprayed coatings have a lower thermal conductivity and are therefore better insulator than EB-PVD. This is attributed to the porous nature and material orientation of the coating which reduces the conduction of heat from its surface towards the substrate [**91**]. However, the plasma sprayed top coats have a very low compliance for thermal expansion due to the direction of the splats and are therefore more prone to spallation failure due to CTE mismatch than EB-PVD coatings. The stresses that develop through thermal cycling are

higher in plasma sprayed coatings which leads to crack initiation, propagation and failure of the coating. Due to their columnar structure, EB-PVD coatings have more in-plane compliance and are therefore more resistant to spallation [**91**]. EB-PVD coatings are therefore seen as superior to plasma sprayed top coats and their widespread adoption has been hindered only by the large capital cost of equipment of approximately $20 million[**107**]. Thermal spray top coats are therefore used for power generation turbines due to their faster process times and low cost while EB-PVD coatings are used for aircraft components due to their improved reliability[**108**].

Some researchers have attempted to mimic the structure of EB-PVD coatings using the plasma-spraying process in order to reduce costs [**109**,**110**,**111**]. In theory coatings with the columnar structure found in EB-PVD coatings could have longer operating life due to the higher thermal expansion compliance. Preliminary results from these studies indicate the coatings fail in thermal cycling tests faster than conventional APS techniques [**110**,**111**]. More development is therefore required before a low-cost alternative to EB-PVD can be successfully used.

While the deposition of the top coat ideally does not affect the underlying bond coat, the high temperatures used during the plasma spray process can have a negative impact on the bond coat. It is expected that these elevated temperatures will cause microstructural changes in the bond coat thus negating efforts to maintain a specific structure. The selection of adequate spraying parameters and the cooling of the substrate are thought to help mitigate the adverse affects that could be potentially induced during the plasma spray process. Furthermore, the bond coat is often subjected to surface pre-treatments in the form of controlled environment heat treatments prior to the deposition of the top coat. The pre-treatments are designed to grow a small layer of protective alpha-alumina oxide in preference to other oxides. Since the early stages of oxidation are the most critical, the application of the top coat after these heat treatments may have no affect on the long-term protection characteristics of the bond coat.

2.4.3.2. CoNiCrAlY bond Coats

Bond coats of the MCrAlY type are typically produced by thermal spraying techniques, more specifically air plasma spraying (APS), low pressure plasma spraying

(LPPS) and high velocity oxy-fuel (HVOF). Due to the different temperatures involved in these processes, the coating quality differs from process to process. The HVOF process uses lower temperatures and higher velocities when compared to plasma spraying and the resulting coating morphology, microstructure and oxidation behaviour are therefore different.

Images of the different microstructures and morphology obtained via the LPPS, CGDS, HVOF and APS deposition of CoNiCrAlY can be seen Figure 2.31 and Figure 2.32. Upon analysis of the images in Figure 2.31, Shibata *et al.* [**112**] concluded that the LPPS coatings were very dense and featured well-flattened particles indicating that most of the particles were molten during the deposition process. The coatings manufactured via APS however had higher porosity attributed to surface oxides developed on the particles during the spraying process. The coatings deposited via HVOF were relatively dense and their porosity was attributed to the lack of deformation of some particles that remained unmelted.

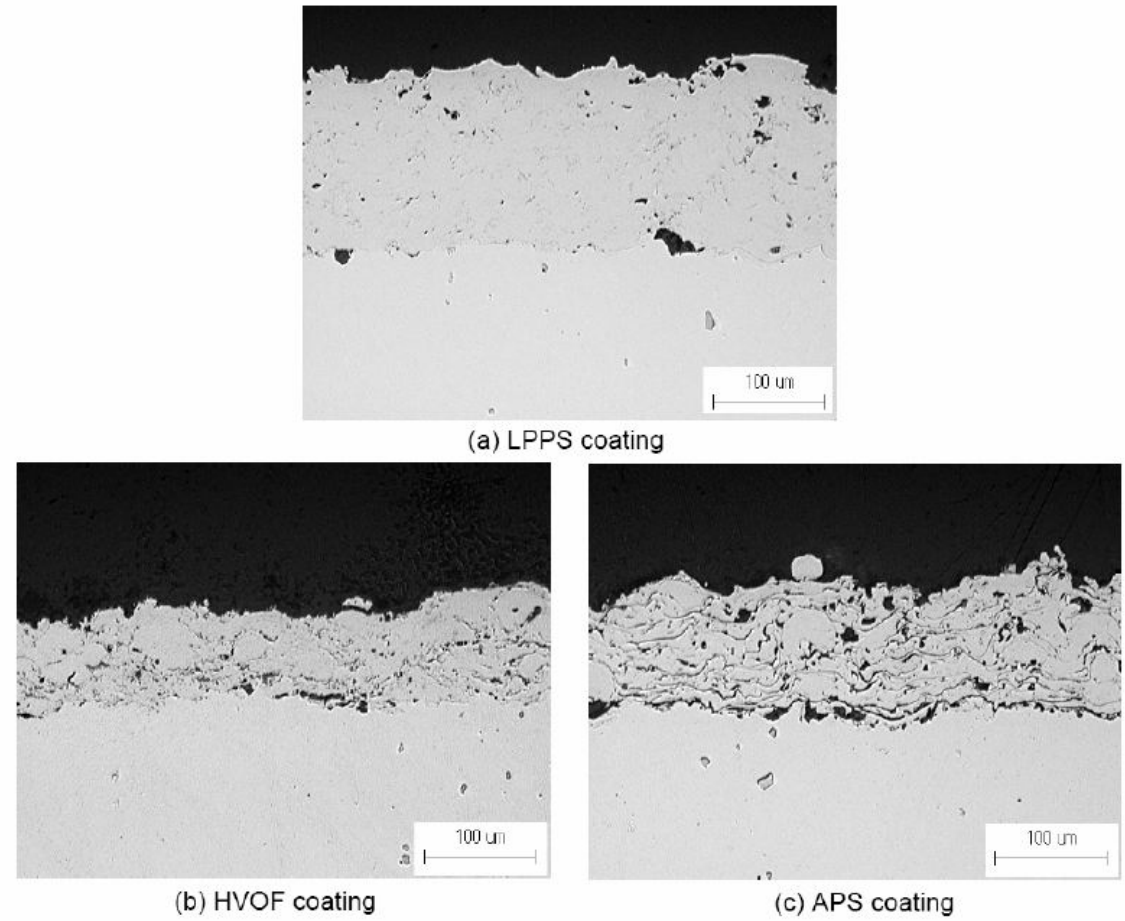

Figure 2.31: Optical microscope images of CoNiCrAlY coatings deposited by a) LPPS, b) HVOF and C) APS (Adapted from [112**])**

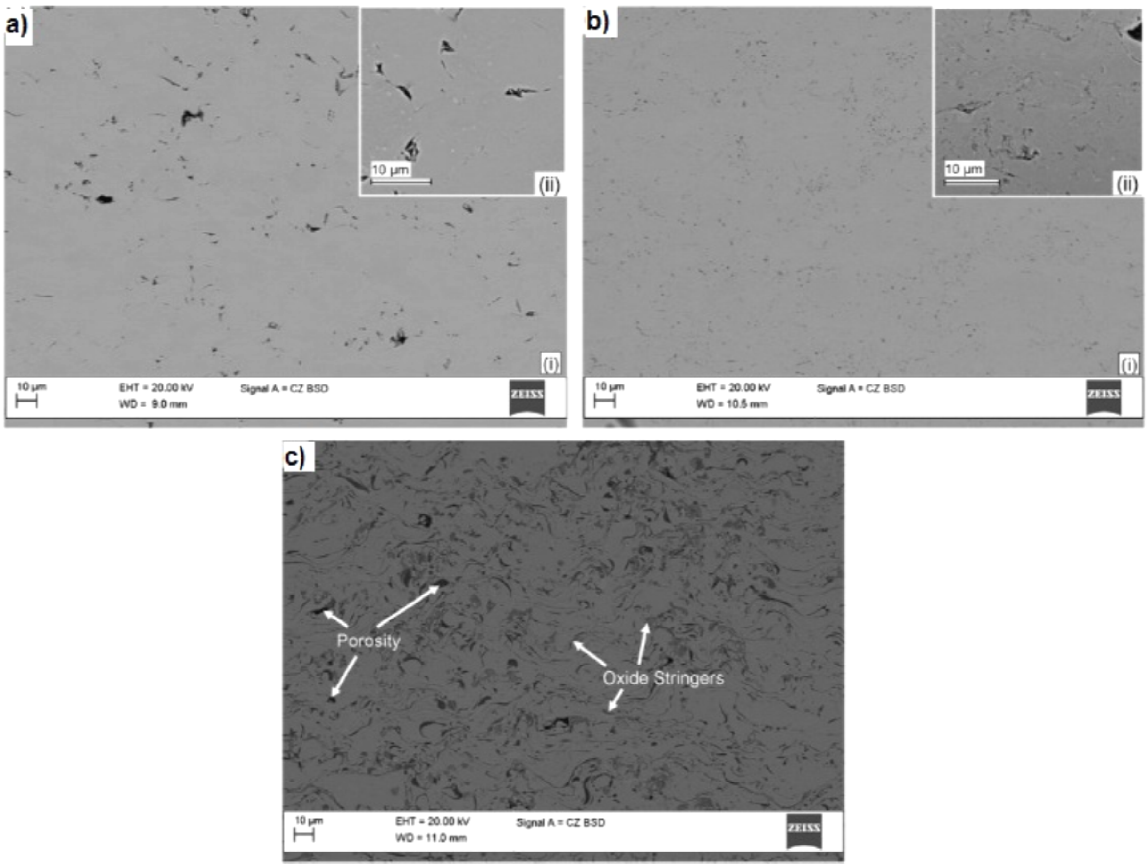

Figure 2.32: Cross-sectional view of CoNiCrAlY coatings manufactured via a) CGDS, b) HVOF and c) APS [11]

Upon further analysis of the three coatings, Shibata *et al.* [**112**] determined that the oxide content of the LPPS, HVOF and APS coatings was 0.16, 0.94 and 1.8 wt. % respectively. The oxygen content of the LPPS is much lower than that of the APS due to the controlled spraying atmosphere while the lower process temperatures of the HVOF process enabled it to have intermediate oxide content. The use of a controlled atmosphere is therefore extremely effective in controlling the oxide content but is significantly more expensive. Shibata *et al.*[**112**] also observed that only the HVOF coatings had a detectable β-phase precipitate. This indicates some microstructural changes were induced by the high temperatures of the LPPS and APS processes.

The effect of the deposition technique on the microstructure of CoNiCrAlY bond coats has also been investigated by Higuera *et al.*[**113**] and Richer *et al.*[**11**]. The cross-section of coatings obtained by APS, HVOF and CGDS are shown in Figure 2.32. When the results of these studies are compared with those of Shibata *et al.*[**112**], the results are quite

similar with the exception of the HVOF coatings of Richer *et al.* [**11**] which appear to be of significantly better quality. The APS coatings all have a higher porosity due to low particle velocities and have high oxide content due to the elevated spraying temperatures. The porosity, oxide content, micro hardness and adhesion strength of the coatings produced by the various spraying techniques are presented in Table 2-5. The HVOF coatings have a higher hardness attributed to the higher plastic deformation due to high particle impact velocities. The adhesion strength of the coatings tested exceeded the adhesion strength of the adhesive therefore specific values are not available.

Table 2-5: Properties of CoNiCrAlY deposited via APS, HVOF and CGDS [113,11]

Property	**APS**[113]	**HVOF**[113]	**APS**[11]	**HVOF**[11]	**CGDS**[11]
Porosity (vol. %)	5.1±0.7	4.6±1.5	5.3±0.5	0.5±0.1	1.0±0.3
Oxide content (vol. %)	5.8±2.1	3.4±0.8	3.82±0.7	0.75±0.23	0.1±0.05
Vicker's Microhardness (HV_{300})	155±18	418±31			
Adhesion Strength (MPa)	>64	>64			

2.4.4. Failure mechanisms

The oxidation type can have a significant impact on the lifetime of the TBC system. Aircraft gas turbines are typically exposed to high cycles where the engine is turned on and off thousands of times during its life. In contrast, industrial gas turbines used for power generation are operated for long periods and may undergo cycling only a few dozen times. Eriksson *et al.*[**104**] investigated the effect of cyclic, isothermal and shock heat treatments on TBC systems. It was found that while isothermal oxidation and cyclic oxidation yield approximately the same TGO thicknesses, the adhesion provided by these scales is different. In cyclic oxidation, the top coat adhesion decreased with increasing TGO thickness while in isothermal oxidation the top coat adhesion increased with increasing TGO thickness. This was explained due to crack formation in the TGO caused by CTE mismatch during thermal cycling. During isothermal oxidation, less thermal stresses are present and the TGO that forms contains less cracks. During thermal shock tests, it was found that the heat gradient

could be quite large with temperatures of the top coat reaching 1250°C while the substrate remained at 950°C. This large thermal gradient could cause increased thermal stresses between the substrate, bond coat, TGO and top coat. The means of oxidation have an impact on the adhesion of the top coat and overall TBC lifetime.

The understanding of the failure modes of TBC systems is crucial in extending their operating life. The failure of TBC systems is associated with the delamination and spallation of the ceramic top coat. Delamination and spallation is usually caused by the emergence and propagation of cracks at the interface between the bond coat and the top coat, in the area where the TGO is formed. The cracks form due to large stresses induced by CTE mismatch during thermal cycling. In a recent study by Shin *et al.*[**102**], the top coat spallation was investigated by means of CT-scan. The delamination of the top coat was found to occur at the edge of samples and propagate inwards. Failure of the TBC can also occur due to mechanical damage in the form of an impact. An image of a spalled TBC sample is presented in Figure 2.33.

Figure 2.33: Example of a spalled TBC coating during thermal cycling [114]**.**

2.4.4.1. Foreign Object Damage

Foreign object damage (FOD) occurs when an object is entrained in a gas turbine and impacts its internal components [**97**]. The impacts can remove parts of the ceramic top coat

or create internal stresses that diminish the thermal protection in the immediate vicinity of the impact site. This damaged area creates a "hot-spot" in the bond coat and can lead to the thermal failure of the coating system. A diagram representing the effect of foreign object damage is presented in Figure 2.34. The problem of FOD is increased since the delaminated ceramic particles must travel through the gas turbine before exiting, creating secondary impacts known as domestic object damage (DOD). In a study by Kzempour-Liacy *et al.* [**115**] the first stage turbine blades of a power plant gas turbine were analysed after 23 872h of operation. Visual observation indicated that more than 90% of the blades were damaged locally mostly on the leading edge. The low thermal cycling of these blades resulted in less thermal fatigue than would be expected in aircraft gas turbines and would explain the long blade lifetime. Although foreign object damage costs an estimated $1.1 billion every year in direct costs and $12 billion in indirect costs [**116**], improvements to TBC coatings cannot decrease the damage incurred.

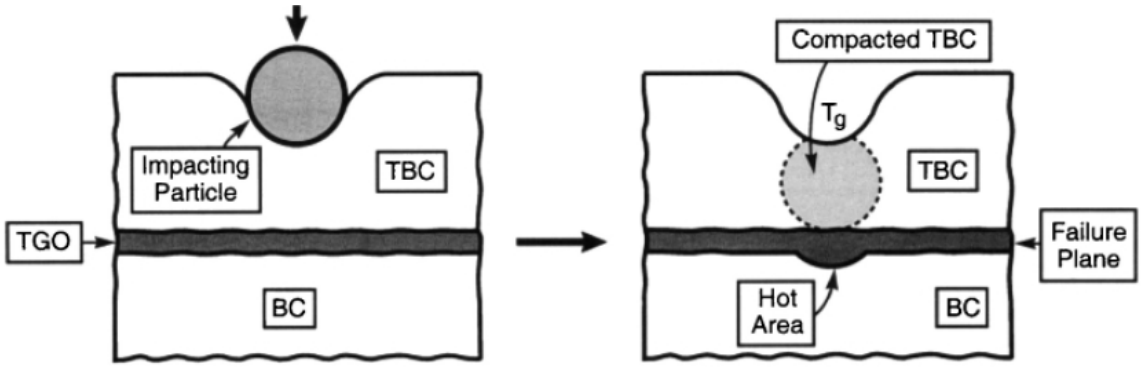

Figure 2.34: Foreign object damage failure mechanism [97]**.**

2.4.4.2. Thermo-mechanical Failure

Failure of TBC systems via thermo-mechanical means is associated with the growth of the TGO during thermal cycling. The growth of the TGO is controlled by parabolic diffusion and can be represented with the following equation:

$$h^2 = 2bt \tag{2.14}$$

where h is the scale thickness, b is the parabolic rate constant and t is the time[**97**]. The lower growth rate of α-Al_2O_3 makes it a favourable oxide as it offers the highest possible turbine life.

Thermo-mechanical failure can be attributed to two phenomena, the "rumpling" of the TGO scale or the uneven growth of the TGO scale. The first case occurs when constant growth of the TGO during thermal cycling induces compressive stresses due to the presence of the bond coat and top coat. Under these stresses, the TGO scale lengthens through out-of-plane displacements resulting in rumpling of the scale [**117**]. These out-of-plane displacements create local stress concentrations where crack initiation occurs. These cracks grow with continuing thermal cycling to eventually cause the spallation of the top coat and TBC system failure. Failure of this type has been observed in various studies [**114**,**118**] and its evolution is depicted in Figure 2.35.

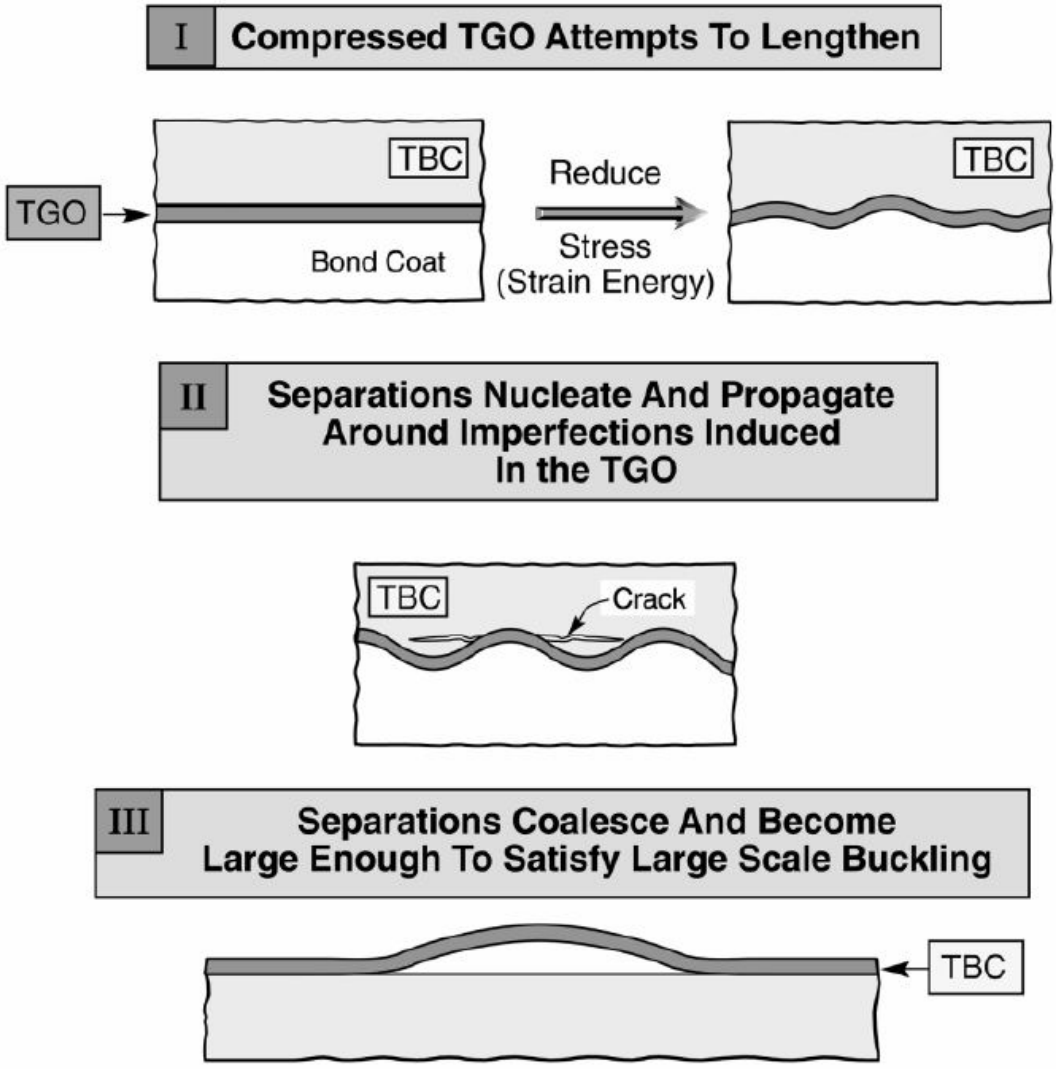

Figure 2.35: Thermo-mechanical failure sequence due to TGO rumpling (Adapted from [97])

The second case occurs when the growth of the TGO increases locally due to variations in bond-coat chemistry or of top-coat porosity. The TGO can therefore grow unevenly and forms oxide imperfections [**117**]. This uneven growth leads to stress concentrations and eventually crack initiation. With continued thermal cycling, these cracks will propagate and result in failure of the TBC system. The evolution of this phenomenon leading to failure is depicted in Figure 2.36.

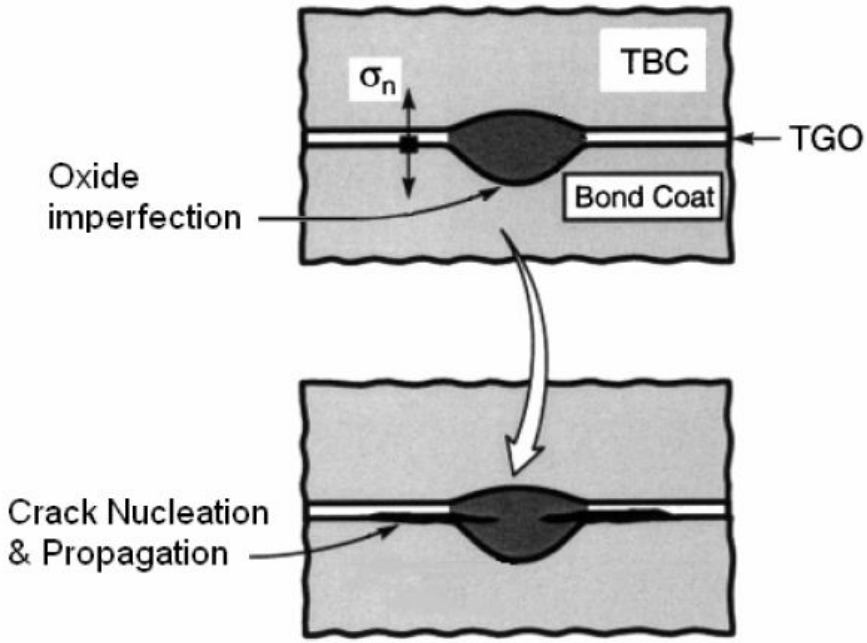

Figure 2.36: Schematic illustration of TBC failure due to uneven TGO growth and oxide imperfections (adapted from [97])

2.4.4.3. Bond Coat Oxidation: Unfavourable Oxides

While under operation, the bond coat is under continual oxidation due to the exposure to high temperature oxygen. This can lead to the eventual failure of TBC system through chemical means. The evolution of the oxidation process is depicted in Figure 2.37. MCrAlY coatings are composed of a γ-phase matrix composed of Ni and/or Co and β-phase precipitates composed of Ni and Al. Upon exposure to high temperature oxygen, the Al in the β-phase diffuses to the surface to create Al_2O_3. As this process continues, a zone of β-phase depletion of increasing width can be observed in the coating [**11**,**112**,**119**]. This has lead to the coating life being generally discussed in terms of β-phase depletion [**112**]. Eventually, when the diffusion of Al becomes unfavourable due to the large depletion zone, oxygen will react with other components of the γ-matrix. The formation of these mixed

oxides has been observed in previous studies [**112**,**11**,**120**]. The study conducted by Shibata *et al.* [**112**] found formation of spinel (NiO) and $NiCo_2O_4$ on top of the Al_2O_3 TGO scale. Tang et al. [**120**] also observed the formation of (Co, Ni) Cr_2O_4 and (Co,Ni)Al_2O_4 on top of the Al_2O_3 TGO scale. These mixed oxides and spinel are fast growing and accelerate the thermo-mechanical failure of TBC systems.

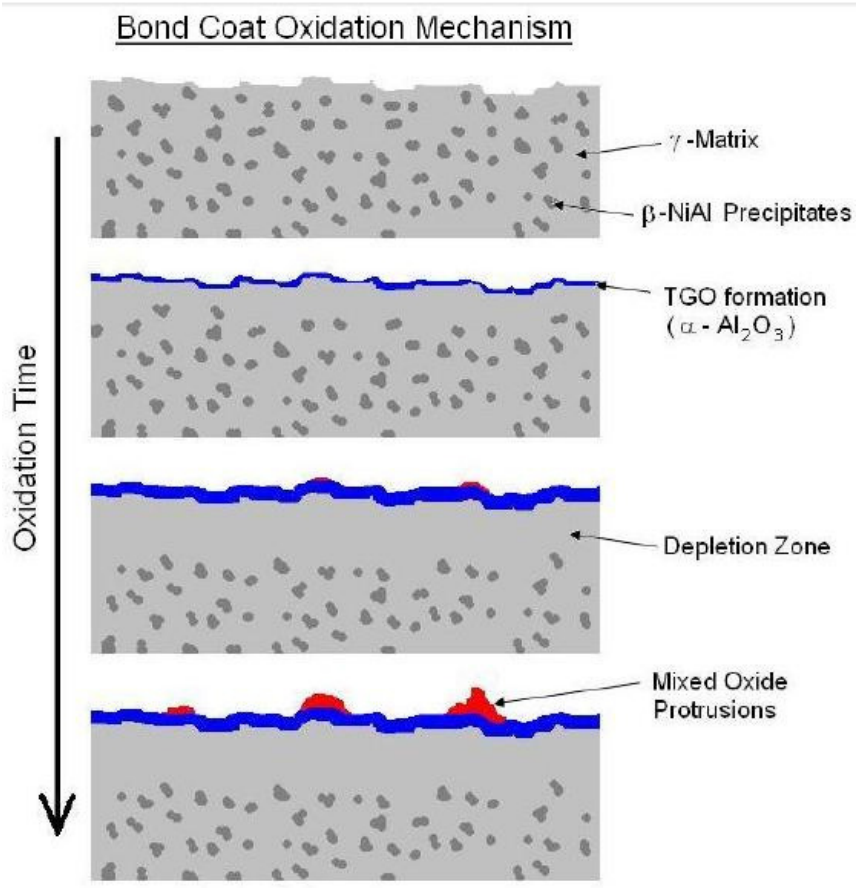

Figure 2.37: Evolution of TGO growth and β-depletion with oxidation time [121]

The depletion of Al and subsequent formation of various mixed oxides is known as the initial stage of the chemical failure of the TBC system. These fast growing mixed oxides increase the TGO growth rate and create protrusions that can cause the rapid thermo-mechanical failure of the TBC system.

2.4.4.4. Bond Coat Hot Corrosion

The exposure of the bond coat to high temperature combustion gases containing sulphur and water vapour can accelerate the failure of the bond coat and has been the focus

of various studies[**122**,**123**,**124**]. A study by Kaplin *et al.* [**122**] showed that bond coats oxidized in the presence of water vapour varying from 0-8% showed different evolutions. At 8% wt. water vapour, the mass gains were found to be the lowest of all cases while at 4% wt. water vapour the mass gains were the highest and the reference 0% wt. mass gains were measure to be between the other two cases. It was observed that the increase of water vapour increases the amount of spinel in the oxide scale up to a point, at approximately 4% wt., where the spinel is thick enough to prevent internal oxidation of the bond coat and leads to lower overall mass gains. The increase in spinel content when exposed to a humid atmosphere has also been confirmed by Zhou *et al.*[**124**]. This increase in mass gain and formation of spinel can lead to the rapid thermo-mechanical failure of the TBC system.

2.4.4.5. Summary of Failure Mechanisms

The primary failure mechanism of TBC systems is directly associated with the growth dynamics of the TGO scale and the oxidation dynamics of the bond coat. The life of TBC systems can be increased by minimizing the growth rate of the TGO scale. The formation of a dense α-alumina layer is therefore desirable due to its lower growth rate and diffusivity of oxygen when compared to spinel and other mixed oxides[**97**,**98**]. The formation of a TGO scale that is uniform and continuous is also desirable to prevent the formation of imperfections in the oxide scale [**97**,**117**]. The depletion of the Al rich β-phase is also detrimental to the oxidation performance of the coating as it will initiate the formation of mixed oxides. Controlling the growth rate, composition and uniformity of the TGO scale will lead to significant increases of TBC lifetime.

2.4.5. Improving performance

Many studies have aimed specifically at improving bond coat performance and durability. These studies have investigated the effects of bond coat microstructure, oxidation temperatures, oxidation environments, composition and manufacturing techniques in order to improve the oxidation behaviour.

2.4.5.1. Bond coat manufacturing techniques

Bond coats are primarily manufactured via HVOF, LPPS, APS however recent studies have explored the possibility of using Cold spraying[**70**,**125**,**126**,**127**,**128**], electrophoretic deposition [**129**], arc-ion-plating[**130**], EB-PVD[**124**,**131**] and magnetron-sputtering[**95**]. There are numerous studies aimed at investigating the influence of the manufacturing technique on the oxidation behaviour of the bond coat[**11**,**112**,**113**,**125**,**126**,**132**,**133**,**134**]. These studies indicate that bond coats sprayed via HVOF constantly outperform those sprayed by APS, VPS and LPPS [**11**,**112**,**125**,**133**,**134**]. Coatings deposited by cold spray have been found to outperform APS [**11**,**125**] and LPPS[**126**] while being very close to HVOF[**11**,**125**]. These studies however use varying qualities of coatings and oxidation temperatures which can affect the resulting coating performance. Shibata *et al.* [**112**] and Richer *et al.* [**11**] attributed higher oxidation rates to coating porosity, the more porous a coating, the lower its oxidation performance. This relation is attributed to the inwards diffusion of oxygen being facilitated by the increased porosity. The deposition method has also been found to affect the oxide content in the coating and the subsequent type of oxide formed. Tang *et al.* [**120**] found that oxides formed during the HVOF process promoted the formation of spinel-type oxides during oxidation. In contrast, a study by Di Ferdinando *et al.* [**134**] has attributed the superior oxidation performance of the HVOF coatings to the formation of Al_2O_3 during the spraying process. Similarly, a study by Toma *et al.* [**132**] comparing HVOF and VPS MCrAlY coatings showed that α-alumina was formed more rapidly and at lower temperatures on the HVOF samples than on the VPS samples. In this study, it was found that the HVOF process formed α-alumina, while another study indicates plasma spraying alumina will usually solidify as γ-alumina[**135**]. It appears that spraying parameters can influence the oxides formed in the coating and subsequently affect the oxidation behaviour of the TBC system.

2.4.5.2. TGO layer composition

The composition of the TGO layer can have a significant effect on the oxidation dynamics of the TBC system. It is favourable to obtain an alumina layer composed of dense, uniform and slow growing α-Al_2O_3 than other mixed oxides, spinel or transition aluminas.

The density of an alumina scale will prevent further oxidation of the coating while its uniformity will prevent spallation of the top coat. The CTE of the YSZ ceramic top coat is $9.0x10^{-6}$ m/mK while for spinel it is $6.4x10^{-6}$ m/mK and for alumina $8.0x10^{-6}$ m/mK. It is therefore favourable to have an oxide layer composed of alumina which has a CTE very close to the YSZ top coat [**136**]. Although most studies agree that α-alumina is the most favourable oxide, many studies do not distinguish it from the other forms of alumina that can form during oxidation.

Much of the current knowledge of alumina comes from the dehydroxilation of aluminum hydroxide through heating at elevated temperatures. Through these experiments it was determined that heating aluminum hydroxide to temperatures below 1100˚C yielded transition aluminas while temperatures above 1100˚C yielded alpha alumina [**135**]. It was also observed that the temperature of formation and structure of the alumina depended on the starting hydroxide. After dehydroxilation of the five types of aluminum hydroxides, seven different transition aluminas were identified [**135**]. The starting hydroxide which most resembles the oxidation of MCrAlY is boehmite (AlO(OH)). The alumina in this reaction progresses through the following states in order: γ, δ, θ and α [**135**,**137**,**138**]. The transformation from one alumina state to another is non-reversible, once δ-alumina is formed, it will not revert back to γ-alumina but with further heating will transform to θ and eventually α-alumina. Similarly, θ-alumina will not revert back to γ- or δ-alumina but will transform to α-alumina and α-alumina will remain in its stable state[**135**]. This transformation however can lead to internal stresses due to densification of the oxide scale. The density of γ-alumina is approximately $3.67g/cm^3$ while the density of α-alumina is $3.99g/cm^3$ [**139**]. Through continued heating at high temperatures, the density of α-alumina can increase through sintering and should be considered in the long-term evolution of the TGO scale.

Identification of the γ, δ and θ transition aluminas as well as α-alumina is usually done via XRD and in some cases through IR spectroscopy as the XRD peaks of δ and θ alumina are hard to distinguish [**138**,**140**]. Due to this fact, some studies do not differentiate between δ and θ alumina treating both as the same alumina state. Identification of morphology has

also been done using SEM images however as there may be no morphology change from one state to the other this is only useful for very short oxidation times or to identify the initially formed alumina [**135**,**137**]. It has been observed that γ-alumina forms platy crystals with hexagonal shape[**135**], δ-alumina is a pseudomorph of γ-alumina[**135**] , θ-alumina forms a whisker or needle-like morphology [**120**,**132**] and the α-alumina shape varies according to its precursor[**137**]. Due to the difficulties in identifying alumina phases with each method, both XRD and SEM analysis must be used in tandem to accurately identify the type of oxides present on the sample.

There are two possible methods to progress through the alumina states, heating at a temperature higher than the transformation temperature of the desired alumina state or holding at a lower temperature for a prolonged period[**135**]. The approximate temperatures of formation of each alumina are found in Table 2-6, the values were taken from various studies which involve different oxidation temperatures, heating rates, heating times and starting materials as such, these are approximate values [**120**,**132**,**137**,**138**,**139**,**140**,**141**,**142**].

Table 2-6: Approximate formation temperature of aluminas

Alumina state	Approximate formation temperature
γ	Up to 700ºC
δ/ θ	750ºC-1000ºC
α	1050ºC and up

Factors other than temperature have been known to affect the formation time of α-alumina, more notably the initial state of the sample. Studies in which some samples were doped with α-alumina prior to heat treatments have shown that as the initial content of α-alumina increases, the θ to α transition temperature decreases [**139**,**142**]. Similarly, samples composed of amorphous alumina have a lower formation temperature of α-alumina than samples that contain γ-alumina [**140**]. In order to obtain the desired oxide the oxidation temperature must therefore be carefully chosen.

The advantages of α-alumina are not only due to its higher density and more uniform oxide scale formation but also due to the solubility of the ceramic top coat. According to Zhou *et al.*[**124**] the ZrO_2 that is contained in the top coat is much more soluble in transition

(γ,δ,θ) aluminas than in α-alumina. This high solubility leads to some top coat material being included in the TGO layer and subsequently to the formation of precipitates during the transition to α-alumina. The precipitates in the TGO are likely to reduce the lifetime of the TBC system by increasing stress concentrations and allowing for the diffusion of oxygen.

2.4.5.3. Bond coat oxidation pre-treatments

Some studies have investigated the effect of an oxidation pre-treatment of the bond coat prior to the application of the ceramic top coat [**127**,**133**,**143**,**144**]. These studies indicate that the pre-treatments with controlled temperatures and oxygen contents can initiate the formation of desirable α-alumina. Heat treatments have also been shown to precipitate β-NiAl in bond coats that previously contained a uniform γ-phase due to changes occurring during the thermal spray process [**11**,**133**]. The heat treatments have also been shown to remove porosity through sintering. A study by Chen *et al.*[**145**] investigated heat treatments in various environments to determine the resulting content of alumina and spinel. In the as-sprayed state, the coating TGO contained 20% alumina and 80% spinel, after heat treatment in vacuum, the TGO contained 70% alumina and 30% spinel while a heat treatment in a low O_2 environment yielded a TGO with 90% alumina and 10% spinel. After high temperature oxidation, it was observed that the as-sprayed coating failed quickly while the vacuum and low O_2 treated samples lasted significantly longer. The vacuum heat treated sample exhibited the longest oxidation life of all three samples. It appears that heat treatments should therefore be carried out under vacuum in order to achieve the longest bond coat life possible.

2.4.5.4. Bond coat surface treatment

Some researchers have investigated the relation of the bond coat surface condition on the oxidation behaviour [**112**,**128**,**143**,**144**,**146**,**147**,**148**]. Their investigations showed increased formation of spinel and mixed oxides after the oxidation of as-deposited coatings. Surface treatment via polishing or shot-peening was shown to decrease the oxide growth rate, and delay the emergence of mixed oxides. After coating deposition is complete, the top surface of the coating is exposed to oxygen and forms oxides that may not be present in the bulk of the coating. These oxides can be detrimental to the long-term oxidation process and their removal through polishing or grinding can greatly increase the lifetime of the TBC system [**149**].

In studies where a top coat was applied, the effect of surface roughness varied by top coat deposition method. In cases where the top coat was deposited via plasma spraying, some roughness was desirable for increased top coat adhesion and TBC system life. On the other hand, top coats deposited via EB-PVD were found to have increased performance if deposited on a polished bond coat. It appears that the bond coat should therefore be polished to remove surface oxides and then either used without a ceramic top coat, have the top coat applied via EB-PVD or have the surface roughened for better adhesion prior to applying the top coat applied via plasma spray.

2.4.5.5. Nanocrystalline bond coat morphology

Significant advantages of bond coat behaviours can be theoretically achieved through the use of nanocrystalline materials. These materials have grain sizes in the nanometre scale and have significantly different properties than conventional grained materials including increased hardness, strength, enhanced diffusivity, reduced density, increased specific heat capacity, higher CTE, lower thermal conductivity and reduced ductility[**150**]. Due to the smaller sizes of the grains, the volume fraction of the grain boundaries can be as high as 50% which significantly increases the ability for diffusion. In addition, nanocrystalline materials exhibit more uniform and better corrosion resistance as well as increased chemical reactivity [**150**]. However, the grain size of nanocrystalline materials can increase rapidly with the exposure to high temperatures negating any positive effects of the small grain size and making such materials difficult to deposit via conventional thermal spraying. Modifications to HVOF and plasma spray techniques and the emergence of cold spraying in particular have only recently enabled the deposition of nanocrystalline materials. The tendency of nanocrystalline materials to behave with superplasticity at low temperatures (0.38 Tm in the case of Ni) [**150**] could have a positive effect on the deposition of these materials via cold-spraying.

As such, many studies have focused on exploring nanocrystalline materials used for bond coats [**95**,**99**,**146**,**151**,**152**,**153**]. A study by Mercier *et al.* [**146**] investigated the oxidation of conventional and nanocrystalline MCrAlY particles. The study showed that after 96h oxidation at 1000°C, the conventional particles had a TGO composed of alumina and mixed oxides while the nanocrystalline particles had a TGO composed exclusively of

alumina due to the increased Al diffusion. Other studies have also confirmed this tendency holds for MCrAlY coatings and have theorised that some oxides introduced in the cryomilling may help in the formation of the alumina layer [**99**,**152**,**153**]. However, a study by Tang *et al.*[**151**] has found that although initial formation of alumina is better for the nanocrystalline coatings, the diffusion of Al into the substrate and to the TGO layer is higher which leads to a more rapid Al diffusion. After 330h of oxidation, the results have shown that both the conventional and nanocrystalline bond coats had approximately the same TGO thickness and composition. Further studies are required to determine if nanocrystalline bond coats are advantageous in long term cyclic and isothermal oxidation.

2.4.5.6. Top coat enhancements

Although most enhancements to TBC systems deal with the failure mechanisms and thus the bond coat and TGO, some improvements can be made to the top coat in order to increase TIT and turbine performance and efficiency. A study conducted by Curry *et al.* [**103**] investigated a top coat stabilized by the addition of dysprosium instead of yttrium. The thermal conductivity of this top coat is significantly lower than the conventional YSZ. It was also found that as the top coat is heated, it sinters and its thermal conductivity rises. The thermal conductivities were measured at various temperatures up to 1200°C and the minimums were found at around 800°C after which radiation raises the thermal conductivity of the top coat. The results of this study are found in Table 2-7.

Table 2-7 : Comparison of Zirconia top coats stabilized with Yttrium and Dysprosium [103]

	YSZ (W/mK)	**DySZ (W/mK)**
Before HT	0.85-1.25	0.5-0.7
After HT	1.4-1.95	0.8-1.25

Other studies have explored the possibility of layering different top coat materials in an attempt to block certain radiation wavelengths and decrease the overall thermal conductivity. The study utilised alternating top coats comprised of YSZ and alumina and successfully achieved a lower substrate temperature [**154**]. These enhancements of the top coat will allow for a rise of the TIT and longer TBC life due to the reduction of the oxidation temperature.

2.4.5.7. Other enhancements

Many studies have explored other enhancements to the TBC system. In a study by Yanar *et al.* [**155**], the addition of a platinum aluminide layer under and over a NiCoCrAlY bond coat was studied under cyclic oxidation. It was found that in both cases, the platinum aluminide layer increased the lifetime of the TBC but the greatest gains were found from the addition of the platinum overlayer. This study however does not consider the effects of a vacuum heat treatment that is applied after the addition of the platinum aluminide layer, prior to the addition of the top coat. As mentioned previously this heat treatment may help form an initial alumina layer and prolong the coating life. Aluminizing treatments to NiCoCrAlY coatings have also been oxidised by Lu *et al.* [**130**]. The results of this study indicated the aluminizing treatments increased hot corrosion resistance, reduced oxidation and decreased coating degradation rates due to the presence of a thin alumina layer.

The addition of certain elements to MCrAlY coatings has been shown to affect oxidation dynamics. The presence of certain elements in the coating such as Hf, Zr, Y or Ce have been shown to prolong TBC life due to the reactive element effect [**156**] and more specifically a reduction in the Y content has been shown to increase Al diffusion [**132**]. A study by Fossati *et al.* [**157**] where small amounts of Ca and Si were added to MCrAlY, 0.085 wt. % and 0.028 wt. % respectively has been shown to reduce Al depletion in the coating. The addition of these elements is said to increase the reactivity to oxygen and create a small alumina layer prior to particle deposition. The results however show a higher mass gain then samples containing the conventional powder. Further experiments are required to demonstrate if the reduced Al depletion is a result of a dense alumina layer or the formation of other mixed oxides and spinel. Another study by Lan *et al.* [**158**] investigated the addition of 0.2 wt.% Dy in an CoNiCrAlY coating. The results indicate that this addition accelerates the θ to α alumina transition and results in lower oxidation weight gain and better overall oxidation resistance.

Research has also been conducted on multiple-layered bond coats. A study by Peng *et al.* [**156**] explored a double layered bond in which the base layer was deposited by plasma-activated EB-PVD in order to obtain a coarse equiaxed structure, and where the top layer was deposited by EB-PVD to obtain a columnar layer. This particular arrangement was

engineered to reduce the diffusion of Al to the surface due to the two different bond coat structures. The TGO thickness of this coating and an EB-PVD deposited coating was measured after oxidation. The TGO of the single layer coating was found to contain Hf diffused from the substrate and had a thickness of 7μm while the TGO of the dual layer coating was free of Hf and had a thickness of 3.6μm. A U.S. patent has also been filed describing a two-layer bond coat [**159**]. In the patented system, the bottom layer remains the same while the top bond coat layer is seeded with alumina particles in an effort to increase the bond coat CTE to more closely match that of the Top coat.

2.4.5.8. Enhancements Summary

Many studies have been devoted to increasing the performance of TBC systems and with particular emphasis on the bond coat. Most of these results are positive but the reason behind their improvements is not well understood. Significant research must be conducted to determine how much improvement is obtained by comparing each modification with coatings of the same composition, spraying techniques, spray parameters, heat treatments and oxidation conditions in order to isolate the actual performance gain.

Chapter 3 - Research Objectives

3.1. General Objectives

The objective of this study is to increase the lifetime of current TBC systems in order to move towards a "prime-reliant" TBC system opening up the opportunity for increased gas turbine performance, efficiency and durability. The investigation of pertinent literature has indicated that TBC failures occur mostly due to oxidation leading to the emergence of mixed oxides and spinel in the TGO. Current thermal spraying technologies introduce defects in the bond coat during the deposition process due to elevated spray temperatures. Bond coats deposited via CGDS are promising as the process uses relatively low temperatures and is capable of retaining the original powder microstructure without the introduction of oxides in the manufactured coating. However due to its recent development, the CGDS process cannot currently achieve particle velocities high enough to reliably deposit MCrAlY bond coats at high deposition rates. To address these issues, this research work proposes to develop a new CGDS nozzle designed to achieve high particle velocities in order to increase the particle deposition rates and coating quality of CoNiCrAlY bond coats. Coatings manufactured with the use of this new nozzle will then be oxidised alongside coatings deposited with the HVOF and APS processes. Differences in microstructure and oxidation evolution will then be compared to determine which coating type is most effective for oxidation resistance. The study will also compare the oxidation of these samples at two different oxidation temperatures in order to analyse the differences in oxide scale formation. Finally, this study will evaluate the impact of as-sprayed surfaces on the oxidation behaviour of bond coats to determine the effect on long-term oxidation.

3.2. CGDS Nozzle Design

3.2.1. General

The first objective of this study is to design a CGDS nozzle capable of depositing high quality CoNiCrAlY bond coats while reducing the gas consumption in order to drive down manufacturing costs. The CGDS technique has many advantages over traditional thermal spray techniques which could be beneficial to bond coats. Specifically, CGDS

coatings have low coating oxide contents, introduce no microstructural changes from the feedstock powder and have compressive residual stresses. These properties of the CGDS process could represent a significant advantage in oxidation performance however current nozzle designs are not capable of depositing dense coatings. A CGDS nozzle must therefore be carefully designed to achieve particle velocities high enough to manufacture a coating free of undesirable porosity. With this in mind, shockwaves and other disturbances introduced by typical straight profiled nozzles must be eliminated. In order to reduce these shockwaves in the nozzle, the method of characteristics will be employed. This will lead to a curved nozzle profile, removing any flow disturbances but will also increase manufacturing complexity. The use of the method of characteristics alone will not ensure particle acceleration, rather it will facilitate it. An optimal nozzle expansion rate must be employed to achieve the high particle velocity required for the deposition of CoNiCrAlY powders. Due to the complexity of the effect of the MOC section on the nozzle geometry-gas and gas-particle interactions, the nozzle will be designed and modelled using CFD software prior to physical manufacturing. Several simulations using the optimal nozzle model will then be conducted to determine the effect of stagnation pressure and stagnation temperature on the particle exit velocities.

3.2.2. Effect of Standoff Distance and Gas Mixtures

The standoff distance of CGDS nozzles can have a great influence on particle velocities and deposition rates. More specifically, the creation of a bow shock above the substrate can slow small particles below the critical velocities of the material. The effect of the standoff distance will therefore be evaluated using the previously developed CFD model. Similarly, different gas mixtures will be investigated to determine their effect on particle velocities. The previously developed CFD model will be modified to include the injection of powders within a gas stream. Both the driving gas and the powder feeding gas will be varied to assess the effect of various mixtures on the final particle velocities.

3.2.3. CGDS Nozzle Manufacturing

Due to the specific curved nozzle profile developed for the CGDS nozzle, new manufacturing techniques had to be developed. Further enhancements are also required in order to prevent nozzle clogging and ensure a long nozzle life.

3.3. Characterization of Short and Long-Term Bond Coat Oxidation Behaviour

3.3.1. General

As was discussed in Chapter 2, most TBC failure methods occur as a by-product of oxidation, more specifically due to the formation of spinel or mixed oxides in the TGO scale. It has been shown that the formation of an α-alumina scale is preferred as it is slow-growing, dense and uniform resulting in increased TBC durability. Microstructural changes in the bond coat resulting from thermal spraying have also been shown to be detrimental to the oxidation performance. Furthermore, oxidation and pre-treatment temperatures have shown to have a significant effect on the oxidation behaviour of TBC systems. It was decided that this study will focus on the oxidation performance of APS, CGDS and HVOF sprayed CoNiCrAlY coatings under two different temperatures. To reduce the complexity of this study and to isolate the bond coat behaviour, it was chosen to study free-standing bond coats without the presence of a superalloy substrate or a ceramic top coat. This approach will allow for the identification of the influence of manufacturing method and heat treatment temperature on the bond coat oxidation behaviour. Although this method will allow for the identification of the best suited deposition process and heat treatment temperature, it must be noted that TGO scales grow faster when a top coat is applied [**160**] and that Al diffusion into the superalloy substrate [**157**,**151**], and diffusion of elements from the superalloy substrate [**131**] can have a significant effect on oxidation performance.

3.3.2. As-Sprayed

It has been demonstrated that surface treatments applied to bond coats prior to the application of the ceramic top coats have been beneficial to the oxidation behaviour. The oxides formed at the surface of coatings appear to accelerate the detrimental oxide formation in the TGO layer. It is unclear if these findings are valid with different manufacturing techniques which will introduce different oxides in the coating. The long and short term oxidation tests of as-sprayed samples will be carried out and compared with grinded samples to determine the effect of grinding for various manufacturing techniques.

3.3.3. Long-Term Oxidation

Although short term oxidation tests can indicate coating lifetime, they cannot accurately describe the behaviour during long-term oxidation. Other factors such as premature Al depletion or rapid formation of mixed oxides can cause a coating appearing to exhibit superior performance to rapidly fail. This study will therefore attempt to compare the long-term isothermal oxidation lifetime of grinded and non-grinded coatings to determine their behaviour past the formation of the initial oxide scale.

Chapter 4 - Equipment and Procedures

This chapter will detail the approach followed and the equipment used to achieve the study objectives. More specifically, the feedstock materials, the spray deposition equipment and the material characterization equipment will be described in detail.

4.1. Feedstock Material

The feedstock material used in this study is a CoNiCrAlY alloy which is commonly used as a bond coat material in TBC systems due to its good oxidation and hot corrosion resistance. This alloy is available in powder form with a variety of size distribution which makes it suitable for deposition using different thermal spray processes. The powders used in this study are commercially available CoNiCrAlY powders from Sulzer Metco labelled AMDRY 9951 and AMDRY 9954. Both powders are identical in composition and spherical in morphology due to the spray atomization process used. They are only distinguished by their particle size distribution: AMDRY 9951 has particles ranging from 5μm to 37μm while AMDRY 9954 has particles ranging from 11μm to 62μm. The specific chemical composition of these powders is presented in Table 4-1: Chemical composition of the AMDRY 9951 and AMDRY 9954 CoNiCrAlY powdersTable 4-1.

Table 4-1: Chemical composition of the AMDRY 9951 and AMDRY 9954 CoNiCrAlY powders

Element	Co	Ni	Cr	Al	Y
Weight %	37.97	32.01	21.22	8.04	0.5

This CoNiCrAlY alloy was selected since it is readily available and is currently used by various gas turbine manufacturers such as General Electric and Rolls Royce. Although each MCrAlY alloy will exhibit its own specific oxidation and hot corrosion behaviour, the selection of this alloy is not thought to affect the final results of this study. This study is analysing trends in oxidation behaviour due to the deposition process and oxidation temperature. These trends should remain the same regardless of the MCrAlY composition due to the inherent similarity of these alloys.

4.2. Equipment for Bond Coat Deposition

This section outlines the equipment used to manufacture CoNiCrAlY bond coats with particular focus on the facilities at the University of Ottawa Cold Spray Laboratory. A brief description of the APS and HVOF systems used to deposit bond coats for comparison is also included.

4.2.1. Feedstock Powder Material Storage and Processing

4.2.1.1. Feedstock Powder Storage

All feedstock powders in use at the University of Ottawa Cold Spray Laboratory are stored in an environmentally controlled fireproof cabinet. The cabinet room is equipped with a dehumidifier and the cabinet itself with a heating coil and sensor system to ensure both temperature and humidity are properly controlled. An image of the powder cabinet is presented in Figure 4.1.

Figure 4.1: View of environmentally controlled powder storage cabinet

4.2.1.2. Feedstock Powder Processing

For spraying consistency, the as-received powders are sieved for aerodynamic considerations or to obtain a narrow particle size variation. This is done through the use of a sieving machine (W.S. Tyler model RX-29) and of multiple drum sieves of the appropriate mesh size (CE Tyler) displayed in Figure 4.2 and Figure 4.3 .

Figure 4.2: Photograph of the sieving machine (W.S. Tyler model RX-29)

Figure 4.3: Photograph of three stacked sieve drums (CE Tyler)

The as-received powder is placed in drum sieves which are arranged in a sequence from largest to smallest. Small particles progressively fall through the larger mesh due to the agitation and vibration of the sieving machine while large particles stay in the upper drum sieve. At the end of the process, each drum sieve contains powder that is larger than its specified mesh size and the smallest of particles fall into a drum container. More drum sieves can be added to increase the granularity of the particle size range. This allows for good control of the powder size distribution.

4.2.2. University of Ottawa Cold Spray Laboratory Facility

The following describes the various features of the CGDS system located in the University of Ottawa Cold Spray Laboratory.

4.2.2.1. Driving and Carrier Gas Supply

The manufacturing of CGDS coatings were conducted with the use of helium as the driving and carrier gas while certain tests were conducted using nitrogen as the driving gas. CoNiCrAlY is a hard material and requires high velocities for deposition. For this reason, high gas velocities are required to accelerate the particles above their critical velocity. As was previously discussed, helium offers the fastest gas velocities due to its high specific heat ratio and low molecular weight. Due to its inert nature, the helium gas will also cause no chemical degradation of the CoNiCrAlY alloy. Although nitrogen will lead to lower particle

velocities, it is a much less costly gas and production of CoNiCrAlY coatings via nitrogen gas could represent significant cost savings.

For the driving gas, the University of Ottawa CGDS system uses six industrial grade high pressure helium gas cylinders joined by a manifold (Figure 4.5). The inlet pressure of the system is controlled by a pressure regulator (Figure 4.4). The use of six cylinders prevents experimental errors caused by pressure fluctuations in the cylinder due to the high volume flow rate of gas. This also allows spraying at high pressures for extended periods of time without requiring changing pressure cylinders.

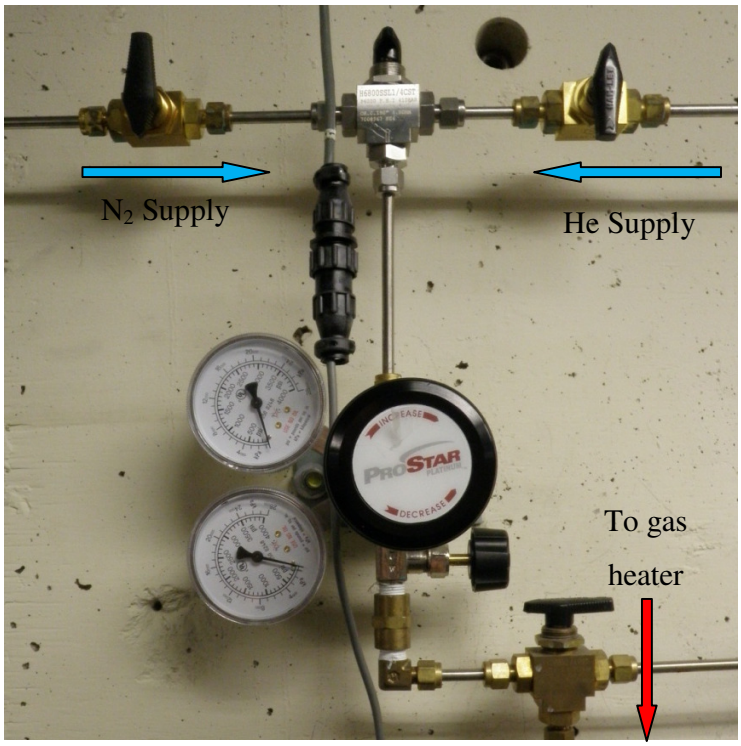

Figure 4.4: View of driving gas pressure regulator showing gas inlets.

Four additional cylinders of high pressure nitrogen are also connected to the nozzle inlet and used to preheat the CGDS system (Figure 4.5). The system gas heater requires some time to reach the desired temperature and does so while gas is flowing to ensure an equalised temperature distribution. Nitrogen is therefore used to preheat the system as it is less costly than helium. Once the system has reached the required temperature, the operator may continue spraying with nitrogen or change the input supply to helium by the use of a three-port ball valve.

Figure 4.5: Photograph of the high pressure gas supply showing a) nitrogen driving gas bottles, b) helium driving gas bottles, c) helium feeding gas bottles

The carrier gas supply consists of a single cylinder of high pressure helium which is regulated via a pressure regulator and a flow regulator (Figure 4.6). This gas is used to ensure a positive pressure difference between the powder feeder and the nozzle powder inlet which entrains powdered particles into the carrier gas flow. The gas flow must remain constant to ensure a uniform material feed while the pressure must be controlled to ensure the particles do not impact the nozzle walls and that the feeder remains below its maximum rated pressure.

Figure 4.6: View of flow regulator (left) and pressure regulator (right) used to control the feeding gas.

4.2.2.2. Spray Chamber

The CGDS spraying chamber consists of acrylic door panels mounted on a rigid table providing visibility and accessibility from all sides. The spray chamber is also equipped with a 1.5hp ventilating fan exhausting through a 0.4μm particulate filter. The spraying chamber is sealed to ensure any powder particles that did not adhere to the substrate remain in the chamber or are collected in the ventilation system. The driving gas line is connected to the spraying chamber via a port connector on the upper panel while the powder flow line is fed through a notch in one of the acrylic doors. A photograph of the spray chamber is depicted in Figure 4.7.

Figure 4.7: Cold spray chamber at the University of Ottawa Cold Spray Laboratory.

The spray nozzle is vertically positioned in the spraying chamber on a linear stage equipped with a micrometer in order to adjust the nozzle stand-off distance (SOD). The nozzle is directly above the substrate holder which is equipped with a computer controlled two-axis traverse system. This system consists of two perpendicular screw tracks activated by electronic stepper motors in an X-axis and Y-axis configuration. A custom computer program developed using LabView controls the motor rotational speed and direction. The number of motor steps required for the displacements is also calculated and yields an accuracy of ±0.01mm/s and 0.0064mm. The software also has the capability of automatically displacing the substrate for spraying multiple passes, spraying surfaces of varying dimensions and overpass ratios (the % a spray line overlaps with the previous line) and having an automatic rapid initial displacement. The X-Y traverse system and nozzle mount is displayed in Figure 4.8 while a screen capture of the software is displayed in Figure 4.9.

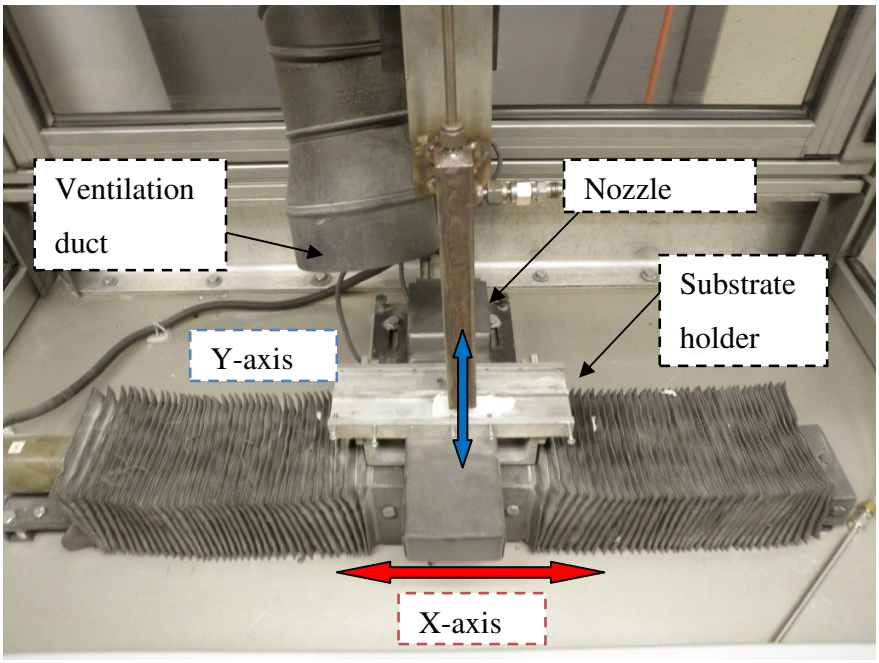

Figure 4.8: View of the two-axis traverse system, ventilation duct and substrate holding system.

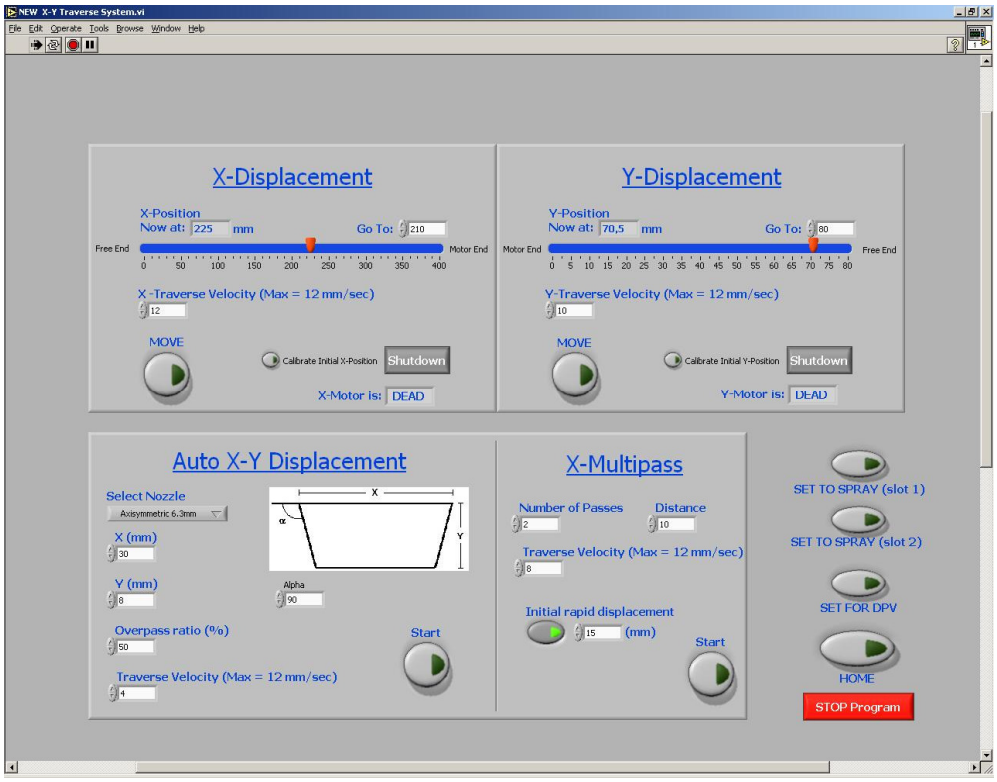

Figure 4.9: Screen capture of the X-Y traverse system control software

The CGDS system also features many measurement probes in order to properly quantify the flow parameters. Pressure transducers and thermocouples are positioned along

the gas lines and most importantly at the nozzle inlet. The inlet pressures and temperatures are used to approximate the stagnation properties at the nozzle inlet and therefore characterize the flow. These values are also used as reference for repeatability purposes. The signals of these probes are collected and displayed via LabView. The data is collected continuously at 10Hz and converted to meaningful units before being displayed in real-time. The data is used to monitor the spray conditions and is also saved in a text file for future reference and analysis. Pressure probes on the supply gas line, near the high pressure cylinders allow the user to monitor the amount of gas remaining in these cylinders and assess when replacement is required. A screenshot of the LabView software displaying a typical temperature and pressure profile is presented in Figure 4.10. Operator readout is displayed on a CRT monitor in the spray chamber with a large pressure and temperature readouts as can be seen in Figure 4.11 and Figure 4.12.

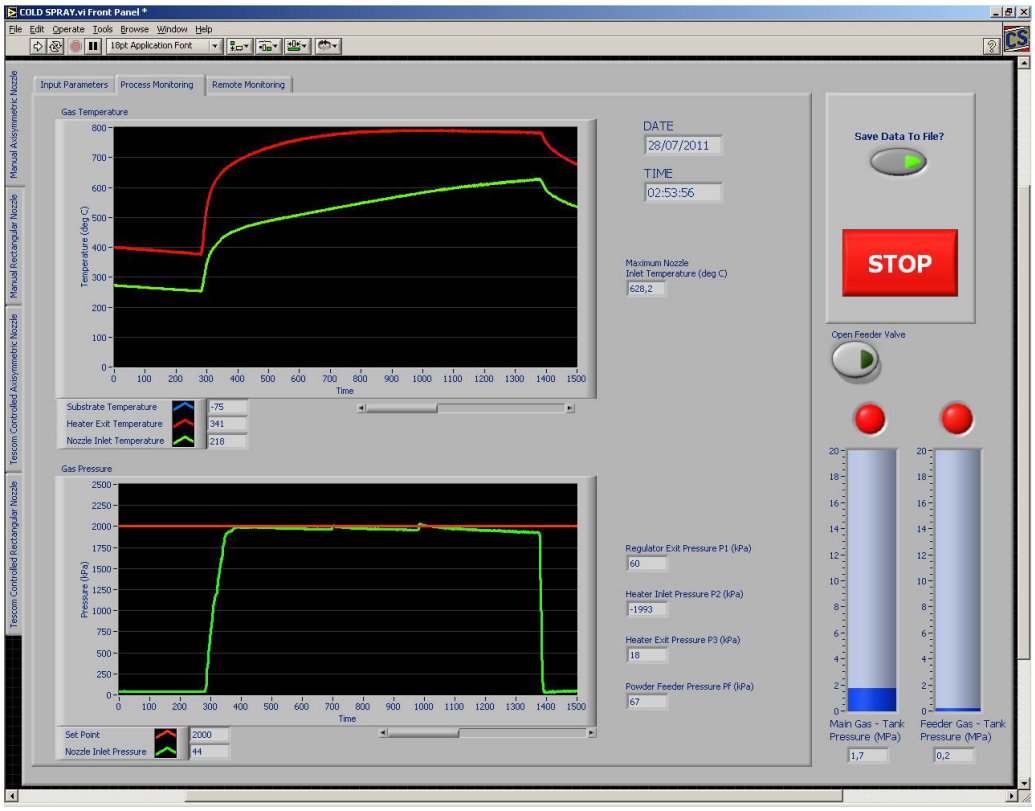

Figure 4.10: Screenshot of the LabView software used for data acquisition and process monitoring

Figure 4.11: View of the CRT display from the operator viewpoint and 30kW power supply

Figure 4.12: Screen capture of the display software used by the operator

4.2.2.3. CGDS Supersonic Nozzle

The CGDS nozzle used in this study was designed specifically for depositing CoNiCrAlY particles through the use of the University of Ottawa Cold Spray System. The completed nozzle is depicted in Figure 4.13: View of custom CGDS nozzle.. A detailed overview of the nozzle design and manufacturing process is presented in Chapter 4 -

Figure 4.13: View of custom CGDS nozzle.

4.2.2.4. Gas Heater

The CGDS system is equipped with an electric resistance gas heater capable of achieving gas temperatures of up to 800°C at the nozzle inlet. The heater consists of a coil-shaped 4m long stainless steel pipe with an outer diameter of 5/8" and is connected to a 30kW DC power supply. As gas flows through the heated pipe, it gains thermal energy by the means of convective heat transfer. The heater power can be varied by modifying the voltage through the use of a variac control giving the user the ability to vary the gas temperature. The heater coil is thoroughly insulated using ceramic wool to prevent any losses to the environment. A photograph of the heater is presented in Figure 4.14 while the power supply is presented in Figure 4.11.

Figure 4.14: Photograph of the insulated driving gas heater

4.2.2.5. Powder Feeder

The powder supplied to the CGDS nozzle is controlled by a commercially available powder feeder (Praxair model 1264, Praxair Surface Technologies). The powder feeder consists of a cylindrical canister in which the feedstock powder is placed prior to spraying. A perforated wheel is located at the base of the canister and mounted to a motor. As the perforated wheel rotates, small amounts of powder fill the holes and are then exhausted through the powder feeder outlet port due to the positive pressure difference between the

canister and the nozzle. The nozzle rotational speed can be varied in order to increase or decrease the amount of powder fed to the nozzle. In order to reduce clogging, the powder feeder is equipped with a hammer that taps the wheel during rotation thus dislodging particles that could potentially clog the system. A photograph of the powder feeder is presented in Figure 4.15.

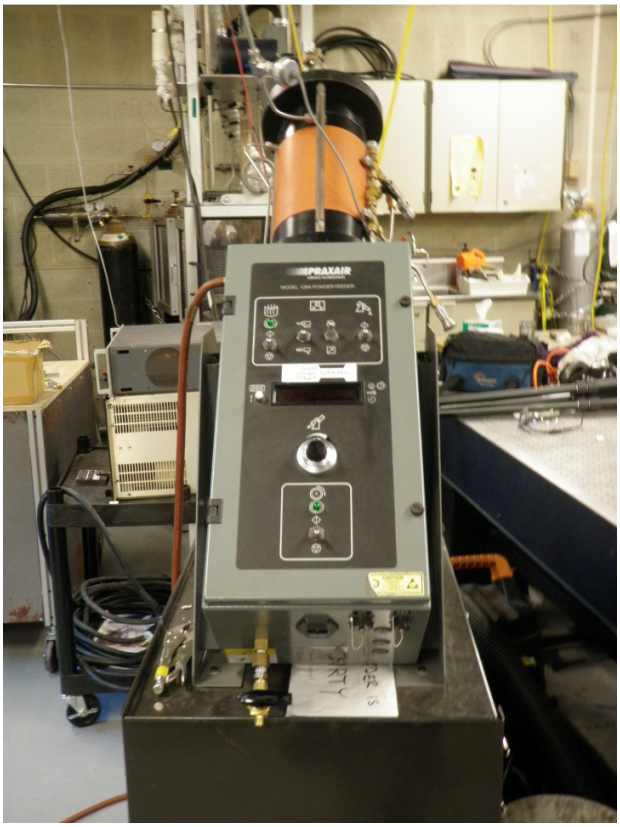

Figure 4.15: Photograph of powder feeder at the University of Ottawa Cold Spray Laboratory

4.2.2.6. Substrate Material

The CoNiCrAlY coatings in this work were deposited on T-6061 aluminum alloy substrates in flat bar form. The substrates were cleaned with acetone to remove any grease or other contaminants that may be on the surface and negatively affect the deposition process. This aluminum alloy was selected due to its wide availability and low cost. Although the bond coats would be typically deposited on a nickel-based superalloy, the substrate material for this study has no importance as it will be sectioned from the bond coat after deposition. The softer aluminum substrate will also facilitate the removal of the bond coat when compared to harder nickel substrates.

4.2.3. Other Thermal Spray Equipment

To compare the oxidation behaviour of CGDS coatings with other thermal spray manufacturing techniques, some samples were manufactured using the APS and HVOF techniques. These coatings were produced using the AMDRY 9954 CoNiCrAlY powder (which has the same composition as the powder used to manufacture the CGDS coatings) as per the powder manufacturer's recommendations. This will allow for effective comparison of the effect of thermal spray processes on the bond coat oxidation behaviour. As the equipment for depositing these coatings is not available at the University of Ottawa, the deposition of the APS and HVOF coatings were outsourced to the Quebec Coating Division of Vac Aero International Inc. The APS coatings were produced with the use of a SG100 plasma torch manufactured by Praxair and using Ar and He as the primary and secondary plasma gases. The HVOF coatings were produced with the use of a DJ2600 HVOF torch manufactured by Sulzer Metco with the use of H_2 and O_2 as the combustion gases. The specific deposition parameters will not be disclosed in order to maintain the manufacturer trade secrets.

4.3. Material Characterization

This section will describe the approach used to characterize the bond coats of this study. More specifically, the methods used to investigate the microstructural changes induced by the thermal spraying processes and the bond coat oxidation behaviour. All analysis was conducted in the University of Ottawa Materials Characterization Laboratory.

4.3.1. Coating Characterization

The various CoNiCrAlY coating samples were investigated qualitatively and quantitatively by various methods to assess their properties. In order to assess coating quality, the cross-sections of the deposited material was examined using optical microscopy, and scanning electron microscopy (SEM) (Zeiss, model Evo10) equipped with secondary electron (SE), backscattered electron (BSE), energy dispersive spectroscopy (EDS), electron backscatter diffraction (EBSD) and x-ray computed tomography (CT) detectors. Prior to microscope investigation, the samples were prepared according to standard metallographic techniques: the samples were sectioned using a saw (Struers Secotom-10), mounted in a thermosetting epoxy resin (Struers LaboPress-3) and then polished (Struers Tegrapol with

TegraForce-5 and TegraDoser-5 attachments). Photographs of this equipment are shown in Figure 4.16 through Figure 4.18.

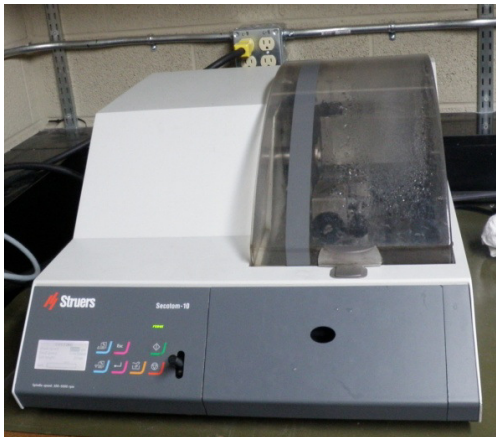

Figure 4.16: Photograph of precision saw (Struers Secotom-10)

Figure 4.17: Photograph of thermosetting resin mounting chamber (Struers LaboPress-3)

Figure 4.18: Photograph of sample polisher (Struers Tegrapol, TegraForce-5 and TegraDoser-5)

Optical microscope images were used to determine the presence of cracks and undeformed particles as well as investigating initial coating quality (Figure 4.19). A camera mounted on the microscope was used with the Clemex Vision Lite software to analyse coating porosity and thickness (Figure 4.20).

Figure 4.19: Photograph of optical microscope

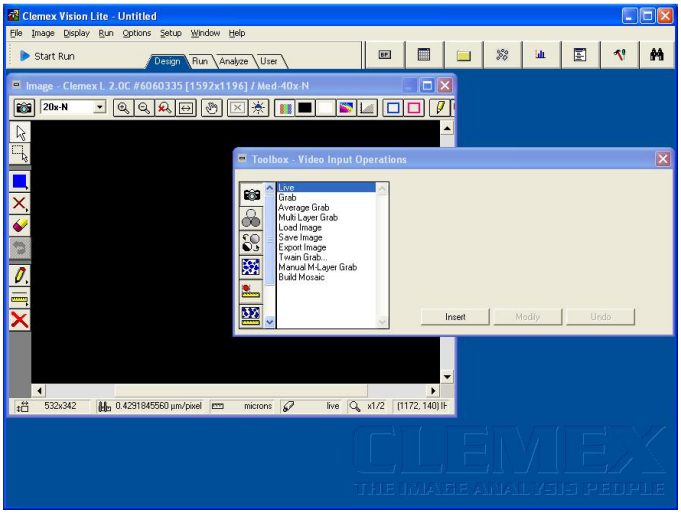

Figure 4.20: Screen capture of Clemex Vision Lite 5.0 software

After optical analysis, additional samples were chosen for investigation via SEM. The samples require an additional processing step to allow electrons to evacuate the observed surface and prevent charge build-up. The samples are therefore sputtered with a thin gold film (Denton Vaccum Desk IV) and grounded to the SEM using conductive adhesive tape. Images of the sputtering machine and SEM are presented in Figure 4.21 and Figure 4.22.

Figure 4.21: Photograph of gold sputter (Denton Vacuum Desk IV)

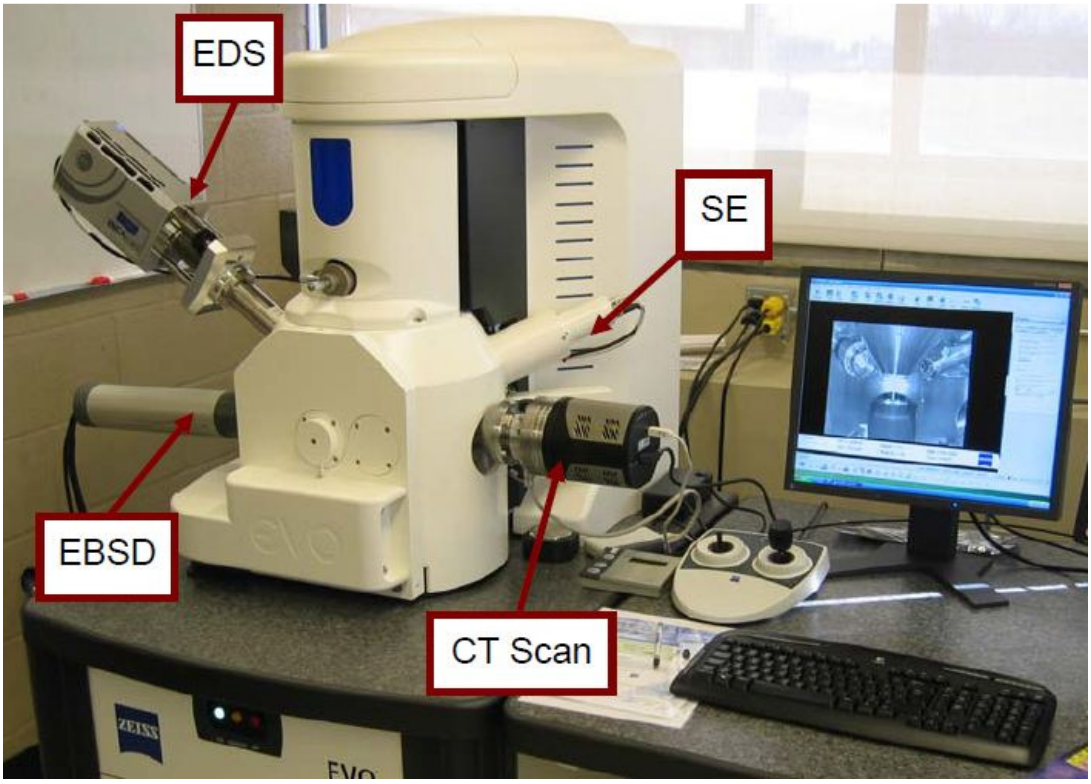

Figure 4.22: Photograph of scanning electron microscope (Zeiss Evo10) with SE, BSE, EDS, EBSD and CT scan detectors (adapted from [121]).

The coating was then analysed under increased magnification in the SEM microscope. BSE and EDS analysis were conducted to determine distribution of elements in the sample. Additionally, X-ray diffraction analysis (XRD) was conducted using a Philips X-Pert model PW 1830 diffractometer with CuKα radiation in order to determine the phase composition of the coatings. The XRD scan utilises X-rays to bombard the sample with varying incident angles. Each crystalline material phase is characterized with a specific crystal lattice size and atomic plane spacing. At each angle of incidence, the amount (count) of X-rays reflected by the sample is measured with a detector. The amount of counts are then plotted with respect to the angle of incidence and can be cross-referenced in a material database to identify the phase composition. A photograph of the XRD system is presented in Figure 4.23.

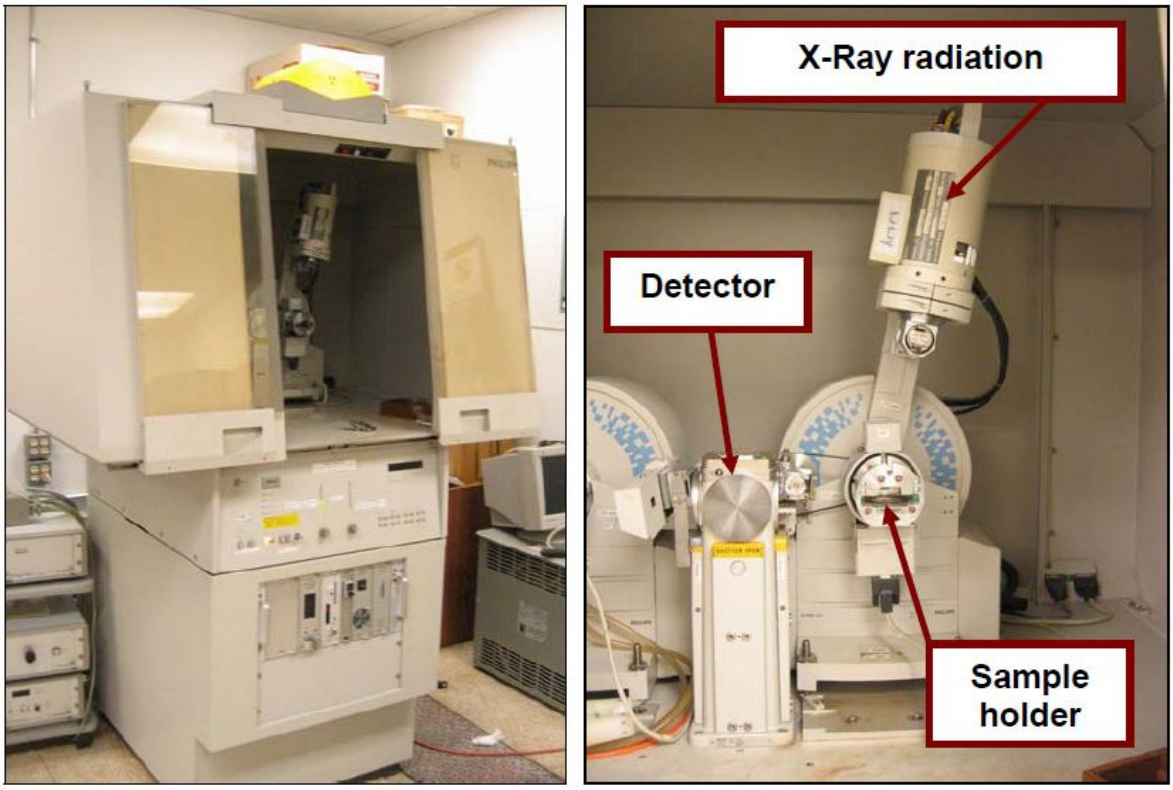

Figure 4.23: XRD equipment used for phase identification of coatings and powders (adapted from [121]).

4.3.2. Bond Coat Oxidation Behaviour

The oxidation behaviour of the coatings sprayed by CGDS, APS and HVOF was assessed by performing high-temperature isothermal oxidation experiments. All samples were sectioned from the substrate and grinded on all sides in order to obtain only the remaining bond coat and remove any oxides formed during the deposition process. Additional samples were grinded on only one side in order to retain the oxide layer formed during deposition for comparison purposes. The sample dimensions were then measured using a digital vernier calliper and each sample was weighed on a high-precision digital scale (Sartorius Extend – model ED124S) in order to determine their surface area and initial weight. The calliper and scale have a resolution of 0.01mm and 0.1mg respectively. The free-standing CoNiCrAlY coating samples were then placed in a high-temperature furnace (Lindberg/Blue) at 1100°C in static atmospheric air. Samples previously oxidised at 1000°C were used for comparison purposes[**121**]. The samples were placed in the oven once it had reached the desired temperature and were left to soak during 1, 5, 25, 50 and 100 hours. The

samples were then removed from the furnace and allowed to cool to room temperature. Once cooled, the samples were weighed in order to determine mass gain due to oxidation and to calculate the oxide growth rate. Additional soak times of 500, 1000, 1500 and 2000 hours were chosen to determine the long-term oxidation behaviour of the samples. Photographs of the scale and furnace are presented in Figure 4.24 and Figure 4.25.

Figure 4.24: Photograph of high temperature air furnace

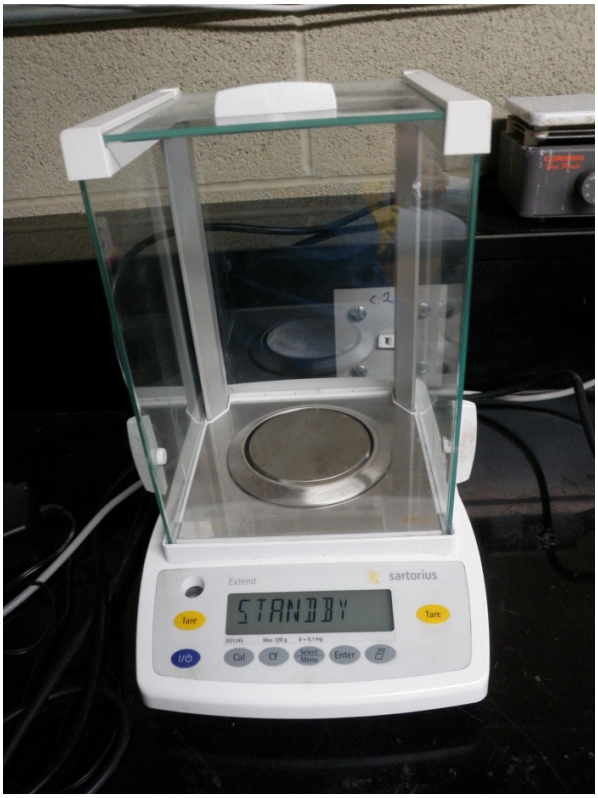

Figure 4.25: Photograph of digital scale (Sartorius Extend – model ED124S)

Following each heat-treatment samples were subjected to XRD analysis to identify the oxides formed on the sample. The XRD analysis provides a means of comparing peak intensities to determine the importance of each oxide type. Comparison of XRD scans allows for the analysis of the evolution of the oxide scales with respect to time. Using this method it is possible to determine the time required to form each oxide and determine the approximate lifetime of the coating.

The samples were then analysed in the SEM microscope. Images were taken of the sample surface to examine the morphology of the oxides. EDS analysis was also conducted to determine the oxide composition and element distribution. Further images of the coating cross-section were taken via SEM and BSE. These images allowed the visualisation of the β-phase depletion zone due to the consumption of the aluminum in the aluminum-rich β-phase during the oxidation process. The cross-section images taken at different oxidation stages were compared to assess the evolution of the oxidation.

Chapter 5 - CGDS Nozzle Design

The previous step of this research project identified that the CGDS nozzle should be improved in order to obtain dense coatings[**121**]. In the previous study, an axisymmetric converging-diverging nozzle with a 2mm diameter throat and 7.3mm exit diameter was used. This nozzle was used with stagnation gas pressure and temperature of 2.0MPa and 550°C respectively and was found capable of accelerating the AMDRY 9951 particles to an average velocity of 557 ± 95 m/s. This enabled the CGDS system to deposit coatings with 1.0 ± 0.3% porosity at manufacturing speeds of 1mm/s. However, the porosity of coatings deposited at higher manufacturing speeds was found to increase to 7.7 ± 2.1% at 5mm/s indicating that the impingement of particles is required to obtain dense coatings with this nozzle. This leads to the conclusion that the particles are not reaching a velocity high enough for proper particle plastic deformation. A new nozzle must therefore be developed to increase the particle impact velocities.

5.1. Nozzle Requirements

The nozzle must meet the following set of requirements in order to effectively and rapidly deposit CoNiCrAlY powder to form dense coatings.

The first requirement was to remove the possibility of shockwaves arising in the nozzle by the use of the Method of Characteristics to determine the nozzle profile. This should lead to a better and smoother acceleration of particles due to the improved gas flow.

The second requirement is the design of a radially injected nozzle in order to reduce the pressure required in the powder feeder. Radial injection requires good control of the feeder gas pressure to ensure particles are entrained by the flow but do not bounce off the nozzle walls and cause degradation. However, a radial injection allows for increased pressure to be used in the driving gas while maintaining low feeder gas pressure. In an axially injected nozzle, the feeder gas pressure must be higher than the driving gas to ensure there is no backflow into the powder feeder. In a radially injected nozzle, the injection point is located downstream of the throat where the driving gas pressure is low due to the rapid expansion of the gas. This allows for an increased driving gas pressure without having to resort to a high-

pressure powder feeder. The higher gas pressures will lead to higher gas density and therefore increase particle velocity.

The third requirement is to limit the feeder gas pressure to a maximum of 1100 kPa while the driving gas is at a pressure of 4.0MPa due to powder feeder limitations. A driving gas pressure of 4.0MPa was determined to be the maximum allowable pressure for the current CGDS system. This limit in feeder gas pressure should be maintained whether nitrogen or helium is used as the feeding gas (the pressure drop past the throat depends on the gas specific heat ratio).

The fourth requirement is the use of a throat measuring 1.4mm in diameter. In theory, this represents a 50% reduction in gas consumption than a throat that measures 2.0mm in diameter when using the same stagnation pressure. Significant cost savings are possible due to the lower consumption of driving gas. Alternatively, the gas inlet pressure can be doubled while maintaining the same driving gas consumption this increases driving gas density which leads to higher particle velocities. Lower driving gas consumption will also allow higher gas temperatures to be reached due to the lower power requirements for heating of the gas.

Finally, the particle velocities of the CoNiCrAlY particles should be high enough to ensure sufficient plastic deformation without the need for particle impingement. This will decrease coating porosity and allow for an increase in coating manufacturing speed.

As an additional design parameter, the nozzle length was chosen to be 200 mm, 100mm shorter than previous nozzles. Although longer nozzles may increase particle velocities, a shorter nozzle is less likely to be affected by boundary layer disruptions in the flow. This nozzle length is thought to be adequate for accelerating particles to the desired velocity.

5.2. Mathematical analysis

In order to design an optimal nozzle, proper understanding of the physics and mathematics associated to gas dynamics and particle acceleration are required. Although these equations were summarized in section 2.2.3, they will be further explored in this section. An attempt will be made to find the optimal nozzle shape mathematically prior to creating simulation models.

The starting point for this analysis is the drag force equation [**32**]:

$$F_d = \frac{1}{2}\rho V^2 C_d A \tag{5.1}$$

Where F_d is the drag force, ρ is the fluid density, V is the fluid velocity, C_d is the drag coefficient of the particle and A is the particle cross-sectional area. For a particle with some initial velocity, the equation is modified to obtain the following:

$$F_d = \frac{1}{2}\rho (V - V_p)^2 C_d A \tag{5.2}$$

Where V_p is the particle velocity. For initial particle acceleration, V_p is zero and can therefore be omitted. Since the gas expansion process is assumed to be isentropic and that the perfect gas law holds, the speed of sound can be calculated with the following equation [**32**]:

$$c = \sqrt{kRT} \tag{5.3}$$

Where c is the speed of sound, k is the gas specific heat ratio, R is the gas constant and T is the gas temperature. In supersonic nozzles, the parameter of interest is the Mach number. Using the speed of sound and the Mach number, it is possible to calculate the gas velocity[**32**]:

$$V = Mc \tag{5.4}$$

Combining equation 5.3 and 5.4 and squaring the velocity term we obtain[**32**]:

$$V^2 = (M\sqrt{kRT})^2 \tag{5.5}$$

We can then substitute equation 5.5 into equation 5.1 to obtain [**32**]:

$$F_d = \frac{1}{2}\rho M^2 kRT C_d A \tag{5.6}$$

For supersonic flows however, the fluid density (ρ) and temperature (T) are a function of the gas specific heat ratio (k) and the local Mach number. We must account for this variation [**32**]:

$$\frac{\rho_o}{\rho} = (1 + \frac{k-1}{2}M^2)^{\frac{1}{k-1}} \tag{5.7}$$

Where ρ_o is the gas stagnation density. Rearranging and substituting for ρ:

$$F_d = \frac{1}{2}\frac{\rho_o}{(1+\frac{k-1}{2}M^2)^{\frac{1}{k-1}}}M^2 kRTC_dA \tag{5.8}$$

Similarly for the temperature [**32**]:

$$\frac{T_o}{T} = 1+\frac{k-1}{2}M^2 \tag{5.9}$$

Where T_o is the gas stagnation temperature. Rearranging and substituting T in equation 5.8 we obtain:

$$F_d = \frac{1}{2}\frac{\rho_o}{(1+\frac{k-1}{2}M^2)^{\frac{1}{k-1}}}M^2 kR\frac{T_o}{1+\frac{k-1}{2}M^2}C_dA \tag{5.10}$$

Reorganising this equation we obtain the following:

$$F_d = \frac{1}{2}\frac{\rho_o T_o M^2 kR}{(1+\frac{k-1}{2}M^2)^{\frac{k}{k-1}}}C_dA \tag{5.11}$$

Solving this equation where k, R, ρ_o and T_o are constants and only dependent on the stagnation properties and the gas type used, a value of M=$\sqrt{2}$ is obtained [**40**]. This represents the ideal Mach number for initial particle acceleration. The nozzle should therefore aim to accelerate the gas flow to this value prior to particle injection in order to maximise the force and therefore the acceleration applied to the particle.

In the previous equations, it was assumed the particle velocity was zero in order to find the ideal Mach number for maximum initial force applied on the particle. However, the particle velocity must be taken into account after the particle velocity is above zero. Proceeding in the same manner as previously starting from equation 5.2 and keeping the particle velocity as a variable we obtain:

$$F_d = \frac{1}{2}\frac{\rho_o}{(1+\frac{k-1}{2}M^2)^{\frac{1}{k-1}}}\left(M\sqrt{kR\frac{T_o}{1+\frac{k-1}{2}M^2}}-V_p\right)^2 C_dA \tag{5.12}$$

Upon solving equation 5.12 for varying particle velocities, the ideal gas Mach number can be calculated. The relative Mach number can then be found by subtracting the

particle velocity from the gas velocity and dividing the result by the speed of sound. Results are presented in Table 5-1.

Table 5-1: Ideal gas and relative Mach numbers for maximum force applied to particle

Particle velocity (m/s)	Gas Mach number	Relative Mach number
0	1.41	1.41
100	1.45	1.38
200	1.49	1.34
300	1.53	1.31
400	1.58	1.27
500	1.62	1.23
600	1.67	1.20
700	1.72	1.16
800	1.77	1.13

The ideal relative Mach number for maximum force applied to the particle is therefore dependant on particle velocity and must be varied according to the particle velocity in the nozzle.

Although applying a maximum force to the particle will result in high acceleration, this does not necessarily mean the particle will be able to reach the highest possible velocities within a finite distance. In order to accelerate particles, a certain amount of work must be done to equal the increase in kinetic energy of the particle and maintain equilibrium in the first law of thermodynamics:

$$dU = dQ - dW \tag{5.13}$$

Where dU is an infinitesimal change in particle energy, dQ is an infinitesimal amount of heat applied to the particle and dW is an infinitesimal amount of work done by the particle. The term for internal energy, U can be separated into potential and kinetic energy as follows:

$$U = E_{pot} + E_{kin} \tag{5.14}$$

In the simplest particle acceleration case, no heat is applied to the particle and any work done on the particle is to increase the kinetic energy. For this case, we can neglect the change in potential energy and any external heating. This leads to the following equation:

$$dE_{kin} = dW \tag{5.15}$$

Work is defined by the following equation:

$$W = Fd \tag{5.16}$$

Where W is the work in J (Nm), F is the force applied and d is the distance during which this force is applied. While the kinetic energy of a particle can be found using the following:

$$E_{kin} = \frac{1}{2}mV^2 \tag{5.17}$$

Where E is the energy in J, m is the particle mass and V is the particle velocity. As can be seen in equation 5.17, the amount of kinetic energy increases exponentially with increasing velocity. The required work to increase particle velocities therefore also increases exponentially as the particle velocity increases.

Another factor which is directly related to the work is the power applied to the particle. The power is the speed at which force is applied or the work done over a time interval. Power is defined by the following:

$$P = FV = F\frac{d}{t} = \frac{W}{t} \tag{5.18}$$

Where P is the power in W, F is the force applied, V is the velocity at which that force is applied, W is the work done and t is time.

Unlike acceleration which can remain constant throughout the acceleration process, the power which must be applied to the particle increases as the particle velocity increases. Consider the sample case where a Nickel particle of 25μm in diameter is constantly accelerated from 0m/s to 800m/s in a distance of 0.2m. The force applied to the particle is $9.32\text{x}10^{-4}$N and the total amount of work done is $1.86\text{x}10^{-4}$ J while the average power required is 0.373W. The instantaneous power required throughout the acceleration is displayed in Figure 5.1.

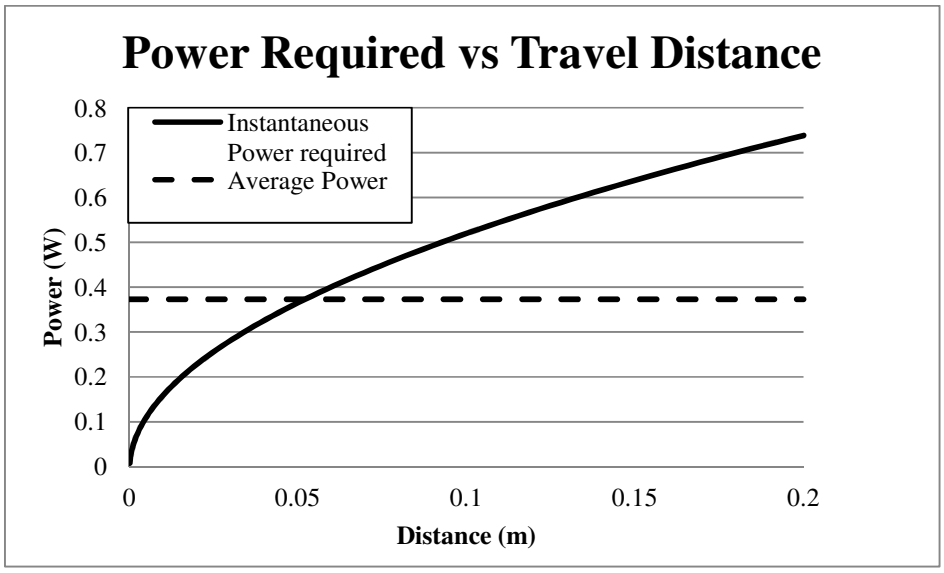

Figure 5.1: Power required for particle acceleration with respect to particle travel distance.

From Figure 5.1, it is evident that the power required to accelerate the particles is not significant during the initial acceleration but becomes important when the particle velocity increases. It can therefore be concluded that while maximizing the force applied on the particle is beneficial for the initial acceleration, once the particle reaches high velocities, the power required for a further increase in velocity becomes significant.

The power applied to the particle can be maximized by proceeding as previously with the following initial equation:

$$P_d = \frac{1}{2}\rho(V - V_p)^3 C_d A \tag{5.19}$$

The particle velocity is assumed to be zero while the gas velocity is substituted by the Mach number and the speed of sound. The fluid density (ρ) is then substituted with equation 5.7 to obtain:

$$P_d = \frac{1}{2}\frac{\rho_o}{\left(1 + \frac{k-1}{2}M^2\right)^{\frac{1}{k-1}}} M^3 (kRT)^{\frac{3}{2}} C_d A \tag{5.20}$$

Substituting the temperature (T) in equation 5.20 with equation 5.9 we obtain:

$$P_d = \frac{1}{2}\frac{\rho_o}{(1+\frac{k-1}{2}M^2)^{\frac{1}{k-1}}}M^3(kR)^{\frac{3}{2}}\frac{{T_o}^{\frac{3}{2}}}{(1+\frac{k-1}{2}M^2)^{\frac{3}{2}}}C_dA \tag{5.21}$$

Simplifying:

$$P_d = \frac{1}{2}\frac{\rho_o {T_o}^{\frac{3}{2}} M^3(kR)^{\frac{3}{2}}}{(1+\frac{k-1}{2}M^2)^{\frac{1.5k-0.5}{k-1}}}C_dA \tag{5.22}$$

Solving this equation where k, R, ρ_o and T_o are constants and are only dependent on the stagnation properties and the gas type used, a value of M=$\sqrt{3}$ is obtained as the ideal Mach number for maximum power applied to the particle.

In the case of maximum power, the particle velocity was assumed to be zero. The particle velocity must be taken into account after the particle velocity is above zero. Proceeding in the same manner as previously starting from equation 5.19 and keeping the particle velocity as a variable we obtain:

$$F_d = \frac{1}{2}\frac{\rho_o}{(1+\frac{k-1}{2}M^2)^{\frac{1}{k-1}}}\left(M\sqrt{kR\frac{T_o}{1+\frac{k-1}{2}M^2}}-V_p\right)^3 C_dA \tag{5.23}$$

Upon solving equation 5.23 for varying particle velocities, the ideal gas Mach number can be calculated. The relative Mach number can then be found by subtracting the particle velocity from the gas velocity and dividing the result by the speed of sound. Results are presented in Table 5-2.

Table 5-2: Ideal gas and relative Mach numbers for maximum power applied to particle

Particle velocity (m/s)	Gas Mach number	Relative Mach number
0	1.73	1.73
100	1.77	1.69
200	1.82	1.66
300	1.86	1.61
400	1.91	1.57
500	1.96	1.53
600	2.01	1.49
700	2.06	1.44
800	2.13	1.41

The ideal relative Mach number for maximum power applied to the particle is dependent on particle velocity and must be varied according to the particle velocity in the nozzle.

It is believed that the optimization for maximum power will yield lower initial particle acceleration, but yield higher particle velocities at the nozzle outlet. Inspection of the normalised Drag force and drag power curves also indicates that the drop in drag force is not extremely significant at the ideal Power Mach number as can be seen in Figure 5.2. To verify this hypothesis, two computational models will be developed in order to explore both scenarios.

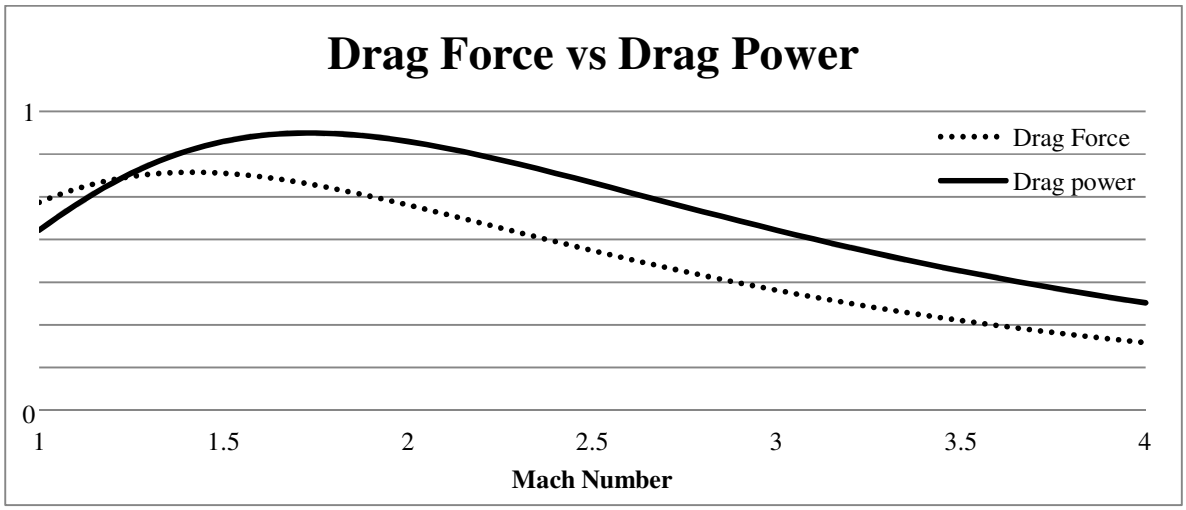

Figure 5.2: Comparison of normalised drag force and normalised drag power with respect to Mach number

The mathematical equations seem to contradict the first impressions upon analysis of the drag equation. By increasing the driving gas velocity, the resulting drag force will increase in conventional fluid mechanics. However, when dealing with supersonic flows, the effect of increasing the velocity by increasing the relative Mach number also reduces the flow density. There is therefore an "ideal" relative Mach number where particle acceleration is maximised, both below and beyond this number, particle acceleration is reduced.

This mathematical analysis assumes that the drag coefficient remains constant regardless of the relative Mach number. When dealing with supersonic flows, this is not the case. Many models and empirical studies have been conducted to attempt to find the drag coefficient for supersonic flows. The particle-flow interaction is extremely complex and affected by a combination of effects found in conventional fluid dynamics and gas dynamics. A bow shock forms in front of the particle reducing the flow velocity to subsonic speeds and increasing pressure in the immediate vicinity of the particle. The particle is subjected to the pressure effects of the shockwave as well as turbulence and the pressure effects of the formation of secondary shockwaves beyond downstream of the particle. An increase in the Mach number alters the angle and location of the shockwaves as well as the turbulent behaviour downstream of the particle. Images of this phenomenon are presented in Figure 5.3 and Figure 5.4.

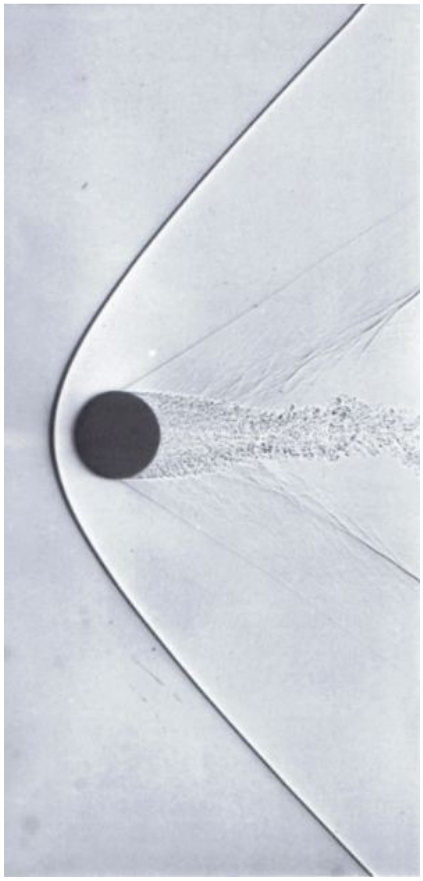

Figure 5.3: Sphere in air flow at M=1.53[161**]**

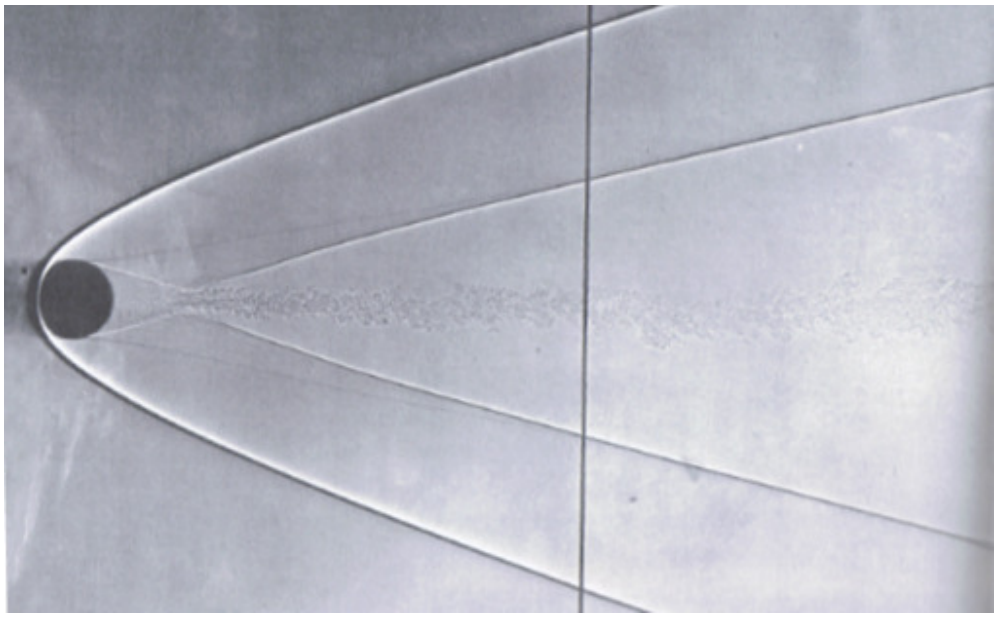

Figure 5.4: Sphere in air flow at M=4.01[161**]**

The calculation of the exact drag coefficient is therefore difficult as it is dependent on many factors which are difficult to account for. In some studies, wave drag is assumed to take precedence at relative Mach numbers above 1. In this form of drag, the highest drag coefficients are found at M=1 and increasing the Mach number reduces the drag coefficient[**32**] as per the equation:

$$C_{D_{th}} = \frac{4}{\sqrt{M_\infty - 1}} \frac{1}{2} \left(\overline{{\sigma_L}^2} + \overline{{\sigma_U}^2} \right) \tag{5.22}$$

Where ${\sigma_L}^2$ and ${\sigma_U}^2$ are the mean of the sum of the particle surface slopes of the lower and upper surfaces of airfoil profile with respect to the chord line squared. However some empirical studies have indicated a more complex drag coefficient evolution such as the one presented in *The Dynamics and Thermodynamics of Compressible Fluid Flow*[**32**] and presented in Figure 5.5.

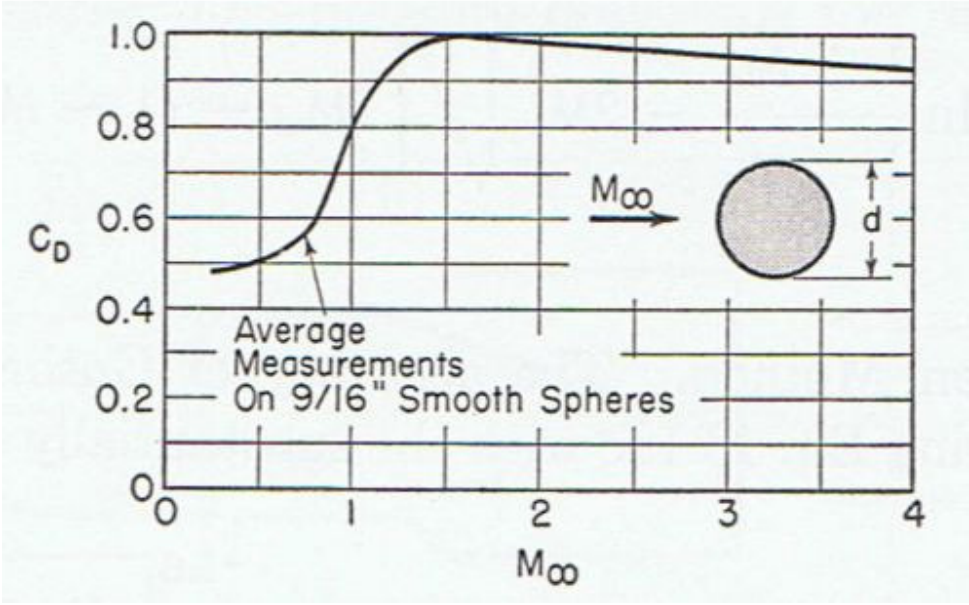

Figure 5.5: Drag coefficient with respect to Mach number [32]**.**

Numerical modelling by Zarei *et al.*[**162**] indicated that the drag coefficient of a particle at Mach 3.5 was 1.3 which is significantly higher than the wave drag of empirical studies. The study by Zarei *et al.*[**162**] also investigated the variation of the drag coefficient on two particles in proximity in a supersonic flow. The drag coefficient on the trailing particle was found to be 1.6. This study indicates there is significant variation in the drag coefficient when multiple particles are present in the flow.

The drag coefficient was therefore assumed to be constant and equal to 1 for the mathematical analysis due to the large variation of optimal solutions depending on the drag coefficient model used. Particles that are not perfectly spherical will also have a significantly different drag coefficient depending on their orientation with respect to the flow. Cryomilled particles which are typically flake-like in shape can have a large drag coefficient when their flat surfaces are perpendicular to the flow while having a near-zero drag coefficient when parallel to the flow. This further complicates the analysis of the particle drag coefficient. Single particle injections were also used to determine particle velocities due to the complex effects introduced by the interaction of the flow with multiple particles.

5.3. Computational Fluid Mechanics

5.3.1. CFD solver details and assumptions

In order to properly characterise the flow, CFD software must simultaneous solve many equations which are simplified through numerous assumptions. Furthermore, the physical domain must be translated into a computational domain through the use of modeling and meshing tools. The details of the CFD software, assumptions and associated meshing tools are outlined in this section.

5.3.1.1. CFD model assumptions

The CFD numerical package used in this study (Fluent v6.3.26) uses various assumptions in order to calculate gas flow and particle acceleration properties. These assumptions are summarised as the following:

1. The flow is a viscous and Newtonian fluid.
2. The local behaviour of the fluid is assumed to be at thermodynamic equilibrium, Stokes relation is valid ($3\lambda + 2\mu = 0$) and strains in the fluid can be expressed by $2\mu S_{ij}$ where $S_{ij} = \frac{1}{2}\left(\frac{\partial u_i}{\partial x_j} + \frac{\partial u_j}{\partial x_i}\right)$.
3. The gas can be modeled by the perfect gas law $P=(\gamma-1)\rho E$.
4. The gas flow is assumed to be compressible and turbulent.
5. The geometry of the nozzle is modeled as two-dimensional and axisymmetric.

6. Morkovin's hypothesis is used: it is assumed that the fluctuations of gas density does not have a significant effect on the turbulent structures in the flow and are therefore negligible. The Navier-Stokes equations can therefore be used to define the flow and any turbulence models are valid for empirical values obtained for incompressible flows.
7. The triple velocity correlation functions for turbulence are assumed to be negligible compared to the double correlations.
8. Boussinesq's hypothesis is used. Turbulent moment and heat fluxes due to the Reynold's averaging process have the same form as laminar flow and are linked to the average flow by eddy viscosity and conductivity.
9. Although it has been proven inadequate with adverse pressure gradient flows, the k-ε turbulence model is used. The drawbacks of this model are not thought to significantly affect the end result due to the analysis region representing a favourable pressure gradient. Analysis outside the nozzle where adverse pressure gradients will be found could lead to inaccurate results however, the influence of the short stand-off distance when compared to the long nozzle is expected to be negligible. The size and mass of the injected particles are also large enough to prevent any inaccuracies to introduce significant errors. The k-ε turbulence model is therefore assumed to be valid for this work.
10. The presence of particles in the flow is assumed to have negligible influence on the flow itself. This assumption is valid for low powder flow rates assumed in this study. The experimental powder flow rates are kept low in order to comply with this assumption.
11. The acceleration of particles is assumed to be caused exclusively by momentum transfer between the gas flow and the particles.
12. All the particles injected are assumed to be spherical and have the properties (density, conductive heat transfer coefficient, specific heat capacity) of nickel.

5.3.1.2. CFD model conservation equations

With the previously stated assumptions, the CFD model attempts to solve the continuity, momentum and energy conservation equations simultaneously. The equations are presented in their averaged Reynolds general form to ensure the local conservation of properties and to account for turbulence effects:

$$\frac{\partial \rho}{\partial t} + \frac{\partial}{\partial x_i}(\rho u_i) = 0 \tag{5.23}$$

$$\frac{\partial}{\partial t}(\rho u_i) + \frac{\partial}{\partial x_i}(\rho u_j u_i) = -\frac{\partial P}{\partial x_i} + \frac{\partial}{\partial x_j}[2\mu S_{ij} + \tau_{ij}] \tag{5.24}$$

$$\frac{\partial}{\partial t}(\rho E) + \frac{\partial}{\partial x_i}(\rho u_j H) = \frac{\partial}{\partial x_i}[-q_{Lj} - q_{Tj}] + \frac{\partial}{\partial x_j}[u_i(2\mu S_{ij} + \tau_{ij})] \tag{5.25}$$

Where $\tau_{ij} = \overline{-\rho u'_i u'_j}$ and $q_{Tj} = -\frac{\mu_T}{Pr_T}\frac{\partial H}{\partial x_j}$.

The two-equation k-ε model is used to complete the equation system. This model uses Boussinesq's turbulent velocity and takes into account non-local effects and flow history. This equation is as follows:

$$\frac{\partial(\rho k)}{\partial t} + \frac{\partial(\rho u_j k)}{\partial x_j} = \tau_{ij}\frac{\partial u_i}{\partial x_j} - \rho\varepsilon + \frac{\partial}{\partial x_j}\left[\left(\mu + \frac{\mu_T}{\sigma_k}\right)\frac{\partial k}{\partial x_j}\right] \tag{5.26}$$

Where $k=\frac{1}{2}\overline{u'_i u'_j}$ and $\varepsilon = \nu\overline{\frac{\partial u'_i}{\partial x_k}\frac{\partial u'_j}{\partial x_k}}$.

The rate of dissipation of turbulence is expressed with the following:

$$\frac{\partial(\rho\varepsilon)}{\partial t} + \frac{\partial(\rho u_j \varepsilon)}{\partial x_j} = C_{\varepsilon 1}\frac{\varepsilon}{k}\tau_{ij}\frac{\partial u_i}{\partial x_j} - C_{\varepsilon 2}\rho\frac{\varepsilon^2}{k} + \frac{\partial}{\partial x_j}\left[\left(\mu + \frac{\mu_T}{\sigma_\varepsilon}\right)\frac{\partial \varepsilon}{\partial x_j}\right] \tag{5.27}$$

Where the turbulent viscosity is given as $\mu_T = \frac{\rho C_\mu k^2}{\varepsilon}$.

The modeling of a particle behaviour in the flow is done using Newton's second law in a Euler-Lagrangian system. This equation of motion is as follows:

$$m_P \frac{\mathrm{du_P}}{\mathrm{dt}} = \frac{1}{2}\rho(u - u_P)^2 A_P C_d \tag{5.28}$$

The drag coefficient is taken from previous work.

5.3.1.3. Creation of Meshed Model

The creation of a computational domain to reflect a physical geometry is achieved through the use of the Gambit pre-processing and meshing software shown in Figure 5.6.

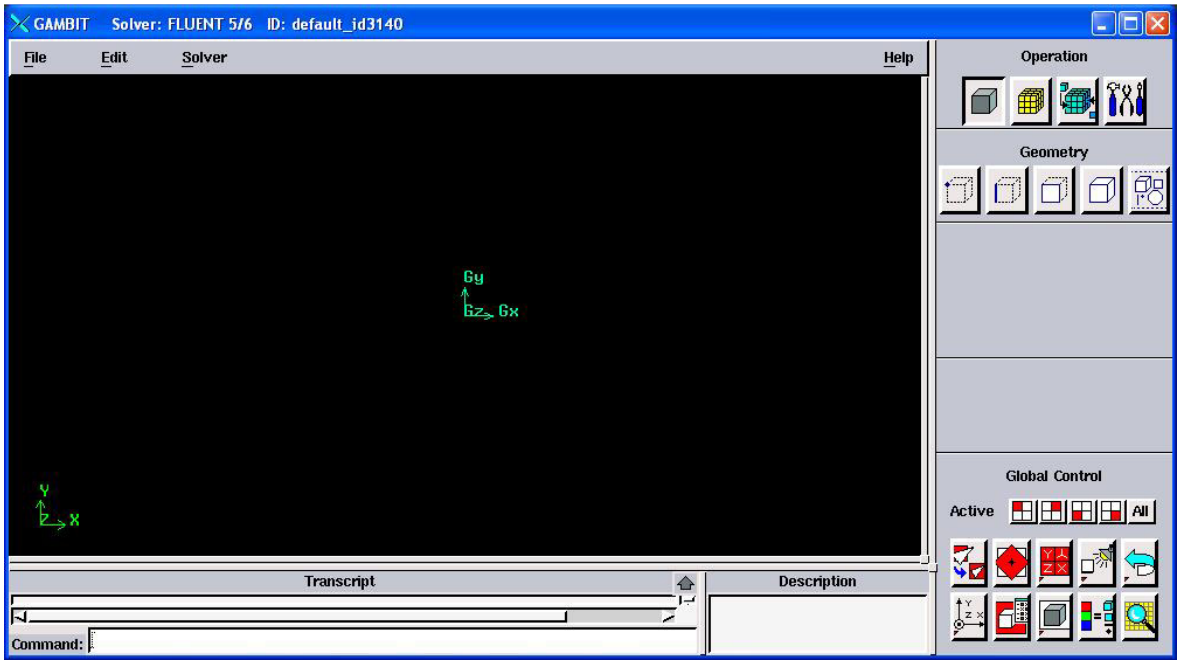

Figure 5.6 : View of the Gambit pre-processing and meshing software.

The gambit software is used to create a virtual model of the geometry of the desired CGDS nozzle. Vertex information is first inputted into the software to specify the important intersections. Edges (lines) are then created by joining two vertexes. These edges are then grouped together to outline a face (section). Each face can be meshed with specific parameters in order to improve model accuracy of key areas or reduce accuracy in unimportant areas. In this case, the nozzle was divided into four distinct sections in order to better characterize the flow. Boundary conditions are then applied to edges in order to define walls, inlets, outlets and a centerline (in order for the solver to determine where the geometry is axisymmetric). Table 5-3details the boundary conditions for each type of surface.

Table 5-3 : List of boundary conditions for each surface type

	Inlet	Outlet	Wall
u	Extrapolated	Extrapolated	0
v	0	Extrapolated	0
P	Known	Known	Extrapolated
T	Known	Known	Extrapolated
k	Known	Extrapolated	Known
ε	Known	Extrapolated	Known

Upon creation of the general nozzle geometry, the Gambit software is used to mesh the interior sections. The meshing type was chosen to be composed of quadrilaterals with varying sizes according to the nozzle section chosen. Particular attention was given to sections of interest, notably the MOC section. A variation of the nozzle exterior area exists due to different models used in this study. These models will be discussed in more detail in the following sections. An overview of the meshing size and location is displayed in Table 5-4.

Table 5-4: Summary of nozzle meshing zones

	Converging section	MOC section	Diverging section	Nozzle exterior
Number of intervals	15	30	60	100
Number of cells	225	900	3600	10000
Total section area (mm^2)	9.6875	2.7525	332.052	100-1000
Average cell area (mm^2)	0.04305	0.0030583	0.0922367	0.01-0.1

Due to the large number of models required for trials, a script was written to automatically generate the models including edges, faces, boundary conditions and mesh size, type and location. A separate vertex file is first input into the gambit software prior to running the script. Examples of the vertex file will be provided in later sections. Automating

the model creation process significantly reduced the time requirement for the creation of new models. An example of this script is available in APPENDIX A.

5.3.1.4. Setup of CFD Software

Simultaneous solving of the conservation equations is conducted via Fluent (version 6.3.26). Discretization of the conservation equations is required in order to solve the equation system via computer. As a density-based solver is used, the flow equations are solved using a second-order scheme while other equations use a first-order scheme. This is achieved through the use of a technique based on the control volume approach where the governing equations are integrated about each control volume to obtain discrete equations. The equation system obtained is linearized and solved using a Gauss-Seidel type solver in an iterative process.

Initial model set-up requires the selection of the driving gas and the definition of initial values of pressure and temperature. The type and location of inlets and outlets must be defined in the solver and inlet gas pressure and temperature must be defined. The location of powder injection is also defined as well as the powder particle size and elemental composition. Finally, initial values are calculated throughout the nozzle interior in order to have initial values for computation.

In order to achieve solution stability, iterations must be conducted with incremental turbulence complexity and decreasing Courant-Friedrichs-Lewy number. The Courant-Friedrichs-Lewy number is used to determine the time step of each iteration. This time step is calculated as follows:

$$\Delta t = \frac{2CFL * V}{\sum_f \lambda_f^{max} A_f} \tag{5.29}$$

Where V is the cell volume, A_f is the face cell and λ_f^{max} is the maximum of the local eigenvalues. If the time step is too large, smaller variations in the flow are not calculated while if it is too small, convergence will require an extremely large amount of iterations.

For most simulations, the following procedure is followed:

1. The initial value of the Courant-Friedrichs-Lewy number was set at 0.025 and the turbulence model is set to invicid (no turbulence).
2. 500 iterations were run.
3. The Courant-Friedrichs-Lewy number is reduced to 0.005 while the turbulence model is changed to Laminar flow.
4. 2000 iterations are run.
5. The Courant-Friedrichs-Lewy number is further reduced to 0.001 while the turbulence model is changed to k-ε.
6. 54000 iterations are run.
7. The Courant-Friedrichs-Lewy number is reduced to 0.0005
8. 40000 iterations are run.

Other simulations requiring different precision were run with different Courant-Friedrichs-Lewy numbers and different amount of iterations but the method remains the same. A script was used to control the initial setup of the simulation. An example of this script is presented in APPENDIX B.

5.3.1.5. Hardware and Performance

All simulations were run on the same hardware consisting of a 64-bit AMD Phenom II X6 hexa-core processor running at 3.7 GHz. The system also featured 4GB of DDR3-RAM operating at 1600 MHz and was running Windows 7 64-bit edition. The Fluent software was started with the following flags in order to take advantage of the six processors, the ability of 64 bit computations and to run in 2D double precision:

2ddp -r6.3.26 -64 -t6

The Fluent software is able to run in parallel over many processors or even many computers. The ability to run simulations in parallel computation over six processors can yield a theoretical performance improvement of 600% when neglecting overhead. In reality the performance improvement is not as drastic due to inter-core communication latency but certainly quite noticeable. Another increase in performance comes from the execution of the program in 64-bit instead of 32-bit. Finally it has been noted that increased text readout in the software can significantly decrease processing performance. This is attributed to latency

involved in outputting the text which thereby halts computation on all processing cores. Although this time is very small, it has an impact on simulations that are run for millions of iterations. The following lines are therefore input into the Fluent software in order to limit the amount of text readout:

/solve/set/flow-warnings no
/solve/set/reporting-interval 100

The combined use of these settings has dramatically decreased the processing time required for each simulation.

5.3.1.6. Conditions for Convergence

The calculated solution is deemed to have converged when the following criteria are met:

1. The sum of the mass flow rates at the inlet and outlet are less than 5%. This verification is done by taking the sum of the mass flow rates in every cell at the inlet and outlet.
2. The numerical residuals of the conservation equations decrease by 3 orders of magnitude. The numerical residuals are the variation of a property from one iteration to the next.

In all cases, the solution was assumed to be converged after the large number of iterations specified in the automated script. Increasing the amount of iterations beyond this point had a negligible effect on the sum of the mass flow rates or on the numerical residuals value. It was therefore assumed that no further convergence could be made.

5.3.2. Design methodology

In order to respect the design requirement for the use of a MOC diverging section, the software Aerospike was used. It can calculate the geometry required for a minimum-length MOC nozzle given the exit Mach number and gas type. An example of this tool in operation is presented in Figure 5.7.

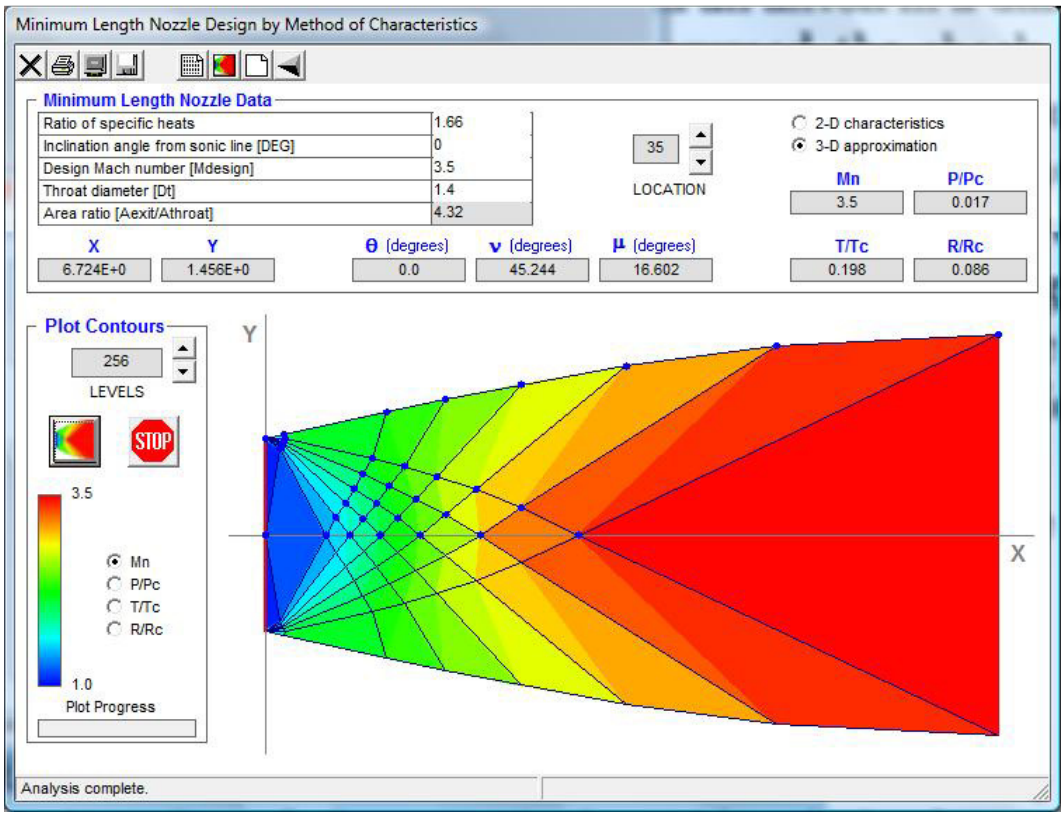

Figure 5.7: Screen caption of Aerospike software in operation

Although the nozzle geometry is calculated using the MOC, it also returns results for the shortest possible nozzle. A straight section must therefore be added at the end of the MOC section in order to achieve any meaningful particle velocity. The straight section should also be at a slight angle to the nozzle axis in order to compensate for the detrimental boundary layer effects that will develop while continuing to accelerate the driving gas and keeping the optimal relative Mach number as discussed previously.

The appropriate angle of the straight section was determined through multiple simulations of varying angle as no mathematical model was developed that could adequately predict particle acceleration without running a full simulation. Models were developed with varying straight section angles and simulations run with these models. The optimal angle was then determined by plotting the exit particle velocities over the nozzle exit diameter, finding a curve fit to the available data (R=0.99 or above) and determining the maximum value of this curve. This method yielded the best possible straight section angle and was validated through additional simulations. This procedure was repeated for four different MOC profiles

in order to confirm the findings of the previously discussed optimal Mach number and to determine if maximal force or maximal power was most efficient.

Once the optimal nozzle geometry was found, various simulations were conducted and additional models developed to determine the effect of stand-off distance, particle inlet and stagnation properties. The effect of gas stagnation properties was conducted on the "Stand-Off Distance" models. Models featuring no MOC section were constructed in order to assess the effect of the MOC section on particle acceleration. The amount of models and simulations conducted in this study are presented in Table 5-5.

Table 5-5: Total number of models and simulations conducted in this study

	Optimal Nozzle	Injection Models	Stand-Off Distance	Non-MOC
Number of models	24	2	5	3
Number of simulations	46	21	138	3

In total, 208 simulations were run on 34 different models for this study. The extensive amount of data gathered from these simulations is therefore not presented in its entirety. Only key simulations and findings are presented in the following sections.

5.3.3. Models and Results

The various simulation models used in this study will be detailed in the following sections. The optimal MOC nozzle model was used to determine the optimal nozzle geometry to obtain the highest possible particle exit velocity and is presented in section 5.3.3.1. A model featuring no initial MOC section (a single straight section) is then presented to validate the optimal MOC nozzle. This straight nozzle profile model is presented in section 5.3.3.2. A model featuring the optimal MOC nozzle with feeding gas injection points is presented in section 5.3.3.3 in order to assess the effect of using various feed and driving gas combinations as well as the effect of heating of the feed gas. Finally, a model using the optimal MOC nozzle which discharges into an atmosphere at ambient pressure and in which a substrate is present is used to assess the effect of stand-off distance. This model is also used to assess the effect of changing the gas stagnation pressure and gas stagnation temperature on the final particle velocity and is presented in section 5.3.3.4.

5.3.3.1. Optimal MOC Nozzle Model

As mentioned previously, the optimal nozzle model consists exclusively of the nozzle profile geometry. This geometry consists of the following elements in order: the inlet, the converging section, the throat, the MOC section, the straight section and the outlet. The model is constructed to determine the optimal nozzle configuration. It is therefore the simplest of the models due to the numerous trials required to find the optimal nozzle design. An example of the vertex file used to create this model is available in APPENDIX C.

A simulation was run on each model with a gas stagnation pressure of 4MPa, stagnation temperature of 900K and helium as the driving gas. The location of the particle injection in the nozzle was determined by the location where the gas pressure first reaches 1100kPa in the diverging section. The velocity of the particles was then determined at the outlet and compared with other models to determine the optimal design. After all simulations were conducted, the optimal model was determined to have a MOC section designed for relative Mach $\sqrt{3}$ and a nozzle exit diameter of 5.12mm. This yielded velocities for nickel particles of 25µm in diameter of 837m/s and velocities of 1750m/s for nickel particles of 5µm in diameter and particle temperatures of 325K and 305K respectively. Simulation results of gas Mach number contours and particle acceleration are displayed in Figure 5.8 and Figure 5.9.

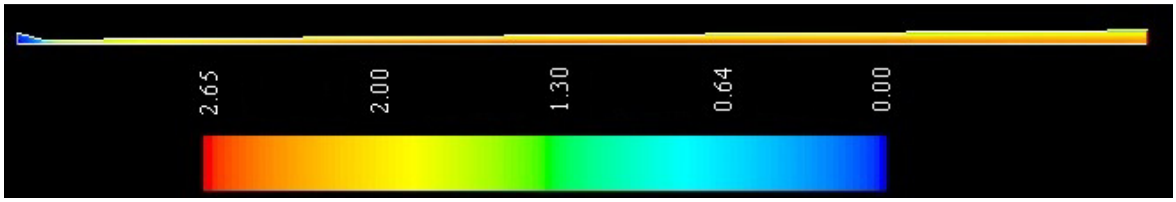

Figure 5.8: Driving gas Mach number contours on optimal nozzle design model.

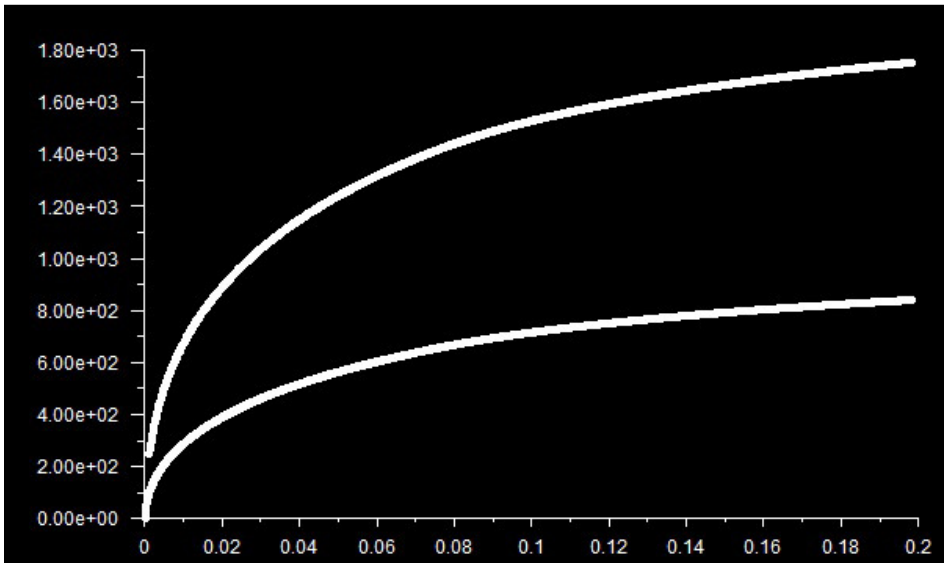

Figure 5.9: Particle velocity (m/s) with respect to travel distance (m) for 5µm (top) and 25µm (bottom) nickel particles in optimal nozzle design

5.3.3.2. Non-MOC Model

For comparison purposes, a nozzle model was created featuring no initial MOC section, the nozzle uses one straight section with constant diverging angle. The nozzle exit diameter was kept at 5.12mm in order to retain the same gas exit Mach number. This yielded particle velocities of 779m/s and 1686m/s and particle temperatures of 337K and 307K for nickel particles of 25µm and 5µm respectively. However as this model was used for comparison purposes the meshing is very coarse and results of this simulation likely do not take into account features such as boundary layers and possibly the occurrence of shockwaves which could significantly slow down the particle velocity. Nevertheless, even without consideration of these factors, the effect of the MOC section increases the final particle velocities. Comparison between this model and the previous model with specific interest into the MOC and throat section is presented in Figure 5.10 to Figure 5.13.

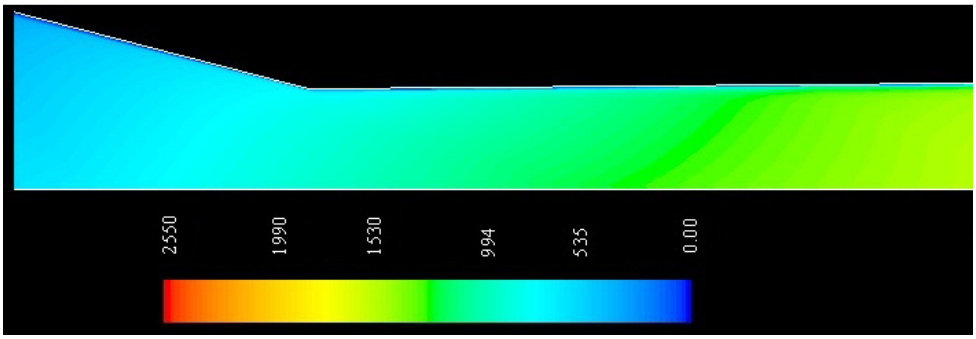

Figure 5.10: Velocity contours (m/s) in non-MOC nozzle, view of throat section.

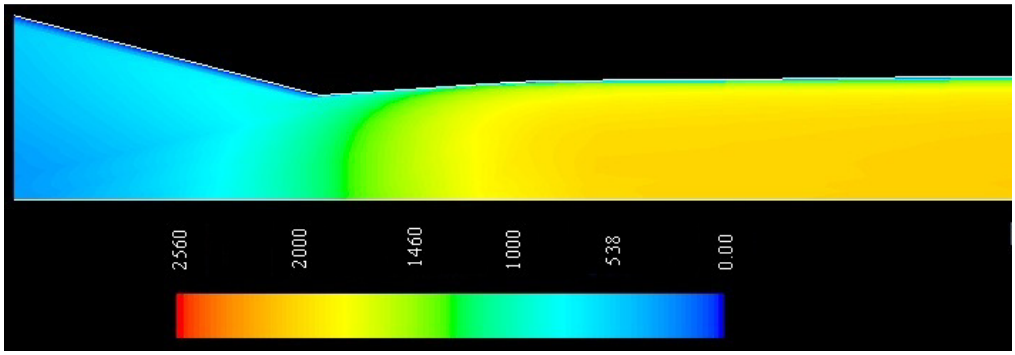

Figure 5.11: Velocity contours (m/s) in MOC nozzle, view of throat section.

Upon observing Figure 5.10 and Figure 5.11 it can be observed that although the nozzle exit velocities are identical, the gas velocity rises much more rapidly in the MOC nozzle. This quick rise in velocity should make the nozzle shorter than the conventional straight nozzle as the gas will reach the optimal Mach number for particle acceleration sooner. The boundary layer effects are also more evident on the MOC nozzle than on the straight nozzle due to the larger velocity gradients.

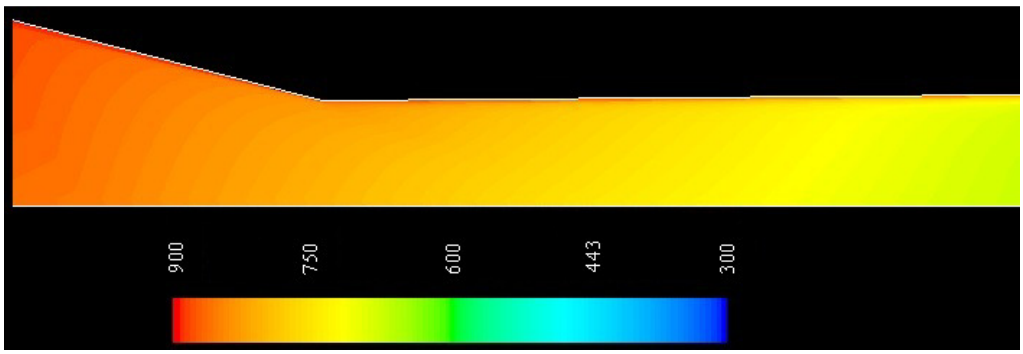

Figure 5.12: Temperature contours (K) in non-MOC nozzle, view of throat section.

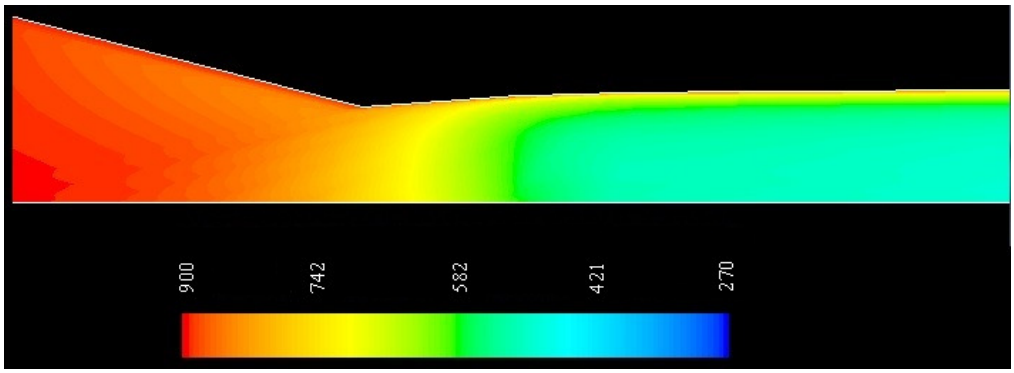

Figure 5.13: Temperature contours (K) in MOC nozzle, view of throat section.

Similarly to the evolution of velocity profiles, the temperature profiles behave quite differently on the MOC and non-MOC nozzles. The temperature remains elevated in the non-MOC nozzle while it drops rapidly in the MOC nozzle. The boundary layer is also quite evident in the MOC nozzle due to the larger thermal gradients. Assuming an injection point at the same distance, the particle temperatures in the non-MOC nozzle will be raised higher than in the MOC nozzle. The temperature of nickel particles injected in the flow of the non-MOC nozzle was measured and is displayed in Figure 5.14.

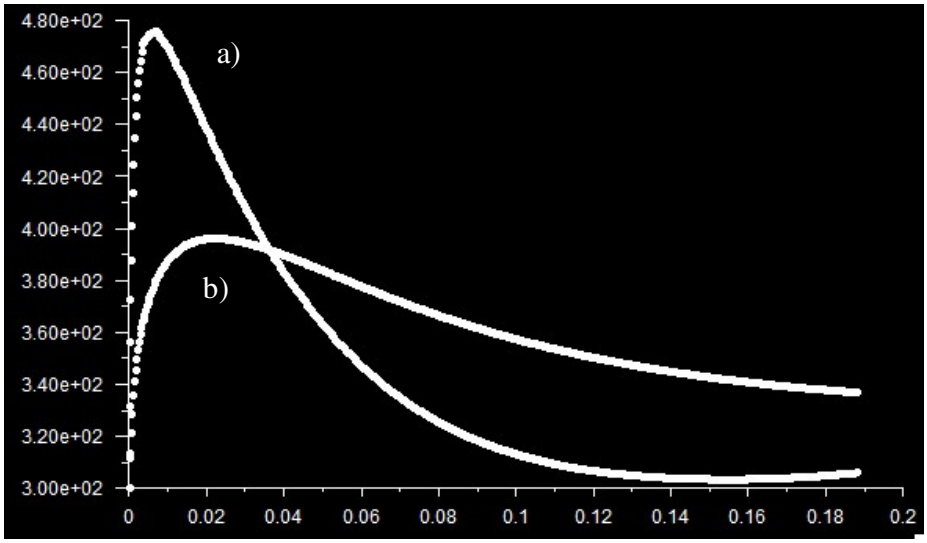

Figure 5.14: Particle temperature (K) with respect to travel distance (m) for nickel particles of a) 5μm and b) 25μm in diameter in non-MOC nozzle.

A comparison between particle velocities and temperatures for the MOC nozzle and the non-MOC nozzle are presented in Table 5-6.

Table 5-6: Comparison of particle velocity and temperature of MOC and non-MOC nozzles

	25µm particles		5µm particles	
	Particle Velocity (m/s)	Particle Temperature (K)	Particle Velocity (m/s)	Particle Temperature (K)
MOC nozzle	837	325	1750	305
Non-MOC nozzle	779	337	1686	307

According to Assadi *et al.* [**43**], the particle critical velocity decreases by 0.4m/s for every degree (K) increase in particle temperature. Although the temperatures of the particles in the non-MOC nozzle are higher, the critical velocity would be reduced by 4.8m/s for 25µm particles and by 0.8m/s for 5µm particles. The velocity advantage of the MOC nozzle is therefore much more significant than the decrease in temperature due to the shorter particle dwell time. The MOC nozzle is therefore better suited for the CGDS process.

5.3.3.3. Injection Model

In order to assess the effect of the gas injected during spraying, a model was developed with a second inlet. Due to the axisymmetric nature of the model, certain modifications to the injection port geometry had to be conducted. It was chosen that the total area of the injection port was to remain constant. Thus instead of having a single injection point as would be found in a physical nozzle, the model uses an injection "ring" to remain axisymmetric. Although this does not accurately reflect the physical geometry, the gas flow through this port should remain the same due to the identical surface area. It is noted that this will not accurately describe the particle trajectory which may "bounce" off the nozzle walls if the injection gas pressure is too high. Nevertheless, this was found to be the best option without reverting to a much more complex 3D model.

The model stability and convergence was far more difficult to achieve than previous models due to the dual-inlets. Two different sets of inlet pressures and temperatures were used, one for the driving gas and one for the feeder gas. If an insufficient pressure was specified for the feeder gas inlet, backflow would occur and divergence would occur in the numerical simulation. Alternatively, if the feeder gas pressure was too high, backflow would occur in the driving gas inlet. Many trials were therefore conducted and the number of

iterations as well as the Courant-Friedrichs-Lewy number had to be carefully selected. The driving and carrier gas types and pressures were varied to determine its effect on particle exit velocity. The results are summarized in Table 5-7:

Table 5-7: Results of injection model

Trial Number	Driving Gas		Feeder Gas		Particle Velocity
	Type	Pressure	Type	Pressure	
1	Helium	1MPa	Helium	350kPa	511m/s
2	Helium	1.5MPa	Helium	400kPa	595m/s
3	Helium	2MPa	Helium	450kPa	649m/s
4	Helium	2MPa	Argon	750kPa	642m/s
5	Helium	2MPa	Argon	600kPa	644m/s
6	Helium	2MPa	Argon	550kPa	638m/s
7	Helium	2MPa	Argon	450kPa	641m/s
8	Nitrogen	4MPa	Helium	1100kPa	564m/s
9	Nitrogen	4MPa	Helium	900kPa	561m/s
10	Nitrogen	4MPa	Nitrogen	1100kPa	553m/s
11	Nitrogen	3.5MPa	Helium	900kPa	542m/s
12	Nitrogen	3MPa	Nitrogen	900kPa	514m/s
13	Nitrogen	2MPa	Helium	450kPa	470m/s

The feeder gas pressures to ensure simulation convergence were found to be approximately the same as used on the physical nozzle during experiments. This indicates that while the nozzle geometry is not exactly accurate, the overall flow characteristics should hold. As expected, the use of helium yields the highest particle velocities. Argon was included as a feeder gas due to its very high density. It was thought that the increased density may help in the particle acceleration process however it appears the faster gas velocity of helium outweighs this fact. The trials with varying pressures of argon feeder gas also appear to have little effect on the final particle velocity. This could be due to some error in the CFD simulation due to approximations in the software or that the simulation converged even if some backflow occurred. In either case, the variation between these trials is less than 1% and should therefore not be seen as a serious model flaw. It is also interesting to note that the

particle velocities when using helium at 1.0MPa are approximately the same as when nitrogen is used at 3.0MPa. If CoNiCrAlY can be deposited using helium at this pressure, there is a potential for significant cost savings by using Nitrogen. Images of the nozzle injection model were taken and are presented in Figure 5.15 through Figure 5.18.

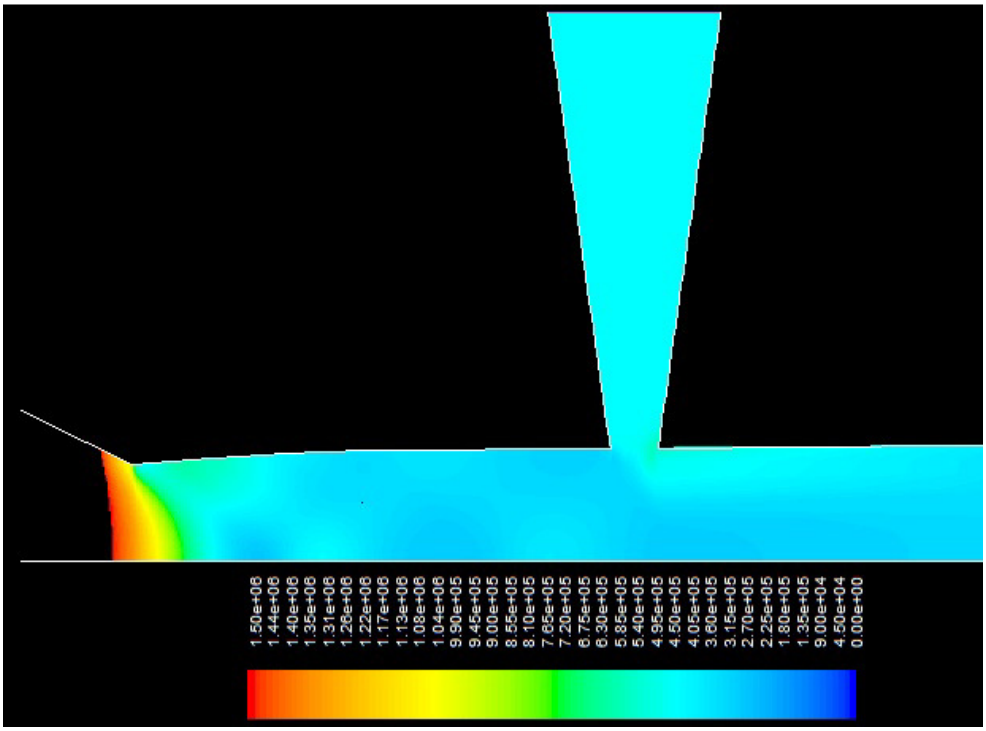

Figure 5.15: View of injection model geometry and pressure contours (overall) with N_2 driving gas at 2MPa and He feeder gas at 450kPa.

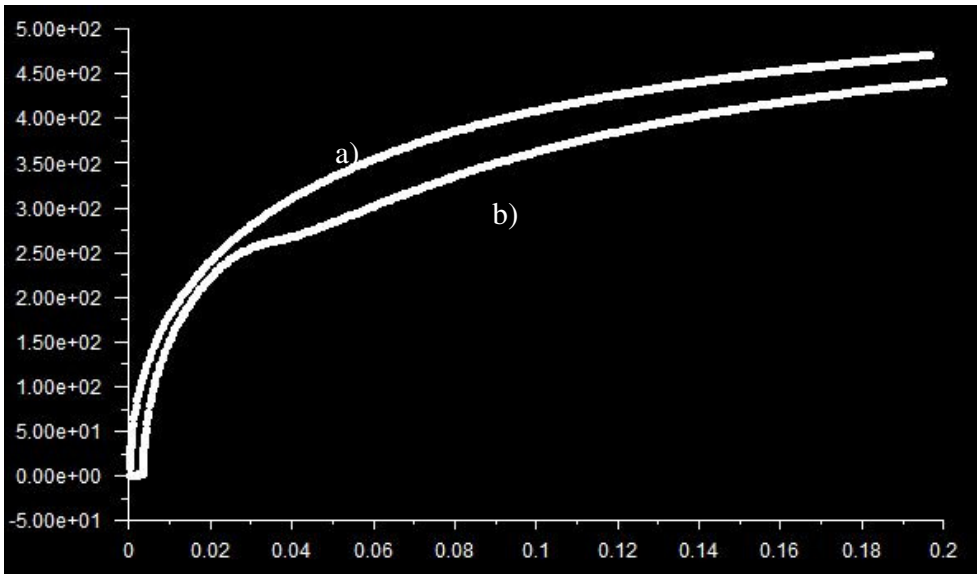

Figure 5.16: Velocities of nickel particles of 25µm with respect to travel distance injected a) directly at the nozzle axis and b) as per the nozzle injection model. N_2 at 2MPa and 900K is used as the driving gas while He at 450kPa is used as the powder feed gas.

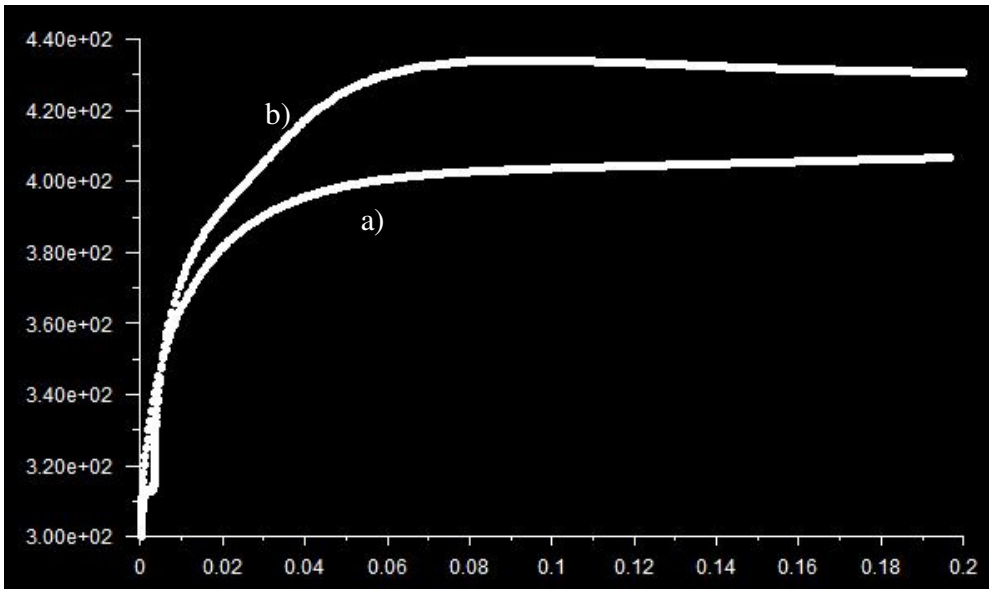

Figure 5.17: Temperatures of nickel particles of 25µm with respect to travel distance injected a) directly at the nozzle axis and b) as per the nozzle injection model. N_2 at 2MPa and 900K is used as the driving gas while He at 450kPa is used as the powder feed gas.

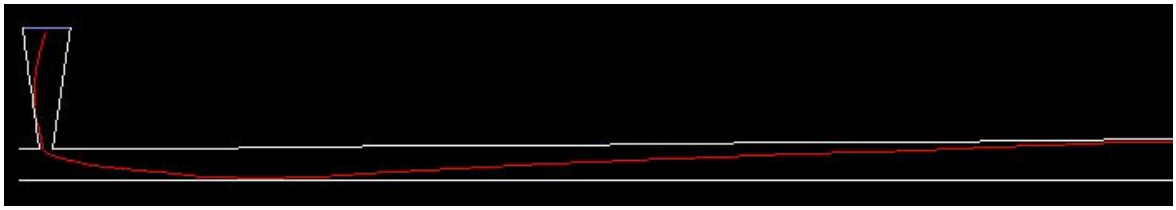

Figure 5.18: View of particle track injected as per the nozzle injection model.

As can be seen in Figure 5.15, the injection of additional gas changes the pressure distribution in the nozzle. The smooth flow is disturbed and small variances in pressure can be observed. This is especially evident near the nozzle wall after the injection point. The velocity and temperature of particles injected through the injection model (B) and those injected at the nozzle axis (A) were compared in Figure 5.16 and Figure 5.17. The particle velocities of the "A" particles are lower by approximately 30 m/s due to the initial radial velocity of the particles which has the effect of "bouncing" the particles off the walls as can be seen in Figure 5.18. The higher dwell time of these particles however increase their exit temperature by approximately 25K when compared to the "B" particles. These small discrepancies between the "A" and "B" particles are relatively small and not thought to be significant.

The effect of heating the feeder gas on the final particle velocity was also explored. Four simulations were conducted where the feeder gas was heated to 900K prior to injection into the nozzle. The addition of energy to the flow by this means will undoubtedly increase particle velocities although the amount of feeder gas is low compared to the driving gas. The results of this investigation are presented in Table 5-8 all other parameters remained the same.

Table 5-8: Results of injection model with heated feeder gas

Trial	**Driving Gas**		**Feeder Gas**		**Particle**
Number	Type	Pressure	Type	Pressure	**Velocity**
1	Helium	2MPa	Helium	450kPa	651m/s
2	Helium	2MPa	Argon	450kPa	644m/s
3	Helium	2MPa	Nitrogen	450kPa	645m/s
4	Nitrogen	2MPa	Helium	450kPa	471m/s

While the results indicate an increase in particle velocity, the gain is less than 1% and deemed negligible. However the particle temperature at the exit of the nozzle is higher as can be seen in Figure 5.19. By comparing this to Figure 5.17, an increase of approximately 150K is found in the particle exit temperature.

Another simulation was conducted in which both the particles and the feed gas were heated to 900K. In this simulation, the particle temperature was increased by 230K when compared to an unheated feed gas. Particle velocities remained unchanged. Judging solely by the particle velocity increase, the added energy requirement and equipment cost to heat the feeder gas appears not to be worth the investment. However the reduction in critical velocity due to the increased particle temperature is approximately 92m/s according to the equation of Assadi *et al.* [**43**]. This reduction in critical velocity will significantly increase the deposition efficiency of the process and warrants further experimental investigation.

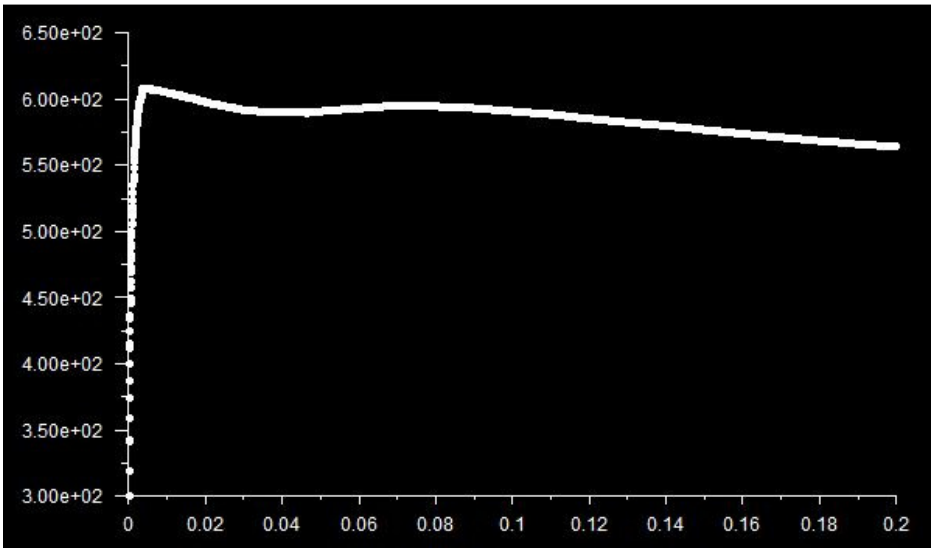

Figure 5.19: Particle temperatures with respect to particle travel distance for particles injected in feeding gas at 900K

5.3.3.4. Stand-Off Distance Model

In order to investigate the effect of stand-off distance on the particle impact velocity, another model was developed. In this case it was decided to move away from the complex model used for particle injection due to the difficulty in obtaining a converging solution. The original nozzle model was therefore modified to include an exterior domain. The width of this exterior domain was chosen to be 10mm as this distance corresponds to the width of the nozzle wall and is also half the width of the substrate (the model is axisymmetric). This simplifies the boundary conditions to be applied on the model as only one outlet is required to respect the actual physical geometry. Two separate models with exterior domain lengths of 10mm and 100mm were constructed as can be seen in Figure 5.20 and Figure 5.21. This model was used to evaluate the effect of the gas stagnation properties and the nozzle stand-

off distance on the particle velocities. The results of the simulations will therefore be presented in the following section.

Figure 5.20: View of stand-off distance model with 10mm exterior domain.

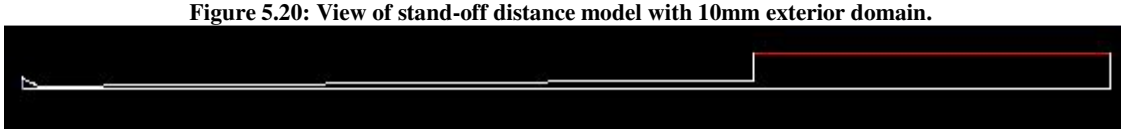

Figure 5.21: View of stand-off distance model with 100mm exterior domain.

5.4. Effect of Gas Stagnation Properties and Nozzle Stand-Off Distance

The stand-off distance model was used to determine the effect of the stand-off distance, as well as the stagnation properties. For this investigation, simulations at different pressures and temperatures were run on both the 10mm stand-off distance model and the 100mm stand-off distance model. A script was written and employed to automate this process. The simulation was first converged for pressure values of 1MPa. Simulations were then run for every increment of 0.25MPa up to a maximum of 4MPa. For these simulations to achieve convergence, 400000 iterations were run at each pressure increment. The first 200000 used a CFL number of 0.01 while the remaining 200000 iterations were run with a CFL number of 0.005. The script used to run these simulations is available in APPENDIX C.

5.4.1. Effect of Gas Stagnation Pressure

While increasing the gas stagnation pressure does not increase the driving gas velocity, the density of the driving gas is increased. The rise in pressure has the effect of increasing the drag on the particles resulting in faster particle exit velocity. The downside to this increased gas stagnation pressure is an increase in driving gas consumption as detailed in Table 5-9.

Table 5-9: Calculated helium gas consumption as a function of stagnation pressure

Stagnation Pressure (MPa)	Flow rate (g/s)
1.0	0.85
1.25	1.04
1.50	1.23
1.75	1.42
2.0	1.62
2.25	1.81
2.50	2.00
2.75	2.19
3.0	2.38
3.25	2.58
3.50	2.77
3.75	2.96
4.0	3.15

The gas flow of the original CGDS nozzle was measured using a simple simulation and compared to the optimal MOC nozzle designed in this study. The original nozzle was calculated to use 2.98 g/s of helium gas at a pressure of 2MPa which is roughly 84% more than the nozzle in this study. The original design requirement of this new nozzle was to halve the gas consumption when compared to the original one. The discrepancy between the design point and the simulated results could be attributed to the difference in the nozzle meshing or the varying degree of convergence of the simulations. The model used to simulate the gas flow of the nozzle in this study is also much more complex and does not have as high a degree of convergence.

The effect of the gas stagnation pressure was investigated while the gas stagnation temperature will remain constant. The data pertaining to the maximum particle velocity of the 100mm model at a stagnation temperature of 900K, for a particle of nickel with 25μm diameter is presented in Table 5-10 :

Table 5-10: Particle velocity as a function of stagnation pressure

Stagnation Pressure (MPa)	Particle Velocity Helium (m/s)	Particle Velocity Nitrogen (m/s)
1.0	531	364
1.25	573	406
1.50	614	436
1.75	648	457
2.0	678	478
2.25	705	491
2.50	730	506
2.75	753	520
3.0	775	533
3.25	795	544
3.50	814	555
3.75	833	565
4.0	851	575

As can be seen from these results, the effect of increasing the stagnation pressure from 1MPa to 4MPa increases the particle velocities by approximately 60%. While the increase in gas density due to the increased pressure can increase the particle velocity, the actual gas velocity remains the same. This limits the effectiveness of raising the gas pressure as the particle velocity nears the gas velocity. The increase in pressure also represents a 370% increase in gas consumption. This indicates that a 100% rise in pressure will raise the particle velocity by approximately 16%. For nitrogen, this increase in gas consumption may not represent significant costs but for an expensive gas such as helium the cost increase could make the process too costly for commercial application. The pressure should be therefore limited to the smallest acceptable value yielding adequate particle velocities.

5.4.2. Effect of Gas Stagnation Temperature

Increasing the gas stagnation temperature will increase the overall driving gas velocity although the Mach number will remain the same. An increase in gas velocity will

increase the drag force on the particles and effectively increase the particle exit velocity as well as particle exit temperature.

The effect of the gas stagnation temperature was explored while the gas stagnation pressure will remain constant. The data pertaining to the maximum particle velocity and particle exit temperatures using the 100mm model at a stagnation pressure of 4MPa, for a particle of nickel with 25µm diameter is presented in Table 5-11 for nitrogen as the driving gas and Table 5-12 for helium as the driving gas. The particle temperature profiles with gas stagnation pressure of 4MPa and stagnation temperature of 900K for nickel particles of 25µm diameter are presented in Figure 5.22 for nitrogen as driving gas and Figure 5.23 for helium as driving gas.

Table 5-11: Effect of gas stagnation temperature on particle velocity with nitrogen as driving gas

Stagnation Temperature	**900K**	**1000K**	**1100K**	**1200K**
Particle Velocity	575m/s	590m/s	603m/s	614m/s
Particle Exit Temperature	376K	399K	422K	444K

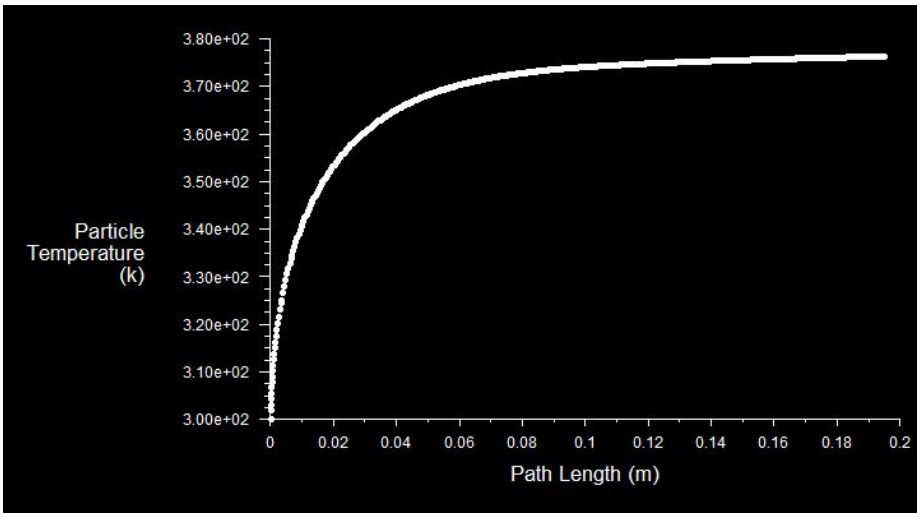

Figure 5.22: Particle temperature profile for 25µm Nickel particle using nitrogen as driving gas with 4MPa stagnation pressure and 900K stagnation temperature.

Table 5-12: Effect of gas stagnation temperature on particle velocity and particle nozzle exit temperature with helium as driving gas

Stagnation Temperature	800K	900K
Particle Velocity	835m/s	851m/s
Particle Exit Temperature	296K	332K

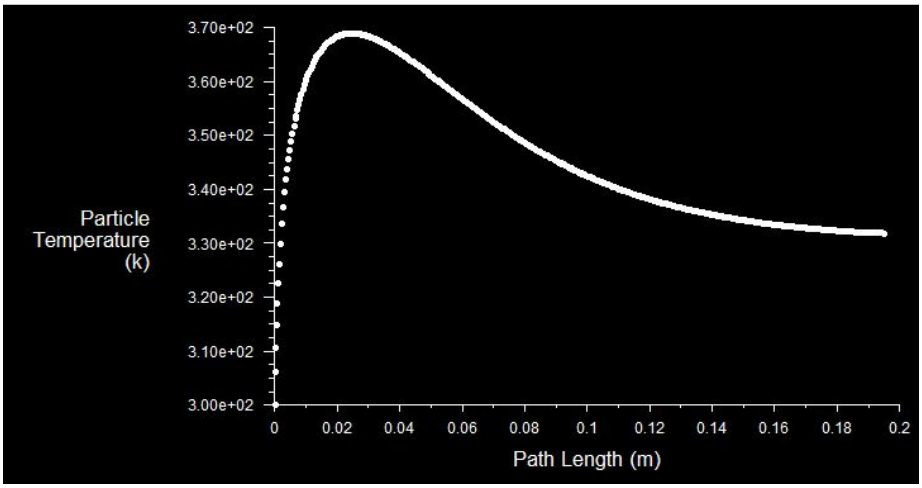

Figure 5.23: Particle temperature profile for 25µm Nickel particle using helium as driving gas with 4MPa stagnation pressure and 900K stagnation temperature.

The resulting particle velocity increases by approximately 2% for every 100K increase in gas stagnation temperature. In order to raise the gas stagnation temperature from 900K to 1000K represents an increase of power requirement of approximately 17%. This indicates that a 100% rise in temperature increases the particle velocity by approximately 12%. An increase in temperature therefore appears to be less efficient at increasing particle velocities than an increase in pressure. However, increasing the gas stagnation temperature also raises the particle temperature. For nitrogen as the driving gas, there is approximately a 22K increase in particle temperature for every 100K in gas stagnation temperature while for helium as a driving gas, the increase is approximately 38K for every 100K rise in gas stagnation temperature.

Simulations at temperatures higher than 900K using helium as the driving gas were not conducted as these temperatures would be higher than can be achieved using the current University of Ottawa Cold Spray Laboratory gas heater. Increases in nitrogen temperatures were explored due to the fact that nitrogen requires less energy to increase in temperature

and there is remaining headroom in the system for such an increase. The particle velocities with the use of nitrogen as a driving gas were also found to be very near the expected critical velocity of CoNiCrAlY. The possibility of using nitrogen as a driving gas was therefore explored through simulations at high temperatures.

5.4.3. Effect of Nozzle Stand-Off Distance

The effect of the stand-off distance on particle impact velocities was investigated using both the 10mm and 100mm models. The 10mm model was used to represent the actual spraying conditions used at the University of Ottawa Cold Spray Laboratory while the 100mm model was used to determine the maximum particle velocities without the interference of a substrate. Using the 100mm model, it was also possible to determine the optimal stand-off distance for maximal particle impact velocities. This optimal stand-off distance neglects any bow-shock effects due to the presence of the substrate. However, since the bow-shock will be weaker at stand-off distances of more than 10mm, any optimal stand-off distance that is found to be above this value should result in higher particle velocities. Additionally, the particle temperature increases with increasing stand-off distance as can be seen in Figure 5.24 for Nitrogen as driving gas and Figure 5.25 for helium as driving gas.

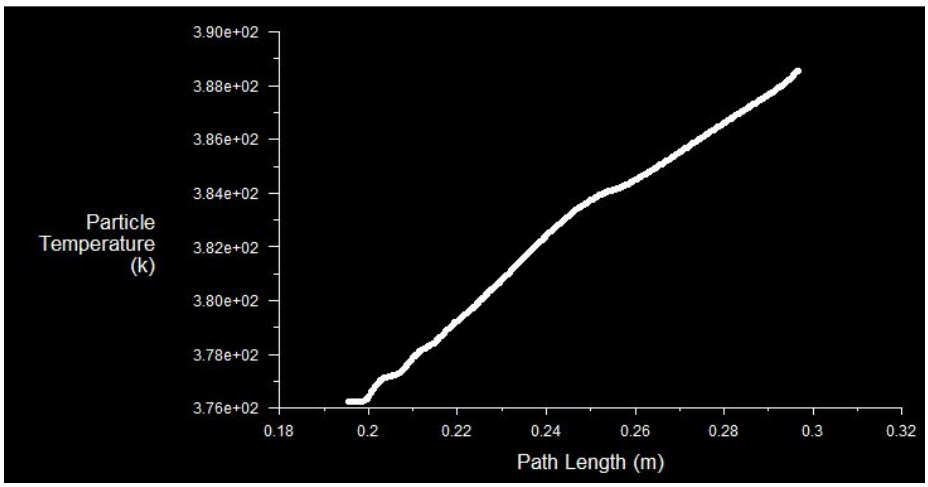

Figure 5.24: Temperature of 25µm Nickel particle with respect to distance outside the nozzle with nitrogen as driving gas.

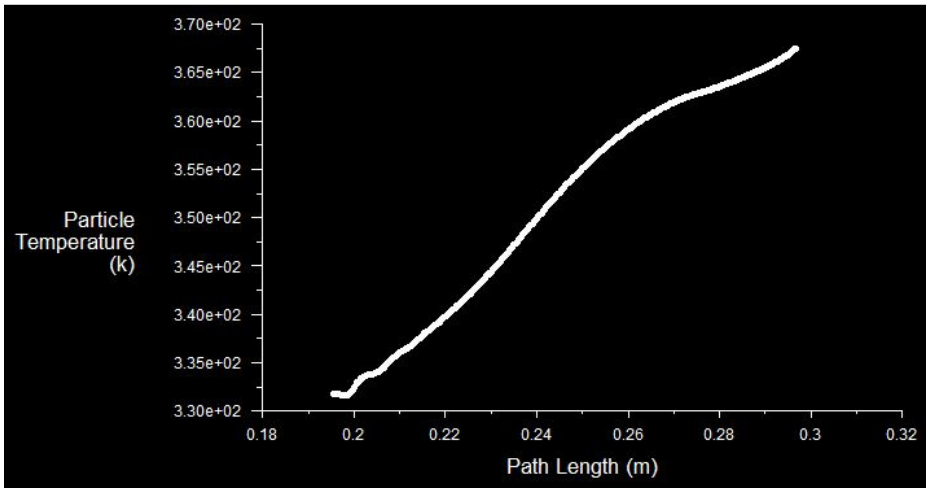

Figure 5.25: Temperature of 25μm Nickel particle with respect to distance outside the nozzle with helium as driving gas.

The maximum particle velocity reached in the 10mm stand-off distance model and then 100mm stand-off distance model for nickel particles of 25μm in diameter are presented in Table 5-13.

Table 5-13: Comparison of maximal particle velocities in the 10mm SOD and 100mm SOD models

Pressure (MPa)	He 900K, 10mm (m/s)	He 900K, 100mm (m/s)	N_2 900K, 10mm (m/s)	N_2 900K, 100mm (m/s)
1	529	531	366	364
1.25	572	573	412	406
1.5	613	614	436	436
1.75	645	648	456	457
2	672	678	473	475
2.25	696	705	488	491
2.5	718	730	501	506
2.75	738	753	513	520
3	758	775	525	533
3.25	776	795	536	544
3.5	793	814	546	555
3.75	810	833	555	565
4	826	851	565	575

As can be seen from Table 5-13, the maximum particle velocity is slightly higher in the 100mm model than in the 10mm model with the exception of 2 cases when N_2 gas is used. These two cases were found to have an over-expanded driving gas which results in shockwaves inside the nozzle, the stand-off distance therefore has no effect. These are also cases where the particle velocity is well below the critical velocity of the material and are therefore not of great importance for this study. The stand-off distance has an increasing influence on particle velocities as the pressure increases. For He driving gas at 1MPa, the difference is approximately 0.04% while at 4MPa the difference rises to approximately 3%. It should be noted that this analysis does not take into account the advantages of the weaker bow shock due to the increased stand-off distance.

The optimal stand-off distance was determined for both Helium and Nitrogen driving gases with stagnation pressures of 1MPa to 4MPa in increments of 0.25MPa and with stagnation temperatures of 800K and 900K in the case of Helium and 900K, 1000K, 1100K and 1200K for the case of Nitrogen. This optimal stand-off distance is based on the distance at which the particle reaches its maximum velocity. The results are indicated in Table 5-14 and Table 5-15.

Table 5-14: Optimal stand-off distance for Helium driving gas

	800K velocity (m/s)	800K SOD (mm)	900K velocity (m/s)	900K SOD (mm)
1	518	***27***	531	***27.5***
1.25	563	***32.5***	573	***31.5***
1.5	604	***33***	614	***34***
1.75	637	***35.5***	648	***36***
2	666	***41.5***	678	***42.5***
2.25	692	***47***	705	***47.5***
2.5	717	***54***	730	***54.5***
2.75	739	***58.5***	753	***59.5***
3	761	***64***	775	***64.5***
3.25	780	***67***	795	***67.5***
3.5	799	***71***	814	***71***
3.75	817	***74.5***	833	***75.5***
4	835	***79***	851	***79***

Table 5-15: Optimal stand-off distance for Nitrogen driving gas

	900K velocity (m/s)	900K SOD (mm)	1000K velocity (m/s)	1000K SOD (mm)	1100K velocity (m/s)	1100K SOD (mm)	1200K velocity (m/s)	1200K SOD (mm)
1	364	***(16.5)***	384	***0.5***	396	***(3.5)***	401	***(6.5)***
1.25	406	***6.5***	420	***6***	427	***6.5***	433	***8***
1.5	436	***11.5***	445	***14.5***	453	***14.5***	460	***15***
1.75	457	***20.5***	466	***21.5***	475	***21.5***	483	***22.5***
2	475	***27.5***	485	***27.5***	494	***28***	503	***28.5***
2.25	491	***31.5***	502	***33***	512	***34***	521	***34***
2.5	506	***38***	518	***38.5***	528	***39***	537	***40***
2.75	520	***42***	532	***43***	543	***43***	552	***44***
3	533	***45.5***	545	***45.5***	558	***46.5***	566	***47***
3.25	544	***49.5***	557	***49.5***	568	***50***	579	***51***
3.5	555	***51.5***	568	***52.5***	581	***53***	592	***54***
3.75	565	***55***	579	***55***	592	***55.5***	603	***56.5***
4	575	***57.5***	590	***58***	603	***59***	614	***59.5***

These results indicate that the stand-off distance appears to be unaffected by increasing stagnation temperature but greatly affected by increasing the stagnation pressure. This is due to the fact that increasing the pressure stagnation pressure increases the pressure ratio as discussed in section 2.2.3. Upon exit from the nozzle, the gas expands and accelerates until the gas pressure is equal to the ambient pressure. This acceleration outside the nozzle increases the particle velocity and therefore the optimal stand-off distance. The higher the stagnation pressure, the longer this acceleration zone lasts. SOD values in parenthesis indicate the maximum velocity is located inside the nozzle, this is due to the gas being over-expanded inside the nozzle and the emergence of shockwaves which slow down the flow. The maximum particle velocities in these cases are inside the nozzle rather than on the outside. Select examples at gas stagnation temperatures of 900K and stagnation pressures of 1MPa, 2MPa and 4MPa are presented in the following sections for further analysis.

5.4.3.1. Stand-off effect with 1MPa stagnation pressure and 900k stagnation temperature

Figure 5.26 to Figure 5.29 compare the effect of the stand-off distance on particle velocity of 5μm and 25μm in diameter nickel particles and driving gas density when using He as a driving gas. As can be seen by comparing Figure 5.26 and Figure 5.27, the particle velocity is greatly reduced with increasing distance. This is caused by the deceleration of the driving gas outside the nozzle. Observing the density contours in Figure 5.28 and Figure 5.29, no strong shocks are observed. The density along the substrate in the 10mm model is also lower than the ambient density indicating that the driving gas flow is deflected by the substrate before returning to ambient density. In contrast, the density in the 100mm model returns to ambient before contact with the substrate.

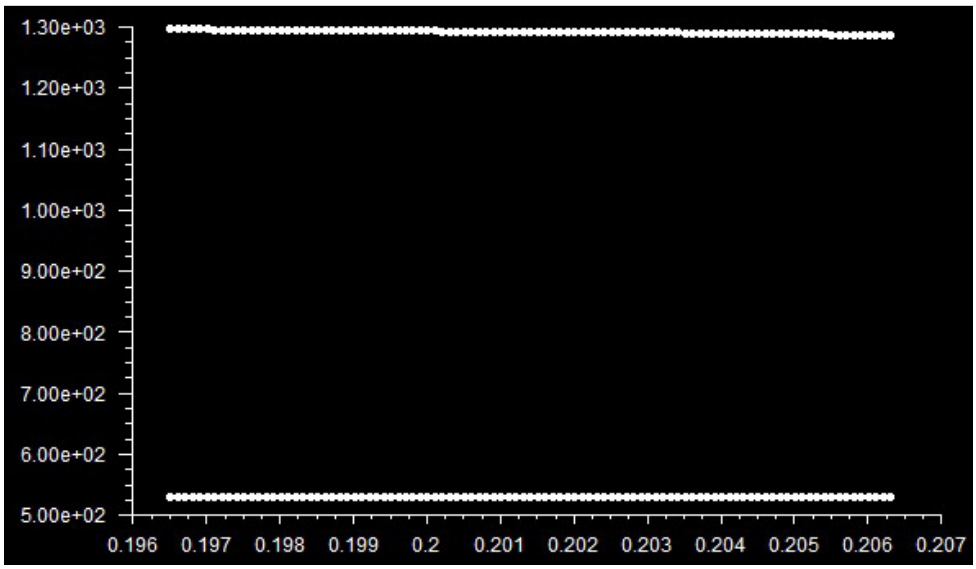

Figure 5.26: Particle velocity of nickel particles of 5μm (top) and 25μm (bottom) in diameter with respect to distance from nozzle throat, showing region between nozzle exit and substrate. Driving gas is He with stagnation properties of 1MPa and 900K using 10mm SOD model.

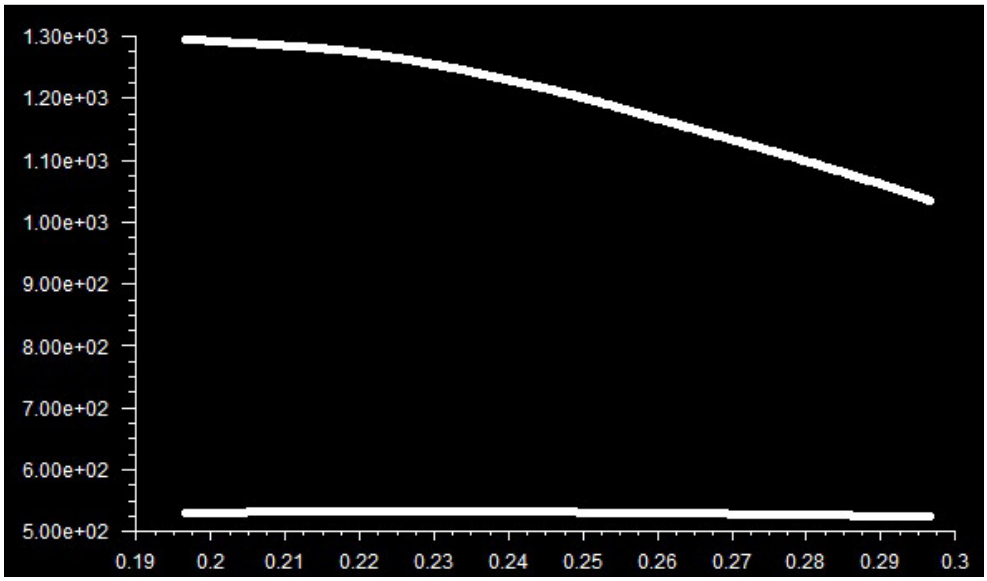

Figure 5.27: Particle velocity of nickel particles of 5µm (top) and 25µm (bottom) in diameter with respect to distance from nozzle throat, showing region between nozzle exit and substrate. Driving gas is He with gas stagnation properties of 1MPa and 900K using 100mm SOD model.

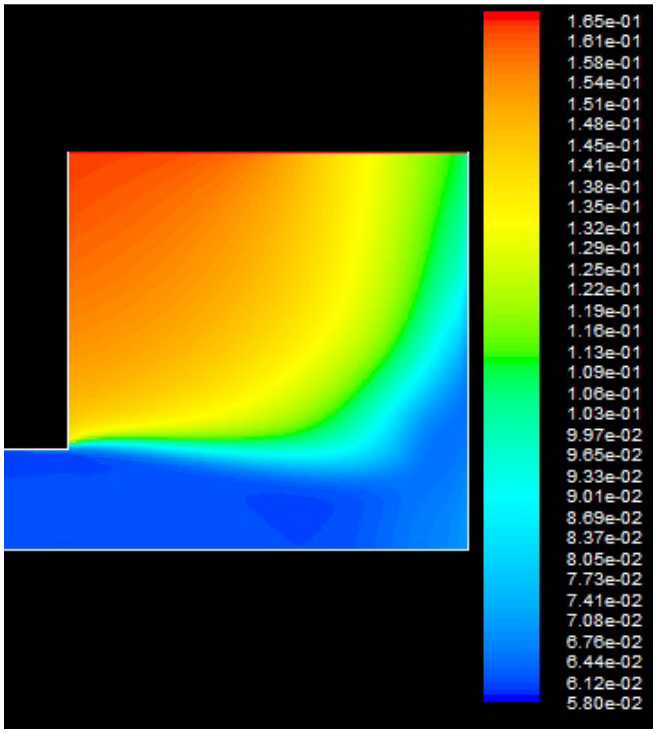

Figure 5.28: Density contours of exterior of nozzle to substrate with He gas stagnation properties of 1MPa and 900k using 10mm SOD model.

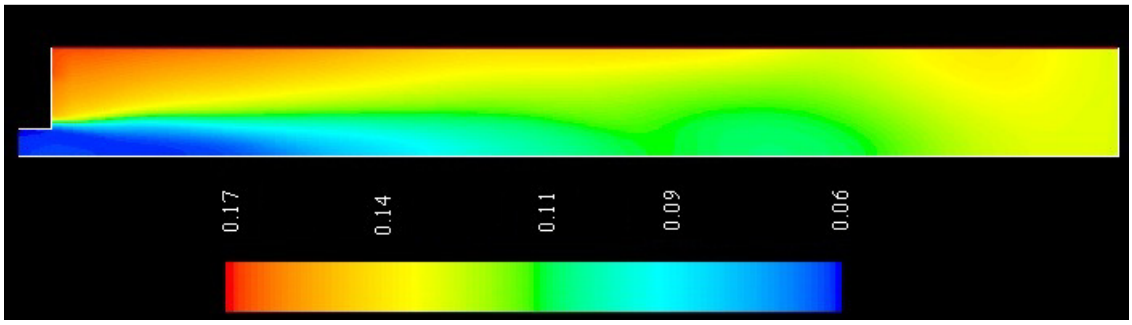

Figure 5.29: Density contours of exterior of nozzle to substrate with He gas stagnation properties of 1MPa and 900k using 100mm SOD model.

Figure 5.30 to Figure 5.33 compare the effect of the stand-off distance on particle velocity of 5μm and 25μm in diameter nickel particles and driving gas density when using N_2 as a driving gas. The behaviour in this case is very similar to the case where He is employed as the driving gas however the effect is amplified. The particle velocities are reduced much more rapidly and the density contours return to ambient density much more rapidly than with the He case. This is due to the different specific heat ratios of the two gases which lead to differences in the resulting pressures, velocities and temperatures of the gases. In this case, the nitrogen gas appears to be over expanded and its velocity therefore drops rapidly outside of the nozzle. A higher stagnation pressure is required to retain the particle velocities after exiting the nozzle.

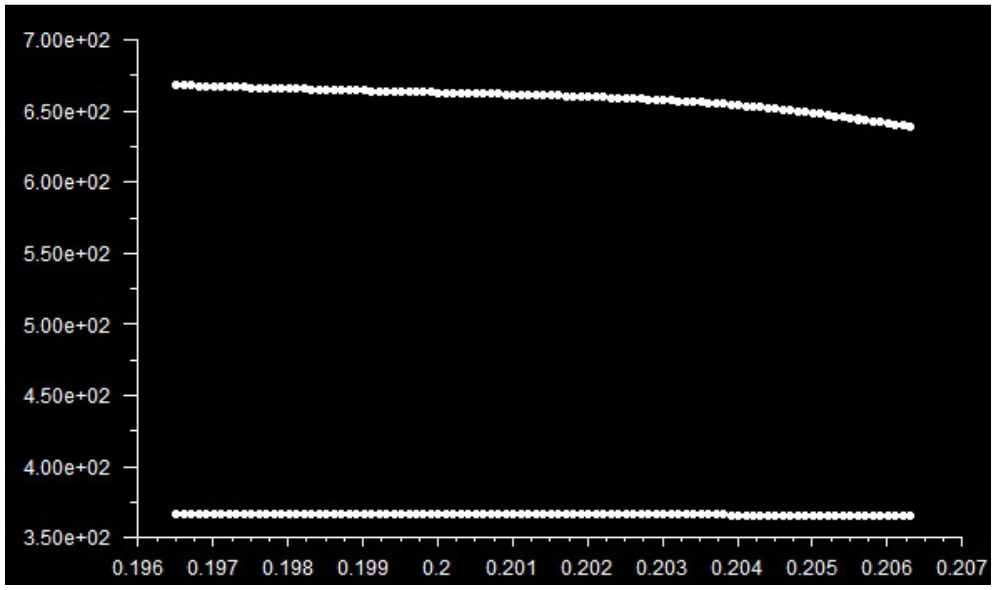

Figure 5.30: Particle velocity of nickel particles of 5µm (top) and 25µm (bottom) in diameter with respect to distance from nozzle throat, showing region between nozzle exit and substrate. Driving gas is N_2 with gas stagnation properties of 1MPa and 900K using 10mm SOD model.

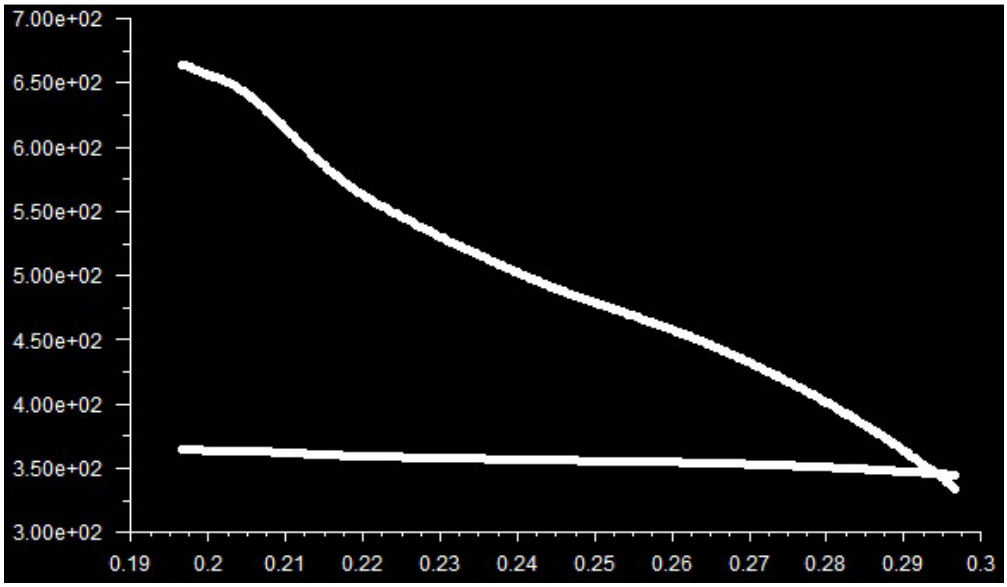

Figure 5.31: Particle velocity of nickel particles of 5µm (top) and 25µm (bottom) in diameter with respect to distance from nozzle throat, showing region between nozzle exit and substrate. Driving gas is N_2 with gas stagnation properties of 1MPa and 900K using 100mm SOD model.

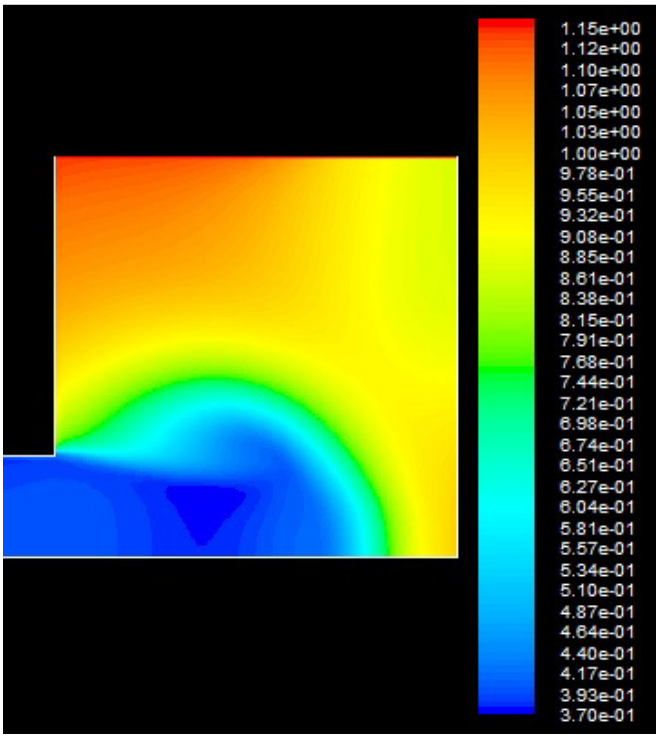

Figure 5.32: Density contours of exterior of nozzle to substrate with N_2 gas stagnation properties of 1MPa and 900k using 10mm SOD model.

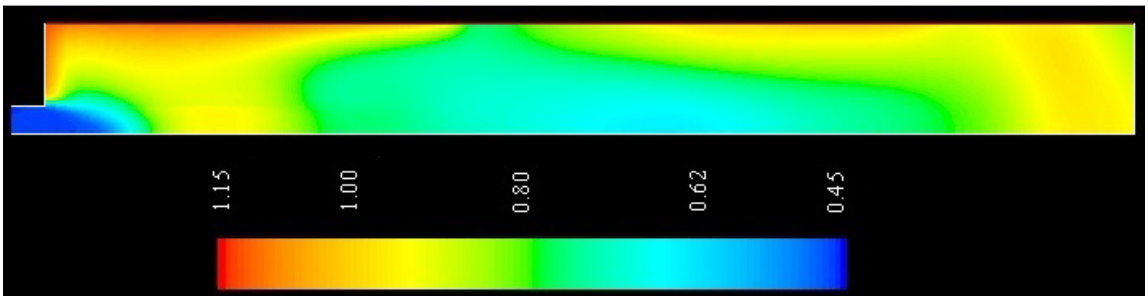

Figure 5.33: Density contours of exterior of nozzle to substrate with N_2 gas stagnation properties of 1MPa and 900k using 100mm SOD model.

5.4.3.2. Stand-off effect with 2MPa stagnation pressure and 900k stagnation temperature

Figure 5.34 to Figure 5.37 compare the effect of the stand-off distance on particle velocity of 5µm and 25µm in diameter nickel particles and driving gas density when using He as a driving gas. Similarly to what was observed with the 1MPa case, the velocity decreases with increasing distance. However, an initial velocity increase is measured at the exit of the nozzle and the maximal velocity is measured further away from this exit than the

1MPa case. Observing the density contours in Figure 5.36 and Figure 5.37, a shock can be observed near the substrate of the 10mm model. The lower density region is also longer in the 100mm model than was observed at 1MPa. This indicates the optimal stand-off distance is further from the nozzle exit than in the 1MPa case.

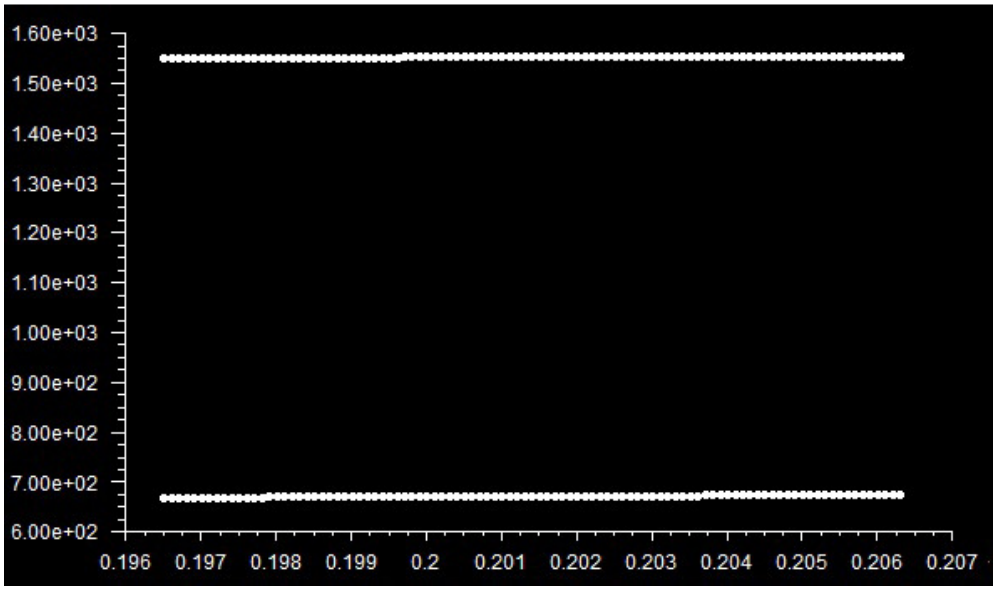

Figure 5.34: Particle velocity of nickel particles of 5µm (top) and 25µm (bottom) in diameter with He gas stagnation properties of 2MPa and 900K using 10mm SOD model.

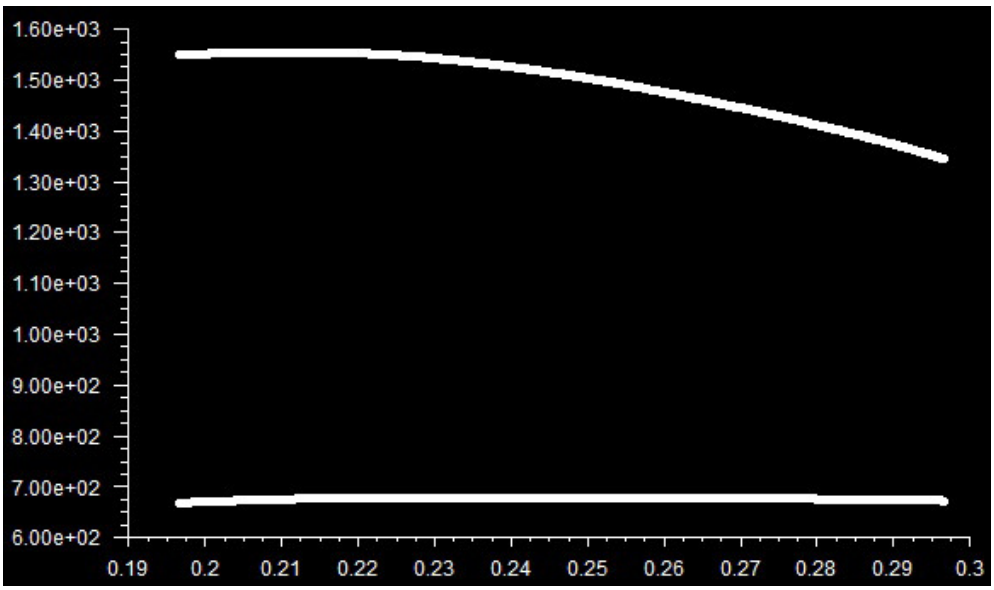

Figure 5.35: Particle velocity of nickel particles of 5µm (top) and 25µm (bottom) in diameter with He gas stagnation properties of 2MPa and 900K using 100mm SOD model.

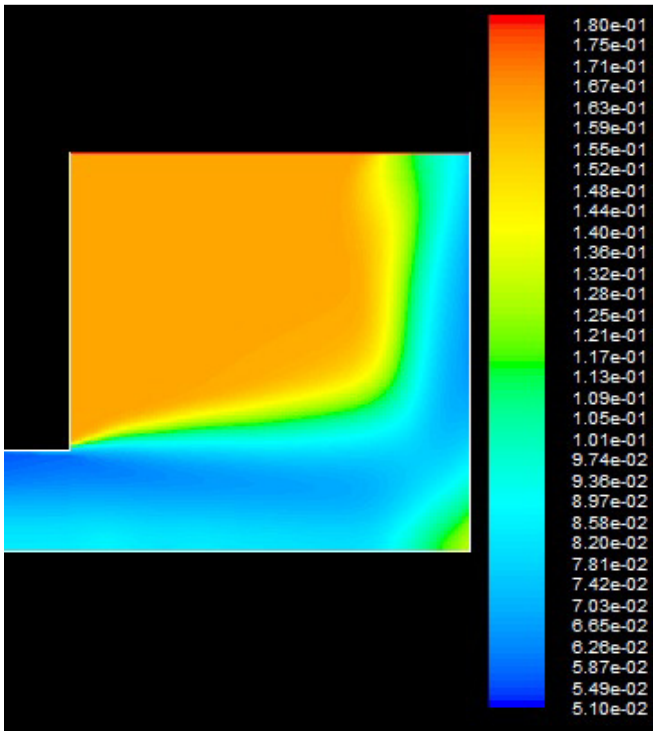

Figure 5.36: Density contours of exterior of nozzle to substrate with He gas stagnation properties of 2MPa and 900k using 10mm SOD model.

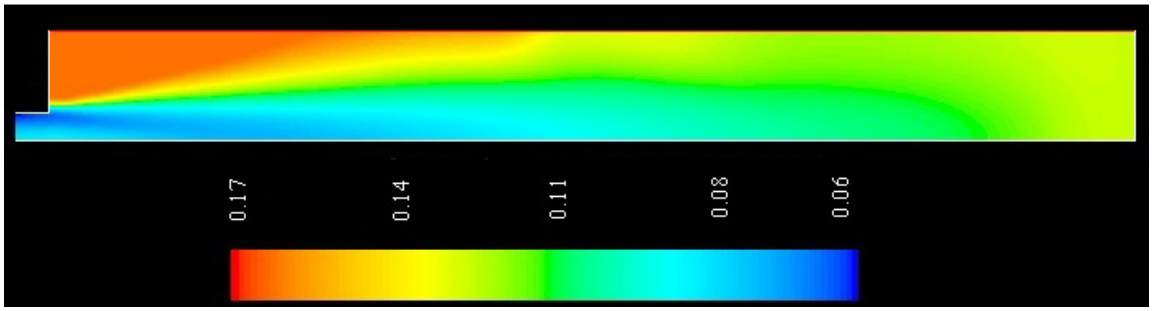

Figure 5.37: Density contours of exterior of nozzle to substrate with He gas stagnation properties of 2MPa and 900k using 100mm SOD model.

Figure 5.38 to Figure 5.41 compare the effect of the stand-off distance on particle velocity of 5µm and 25µm in diameter nickel particles and driving gas density when using N_2 as a driving gas. Much like in the He case, the particle velocities are not reduced as much then when using 1MPa as the stagnation pressure. The drop in velocity remains much higher than in the He case. The bow shock also appears to be stronger when using N_2 then when using He.

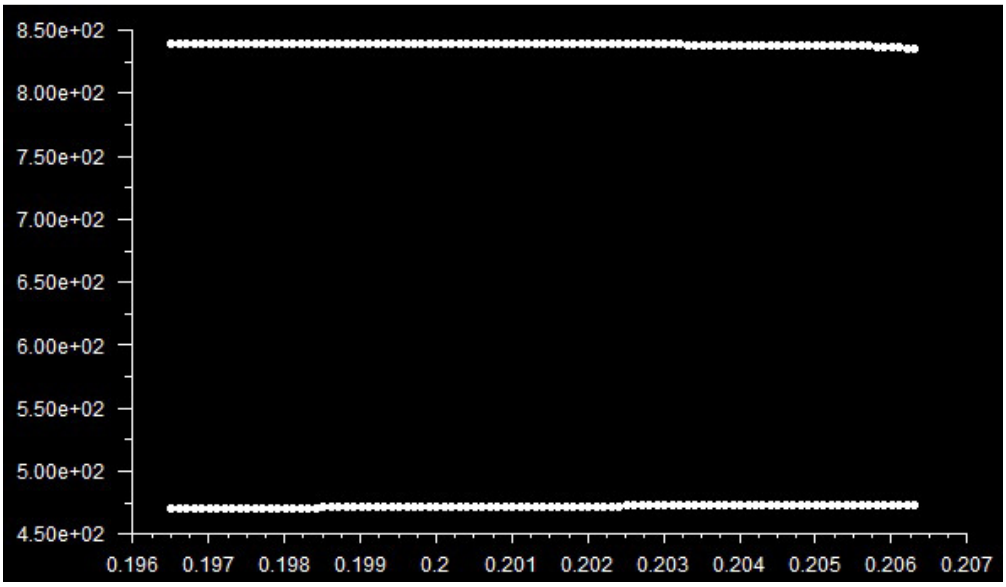

Figure 5.38: Particle velocity of nickel particles of 5μm (top) and 25μm (bottom) in diameter with N_2 gas stagnation properties of 2MPa and 900K using 10mm SOD model.

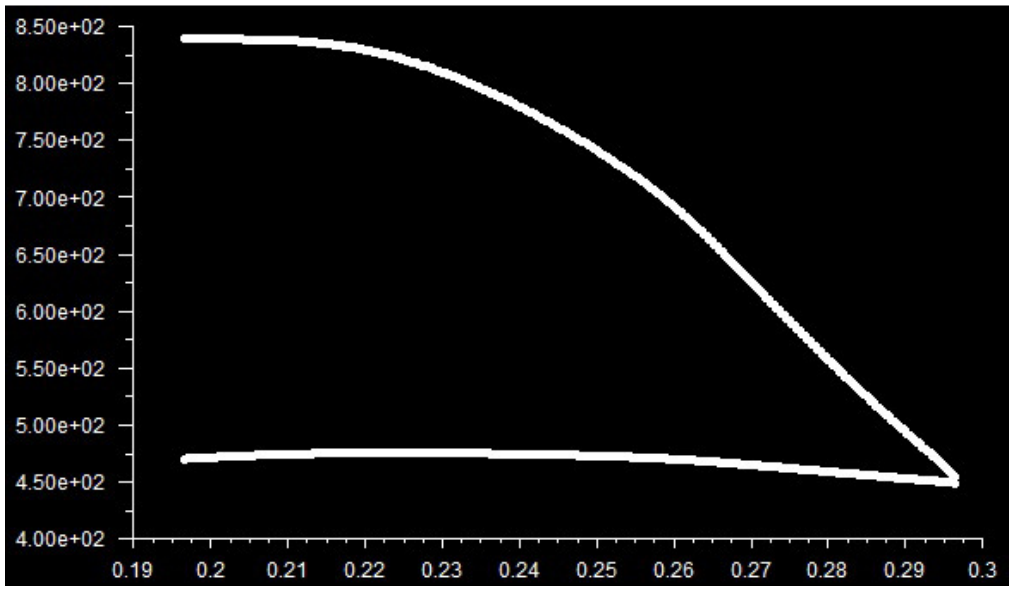

Figure 5.39: Particle velocity of nickel particles of 5μm (top) and 25μm (bottom) in diameter with N_2 gas stagnation properties of 2MPa and 900K using 100mm SOD model.

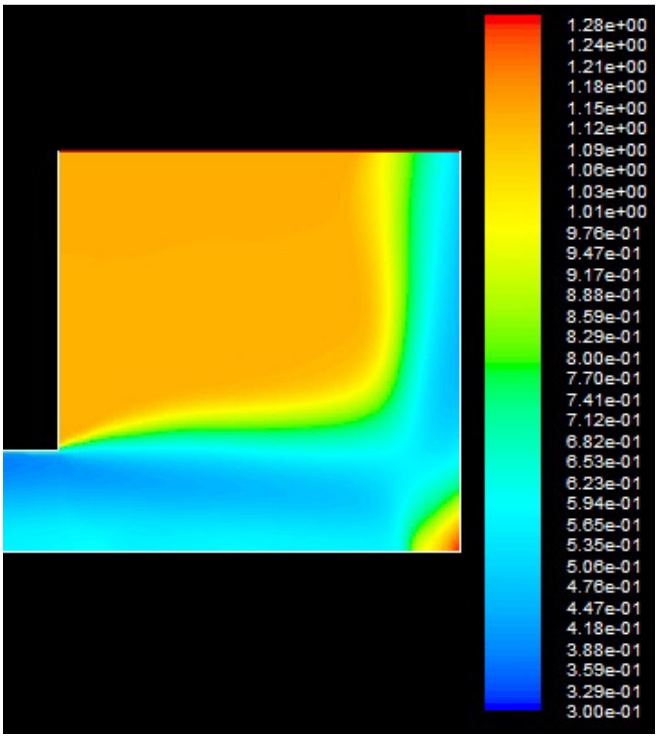

Figure 5.40: Density contours of exterior of nozzle to substrate with N_2 gas stagnation properties of 2MPa and 900k using 10mm SOD model.

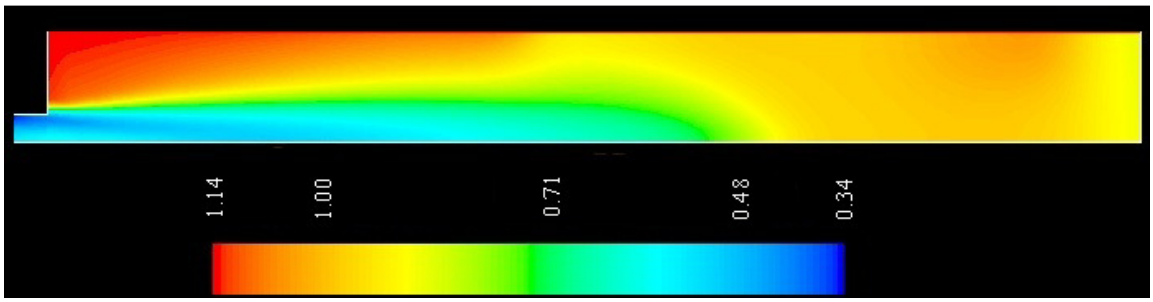

Figure 5.41: Density contours of exterior of nozzle to substrate with N_2 gas stagnation properties of 2MPa and 900k using 100mm SOD model.

5.4.3.3. Stand-off effect with 4MPa stagnation pressure and 900k stagnation temperature

Figure 5.42 to Figure 5.45 compare the effect of the stand-off distance on particle velocity of 5µm and 25µm in diameter nickel particles and driving gas density when using He as a driving gas. This case follows the trend of the 1MPa and 2MPa cases. The particles continue accelerating past the nozzle and the maximum velocity is reached further away from the nozzle exit. Observing the density contours, there appears to be a

much stronger shock in this case when compared to the other two cases. Shock diamonds are also observed in the 100mm model at the exit of the nozzle. These are caused by the adjustment of the gas flow to the ambient pressure through the use of expansion and compressive shockwaves.

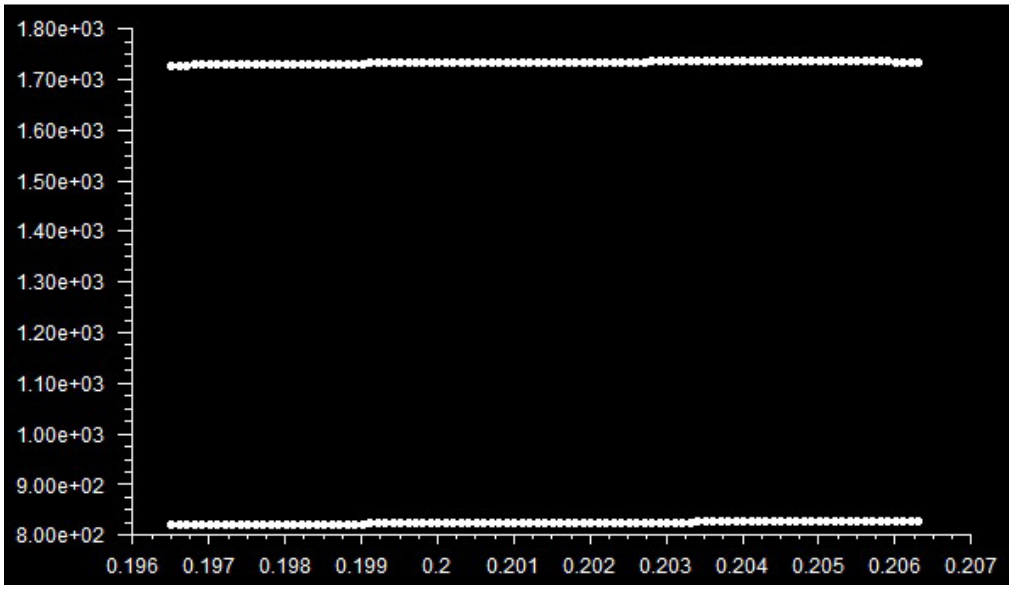

Figure 5.42: Particle velocity of nickel particles of 5µm (top) and 25µm (bottom) in diameter with He gas stagnation properties of 4MPa and 900K using 10mm SOD model.

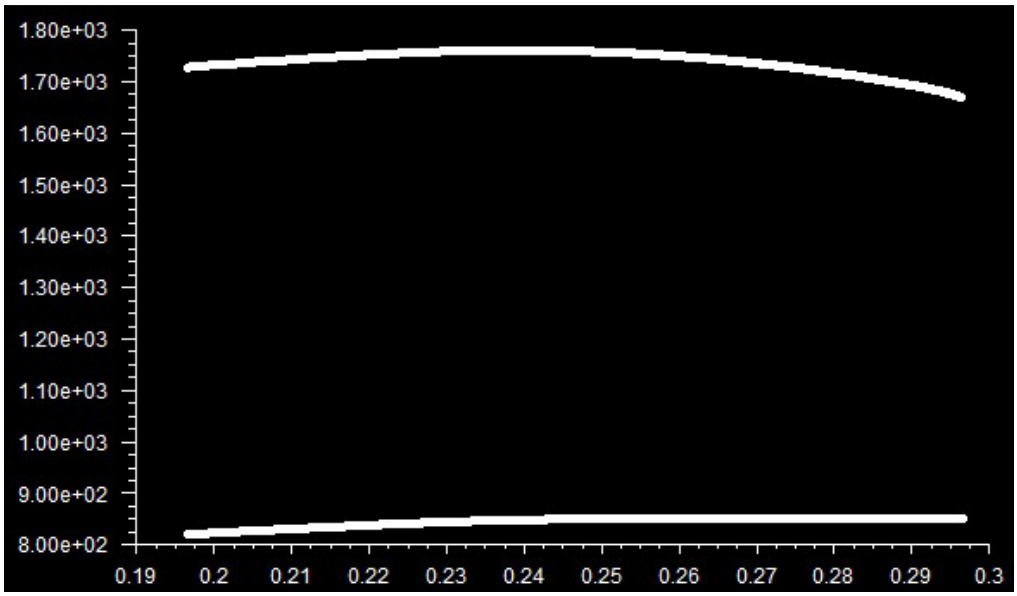

Figure 5.43: Particle velocity of nickel particles of 5µm (top) and 25µm (bottom) in diameter with He gas stagnation properties of 4MPa and 900K using 100mm SOD model.

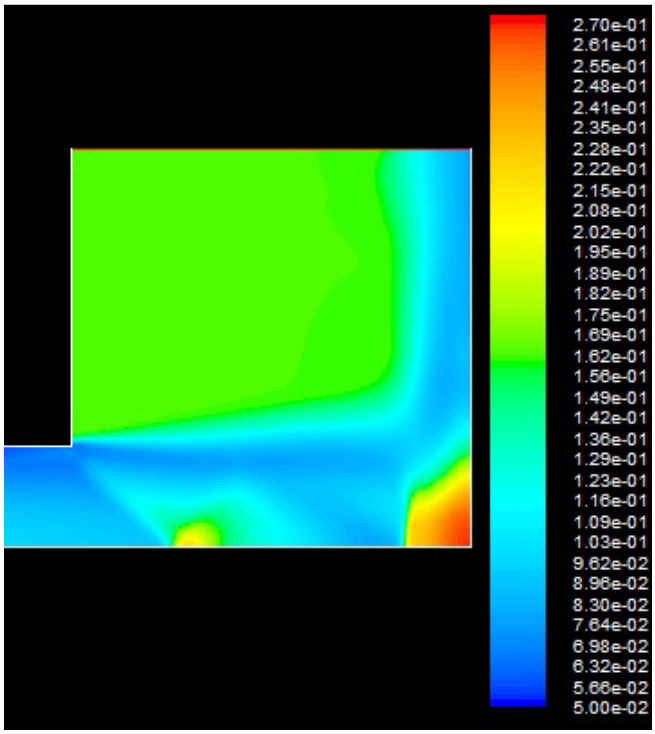

Figure 5.44: Density contours of exterior of nozzle to substrate with He gas stagnation properties of 4MPa and 900k using 10mm SOD model.

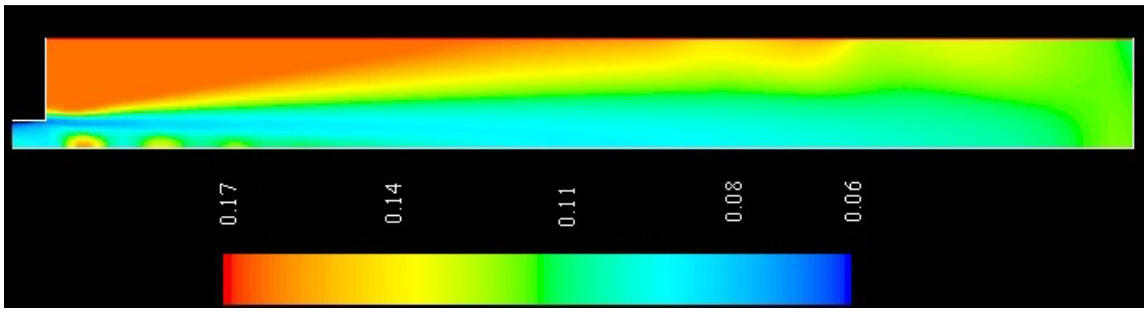

Figure 5.45: Density contours of exterior of nozzle to substrate with He gas stagnation properties of 4MPa and 900k using 100mm SOD model.

Figure 5.46 to Figure 5.49 compare the effect of the stand-off distance on particle velocity of 5µm and 25µm in diameter nickel particles and driving gas density when using N_2 as a driving gas. The results for the 4MPa case are consistent with the previous results: the bow shock observed is larger than in the He case and shock diamonds are observed at the exit of the nozzle. Particles also keep accelerating past the nozzle exit and appear to be affected by the strong bow shock present in the 10mm model.

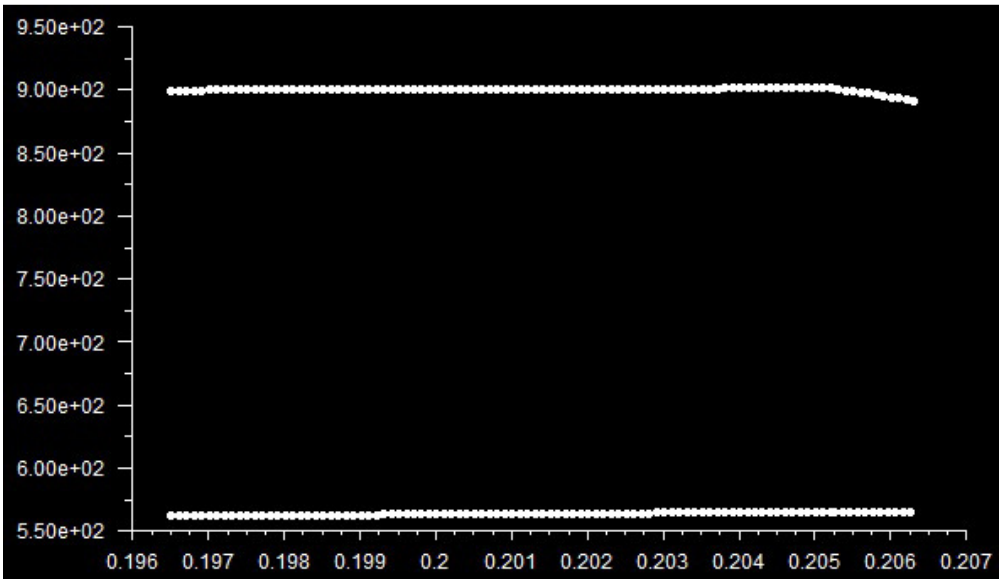

Figure 5.46: Particle velocity of nickel particles of 5µm (top) and 25µm (bottom) in diameter with N_2 gas stagnation properties of 4MPa and 900K using 10mm SOD model.

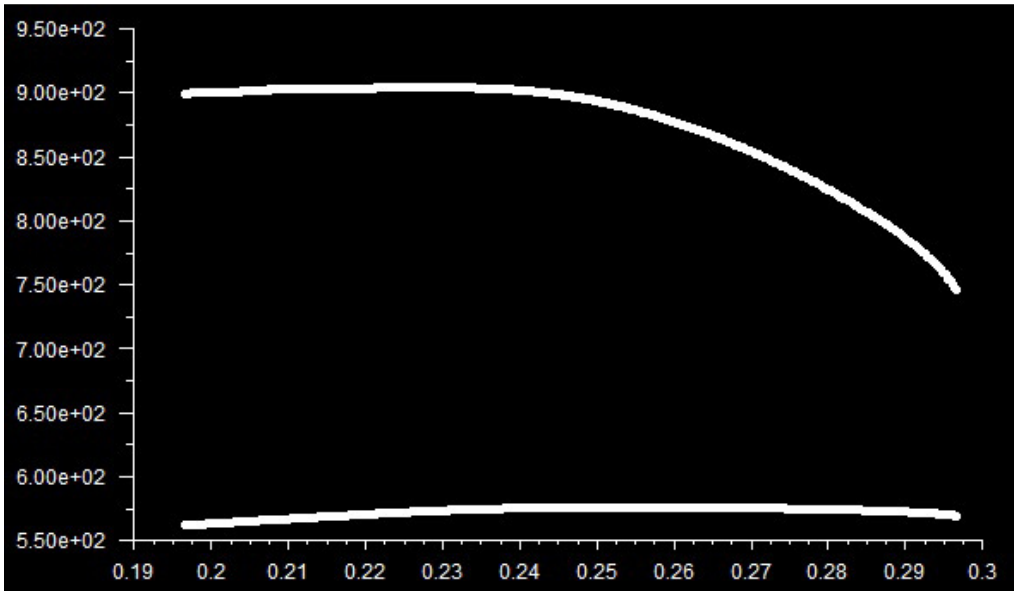

Figure 5.47: Particle velocity of nickel particles of 5µm (top) and 25µm (bottom) in diameter with N_2 gas stagnation properties of 4MPa and 900K using 100mm SOD model.

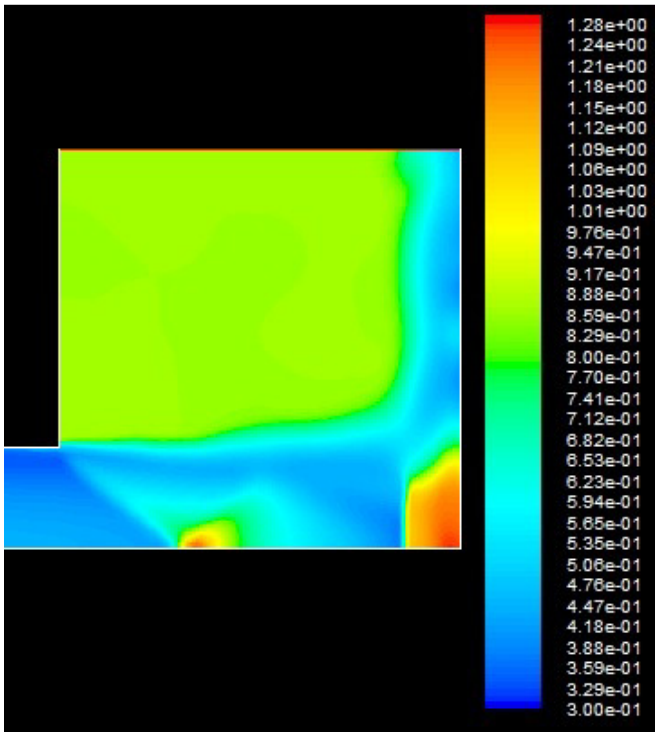

Figure 5.48: Density contours of exterior of nozzle to substrate with N_2 gas stagnation properties of 4MPa and 900k using 10mm SOD model.

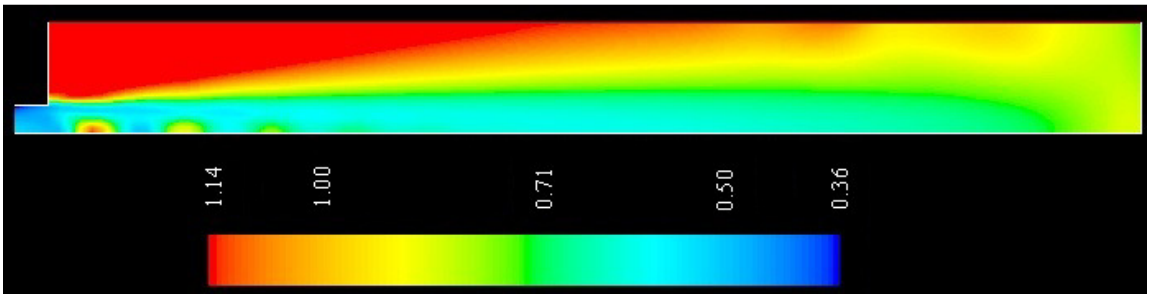

Figure 5.49: Density contours of exterior of nozzle to substrate with N_2 gas stagnation properties of 4MPa and 900k using 100mm SOD model.

5.5. Summary of Optimization Simulations

In this study, various simulations were run to determine the optimal nozzle design and determine the effect of the stagnation pressure, stagnation temperature and stand-off distance on the particle velocity. It was determined that the optimal nozzle shape to achieve the design requirements would feature an initial MOC section to accelerate the gas to M=$\sqrt{3}$ followed by a straight section to maintain this optimal relative Mach number.

The effect of modifying the stagnation properties was then investigated. Increasing gas stagnation temperature was found to increase the maximum particle velocity by approximately 11.8% for a 100% increase in power. Increasing the gas stagnation pressure was found to increase the maximum velocity by approximately 16% for a 100% increase in gas consumption. Although increasing the gas pressure seems more efficient, the cost of gas can be much greater than the cost of electricity, especially in the case of helium.

An injection model was constructed to analyse the effect of injecting the powder via gas downstream from the throat. Analysis of this model led to the finding that the particles injected using this method had slightly lower particle velocities due to the initial radial velocity of injection but had higher particle temperatures due to the increased dwell time. Additionally, heating of the feed gas was investigated. It was found that heating the feed gas slightly increased the particle velocities (less than 1%) but significantly increased the particle temperature (approximately 150K). Heating of the particles as well as the feed gas resulted in a particle temperature increase of 230K. Simulations were conducted with various mixes of driving and feed gas in an attempt to increase particle velocities however no significant advantage was found.

Finally, the effect of the stand-off distance was investigated for various stagnation temperatures and pressures. It was found that an increase of 3% of particle velocities could be achieved by increasing the stand-off distance for particles of 25μm in diameter. However the model does not accurately take into account the bow shock and as such, the actual increase in particle velocities should be higher than what was determined by the simulations.

Chapter 6 - Manufacturing and Testing of CGDS Nozzle

6.1. Manufacturing of CGDS nozzle

Once the optimal CGDS design was selected, it was necessary to select a manufacturing method capable of accurately replicating the geometry. It was chosen to manufacture the nozzle using two metal plates in which half the nozzle shape was machined. The plates were then aligned, sandwiched together and welded to form the full nozzle. A mounting bracket and fittings were then welded to the nozzle in order to ensure compatibility with the cold spray system at the University of Ottawa Cold Spray Laboratory.

In order to ensure the geometry of the nozzle was accurate, the machining was done using a HAAS TM-2 Computer Numerical Control (CNC) mill with an accuracy of ±25μm depicted in Figure 6.1.

Figure 6.1: View of CNC Mill (Haas model TM-2)

A virtual model of the nozzle was created using SolidWorks 2010 in order to be accurately machined into the nozzle material. In order to facilitate the machining process, the MOC section coordinates were simplified to a second order equation. This simplification was found to induce an error less than 25μm (less than the accuracy of the CNC mill) and deemed to not affect the final design. The model of the nozzle is presented in Figure 6.2 while the engineering drawings are available in APPENDIX E.

Figure 6.2: Solidworks model of optimal nozzle

The nozzle material was chosen to be 310-stainless steel due to its combination of hardness, machinability and resistance to heat. Each side of the nozzle are machined to an identical profile and take approximately 14 hours to manufacture on the CNC mill. Additional holes which are used to line up the two halves for welding were also milled. A hole of 1.5mm in diameter was drilled in one of the halves past the throat to allow the injection or particles in the gas stream. The resulting machined halves are presented in Figure 6.3. A detailed view of the throat, MOC section and particle injection port are presented in Figure 6.4.

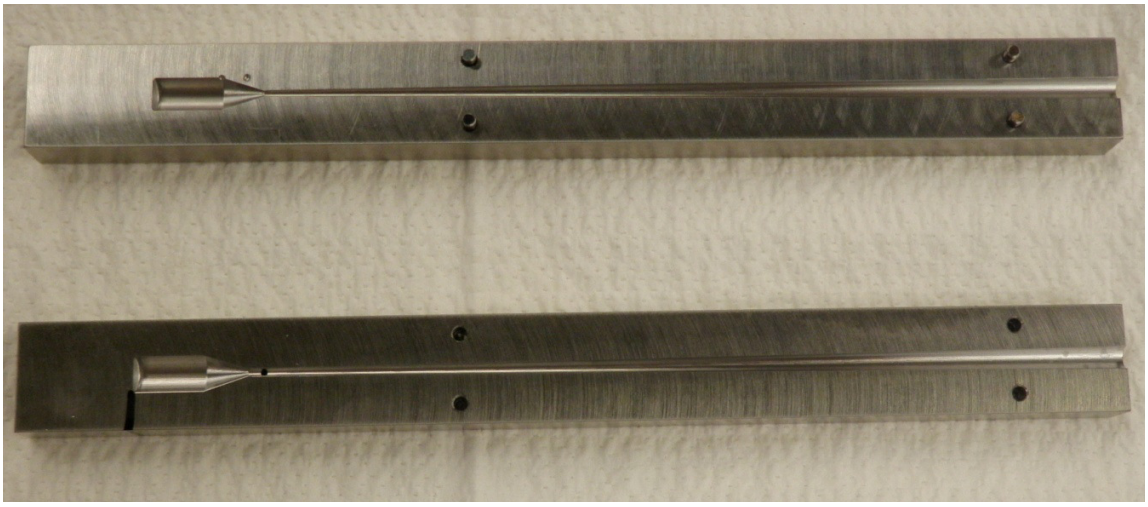

Figure 6.3: View of nozzle sections after manufacturing

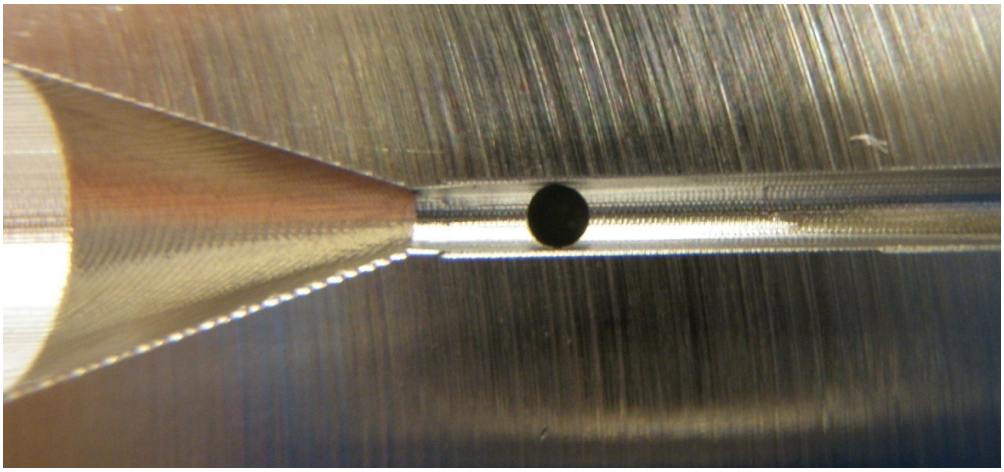

Figure 6.4: Detailed view of throat area, MOC section and particle injection

The two nozzle sections were then sandwiched together, assembled with the fittings and aligned before being welded. Stainless steel fittings with a ¼" NPT threat were used to

ensure compatibility with the existing CGDS system for both the nozzle inlet and particle inlet. The nozzle was then welded to a holding plate used to mount the nozzle in the CGDS system. The resulting nozzle is shown in Figure 6.5.

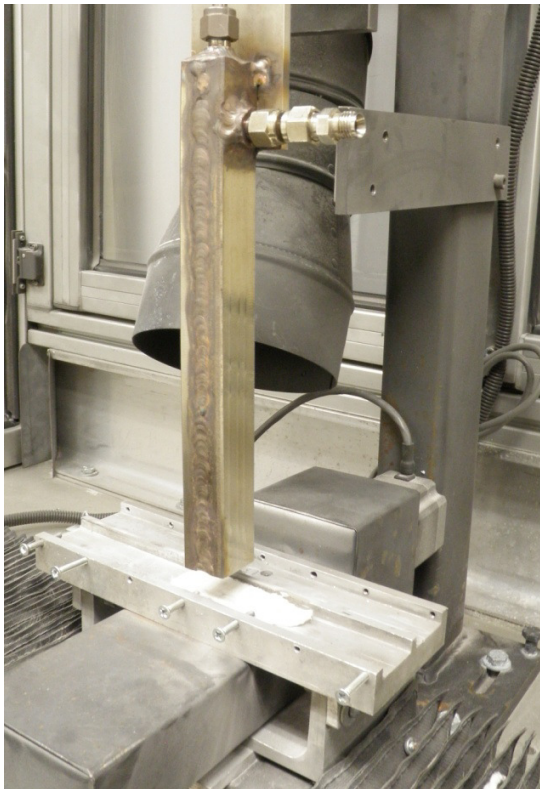

Figure 6.5: View of the fully assembled CGDS nozzle in the University of Ottawa cold spray system.

6.2. Testing of CGDS Nozzle

The nozzle was first tested with the spraying parameters that were found optimal in the previous study[**121**]: Al-6061 substrate, Helium driving gas, 2MPa gas stagnation pressure, 550°C gas stagnation temperature and 1mm/s substrate travel speed. The resulting coating was very thick (>1mm) but peeled immediately from the substrate during cooling due to the dissimilar coefficients of thermal expansion between the coating and substrate. The gas consumption was also found to be much lower than in the previous study which led to a much more stable gas temperature. This is in agreement with the 1D mass flow approximations:

$$m = \rho V A \tag{6.1}$$

where m is the mass flow rate, ρ is the gas density, V is the gas velocity and A is the cross-sectional area. In the case of a supersonic nozzle, the mass flow rate is determined at the throat of the nozzle where the flow is choked. With stagnation temperatures constant, the mass flow rate is only affected by the throat area. According to equation 6.1 the gas flow rate of the nozzle in this study should be half that of the nozzle in the previous study due to the reduction in throat area from 2mm in diameter to 1.4mm in diameter.

A second test was conducted with identical properties but with a slightly increased gas stagnation temperature of 600°C and different substrate travel speeds. An initial rapid displacement at the maximum velocity of the system (12mm/s) after observing initial coating build-up was previously found to reduce peeling of the coating which typically occurs at locations exposed to the gas/particle stream for prolonged periods. The peeling was attributed to the high degree of coating build-up at the initial spot which increases thermal stresses during coating cooling due to the difference in thermal expansion coefficients of the substrate and coating. These prolonged exposures produce "spots" at the beginning and end of the spraying phase and when changing speeds on the computer program. The second spray sequence therefore used the 12mm/s initial displacement for 10mm followed by 45mm at 5mm/s, 25mm at 8mm/s and 25mm with two passes at 8mm/s. This test was used to determine the coating thickness of each substrate travel speed and the associated coating porosity. A photograph of this test sample is presented in Figure 6.6.

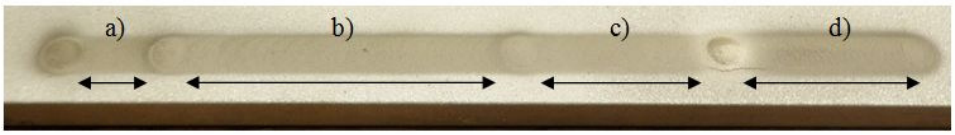

Figure 6.6: CoNiCrAlY deposition using CGDS nozzle with He gas stagnation properties of 2MPa and 900K and with substrate travel speeds of a) 12mm/s, b) 5mm/s, c) 8mm/s, d) two passes of 8mm/s.

The thickness of each section was measured and is summarised in Table 6-1.

Table 6-1: Summary of coating thicknesses at different substrate travel speeds

Travel speed (mm/s)	Thickness (μm)
12	240
5	440
8	370
2x8	770

The sample was then sectioned and cross-sectional images were taken to determine coating porosity at each travel speed. The coating porosity was found to be independent of the travel speed indicating the nozzle accelerates particles beyond the material critical velocity. This is an improvement of the previous nozzle where impingement was required to achieve low porosity levels [**121**]. An example of the coating cross section is presented in Figure 6.7.Additional tests were conducted with lower gas pressures in an attempt to further reduce processing costs. CoNiCrAlY coatings were successfully deposited at a gas stagnation pressure of 1.5MPa and gas stagnation temperature of 585°C resulting in a coating porosity of approximately 2%. An additional test was conducted with a gas stagnation pressure of 1MPa and a gas stagnation temperature of 495°C resulting in an extremely thin coating. The low coating thickness was attributed to the nearly 100°C reduction in gas stagnation temperature. This drop in temperature is caused by a decrease in turbulence in the gas heater due to lower process temperatures.

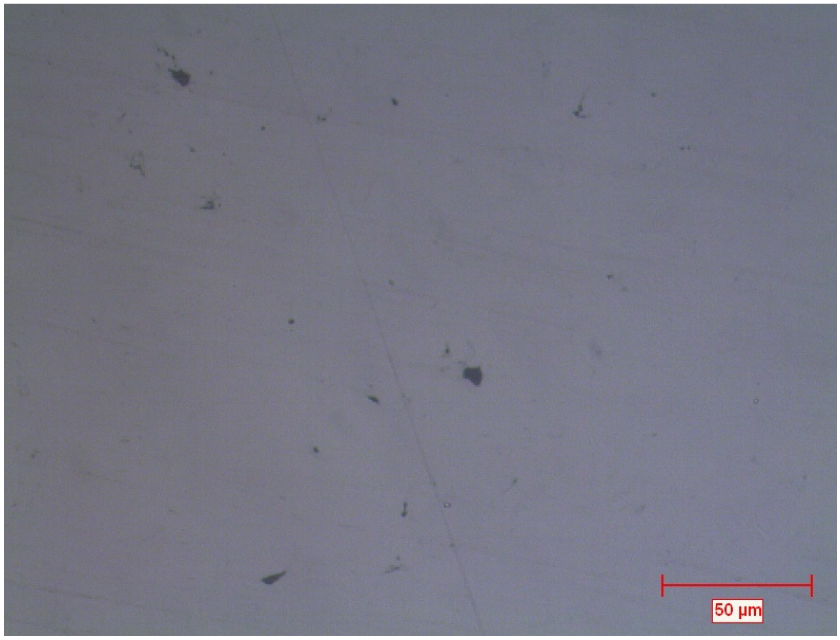

Figure 6.7: View of CoNiCrAlY coating deposited by CGDS

Several tests were then conducted using nitrogen as the driving gas. According to the simulations conducted in Chapter 4 -, nitrogen gas at a pressure of 4MPa can be used to reach particle velocities equivalent to using helium at a pressure of 1.25MPa. An initial test was conducted using copper as the coating material and nitrogen gas stagnation pressure of 2MPa and stagnation temperature of 450°C to determine CGDS feasibility using nitrogen. This test resulted in successful deposition of a thick copper coating. CoNiCrAlY particles are very difficult to deposit compared to copper particles and according to the simulations, a pressure of 4MPa is required to match the particle velocities of helium. Testing was therefore conducted at the maximum nitrogen pressure the University of Ottawa Cold Spray system could reach, 3.2MPa and at temperatures of approximately 680°C. This resulted in minimal coating build-up as can be seen in Figure 6.8.

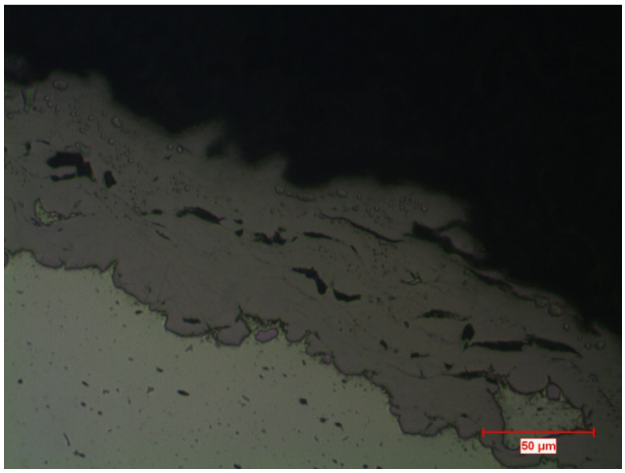

Figure 6.8: View of CoNiCrAlY coating deposited using nitrogen driving gas.

However, subsequent attempts to obtain coatings using the original parameters with helium gas also proved unsuccessful. The coatings were found to have undeformed particles, much greater porosity and a lower thickness than previous results. An image of the low-quality coatings are displayed in Figure 6.9. After further investigation, it was concluded that the nozzle was fouled.

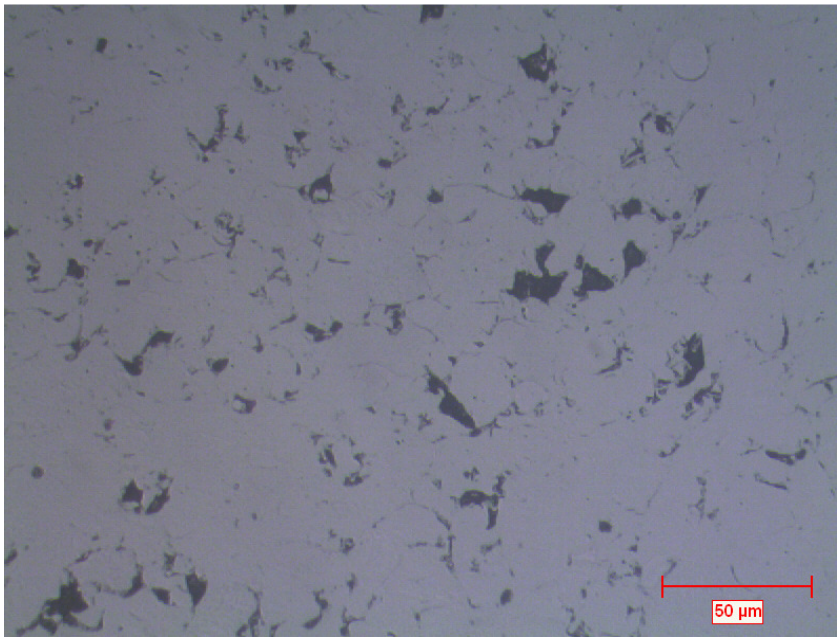

Figure 6.9: Cross-section view of CGDS coating deposited with fouled nozzle.

6.3. Nozzle Clogging Investigation

To investigate the extent of the fouling in the nozzle, the two sandwiched sections were sectioned by milling the welded areas. This method allows for the observation of the nozzle interior without damaging the nozzle itself. It also allows the nozzle to be re-assembled should there be no visible damage. The separated nozzle sections are shown in Figure 6.10.

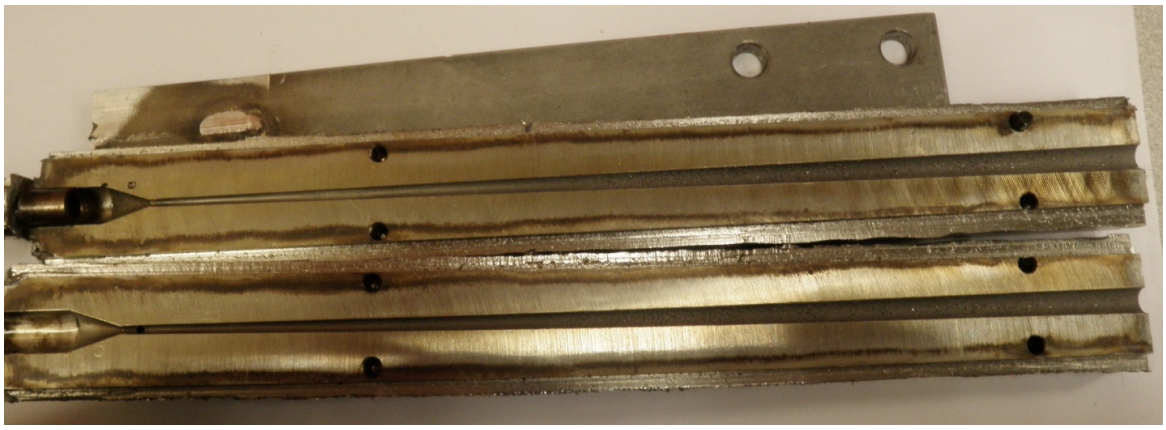

Figure 6.10: View of separated clogged nozzle sections

Upon close observation of the nozzle, fouling is apparent on the nozzle walls downstream from the powder injection point. The fouling appears to be a build-up of copper and CoNiCrAlY powder particles. This could be attributed to improper powder feeding pressures which would make the particles impact the nozzle walls and adhere to them with sufficient plastic deformation. The fouling is thought to have been initiated by the use of copper particles which are much easier to deposit and therefore are more likely to foul the nozzle. The copper deposits then alter the driving gas flow possibly inducing shockwaves which would result in lower particle exit velocities and an increased risk of nozzle fouling. Detailed views of the nozzle sections are presented in Figure 6.11 to Figure 6.13.

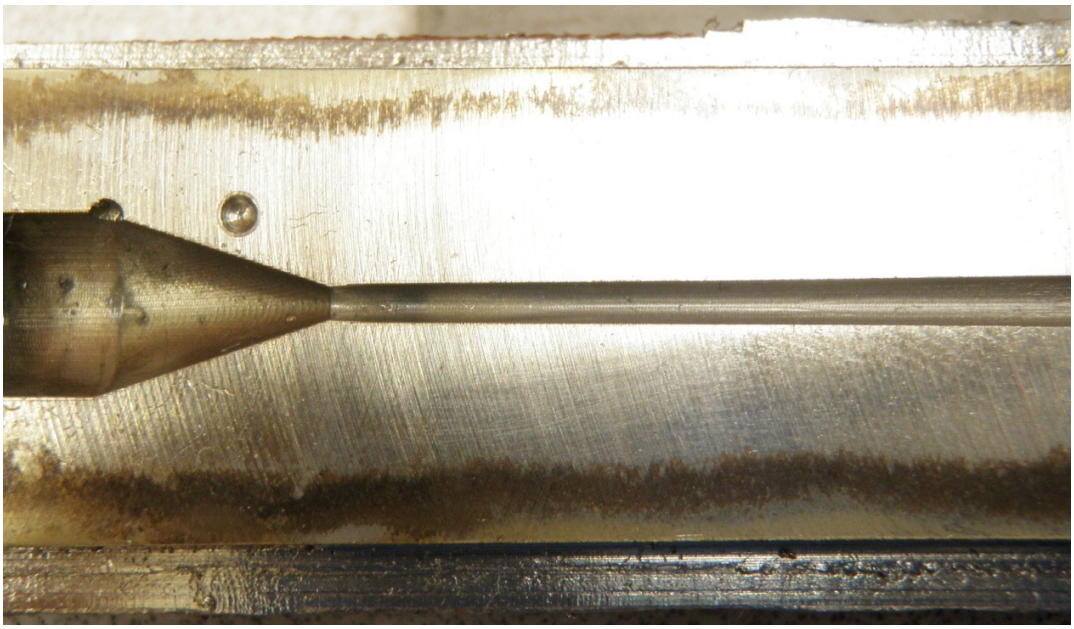

Figure 6.11: Detailed view of clogged nozzle: throat area

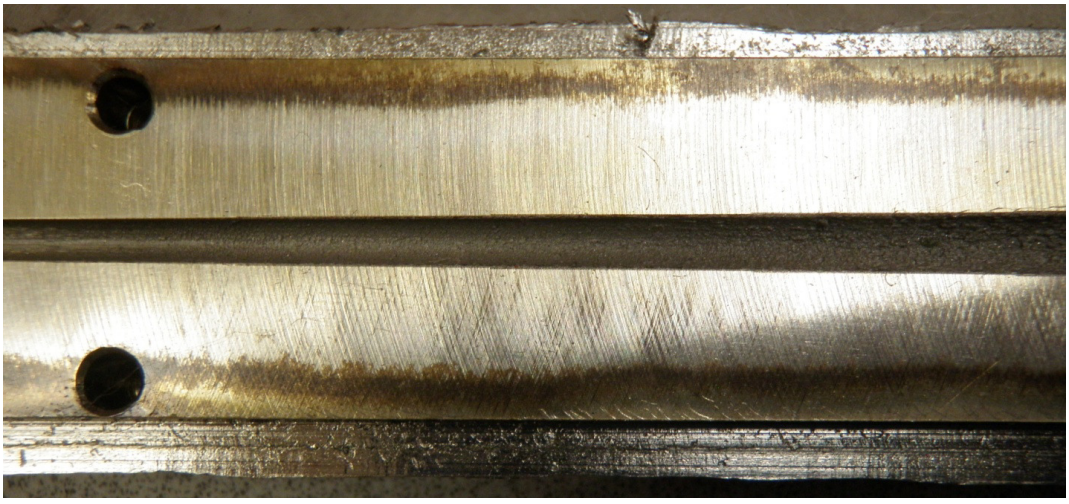

Figure 6.12: Detailed view of clogged nozzle: downstream of throat

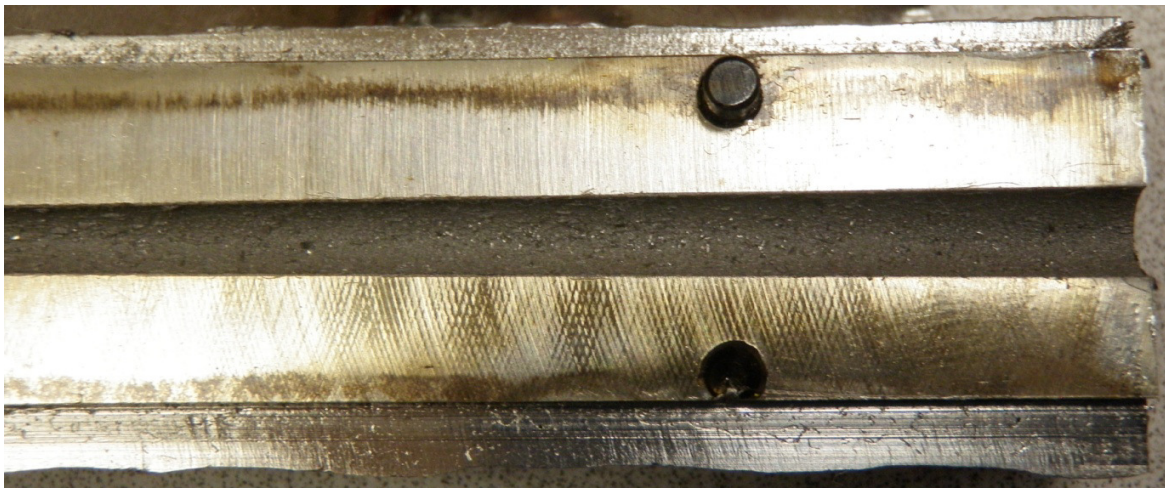

Figure 6.13: Detailed view of clogged nozzle: exit area

Additional images were taken with an optical microscope in order to assess the particle composition and particle sizes through visual analysis. The difference between CoNiCrAlY and Cu particles is quite evident via visual inspection removing the need for EDS analysis.

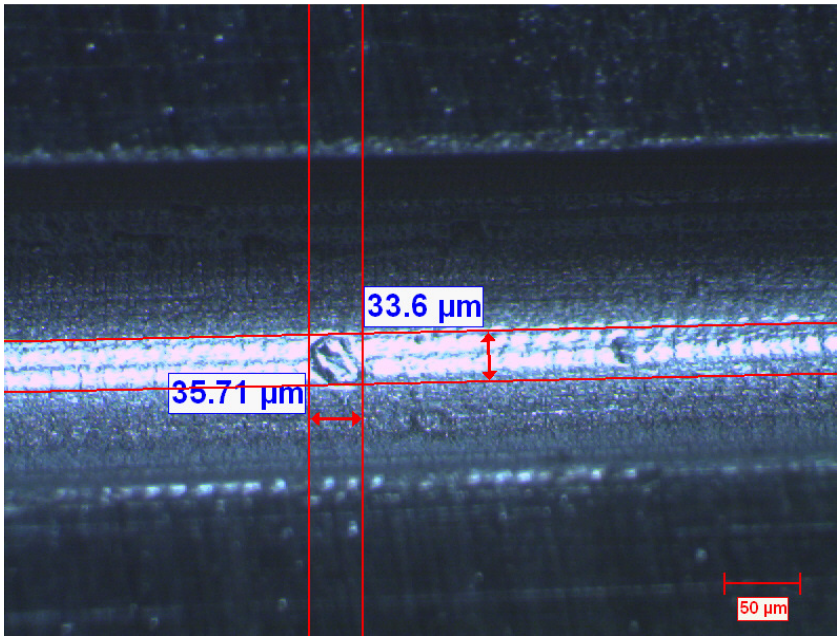

Figure 6.14: Magnified view of the fouled nozzle showing the measurement of a copper particle.

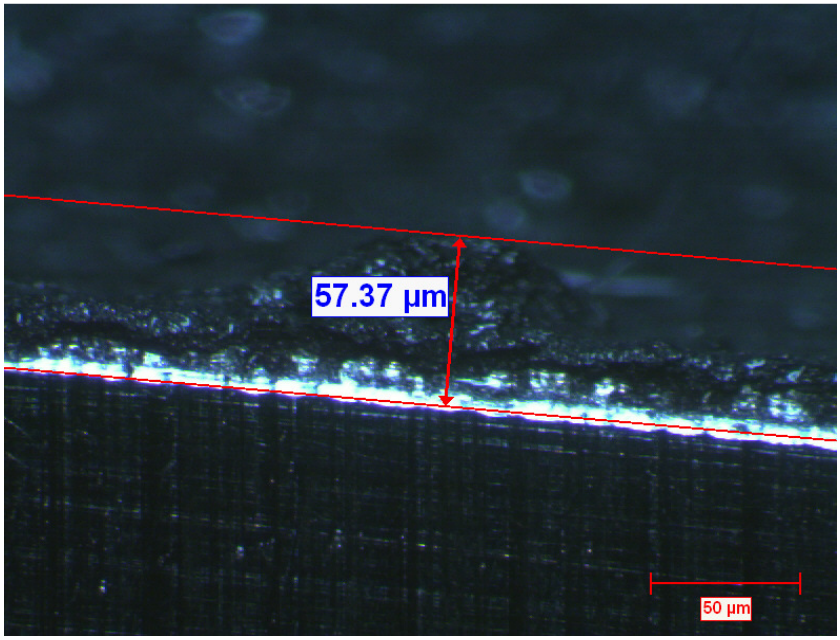

Figure 6.15: Magnified view of the build-up on the wall of the nozzle.

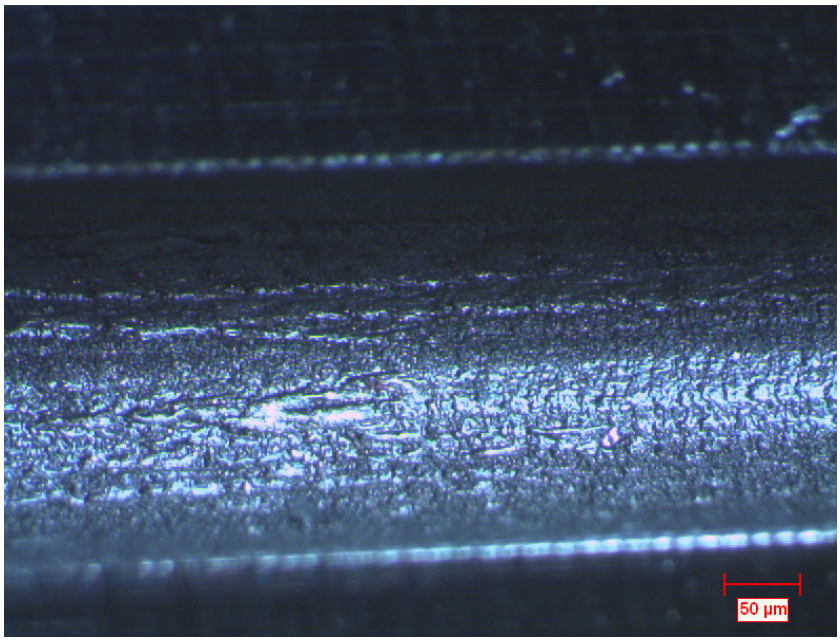

Figure 6.16: Magnified view of the fouled nozzle interior.

6.4. Solution to Nozzle Clogging

In an attempt to reduce the clogging in the nozzle, it was concluded that the nozzle should be constructed of a hard material less likely to deform under particle impact. Machinable ceramics were investigated as a potential nozzle material but were found to be

unsuitable due to their reaction to coating trials and the difficulty in using the “sandwich” technique since welding is not an option. The approach taken was to construct a nozzle from 310 stainless-steel and coat the interior with tungsten carbide. The tungsten carbide coating will increase the hardness of the nozzle while the use of stainless steel will allow for good machinability and the ability to weld the two sections together. A second SolidWorks model was constructed with increased tolerances to account for the coating thickness. The profile was machined into stainless steel bars and sent to Vac Aero International Inc. (Boucherville, Québec, Canada) for coating via the HVOF process. The coated nozzle sections are presented in Figure 6.17 to Figure 6.20.

Figure 6.17: View of coated nozzle

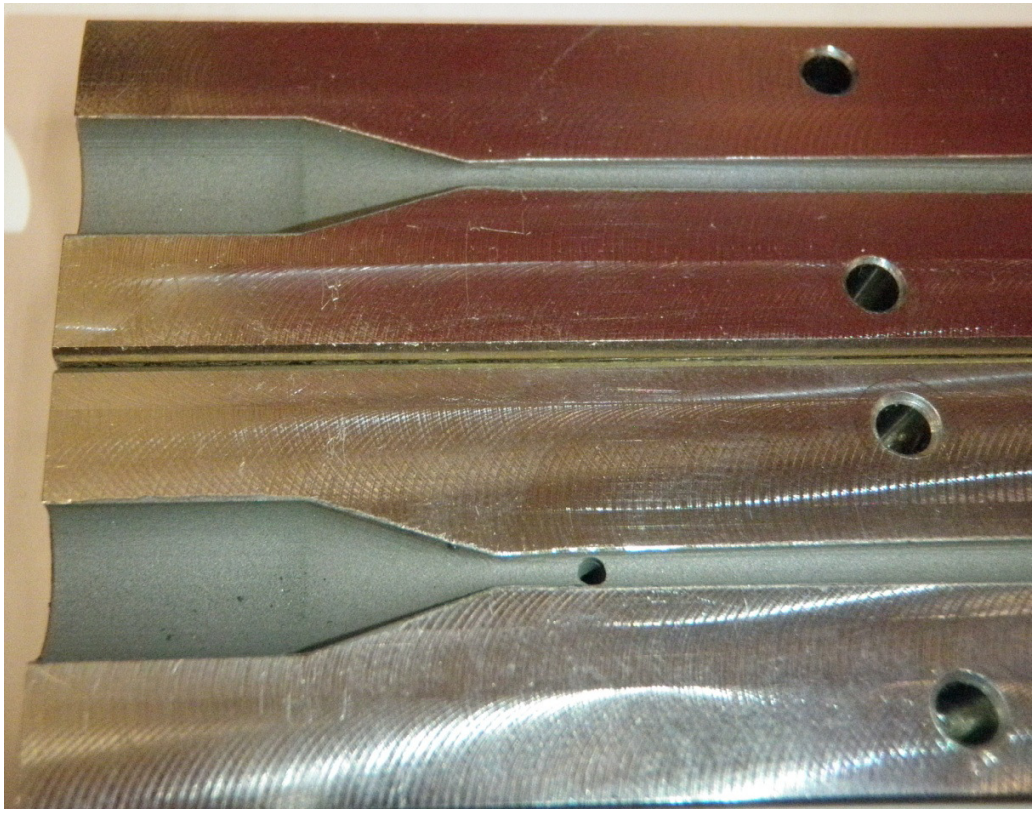

Figure 6.18: Detailed view of coated nozzle: throat area

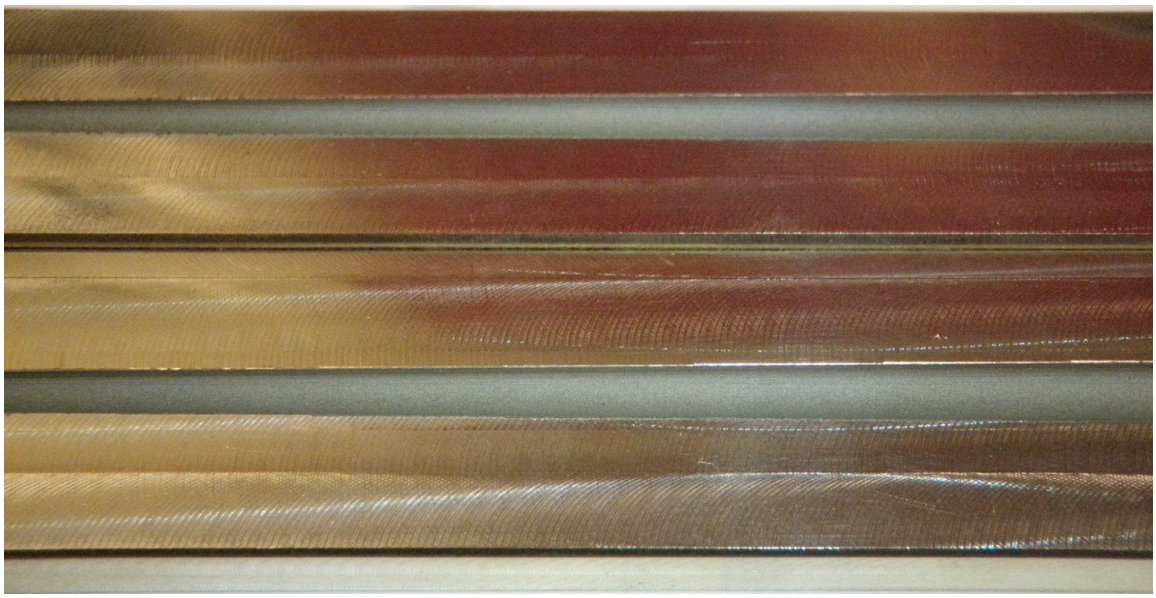

Figure 6.19: Detailed view of coated nozzle: downstream from throat

Figure 6.20: Detailed view of coated nozzle: nozzle exit

6.5. Nozzle Manufacturing and Testing Summary

The nozzle designed in this study was successfully manufactured using a CNC mill to machine half of the nozzle profile onto two metal plates. The plates were then assembled using a sandwich technique to form the full nozzle. Coatings were successfully produced using this nozzle. However after several sprays, coating quality was found to have significantly decreased. Upon further investigation, it was determined that nozzle clogging was responsible for the low quality coatings. A version of the nozzle was then designed in which the nozzle profile was coated with tungsten carbide to limit nozzle clogging.

Although the fouling issues posed problematic for long-term spraying, the CGDS bond coats produced using the un-coated nozzle were deemed of acceptable quality for this study. The coated nozzle solution was manufactured after the completion of the bond coat oxidation experiments and its durability and performance has yet to be tested.

Chapter 7 - Characterization of Feedstock Powders

The CoNiCrAlY powder used in this study were characterised to determine the specific powder structure and properties prior to coating deposition. The analysis using SEM, XRD and TEM was conducted by Richer [**121**] as part of the initial stages of this research project. These findings were confirmed through additional SEM and XRD analysis.

The CoNiCrAlY alloy has a nominal composition of Co-32Ni-21Cr-8Al-0.5Y (wt. %) and is manufactured through spray atomization. The spherical powder particles are available in two different size ranges (Sulzer Metco): AMDRY 9951 (5-37μm) and AMDRY 9954 (11-62μm). An image of the two powders is presented in Figure 7.1. Analysis of the powder size distribution indicates it falls in the ranges specified by the manufacturer.

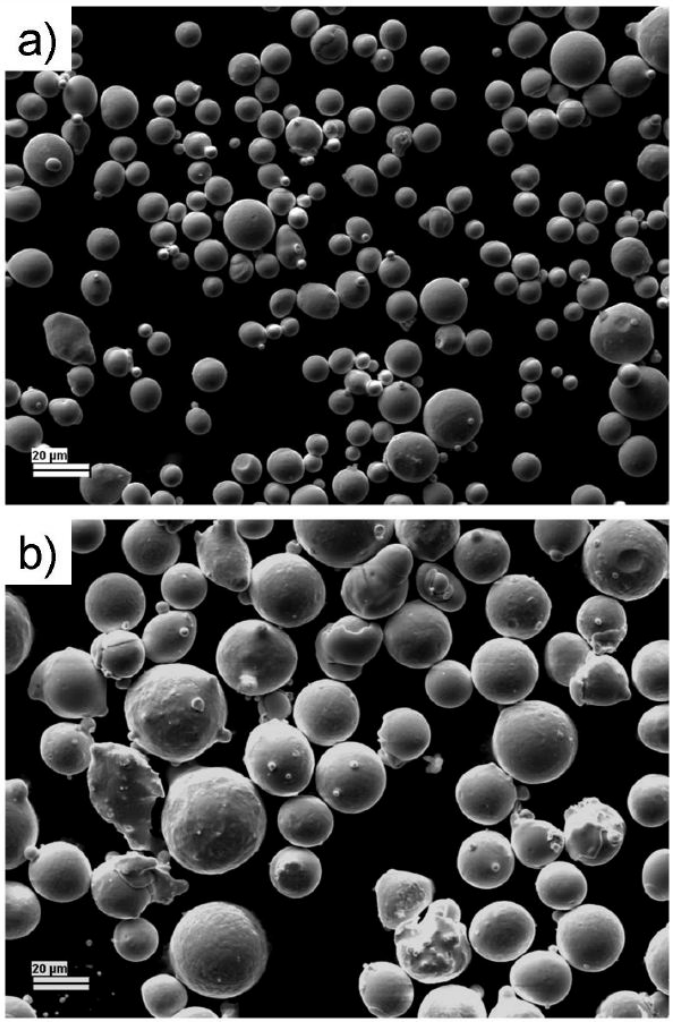

Figure 7.1: SEM images of the as-received CoNiCrAlY powders showing a) the AMDRY 9951 and b) the AMDRY 9954[121]**.**

Upon examination of the cross-section of an AMDRY 9951 powder particle, the two-phase γ/β structure typical of MCrAlY materials is apparent. An image of the cross section is presented in Figure 7.2. The light grey area observed corresponds to the γ-matrix while the darker precipitates correspond to the β-NiAl phase. EDS analysis revealed the powder oxide content to be 0.03±0.03 (wt. %).

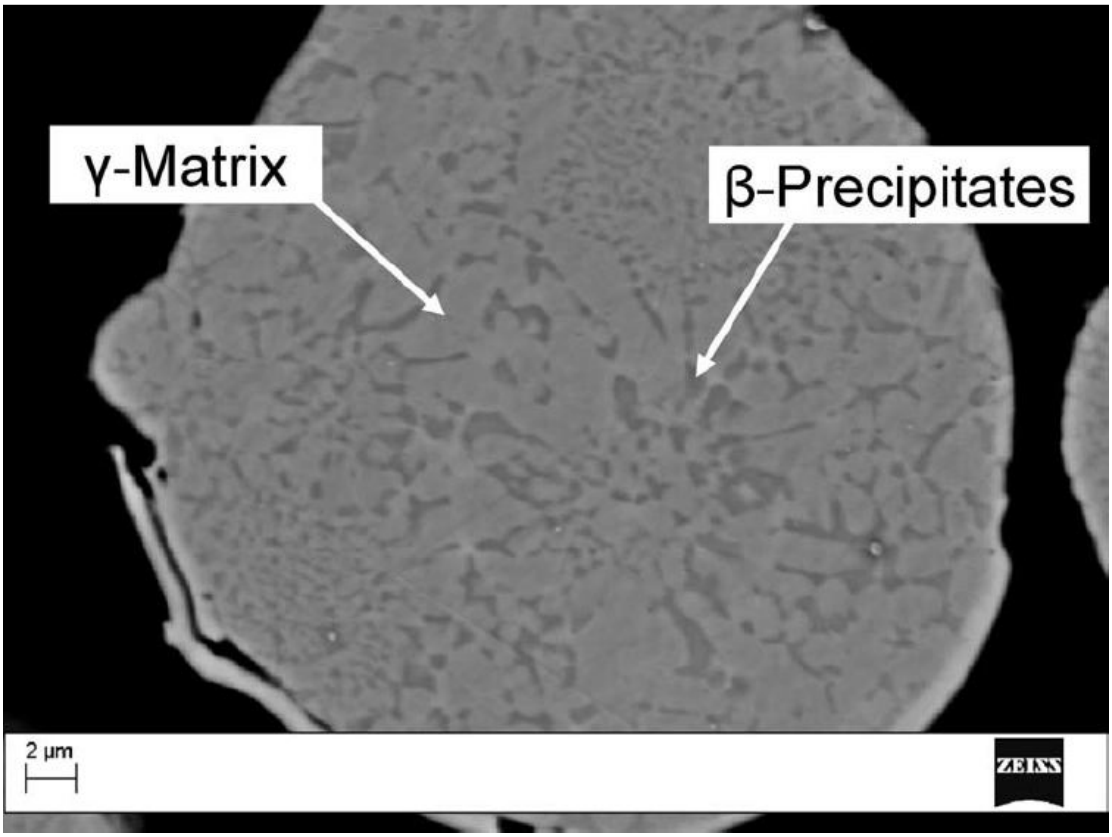

Figure 7.2: Cross-section of as-received CoNiCrAlY particle showing two visible phases [121**].**

XRD analysis was conducted on both the AMDRY 9951 and AMDRY 9954 powders to identify phase composition and determine any differences between the powders. The XRD scans were conducted with a step size of 0.01° and a step time of 2 seconds with 2θ values ranging from 20° to 85°. All XRD analysis conducted by Richer [**121**] used these parameters while XRD analysis conducted for this study used a step size of 0.01°, a step time of 2 seconds with 2θ values ranging from 25° to 79° in order to reduce the time required for each analysis. This reduction in 2θ values is justified as no significant peaks have been observed in the rages of 20° to 25° and 79° to 85°. Results of the XRD analysis of the two powders are displayed in Figure 7.3.

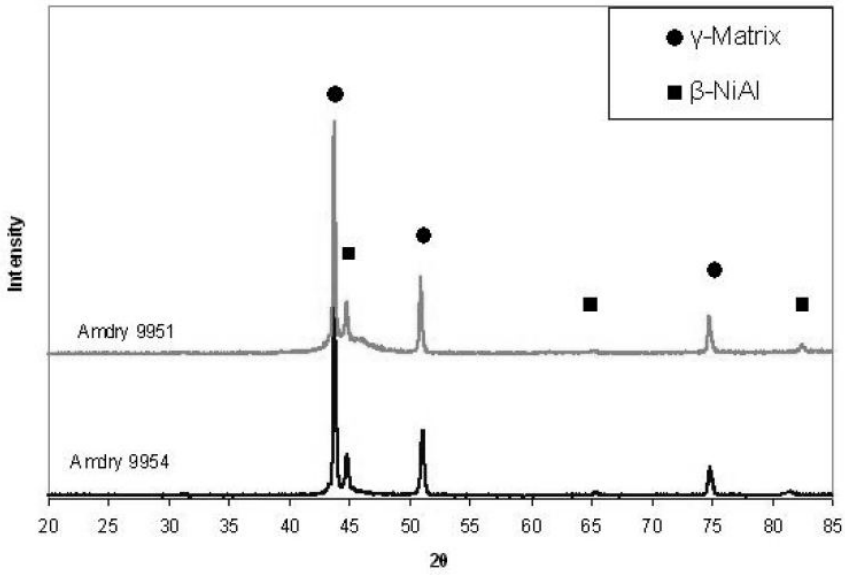

Figure 7.3: XRD spectra of AMDRY 9951 and AMDRY 9954 CoNiCrAlY powders [121]**.**

The XRD analysis revealed peaks associated to an fcc γ-matrix consisting of a Co-Ni-Cr solid solution. The presence of a second phase with weaker peaks is also identified as a NiAl bcc β-phase. A small broad peak under the largest β-phase peak is identified in the AMDRY 9951 powder but not the AMDRY 9954 powder, this suggest it is due to the presence of very fine particles (5-11μm). The powder was produced using spray atomization which can lead to fast particle solidification and cooling rates. Due to the small particle size, rapid cooling could lead to the presence of an amorphous structure. This would explain the presence of this broad peak in which is found in the finer powder (AMDRY 9951) but not the coarse one (AMDRY 9954).

Chapter 8 - Characterization of As-Sprayed CoNiCrAlY Coatings Manufactured by Various Deposition Techniques

The morphologies of coatings deposited via the APS and HVOF process will be compared to those deposited via CGDS with the nozzle designed in Chapter 4 -and manufactured as detailed in Chapter 5 -. The quality of the as-sprayed coatings will be investigated by characterizing the morphology (structure, porosity, defects and oxide content) as well as the microstructure (phase composition and grain structure).

8.1. CGDS Coatings

The coating cross-section of the as-sprayed CGDS coatings can be seen in Figure 8.1. The coating has very little porosity and no visible defects and appears to be of high quality. Porosity measurements on this coating resulted in an average porosity of 0.6±0.2% which is lower than the results obtained by Richer [**121**] of 1.0±0.3% indicating the CGDS nozzle is functioning as designed. The pores observed in the coating are typically small in diameter and are likely due to certain particles having low velocity resulting in insufficient plastic deformation. Using a slower substrate traverse speed, impinging particles could increase the plastic deformation and result in lower coating porosity. EDS analysis of the coating revealed an oxide content of 0.10±0.2 (wt. %)[**121**]. Comparing this to the oxide content of the original feedstock powder of 0.03±0.2 (wt. %)[**121**] indicates that very little oxidation occurs during the CGDS process.

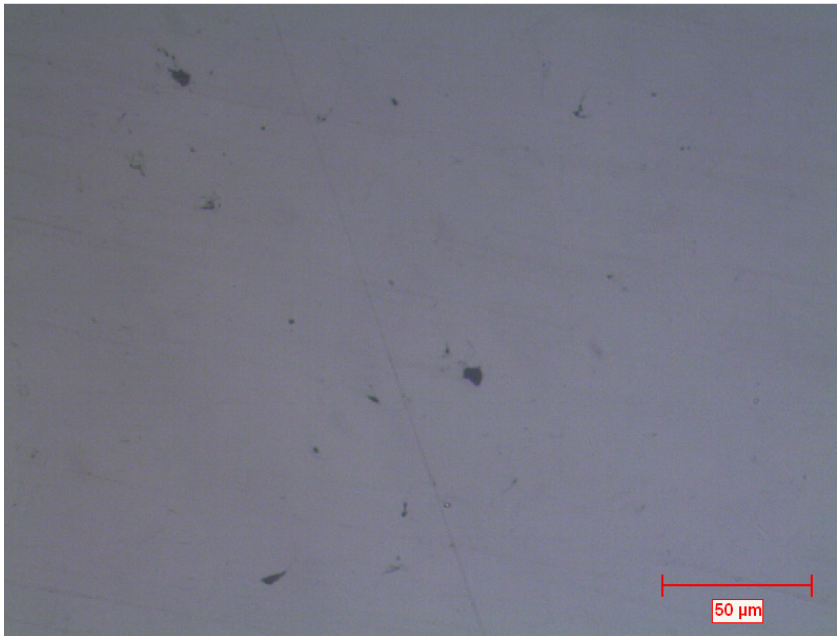

Figure 8.1: View of CGDS CoNiCrAlY cross-section

The γ/β phase microstructure that was observed on the original feedstock powder particles has not been retained in the CGDS coating. This has been attributed to grain refinement and the dissolution of the β-phase precipitates into the γ-matrix due to severe plastic deformation as was investigated by Richer [**121**] after analysis via XRD and TEM. The coatings obtained in this study are therefore very similar to those in the previous study [**121**] but feature 40% less porosity.

8.2. APS Coatings

Cross-sectional images of the CoNiCrAlY coatings deposited via APS using the AMDRY 9954 powder are available in Figure 8.2.

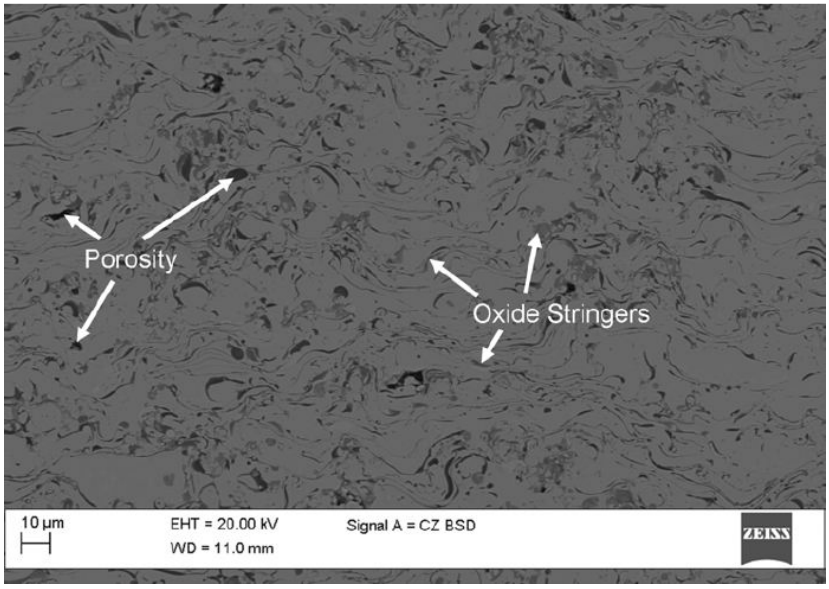

Figure 8.2: Cross-section view of APS CoNiCrAlY coating [121].

Visual investigation of the coatings via microscope shows it exhibits large amounts of porosity and inter-splat cracking. The average porosity of the APS coating was measured to be 5.3±0.5% which is significantly higher than the CGDS coating. The increase in defects is attributed to the melting and rapid solidification of molten material. As the molten material cools, it shrinks and contracts which can result in cracks and porosity in the coating. Larger particles also require more heat to melt and may not be fully melted upon impact which would result in insufficient plastic deformation and increased porosity. Oxide stringers are visible in the coating microstructure and are attributed to in-flight oxidation of the particles. EDS investigation of the coating evaluated the oxide content at 3.82±0.70 (wt. %) indicating the coating process severely increases the oxides in the coating.

The APS coatings also show no sign of β-phase precipitates suggesting that either microstructural transformations occurred during the deposition process or that oxidation of the coating has led to a reduction in non-oxidised Al, which is found in large quantities in the β-phase. XRD analysis of the APS coating revealed the presence of mixed oxides notably $NiCr_2O_4$, Cr_2O_3, $CoAl_2O_4$ and $NiCo_2O_4$. The extensive oxidation of the APS coating explains the finding of these mixed oxides and the absence of the β-phase. An XRD analysis of the as-sprayed APS coatings is presented in Figure 8.3.

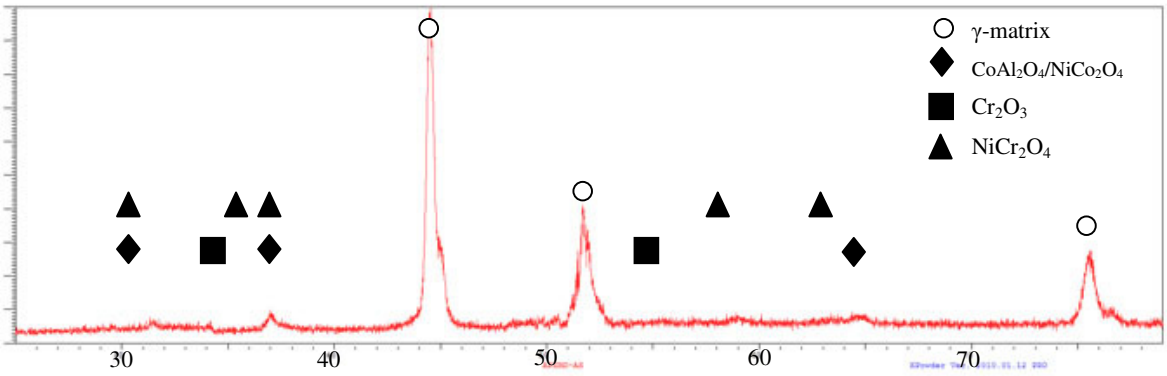

Figure 8.3: XRD analysis of as-sprayed APS coating

8.3. HVOF coatings

Cross-sectional images of the CoNiCrAlY HVOF coatings manufactured using the AMDRY 9954 powder are presented in Figure 8.4.

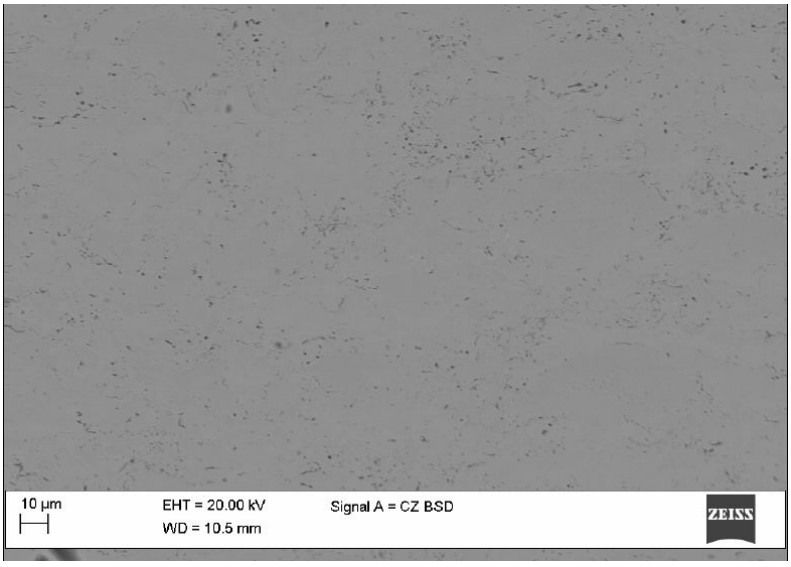

Figure 8.4: Cross-section view of HVOF CoNiCrAlY coating[121].

Visual investigation of these coatings shows very little porosity and no visible cracks. The average porosity of the coating was measured to be 0.5±0.1% which is slightly lower than the CGDS coating and significantly lower than the APS coating. The coating process therefore exhibits sufficient particle deformation and should be comparable to the CGDS coatings in this study. The HVOF coatings were also found to have a low oxide content of 0.75±0.23 (wt. %) through EDS measurements. This oxide content is significantly lower than

the APS coatings but much higher than the CGDS coatings and is attributed to the high process temperatures.

The γ/β structure was also not retained in this coating after the deposition process. The absence of the β-phase in this coating was explained by Richer [**121**] as the same phenomenon found in the CGDS coating: dissolution of the β-phase due to severe plastic deformation. The HVOF process in this study features low oxide content which indicates the process had higher particle velocities and lower particle temperatures than typical HVOF coatings found in literature.

XRD analysis was conducted on the as-sprayed HVOF coatings to investigate the phases formed during the spray process. The XRD analysis of the HVOF coating reveals that it is very similar to the CGDS coating in phase composition as analysed by Richer[**121**] likely due to the severe plastic deformation of the process. The XRD analysis is presented in Figure 8.5.

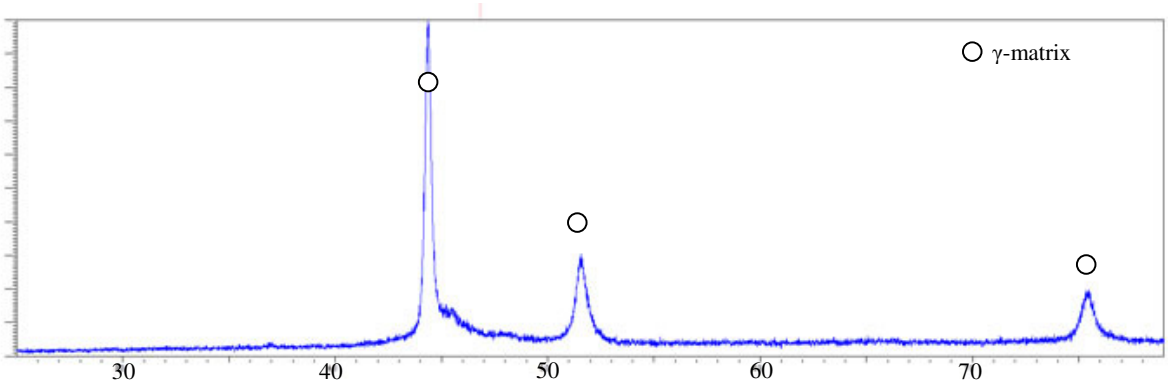

Figure 8.5: XRD analysis of as-sprayed HVOF coating.

8.4. Summary

The average porosity level and oxide content of the coatings as well as the feedstock powder are summarised in Table 8-1.

Table 8-1: Summary of as-deposited coating properties

Material	Coating porosity (%)	Oxide content (wt.%)
Feedstock powder	N/A	0.03±0.03
CGDS coating	0.6±0.2	0.10±0.05
HVOF coating	0.5±0.1	0.75±0.23
APS coating	5.3±0.5	3.82±0.70

The CGDS and HVOF coatings exhibit the most desirable structure with the CGDS having slightly higher porosity and the HVOF having more oxide content. The APS coating is the least favourable of the three with high coating porosity and oxide content. The CGDS and HVOF coatings show very little visible defects when compared to the APS coating further reinforcing the high quality of the CGDS and HVOF coatings.

The coating microstructure in all cases indicated the absence of the β-phase observed in the original feedstock powder. This was attributed to a high degree of oxidation in the APS coatings and to severe plastic deformation of the CGDS and HVOF coatings leading to dissolution of the β-phase. Finally, the HVOF coatings were found to be more similar to CGDS coatings than typical HVOF coatings found in literature due to severe plastic deformation and low particle oxidation.

Chapter 9 - Oxidation Behaviour of CoNiCrAlY Bond Coats Manufactured by Various Deposition Techniques

The experimental results obtained from the oxidation of the CoNiCrAlY bond coats deposited in this study will be presented in this section. The oxidation tests were conducted in three series of trials. All oxidation experiments were carried out in an air furnace at 1100°C. In the first series, coatings deposited via CGDS, APS and HVOF are analysed to determine the initial oxidation growth rate and oxide scale composition. This series begins with the as-sprayed coatings up to 100h of oxidation time which is thought to be the time at which the initial oxidation stage ends. The second series of trials analyses the oxidation behaviour of non-grinded APS and HVOF bond coats. This is to analyse the effect of the grinding step used in the previous trials. The third series of trials analyses the oxidation behaviour of APS and HVOF, grinded and non-grinded bond coats after the initial oxidation stage, during the expected useful lifetime of the coating. This series begins at 100h of oxidation and continues until coating failure or 2000h of oxidation time, whichever comes first. The oxide growth rates and scale composition will then be compared with results obtained at an oxidation temperature of 1000°C as was conducted by Richer in the previous study[**121**].

All oxidation experiments are carried out in the same manner. All samples were grinded on both sides prior to oxidation with 320-grit SiC paper. The grinding step is conducted to obtain a constant surface roughness as well as remove any surface oxides caused by the deposition process. The presence of oxides at the surface of the coating is caused by the high-temperature exposure to ambient oxygen immediately after the deposition process. This oxide layer is thought to be detrimental to the long-term oxidation process of the coatings. Removal of this oxide layer is important in order to understand the intrinsic TGO formation process. However, the removal of this oxide layer also introduces an extra grinding step which increases manufacturing costs. In order to quantify the increase in performance offered by the extra grinding step, a set of samples were only grinded on the substrate side. Samples are carefully weighed and measured using a digital weighing scale (Sartorius Extend model ED124S) and a digital vernier calliper with proper cataloguing of data. Samples are then placed in a high temperature air furnace for varying soak times. Once

a soak time is completed, the samples are removed from the air furnace and left in ambient air to cool. The samples are then weighed again and the data catalogued. To ensure accuracy, each sample is weighed three times at each data point. The samples are then either placed in the oven for the next soak or processed for surface or cross-sectional analysis. The oxidation process is a surface phenomenon and therefore depends on the exposed surface area of the sample to the high temperature oxygen. The mass gains are therefore normalised for each sample according to the sample surface area. The surface area associated to roughness and porosity was assumed to be negligible. Multiple samples are oxidised and weighed and their average mass gain per unit area is used (the exact number will be specified in each subsection). Error bars were added to represent the standard deviation between samples and the average. Data points are linked by lines for clarity purposes only.

Samples were processed at each soak time to investigate the oxide scale composition and morphology through a combination of XRD, EDS, SEM and BSE analysis. These techniques are used to identify the phases and oxide morphologies that emerge on the coating as well as identification of their composition through elemental mapping. For the XRD analysis, a sample was specifically chosen to undergo all XRD analyses throughout the oxidation steps in order to maintain a consistent oxide evolution. To perform analyses via EDS, SEM and BSE, a sample was removed after the soak, weighed and then cut in half. The first half of the sample was then analysed via SEM and EDS for images of the surface oxide morphology and elemental mapping of the surface. The other half of the sample was mounted in resin and grinded for analysis of the cross-section via SEM and BSE. The cross-sectional analysis provides an overview of the behaviour of the coating interior as well as the thickness of the oxide scale.

9.1. Initial oxidation experiments

The initial oxidation experiments are conducted to assess the initial formation stages of the oxide scale. Soak times of 1, 5, 25, 50 and 100 hours were chosen in order to give a good overview of the oxidation dynamics during this stage. Samples oxidised at 1000°C by Richer[**121**] are also included for comparison purposes. It should be noted that no data point was available at 1000°C for 1hour oxidation time.

9.1.1. Oxide growth rates

The oxide growth rate results are depicted in Figure 9.1. All data points are the average of 5 samples.

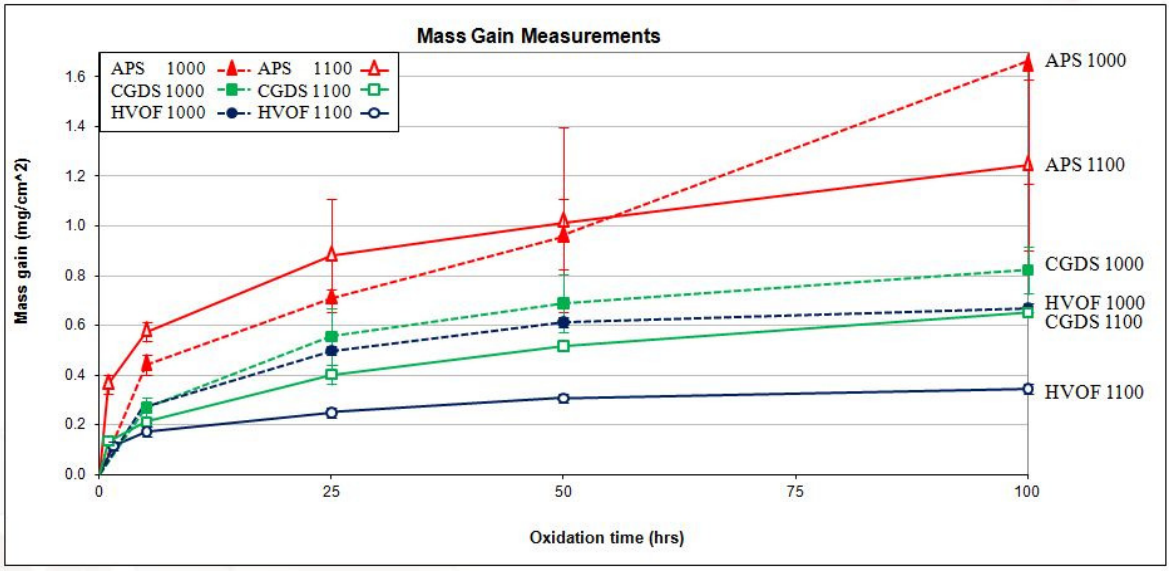

Figure 9.1: Mass gain measurements as a function of oxidation time at 1100°C for CoNiCrAlY coatings deposited by CGDS, HVOF and APS up to 100h.

Of the three deposition techniques considered in this study, the HVOF coating exhibits the lowest overall oxide growth followed closely by the CGDS coating while the APS coating exhibits the highest initial oxide growth rate. The CGDS and HVOF samples also have much narrower error bars indicating the coating quality is consistent throughout all samples. In the case of APS however, the error bars are quite large which indicates a large variation between samples. The oxidation behaviour of APS samples will therefore be less predictable than the other coating methods thus making it less suitable for in-service components.

Comparing the mass gain results obtained at 1000˚C with the results at 1100˚C, the HVOF and CGDS samples show significantly less mass gain at 1100˚C. The CGDS coatings oxidised at 1100°C seem to have an increased mass gain rate between 50h and 100h when compared to those oxidised at 1000°C. In the case of the APS samples, mass gain is higher at 1100˚C for the first 50h but the mass gain-time slope from 50h to 100h is significantly lower and the samples exhibit lower overall mass gains at 100h. The mass gain curves also exhibit a logarithmic type growth in all cases which indicates the rate of mass gain past 100h will be

very slow. The samples oxidised at 1100˚C appear to reach the slow-growing stage more rapidly than the samples oxidised at 1000˚C. It should be noted that a comparison of the APS and HVOF samples of this study with those found in literature was conducted by Richer [**121**] and indicated that the coatings used in this study are of particularly high quality. The mass gain of samples used in this study are compared with HVOF samples oxidised by Saeidi *et al.*[**133**] and Shibata *et al.*[**112**] in Figure 9.2.

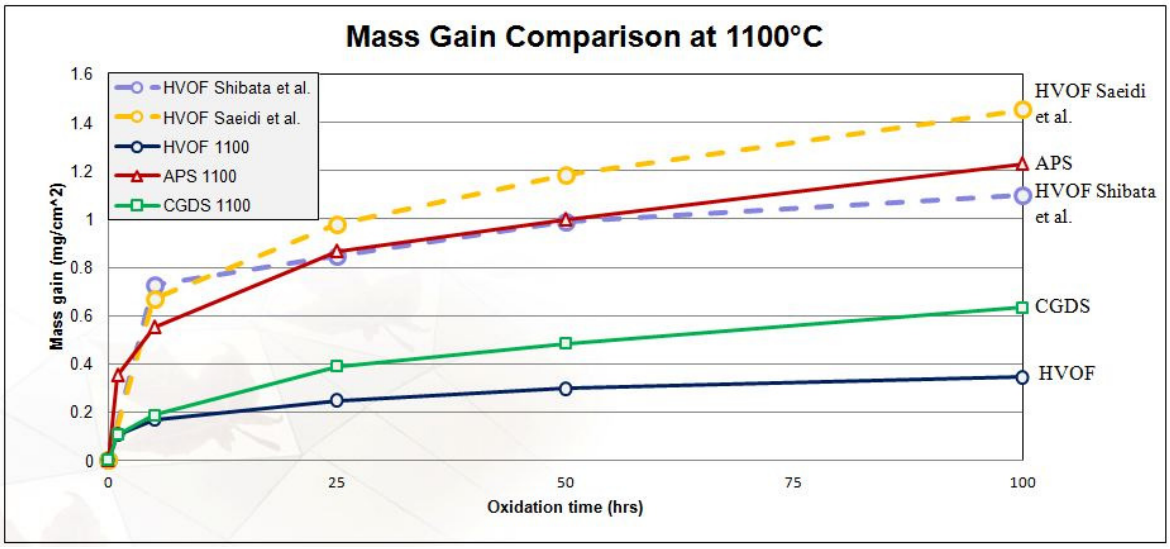

Figure 9.2: Comparison of mass gain of HVOF, CGDS and APS oxidised at 1100°C with HVOF samples of Saeidi et al. and Shibata et al. oxidised at 1100°C

Although the CGDS coatings exhibit very similar porosity and less oxidation than the HVOF coatings, the measured mass gain is higher. This difference is thought to be caused by the presence of oxides in the HVOF coating which may accelerate the formation of an α-alumina layer and reduce further oxidation. The seeding of α-alumina particles has been previously found to decrease the transition time from θ-alumina to α-alumina [**139**,**142**]. If α-alumina was formed during the HVOF process, as has been reported by some researchers[**132**], the formation of a dense α-alumina layer could occur more rapidly on the HVOF samples than the CGDS samples and could explain the difference in mass gain. Another theory for the difference in mass gain between the two coatings is that the presence of oxides in the coating acts as obstacles for the diffusion of aluminum and thus reduces the oxide growth rate[**133**]. The oxidation process in the CGDS and HVOF samples is heavily influenced by the aluminum diffusion from the Al-rich β-phase to the surface oxide layer[**123**]. As oxidation progresses, a β-phase depletion zone can be observed on the coating

cross-section near the oxidation surface due to the aluminum diffusion. This is represented schematically in Figure 9.3.

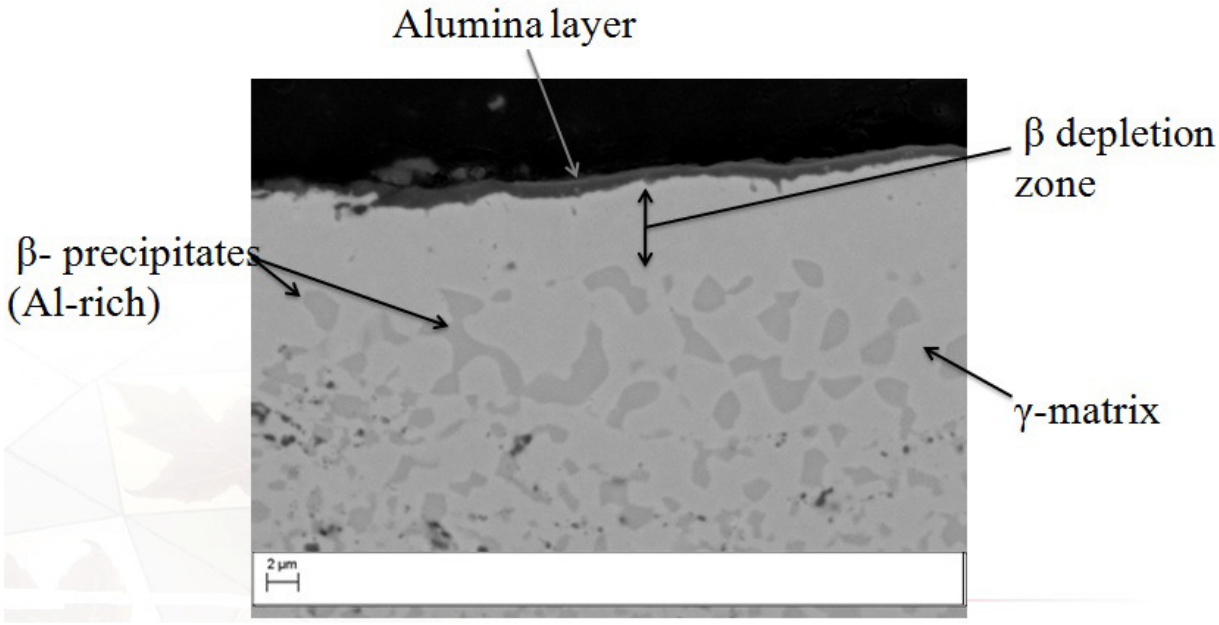

Figure 9.3: Schematic representation of oxidation process showing β-phase depletion zone.

Cross-section images of the HVOF and APS samples at 1100°C and 1000°C are presented in Figure 9.5 and Figure 9.6. Due to the similarity between the HVOF and CGDS cross-sectional images, only the HVOF samples are presented. The cross-section images of CGDS and HVOF samples oxidised at 1000°C for 100h are presented in Figure 9.4.

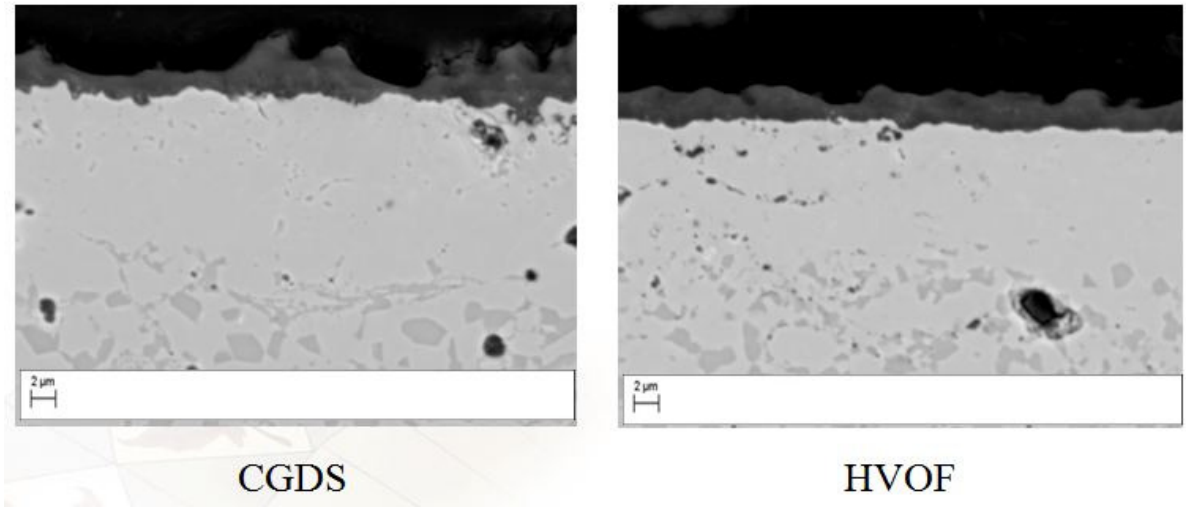

Figure 9.4: Comparison of CGDS and HVOF cross-sections after oxidation at 1000°C for 100h.

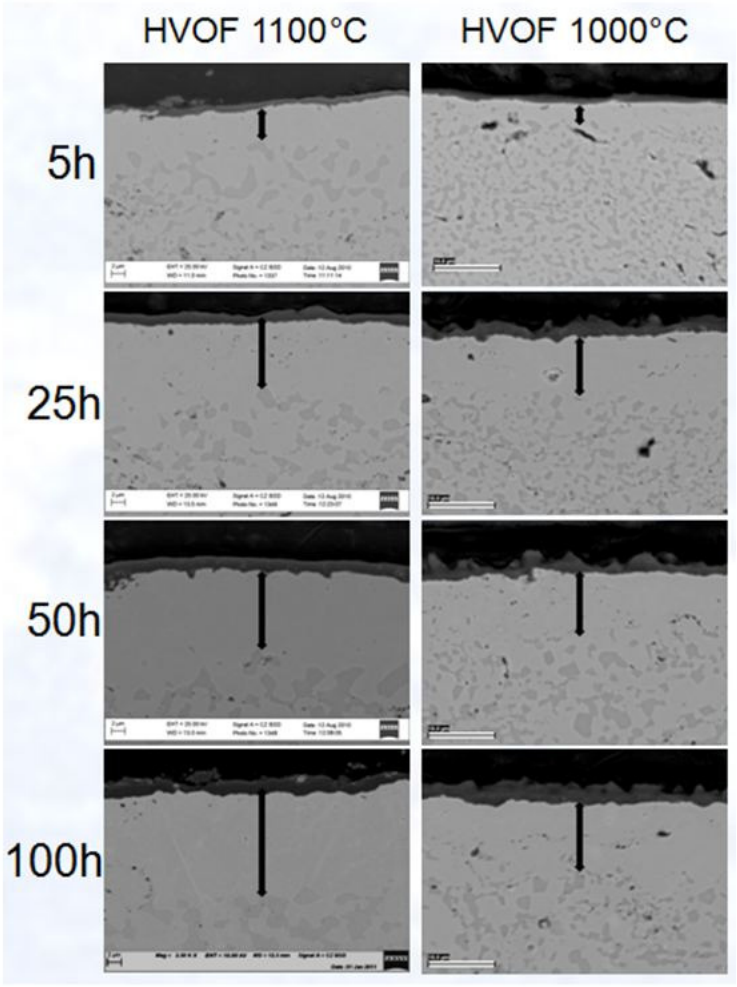

Figure 9.5: Evolution of the oxide scale and depletion zone as a function of oxidation time for CoNiCrAlY coatings manufactured by HVOF. All images were taken at the same magnification (2500x)

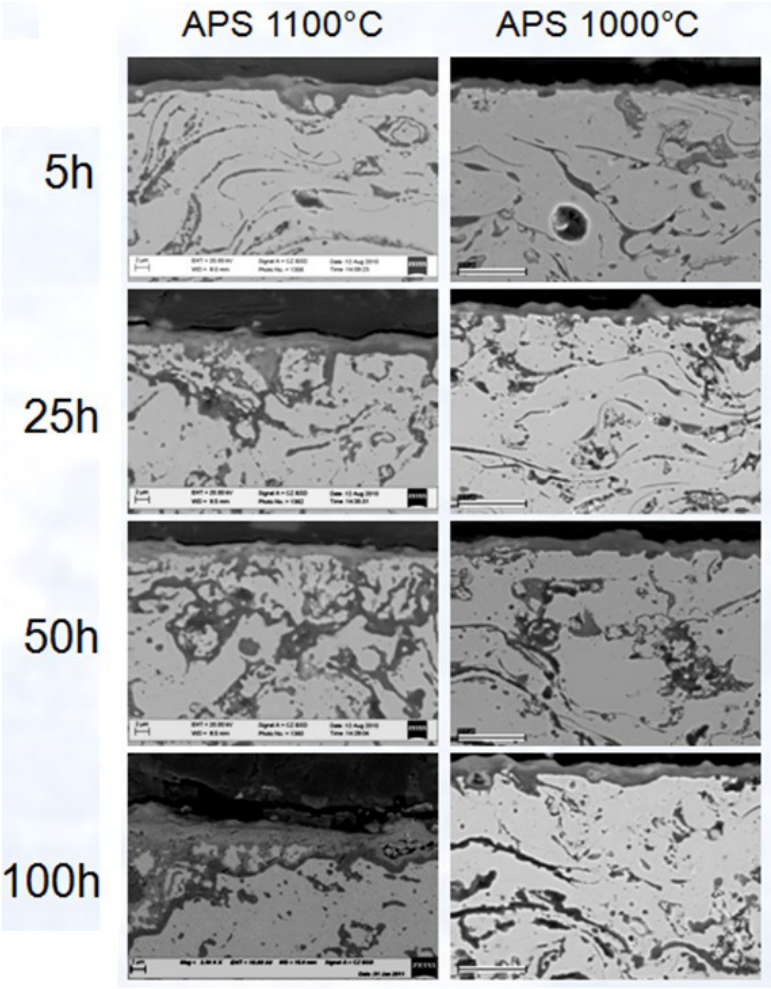

Figure 9.6: Evolution of the oxide scale and depletion zone as a function of oxidation time for CoNiCrAlY coatings manufactured by APS. All images were taken at the same magnification (2500x)

Upon examination of the cross-section images of Figure 9.5 and Figure 9.6, it can be observed that the β-phase precipitates and the β-phase depletion zone are larger on the HVOF samples oxidised at 1100°C than the samples oxidised at 1000°C. This is likely due to the increased amount of aluminum diffusing to the surface in order to form a dense α-Al_2O_3 scale. No β-phase is detected on the APS samples due to the severe in-coating oxidation caused by the spraying process.

The oxide scale on the HVOF samples oxidised at 1100°C appears to be slightly thinner than the oxide scale on the samples oxidised at 1000°C. Additionally, the oxide scale at 1100°C appears to be more uniform which is indicative of an α-alumina layer. An α-alumina scale is favourable as it is slow growing, uniform, dense and reduces further oxidation of the coating. The formation of such a layer on the HVOF samples oxidised at

1100°C would explain the lower mass growth rates as well as the lower oxide thickness and the uniformity of the oxide scale.

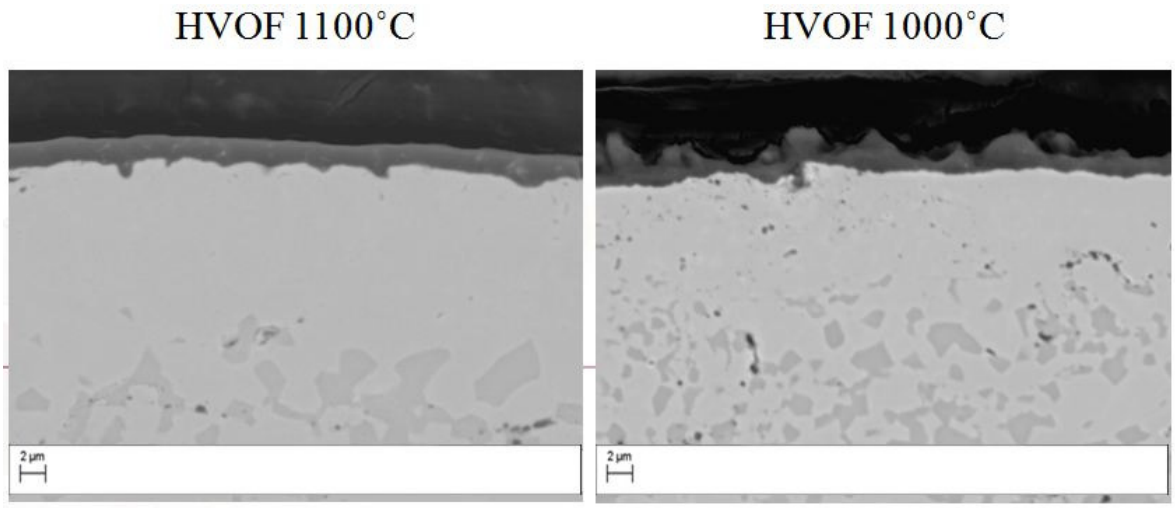

Figure 9.7: Comparison of cross-section of HVOF samples oxidised at 1100°C and 1000°C for 100h.

Upon observation of the CGDS samples oxidised for 100h and presented in Figure 9.8, we can identify a few differences between the sample oxidised at 1100°C and the one oxidised at 1000°C. As was seen in the HVOF samples, the β-phase precipitates are larger at 1100°C while the surface profile is much smoother. The β-phase depletion zone also appears to be approximately the same size at both oxidation temperatures. Certain mixed oxides can be observed in the TGO at 1100°C (lighter areas).

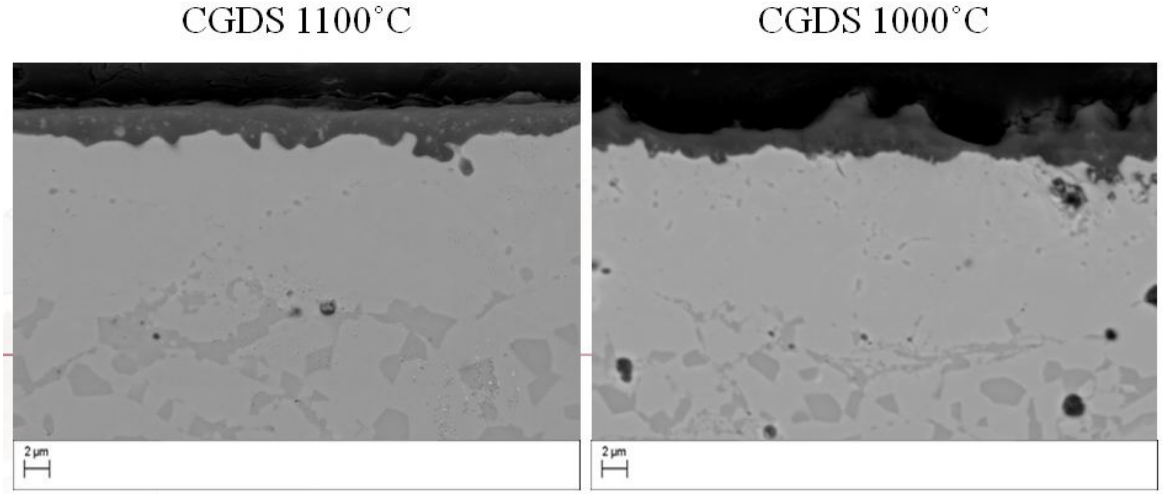

Figure 9.8: Cross section comparison of CGDS oxidised for 100h at 1100°C and 1000°C.

Upon observation of the APS samples oxidised for 100h and presented in Figure 9.8, it is very difficult to draw any differences between the sample oxidised at 1100°C and the one oxidised at 1000°C. Both samples exhibit a dual-scale oxide layer with a lighter mixed layer on top and an Al_2O_3 layer near the coating.

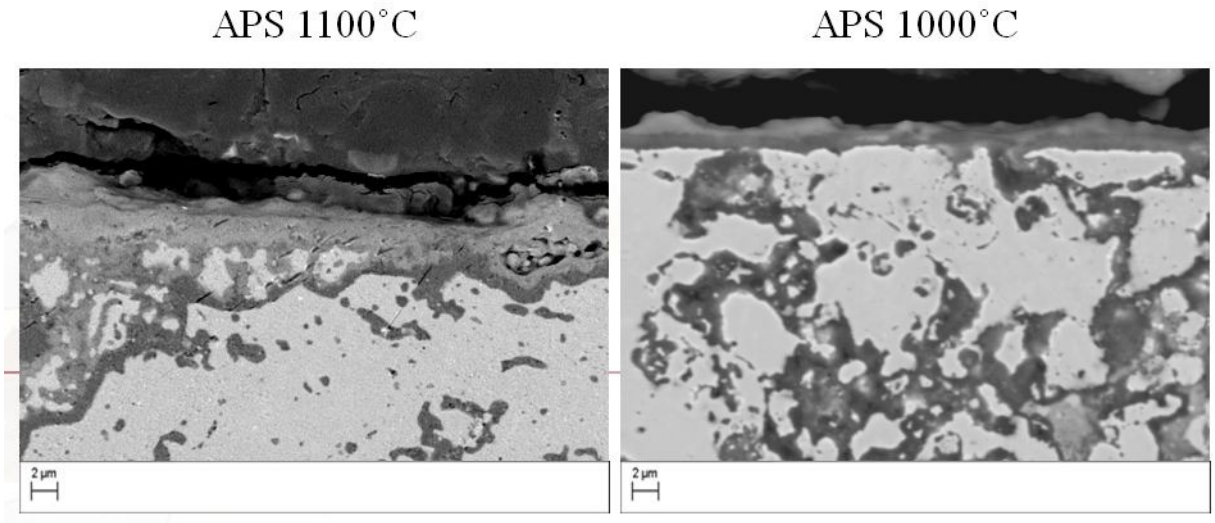

Figure 9.9: Cross-section comparison of APS oxidised for 100h at 1100°C and 1000°C

As was explained in Section 2.4.5.3, the formation temperature of α-alumina is approximately 1050°C. Oxidation of the bond coat at a temperature of 1100°C promotes the formation of α-alumina over other transition aluminas such as γ, δ or θ-alumina which are less uniform, faster growing and more porous to oxygen. The rapid formation of an α-alumina layer would lead to lower mass growth rates as well as a thinner and more uniform oxide scale which appears to be the case for samples oxidised at 1100°C. Further analysis of the oxide scale composition and morphology is conducted in the following section.

9.1.2. Oxide scale composition and morphology

The oxide scale composition and morphology was assessed through the use of XRD and EDS analysis presented in Figure 9.10 to Figure 9.22.

9.1.2.1. HVOF samples

XRD analysis of the HVOF samples indicates early formation of α-Al_2O_3, θ-Al_2O_3 and traces of γ-Al_2O_3 on both the 1000°C and 1100°C samples. However the samples at 1100°C appear to have more α-Al_2O_3 and less transition aluminas. This is consistent with the

conclusions drawn in the previous section. Throughout the various oxidation times, there are not many significant changes in peaks for the HVOF samples. This indicates the oxidation process is quite stable and oxides formed in the initial stages are maintained. After 100h of oxidation, the samples oxidised at 1000°C continue to exhibit peaks for γ-Al_2O_3, θ-Al_2O_3 and α-Al_2O_3 as well as some signs of Cr_2O_3 oxides beginning to develop. In contrast, for the samples oxidised at 1100°C the peaks for θ-Al_2O_3 have almost disappeared while those of α-Al_2O_3 remain. No other oxide is detected. The XRD spectra of the samples oxidised at 1100C are displayed in Figure 9.10 and Figure 9.11.

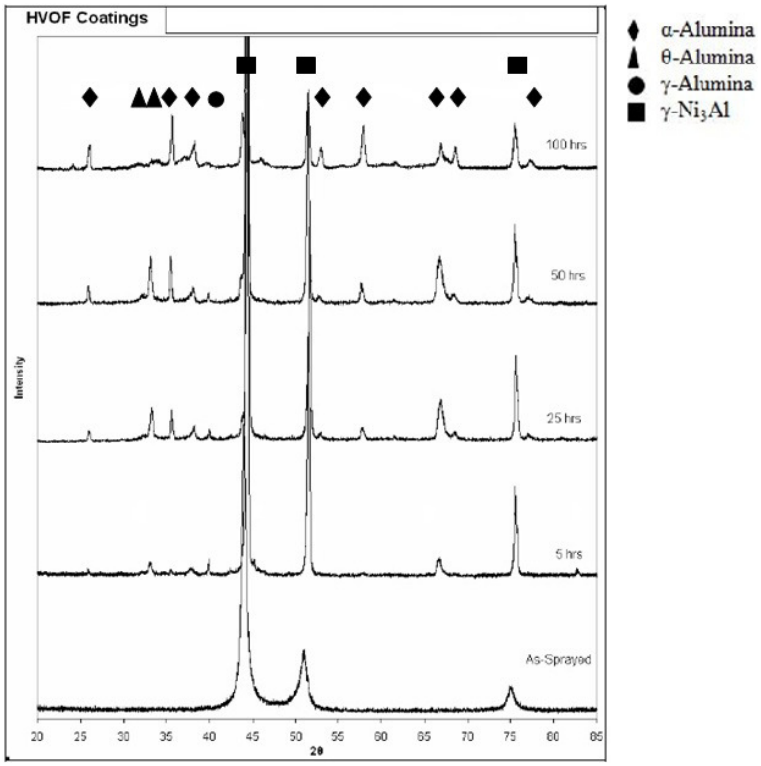

Figure 9.10: XRD spectra of HVOF coating after various oxidation times at 1000°C (adapted from[121])

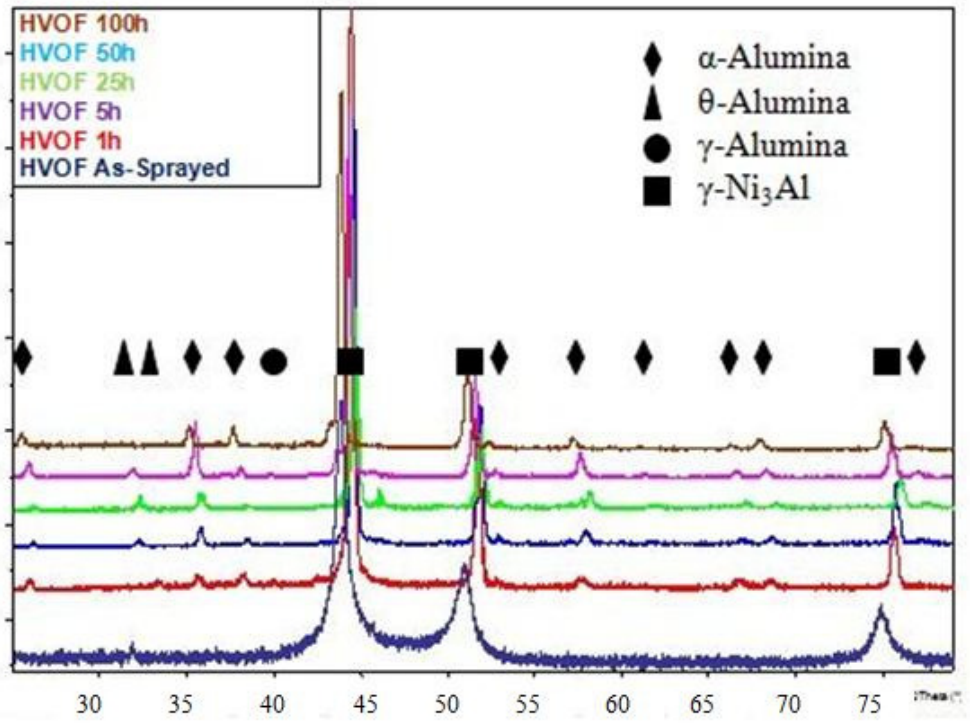

Figure 9.11: XRD spectra of HVOF coating after various oxidation times at 1100°C

As can be seen from the surface SEM image

Figure 9.12, the HVOF sample oxidised for 100h at 1100°C is mostly smooth and uniform with a few oxide protrusions. The EDS analysis reveals that the surface composition mostly consists of aluminum and oxygen with some traces of chromium, nickel and cobalt. This indicates the surface is mostly composed of alumina confirming what was previously suggested in section 9.1.1 and supported via XRD analysis.

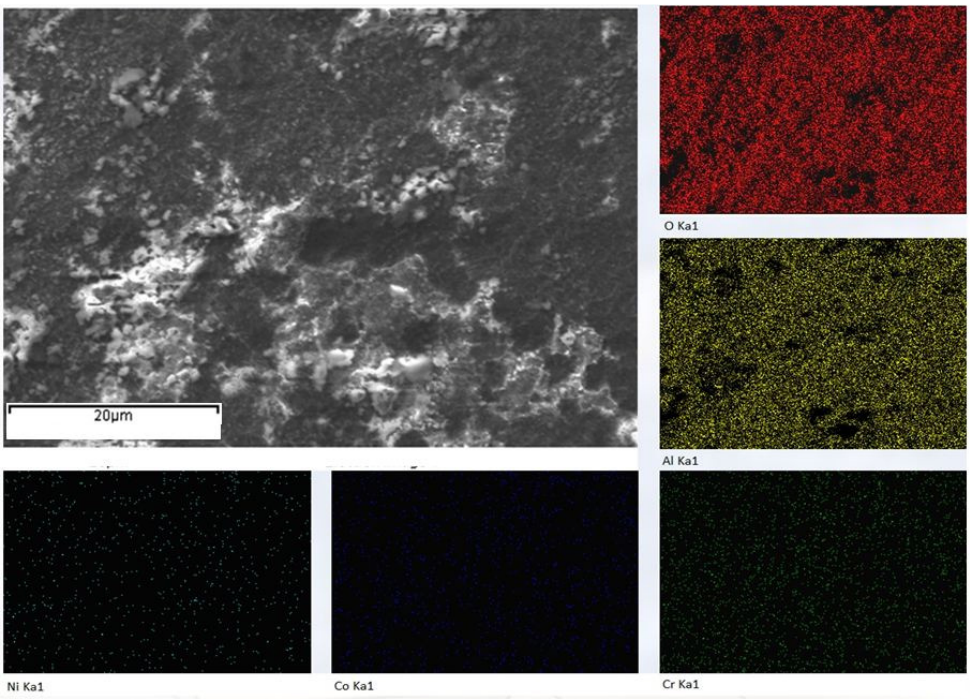

Figure 9.12: SEM image and EDS elemental mapping showing the surface oxide morphology of a CoNiCrAlY HVOF coating following 100h of oxidation at 1100°C

The samples oxidised at 1000°C Figure 9.13 show a whisker-like morphology indicative of θ-Al_2O_3. The EDS analysis indicates mostly alumina with higher traces of Co, Cr and Ni than found at 1100°C. When the EDS findings are compared to those of the XRD analysis, it is likely that the surface oxides are composed of α-Al_2O_3 and θ-Al_2O_3.

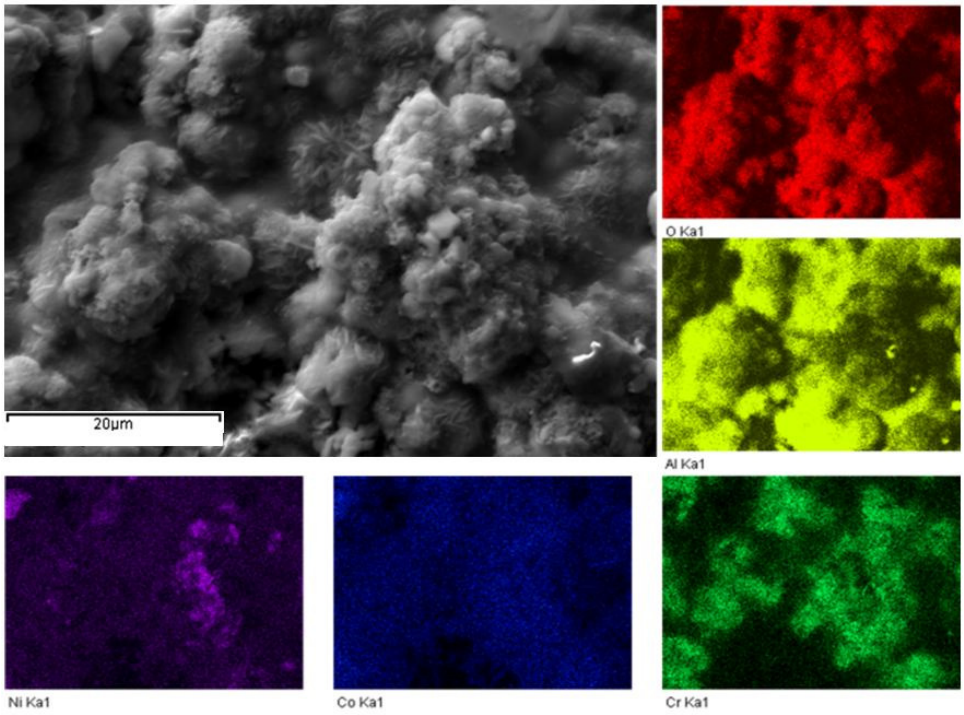

Figure 9.13: SEM image and EDS elemental mapping showing the surface oxide morphology of a CoNiCrAlY HVOF coating following 100h of oxidation at 1000°C [121]

As can be seen in Figure 9.14, the surface profile of the HVOF sample oxidised at 1100°C for 100h is much smoother than the one oxidised at 1000°C for 100h. The smooth surface profile on the sample oxidised at 1100°C indicates the presence α-Al_2O_3, while the protrusions and whisker-like morphology on the sample oxidised at 1000°C indicate mixed oxides and θ-Al_2O_3 respectively. A magnified view of the HVOF sample oxidised at 1100°C is presented in Figure 9.15.

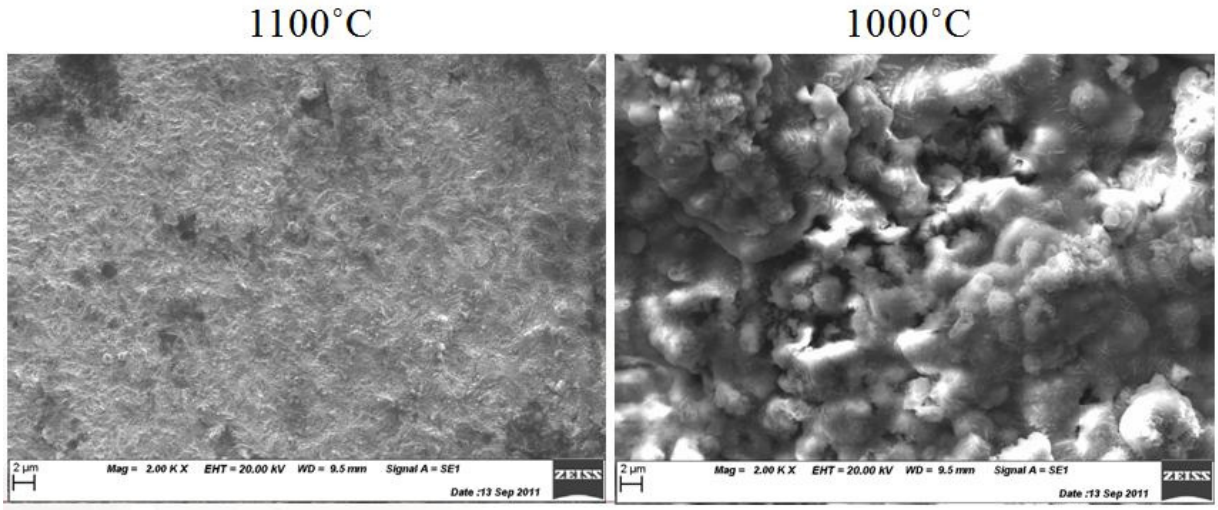

Figure 9.14: Comparison of HVOF surface profile after 100h oxidation (2000x)

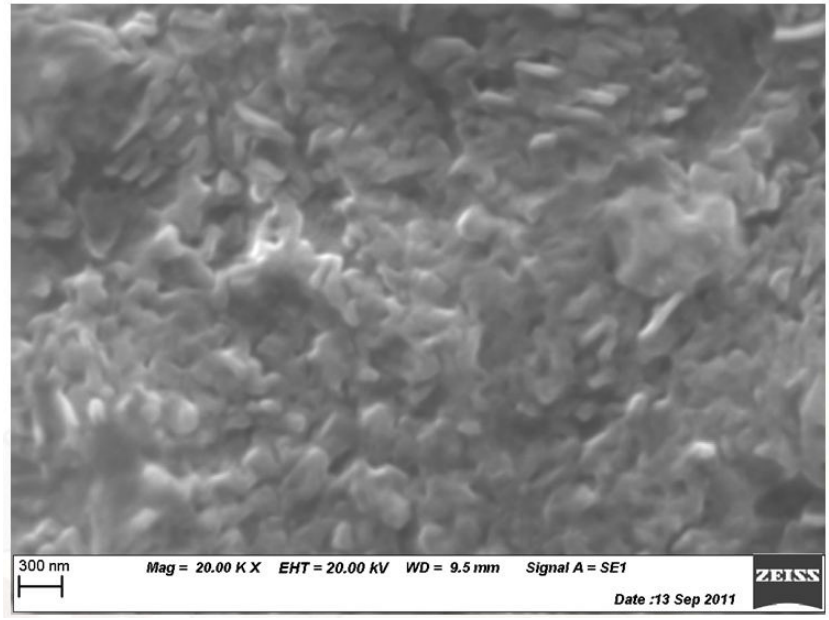

Figure 9.15: Magnified view of HVOF surface profile oxidised at 1100C for 100h (20000x).

Through XRD and EDS analysis it appears that the HVOF coatings oxidised at 1100°C form α-Al_2O_3 more quickly than those oxidised at 1000°C. The samples at 1000°C appear to be forming less protective θ-Al_2O_3 which then eventually transitions to α-Al_2O_3 leading to the distinctive θ-Al_2O_3 whisker-like oxide morphology on the surface of the specimens.

EDS elemental mapping of the cross-section of HVOF samples oxidised at 1100°C are presented in Figure 9.16. The surface oxide layer appears to be composed exclusively of

Al and O. It is interesting to note the Al-rich β-phase which are easily identified in the Al mapping and show the depletion zone that was previously identified with BSE imaging.

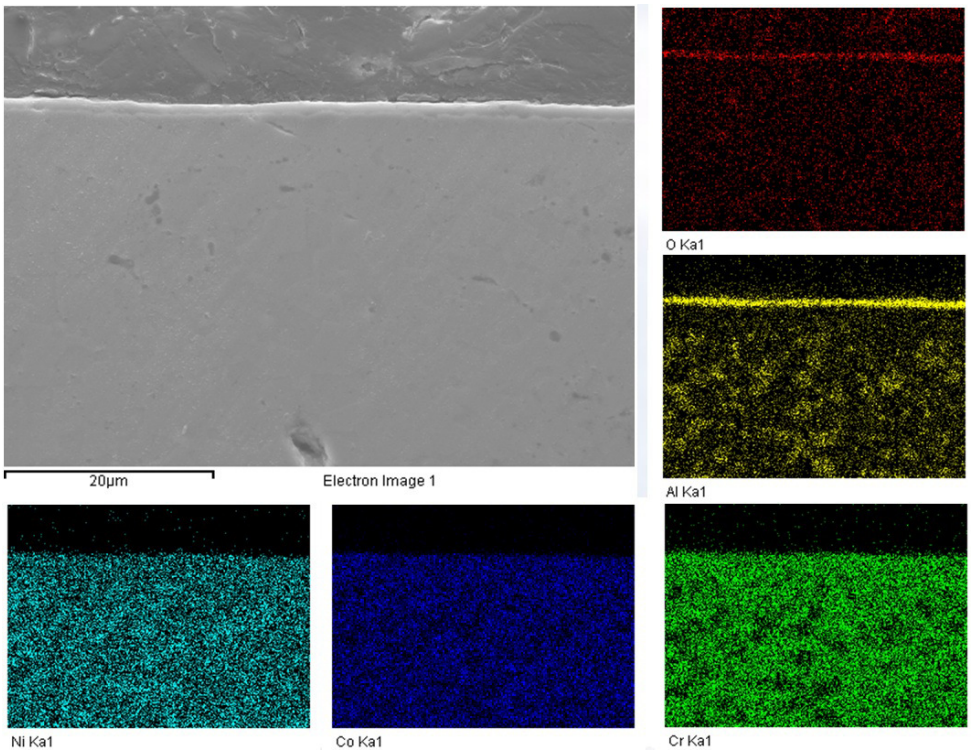

Figure 9.16 : SEM image and EDS elemental mapping showing the cross-section of a CoNiCrAlY HVOF coating following 100h of oxidation at 1100°C

In summary, the HVOF samples oxidised at 1100°C feature a lower mass gain than the samples oxidised at 1000°C due to the early formation of α-Al_2O_3. The surface profile of the sample oxidised at 1100°C is also much smoother due to the formation of α-Al_2O_3 instead of mixed oxides or transition aluminas found on the sample oxidised at 1000°C. An oxidation temperature of 1100°C is more favourable in terms of mass gain and oxide layer composition in the case of HVOF coatings.

9.1.2.2. APS Samples

The XRD analysis of the APS samples indicates the presence of multiple oxides in the as-sprayed state which could explain its poor oxidation resistance. The XRD spectra is presented in and Figure 9.18. Observing the XRD spectra of the APS samples, there is much less difference between 1000°C and 1100°C. The presence of mixed oxides is detected throughout the oxidation stages with increasing quantity as oxidation progresses. On samples oxidised at 1100°C and 1000°C early formation of θ and α-Al_2O_3 are detected as well as

minor traces of mixed oxides (spinel). The traces of mixed oxides increase as the oxidation progresses. After 100h of oxidation, the samples oxidised at 1100°C show signs of θ and α-Al_2O_3 as well as NiO and various mixed oxides. The samples oxidised at 1000°C show small signs of α-Al_2O_3, mixed oxides and Cr_2O_3 as well as large peaks for NiO. From comparison of the XRD spectra, it is clear that the APS samples offer less protection to oxidation than the HVOF samples. It appears that the APS samples oxidised at 1100°C perform better than those at 1000°C due to the smaller amount of mixed oxides, Cr_2O_3 and NiO.

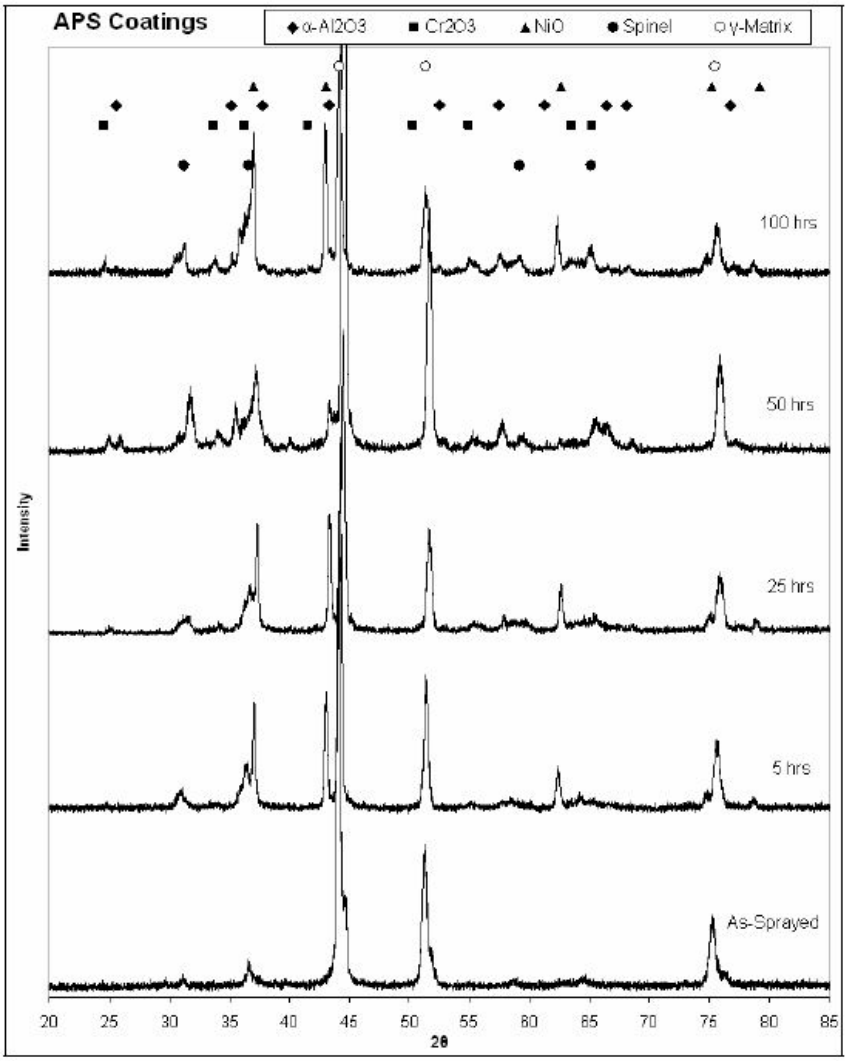

Figure 9.17: XRD spectra of APS coating after various oxidation times at 1000°C

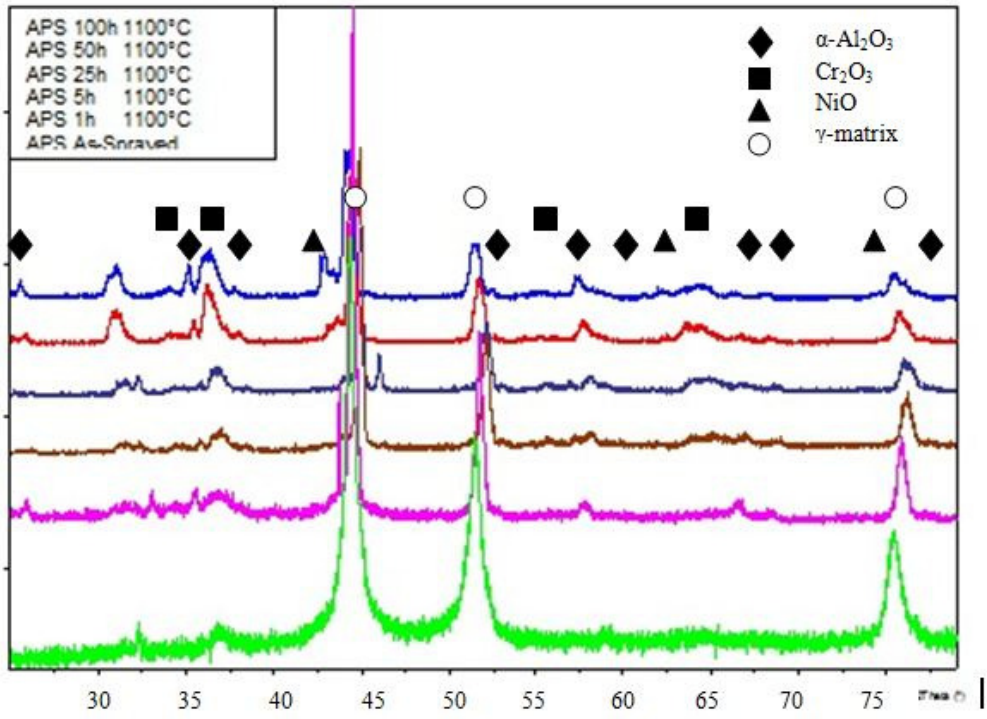

Figure 9.18: XRD spectra of APS coating after various oxidation times at 1100°C

The APS sample surface SEM image for the sample oxidised at 1100°C (Figure 9.19) reveals a much more irregular surface profile than was found for the HVOF samples. EDS analysis reveals the surface is rich in oxygen with concentrations of aluminum, chromium and cobalt and traces of nickel. This indicates that the oxide layer is partially composed of alumina with concentrations of other mixed oxides.

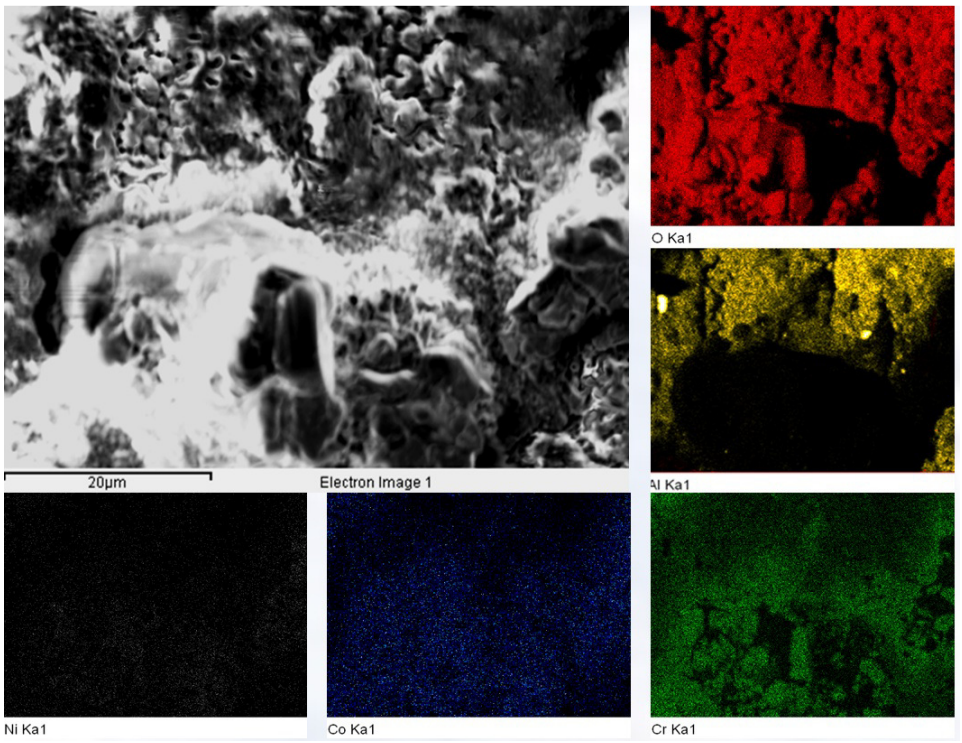

Figure 9.19: SEM image and EDS elemental mapping showing the surface oxide morphology of a CoNiCrAlY APS coating following 100h of oxidation at 1100°C

A similar irregular profile can be observed on the samples oxidised at 1000°C (Figure 9.20). When compared to the samples oxidised at 1100°C, the EDS analysis indicates there is more nickel present but less chromium. This is consistent with the XRD analysis which indicated a strong presence of NiO in these samples.

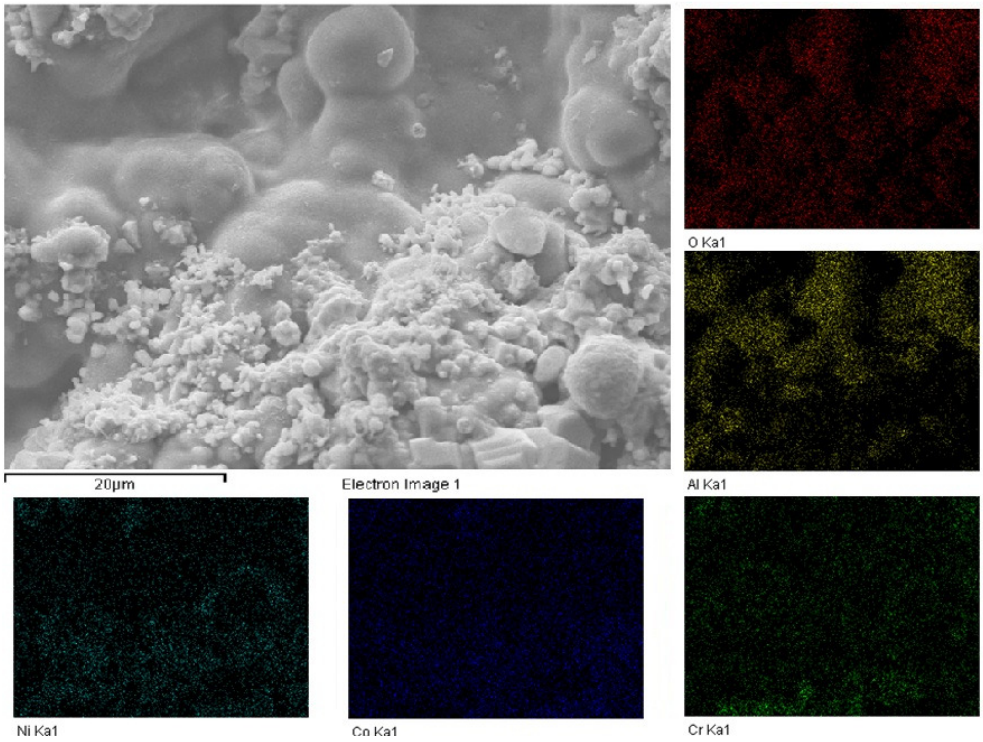

Figure 9.20: SEM image and EDS elemental mapping showing the surface oxide morphology of a CoNiCrAlY APS coating following 100h of oxidation at 1000°C

It is difficult to determine which oxidation temperature is better for the APS samples as both show signs of unfavourable oxide formation. From the XRD analysis it appears as though the APS samples oxidised at 1100°C perform slightly better however, the EDS analysis appears to indicate that the samples oxidised at 1000°C perform better. This discrepancy can be explained by the large variance in coating quality of the APS samples. The mass gain of the samples should therefore be taken as a better indication than surface analysis due the larger amount of samples in that analysis.

EDS elemental mapping of the cross-section of the APS sample oxidised at 1100°C is shown in Figure 9.21. The surface oxide layer appears to be formed of O, a large amount of Cr and combination of Al, Co and Ni. The extensive oxidation is also apparent in the coating. It is interesting to see that the internal oxidation appears to be exclusively composed of Al and O. The severe depletion of Al could explain the formation of mixed oxides on the surface.

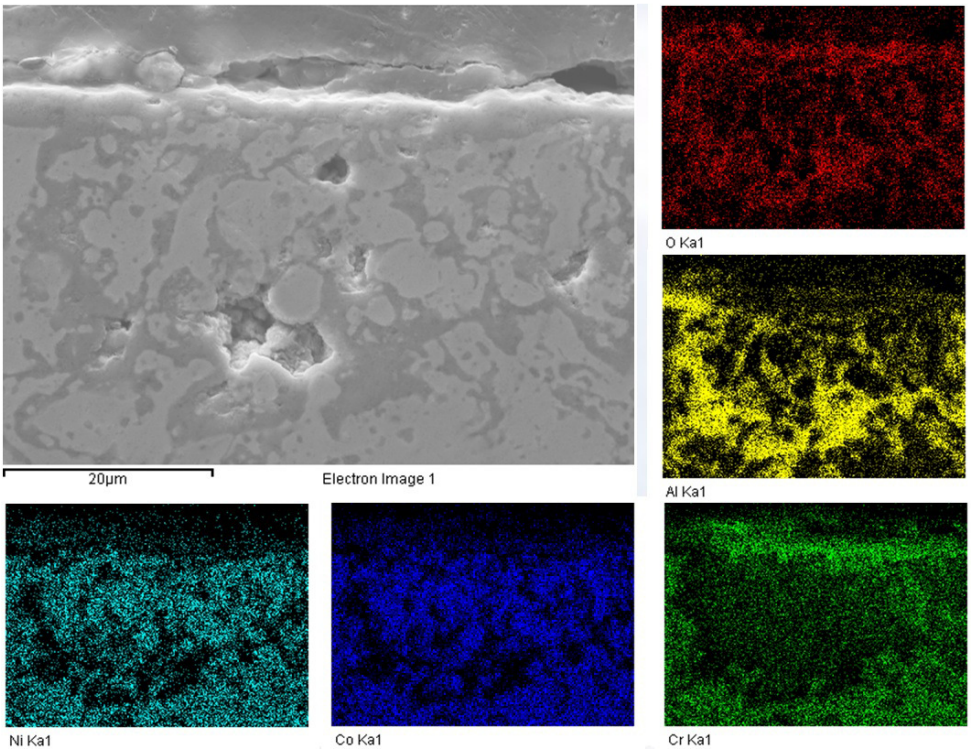

Figure 9.21 : SEM image and EDS elemental mapping showing the cross-section of a CoNiCrAlY APS coating following 100h of oxidation at 1100°C

In summary, the APS samples oxidised at 1100°C has a higher initial mass gain but appears to stabilise more quickly with respect to the sample oxidised at 1000°C and has a lower mass gain after 100h oxidation. In both cases, the APS samples offer poor oxidation performance but it appears an oxidation temperature of 1100°C offers slightly better performance due to the reduced presence of mixed oxides.

9.1.2.3. CGDS Samples

Unfortunately, no CGDS samples were available for XRD analysis due to nozzle clogging issues as described in section 6.3 which required prolonged investigation and manufacturing times due to the limited availability of the HVOF spraying time (section 6.4). However, EDS analysis and cross-section images were taken after 100h of oxidation.

The CGDS sample surface SEM image for the sample oxidised at 1100°C as seen in Figure 9.22 indicates a smooth and uniform surface with some oxide protrusions. The EDS analysis reveals the surface is mostly composed of aluminum and oxygen with some traces

of chromium, cobalt and nickel. The surface oxides appear to be more varied than in the case of the HVOF samples. However, alumina seems to dominate the oxidised surface of the CGDS coating.

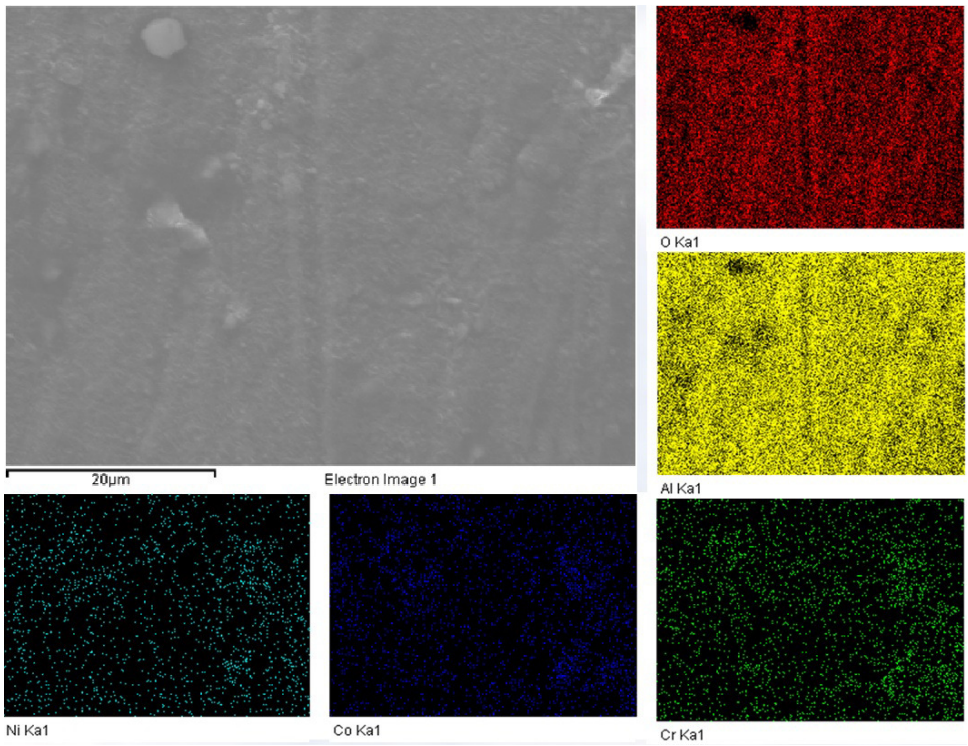

Figure 9.22: SEM image and EDS elemental mapping showing the surface oxide morphology of a CoNiCrAlY CGDS coating following 100h of oxidation at 1100°C

In contrast, the sample oxidised at 1000°C as seen in Figure 9.23 exhibits a whisker-like morphology indicative of θ-Al_2O_3. EDS analysis indicates the sample oxidised at 1000°C is quite similar to the one oxidised at 1100°C.

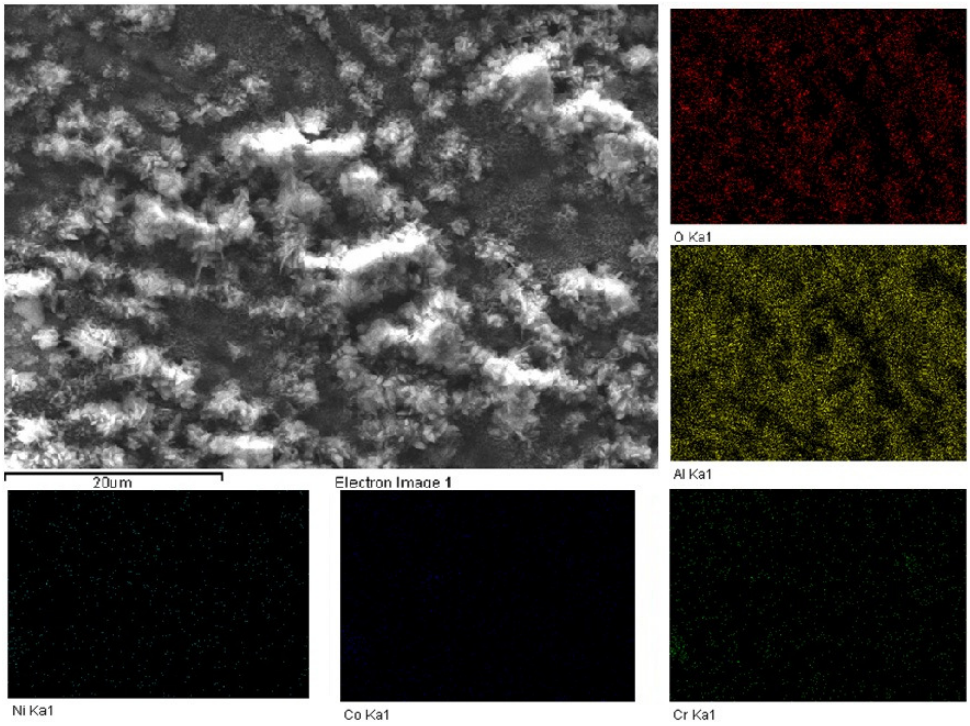

Figure 9.23: SEM image and EDS elemental mapping showing the surface oxide morphology of a CoNiCrAlY CGDS coating following 100h of oxidation at 1000°C

The presence of oxides other than Al_2O_3 indicates the CGDS coatings have a slightly inferior oxidation performance than the HVOF coatings but quite superior to the APS coatings. The CGDS samples oxidised at 1100°C also appear to perform better than those oxidised at 1000°C.

The EDS analysis of the cross-section of the CGDS coating oxidised for 1100°C is presented in Figure 9.24. The surface oxides appear to be exclusively composed of Al and O and overall elemental distribution is quite similar to the HVOF coating.

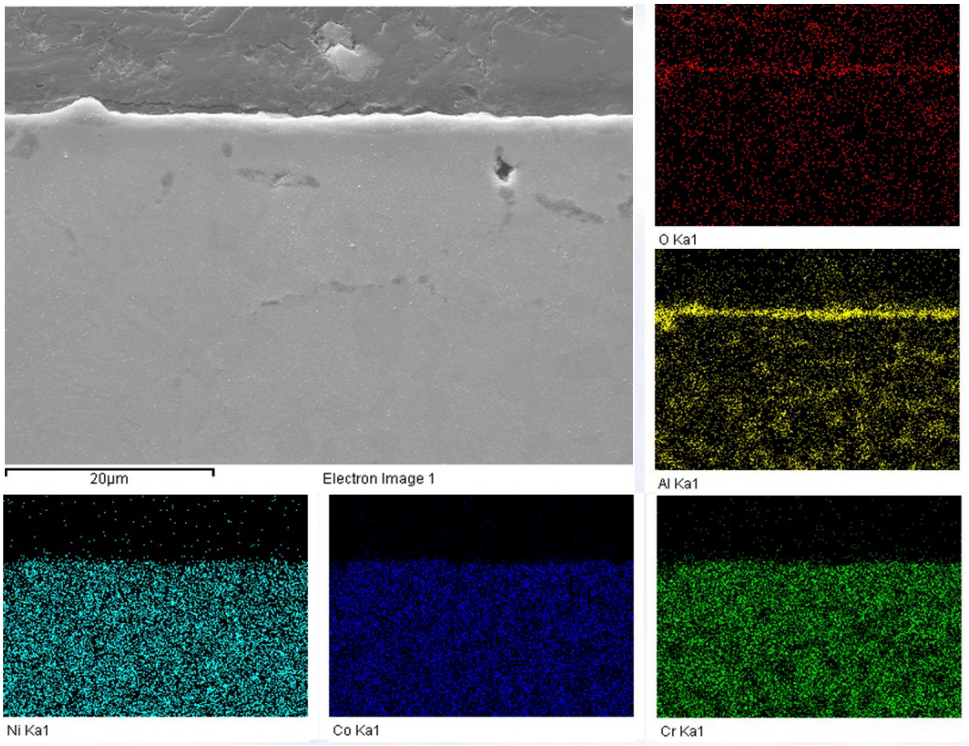

Figure 9.24: SEM image and EDS elemental mapping showing the cross-section of a CoNiCrAlY CGDS coating following 100h of oxidation at 1100°C

9.1.3. Summary

Despite having an oxidation temperature 100°C higher, which was previously thought to reduce the coating oxidation resistance, the samples oxidised at 1100°C have a better oxidation performance than samples oxidised at 1000°C. This increase in performance can be explained by the rapid formation of a thin α-alumina oxide scale which protects the coating from further oxidation. Since the formation temperature of α-alumina is approximately 1050°C, the increase of 100°C enables the formation of this α-alumina scale as opposed to a θ-alumina scale. Although both are alumina scales, the α-alumina offers better protection from oxidation as it prevents the inward diffusion of oxygen to a greater degree than θ-alumina. Additionally, the oxide morphology of α-alumina is favoured as it is uniform as opposed to growing in protrusions. This has the ability to decrease the stresses between the bond coat and the top coat under thermal cycling. Although the oxidation temperature is higher, the formation of an α-alumina layer not only offers better oxidation protection but could also minimise the stress between the bond coat and top coat which will increase overall TBC lifetime.

Overall, the HVOF coating offers the best performance closely followed by the CGDS coatings and the low-performing APS coatings. The performance difference between the CGDS and HVOF coatings is difficult to analyse without XRD data for the CGDS samples. From data gather using XRD and EDS analysis, the HVOF samples are forming exclusively Al_2O_3 while the CGDS samples appear to be forming some mixed oxides. As the main difference between the CGDS and HVOF coatings is the internal oxides, it is believed that they are the reason for the increased performance. The oxides present in the HVOF coating, created during the spraying process, could accelerate the formation of Al_2O_3 by acting as seed particles. These oxides could also slow the diffusion of aluminum to the surface which would reduce the measured mass gain. The coatings manufactured by APS perform poorly at both oxidation temperatures but appear to stabilise more quickly at 1100°C. The CGDS coatings oxidised at 1100°C are also able to outperform the HVOF coatings oxidised at 1000°C in both mass gain and according to the EDS elemental analysis.

9.2. Non-grinded oxidation experiments

The analysis of as-sprayed coatings is important in determining the effect of the oxide layer formed during the spray process on the long-term oxidation dynamics of the bond coat. The grinding of the bond coat removes oxides formed during the spraying process which could adversely affect the overall oxidation dynamics. It is expected that the mass-gain of the non-grinded coatings will be higher due to the presence of mixed oxides which will impede the early formation of protective α-alumina. Due to processing difficulties, the CGDS samples were not included in this part of the study.

9.2.1. Oxide growth rates

As can be seen in Figure 9.25, the mass gain for the as-sprayed coatings is initially higher than their grinded counterpart. In the case of the APS coating, the mass gain increases dramatically when compared to the grinded sample indicating the oxides present during the spraying process are detrimental to the coating oxidation behaviour. The non-grinded HVOF coating has an initial mass gain higher than both the HVOF coating oxidised at 1000°C and the one oxidised at 1100°C. However its mass gain curve rapidly stabilizes and exhibits behaviour similar to the grinded sample at 1100°C. It appears that while the initial mass gain is higher for the non-grinded sample, the mass gain stabilises just as rapidly as the grinded sample as both exhibit a lower mass gain than the HVOF sample oxidised at 1000°C after 100h. Specific values are presented in Table 9-1. The initial increase is likely due to increased surface roughness which allows for more surface oxide formation. The growth of the initial surface oxides also increases the initial mass gain while delaying the formation of a protective α-Al2O3 layer. However, once the α-Al2O3 layer is formed under the surface oxides, the oxide growth rate is slowed by the reduction of oxygen diffusion in the coating. The mass gain rate remains slightly higher than the grinded samples due to the delayed formation of the α-Al2O3 layer as well as the increased surface roughness.

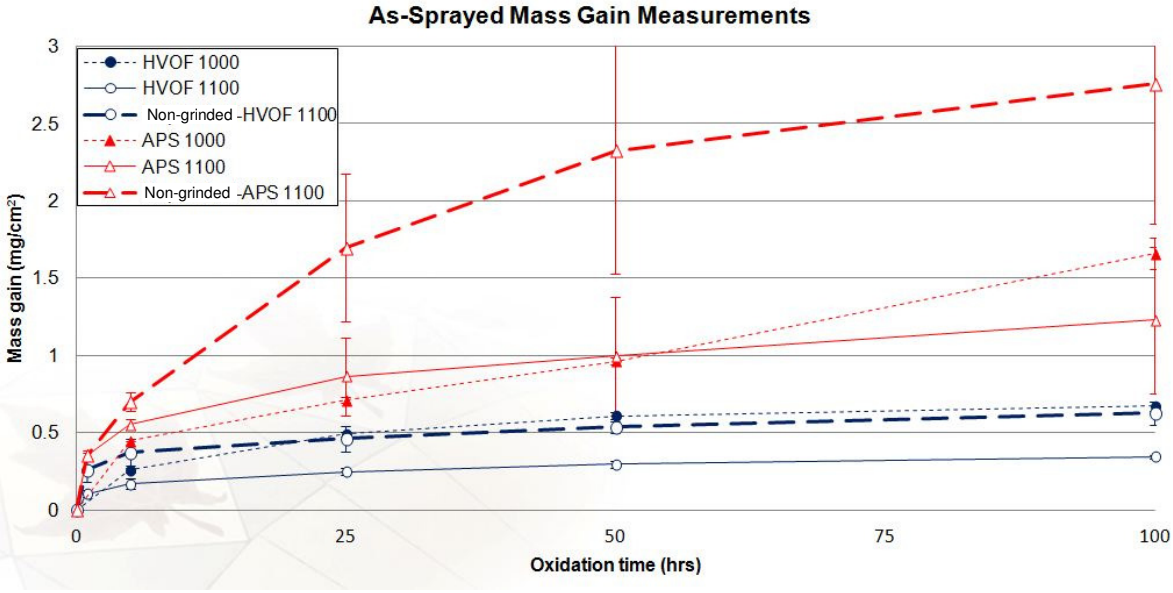

Figure 9.25: Mass gain measurements of non-grinded HVOF and APS coatings oxidised at 1100°C

Table 9-1: Mass gain with respect to oxidation time at for HVOF oxidised at 1000°C and 1100°C, as-sprayed HVOF (AS-HVOF) oxidised at 1100°C, APS oxidised at 1000°C and 1100°C and as-sprayed APS (AS-APS) oxidised at 1100°C.

Oxidation time	HVOF 1000°C (mg/cm^2)	HVOF 1100°C (mg/cm^2)	AS-HVOF 1100°C (mg/cm^2)	APS 1000°C (mg/cm^2)	APS 1100°C (mg/cm^2)	AS-APS 1100°C (mg/cm^2)
1h	N/A	0.11	0.21	N/A	0.35	0.35
5h	0.26	0.17	0.31	0.45	0.55	0.70
25h	0.49	0.25	0.40	0.71	0.87	1.70
50h	0.61	0.30	0.51	0.97	1.00	2.33
100h	0.67	0.34	0.57	1.66	1.23	2.76

Images of the cross-section of oxidised coatings presented in Figure 9.26 indicate the oxide layer grows in a two-phase structure. The initial (top) oxide layer forms as a result of the oxides present at the surface of the coating due to the spraying process while the bottom layer grows as oxidation progresses. Observation of Figure 9.26 confirms that the bottom (darker) oxide layer grows with oxidation time while the top layer is highly variable but appears to be of constant average thickness after the protective alumina scale is formed. The top layer is therefore expected to be composed of mixed oxides while the bottom layer should be composed of Al_2O_3. Further analysis via EDS and XRD is required to confirm the composition and growth of these oxides.

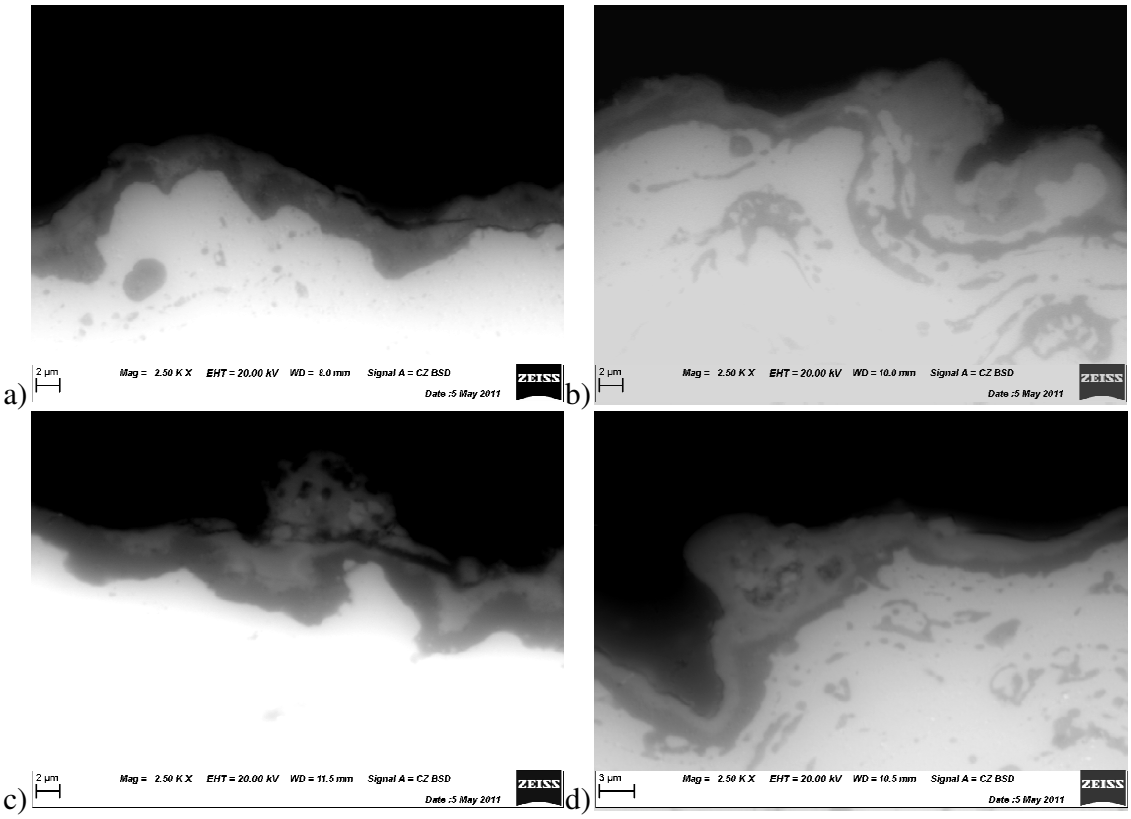

Figure 9.26: SEM image of non-grinded coatings showing two-phase oxide layer consisting of lighter layer composed of mixed oxides and darker layer composed of Al_2O_3 of a) HVOF 25h, b) APS 25h, c) HVOF 50h d)APS 50h. All images were taken at 2500x.

The identification of oxide layer growth is impractical due to the irregularity of the coating surface and oxide-layer composition (Figure 9.27). It appears however that there is some growth of the bottom oxide layer as oxidation time increases. This indicates the top oxide layer is porous and allows the penetration of oxygen through its thickness. Due to the increased surface roughness when compared to grinded samples, an analysis of β-phase depletion in the HVOF coating is impractical.

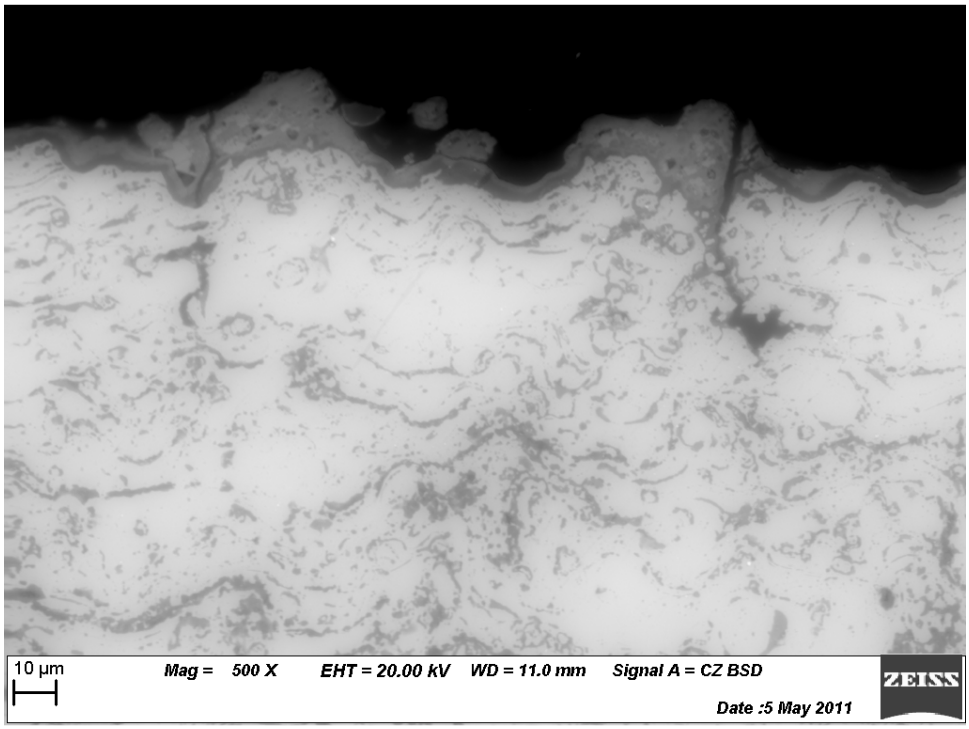

Figure 9.27: SEM image of non-grinded APS after 25h oxidation showing two-phase oxide layer at 500x magnification.

9.2.2. Oxide scale composition and morphology

9.2.2.1. HVOF Samples

XRD analysis of the non-grinded HVOF samples (Figure 9.28) indicates the initial presence of γ-Al_2O_3 and traces of α-Al_2O_3 while other oxides are indistinguishable from the background. After 1h of oxidation at 1100°C there is an increase of α- Al_2O_3 while there appears to be less γ-Al_2O_3. Indications of θ-Al_2O_3 and Cr_2O_3 are also present while there are traces of $NiCr_2O_4$ and $CoAl_2O_4$/$NiCo_2O_4$ (presented as one oxide due to their similar XRD profile). The XRD profile after 5 and 25 hours is very similar. The amount of α-, γ- and θ-Al_2O_3 has increased while the content of other oxides seems to remain constant. After 50h, an increase of α-, γ- and θ-Al_2O_3 as well as $NiCr_2O_4$ and $CoAl_2O_4$/$NiCo_2O_4$ is detected while the amount of Cr_2O_3 appears to be diminished. The final measurement after 100h oxidation indicates the presence of α-, γ- and θ-Al_2O_3, as well as $CoAl_2O_4$/$NiCo_2O_4$ and traces of $NiCr_2O_4$ and Cr_2O_3. There are clearly more mixed oxides than were detected for the grinded HVOF samples as expected.

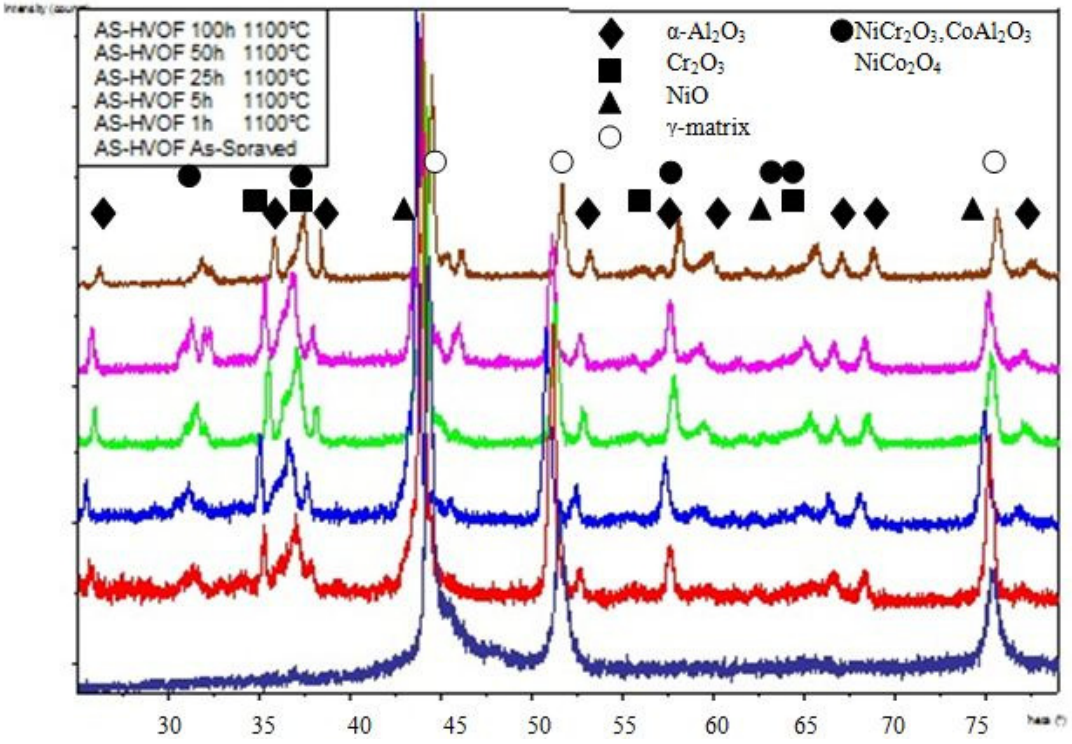

Figure 9.28: XRD spectra of non-grinded HVOF coatings after various oxidation times at 1100°C

EDS elemental mapping of the as-sprayed HVOF coating (Figure 9.29) indicates the presence of Al, Ni, Co and Cr with traces of O. The type of oxides present on the surface cannot be identified since all the elements are detected in approximately the same concentrations. The oxides detected in this as-sprayed state are expected to remain the same throughout oxidation and possibly act as initial oxide formation sites.

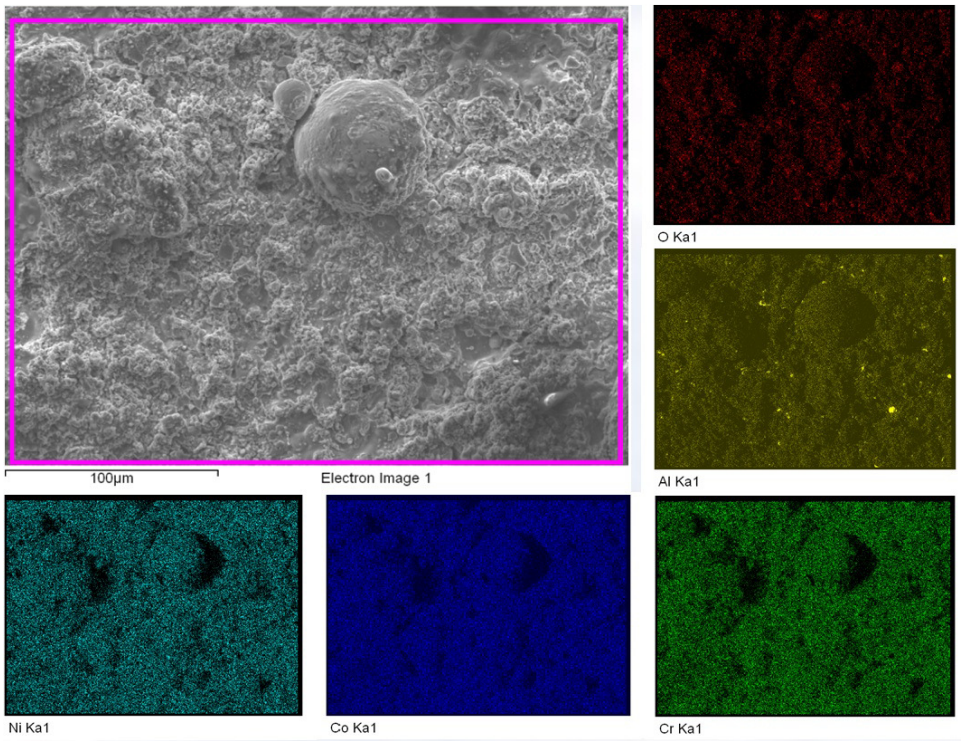

Figure 9.29: SEM image and EDS elemental mapping showing the surface oxide morphology of an non-grinded CoNiCrAlY HVOF coating in as-sprayed condition.

The EDS elemental mapping of the non-grinded HVOF samples oxidised for 100h at 1100°C is presented in Figure 9.30. There appears to be a large quantity of oxygen and a moderate amount of Cr as well as signs of Ni and Co. Although there is an initial amount of oxidation, it does not seem to significantly affect the oxidation behaviour of the HVOF samples. Alumina remains the favoured oxide formed at 1100°C.

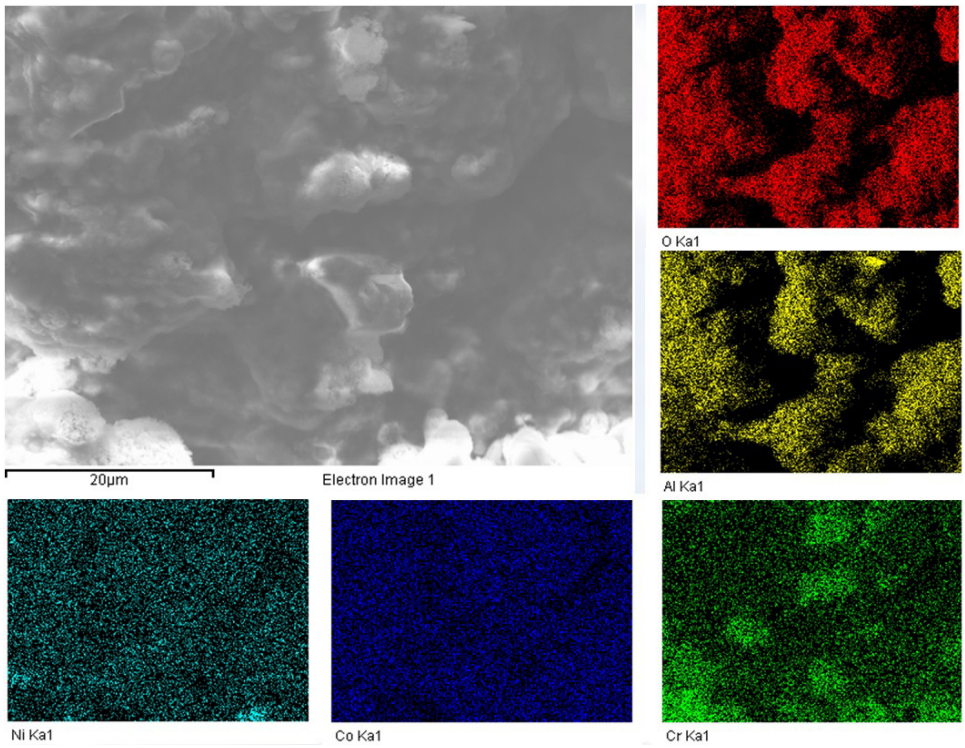

Figure 9.30 : SEM image and EDS elemental mapping showing the surface oxide morphology of an non-grinded CoNiCrAlY HVOF coating following 100h of oxidation at 1100°C.

The EDS elemental mapping of the cross-section of the non-grinded HVOF coating oxidised at 1100°C for 100h is presented in Figure 9.31. The dual-oxide layer is quite evident in this image. Oxygen mapping is used to identify the location oxide layer while the other elements determine the oxide layer composition. In these images, Ni, Co and Cr can be identified in the coating itself as well as in the top oxide layer while a "gap" exists between the oxide layer and the coating. This area is dominated by Al, the varying composition indicates there are two distinct oxide layers. The top layer appears to be composed primarily of O and Al with moderate amounts of Ni, Co and Cr while the bottom layer is composed exclusively of O and Al. An internal oxide can be identified as Al_2O_3 while there is no evidence of the Al-rich β-phase in this mapping. This could be due to image being taken to encompass the rough surface of the coating and thus less of the actual coating is in the image. It is also possible that Al-depletion occurs more rapidly in non-grinded coatings.

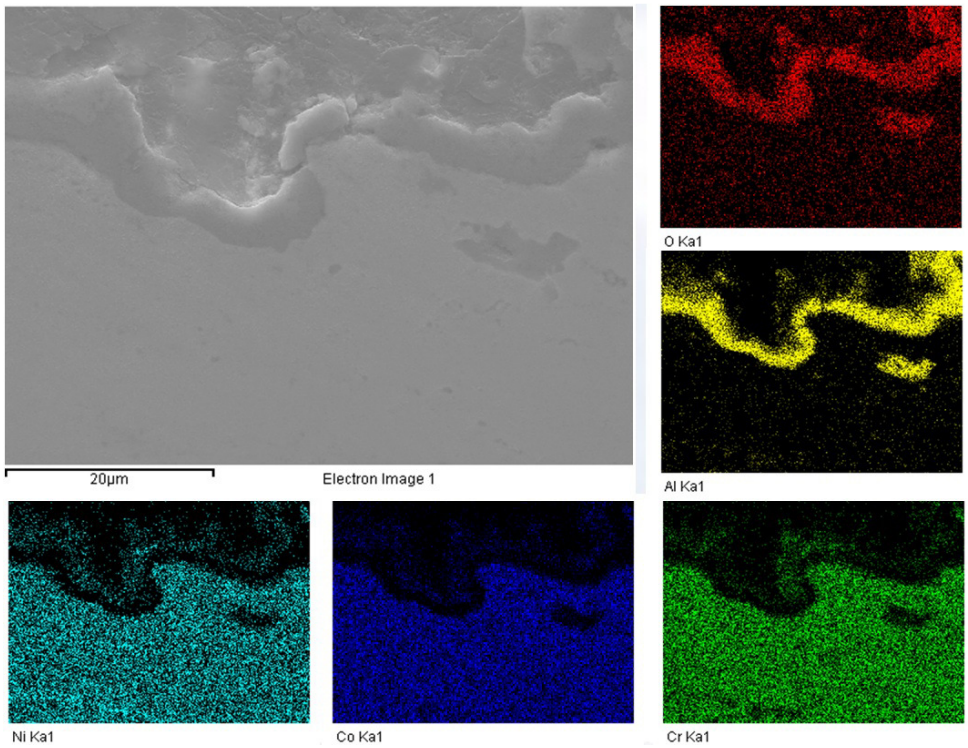

Figure 9.31 : SEM image and EDS elemental mapping showing the cross-section of an non-grinded CoNiCrAlY HVOF coating following 100h of oxidation at 1100°C

9.2.2.2. APS Samples

The XRD analysis of the non-grinded APS sample indicates the presence of $NiCr_2O_4$ and Cr_2O_3 in the as-sprayed condition. After 1h oxidation time, an increase in $NiCr_2O_4$ and Cr_2O_3 and the presence of NiO is detected while a large amount of CoO and traces of α-Al_2O_3 is present. The oxides content after oxidation to 5h remains relatively constant with the exception of a large increase of γ-Al_2O_3 and the detection of θ-Al_2O_3. Oxide composition remains relatively constant thereafter with a reduction of $NiCr_2O_4$, γ-Al_2O_3, θ-Al_2O_3 and Cr_2O_3 and an increase of NiO. The XRD analysis for this sample is dominated by a large peak for CoO throughout the oxidation times. It appears the surface oxides present during spraying favour the formation of CoO which was not as prevalent on the grinded APS samples.

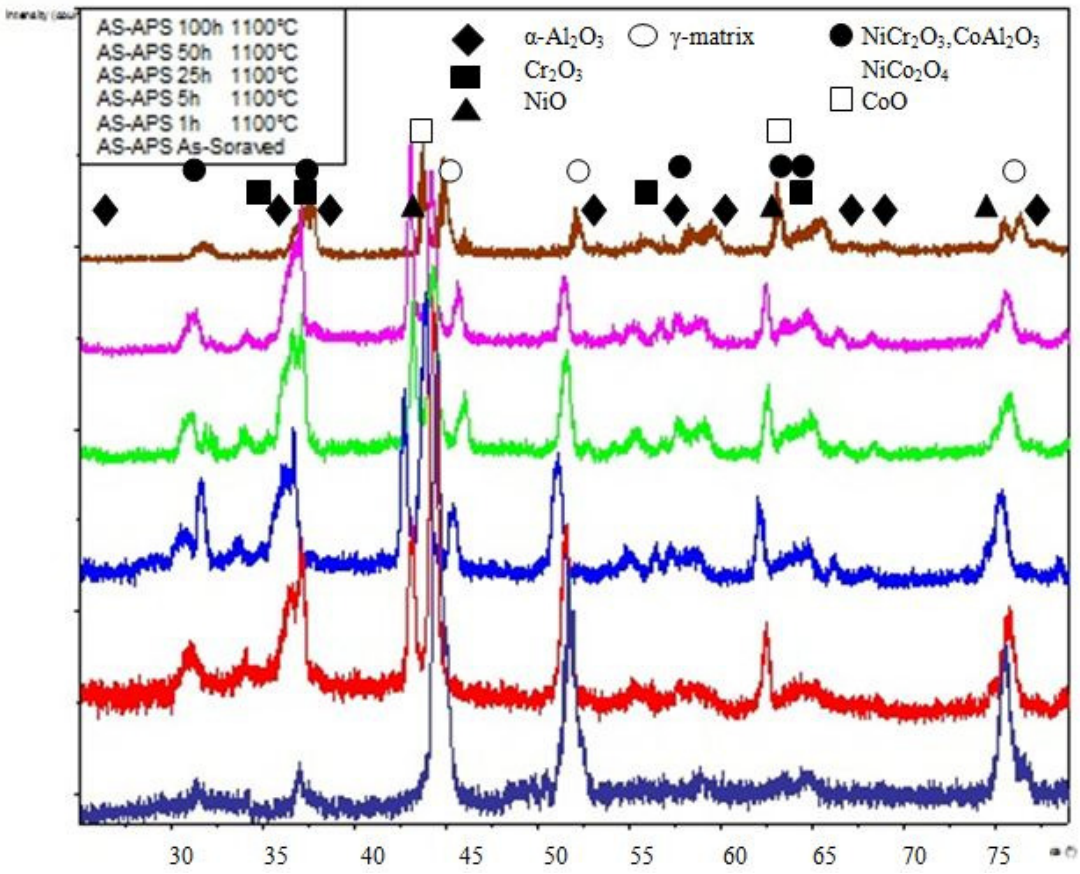

Figure 9.32: XRD spectra of the non-grinded APS coatings after various oxidation times at 1100°C

EDS analysis of the as-sprayed APS coating (Figure 9.33) indicates the presence of Al, Ni, Co, Cr and O. While the specific oxides cannot be determined, there appears to be a higher concentration of Al_2O_3 and higher overall oxide content in the APS sample when compared to the HVOF sample.

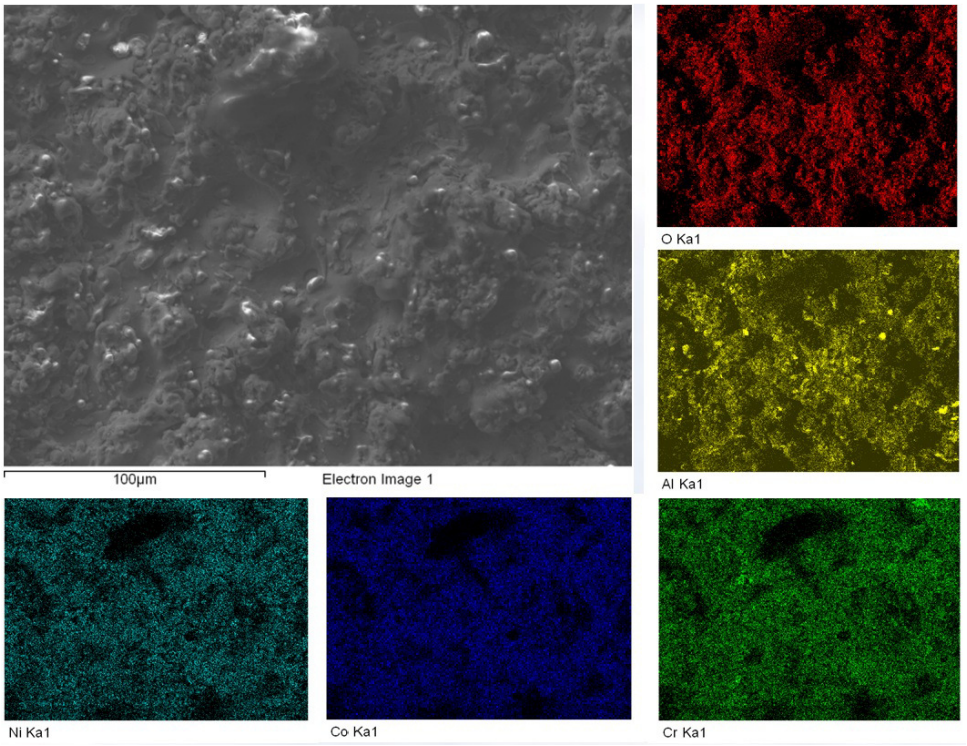

Figure 9.33: SEM image and EDS elemental mapping showing the surface oxide morphology of an non-grinded CoNiCrAlY APS coating in as-sprayed condition.

The EDS elemental analysis of the non-grinded APS sample oxidised for 100h at 1100°C is presented in Figure 9.34. The surface oxide composition appears to be mostly Al with a significant amount of Ni, Co and Cr. The elemental distribution of the surface of the non-grinded APS samples appears to be very similar to that of the grinded APS sample.

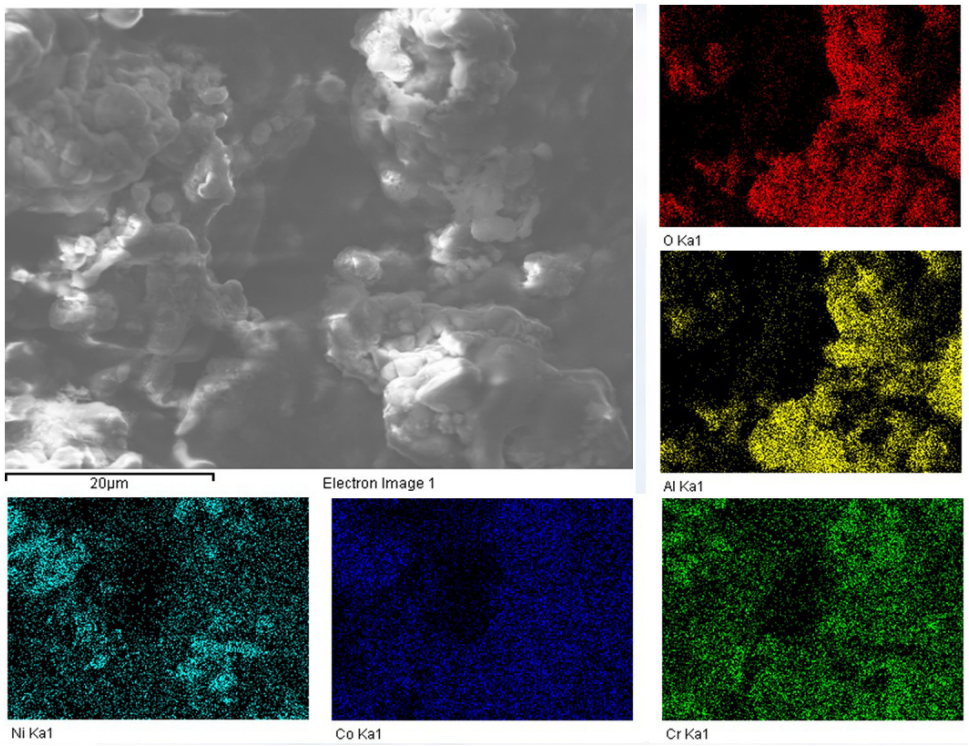

Figure 9.34 : SEM image and EDS elemental mapping showing the surface oxide morphology of an non-grinded CoNiCrAlY APS coating following 100h of oxidation at 1100°C.

The EDS elemental mapping of the cross-section of the non-grinded APS coating oxidised at 1100°C for 100h is presented in Figure 9.35. The dual-oxide layer is quite evident in this image. As was seen in Figure 9.31, a gap in the elemental mapping of Ni, Co and Cr exists between the oxide scale and the coating. This area is composed of Al as well as O which indicates there are two distinct oxide scale compositions. The top layer appears to be composed primarily of O, Co and Cr with moderate amounts of Al and Ni while the bottom layer is composed exclusively of O and Al. This is in accordance with the XRD analysis of this coating.

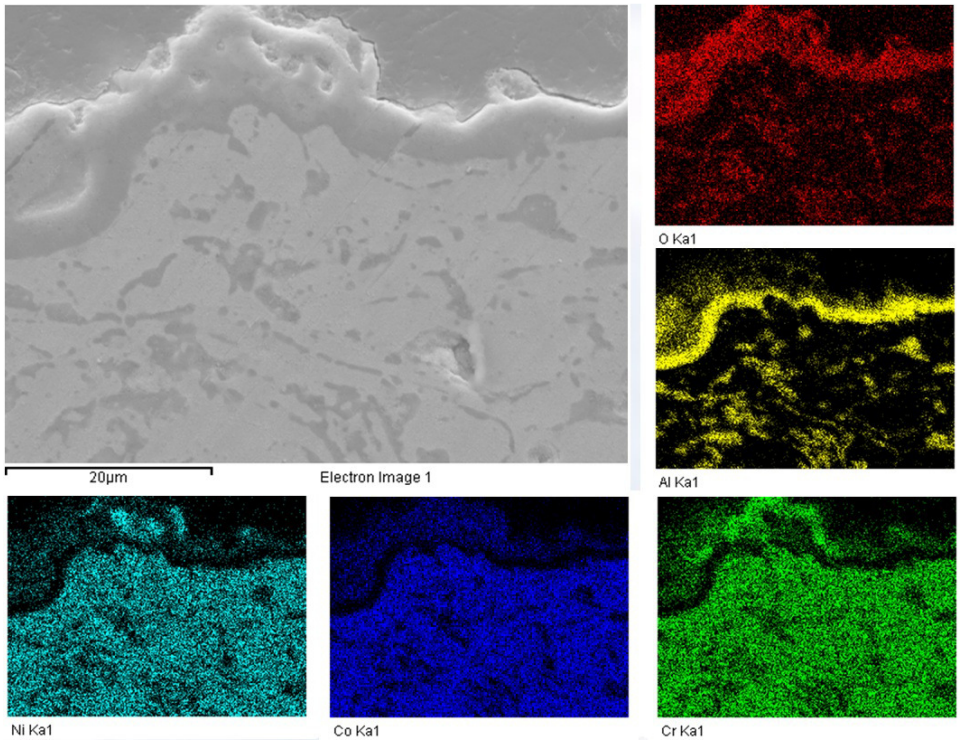

Figure 9.35 : SEM image and EDS elemental mapping showing the cross-section of an non-grinded CoNiCrAlY APS coating following 100h of oxidation at 1100°C

9.3. Long-term oxidation experiments

Mass gains of the HVOF and APS, grinded and non-grinded samples were taken after 100h to indicate the oxidation behaviour of the coatings in a long term application. In contrast with the previous sections, not all data points represent the average value of 5 samples due to the need to sacrifice samples for SEM cross-sections, surface SEM and EDS. The values obtained should therefore be taken as indicative only especially in the case of large standard deviations such as the APS coating values. The HVOF samples retain a very low standard deviation throughout and thus those values should hold with a larger sample pool.

9.3.1. Oxide growth rates

As can be seen from Figure 9.36, the mass gain values of the HVOF samples continue to exhibit a logarithmic behaviour beyond 100h and until the maximum soak time of 2000h. The mass gain progresses slowly and the coating does not appear to have reached the end of its al-rich lifecycle. Further oxidation tests should be conducted past 2000h to determine the actual lifetime of HVOF coatings. In contrast, the mass of the APS coating continues to rise after 1000h, and spallation is detected at 2000h. It is unclear at which point the alumina-rich lifecycle ends and where spallation begins. The specific mass gain values are presented in Table 9-2.

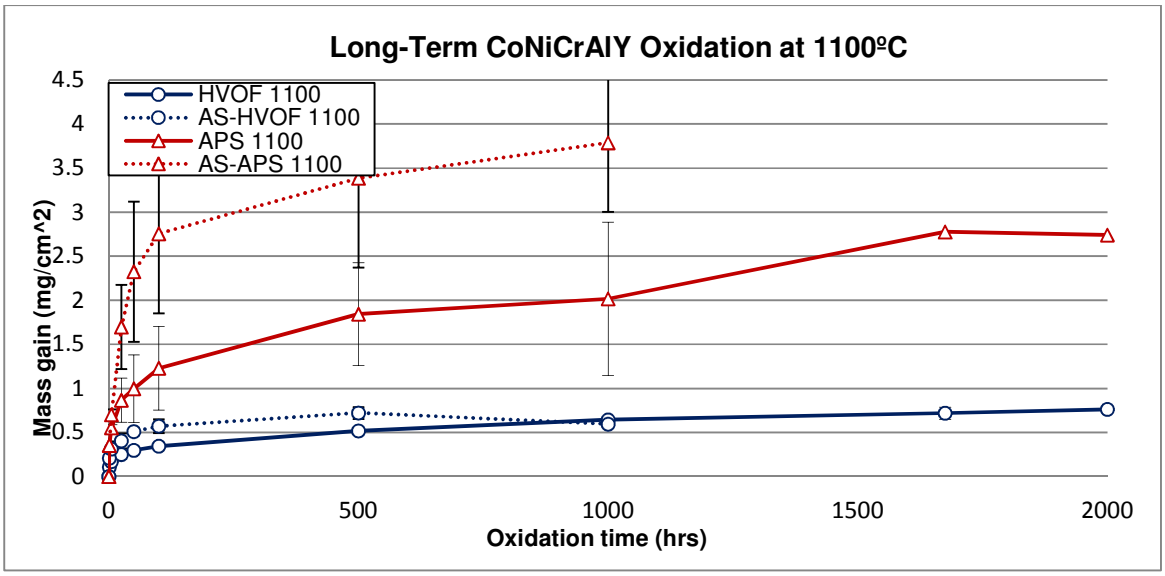

Figure 9.36: Mass gain measurements as a function of oxidation time at 1100˚C for CoNiCrAlY coatings deposited by HVOF and APS and grinded on all sides as well as HVOF (AS-HVOF) and APS (AS-APS) coatings without the removal of oxides formed during spray process.

Table 9-2: Mass gain measurements of samples oxidised at 1100°C from 100h to 2000h

	HVOF	APS	AS-HVOF	AS-APS
100h	0.34	1.23	0.57	2.76
500h	0.52	1.84	0.72	3.39
1000h	0.64	2.02	0.59	3.79
1500h	0.72	2.78	N/A	N/A
2000h	0.76	2.74	N/A	N/A

The non-grinded HVOF sample mass gain remained similar to the grinded samples until 1000h where spallation was detected. The spallation appears to be due to the large thermal stresses induced during the air quench of the samples. Since one side of the sample is grinded to remove any traces of the substrate and the other is covered in oxides, the thermal expansion coefficients between both sides of the sample differ. This induces stresses during the rapid cooling of the samples strong enough to progressively bend the samples. With a slower cooling and heating method, these samples will likely endure longer oxidation times without spallation. Photographs of these samples are presented in Figure 9.37

a) 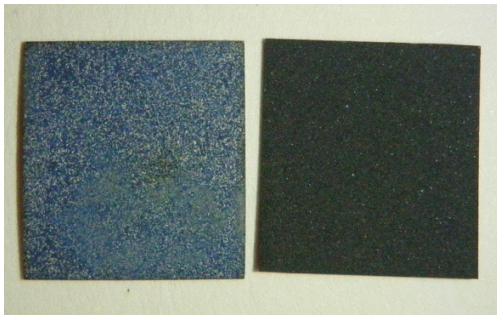 b) 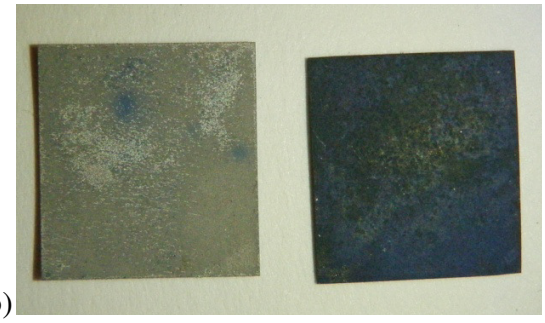

Figure 9.37: Photograph of HVOF (left sample) and APS (right sample) samples showing a) non-grinded surface and b) grinded surface following 1000h of oxidation at 1100°C

a)  b) 

Figure 9.38: Photograph of HVOF sample following 1000h of oxidation at 1100°C a) non-grinded surface and b) grinded surface

The mass gain of the non-grinded APS samples progressed similarly to the grinded samples. Spallation was detected at 1000h on the samples although mass gain was still rising. The spallation was identified visually rather than by measurements but is clearly visible in Figure 9.37b) (left sample). Spallation was not as pronounced for the APS samples when compared to the HVOF samples. This is likely due to the similarity of the thermal expansion coefficient of the oxides already present in the APS coating, those formed on the grinded side and present on the non-grinded surface. Due to this fact, it appears the lifetime of non-grinded APS samples is longer than the non-grinded HVOF samples when rapid heating and cooling rates are induced.

The grinded samples lasted approximately twice as long as the non-grinded ones. This indicates a significant advantage to grinding the bond coat especially in the case of the HVOF bond coat where spallation was not detected even after 2000h. The oxides that form on the surface as a result of the spraying process coupled with the increased surface roughness are detrimental to the long-term oxidation of these samples. The oxide layer grows from the surface and its adhesion strength is reduced to a point where spallation occurs. In the case of HVOF, the mass gain increase due to these oxides does not appear to be significant in the short term but significantly reduces the expected lifetime of the part. In the APS case, the mass gain increase due to the oxides is high and spallation occurs earlier. For both coating methods removal of the oxides caused by the spray process is beneficial to the long-term oxidation.

As can be seen from the HVOF samples in Figure 9.39, the oxide scale continues to grow slowly and the β-phase depletion increases with oxidation time. No large variation from the initial oxide evolution is observed. In contrast, the APS samples have a large variation of oxide thickness and exhibit a dual-layer oxide scale. The alumina layer appears to be growing as the oxidation progresses.

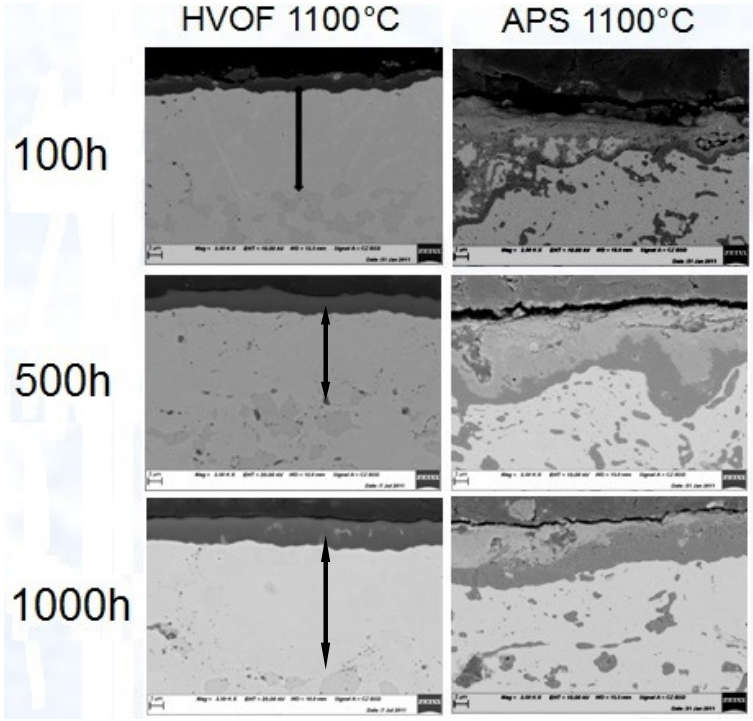

Figure 9.39: Evolution of the oxide scale and depletion zone as a function of oxidation time at 1100°C for CoNiCrAlY coatings manufactured by HVOF and APS and oxidized over 100h. All images were taken at the same magnification (2500x).

9.3.2. Oxide scale composition and morphology

9.3.2.1. HVOF Samples

After 500 hours of oxidation at 1100°C, the HVOF surface profile remains mostly uniform with indications of oxide formation on the surface. The EDS analysis reveals that the surface is mostly composed of oxygen and aluminum but with higher concentrations of chromium than observed on the sample oxidised for 100 hours.

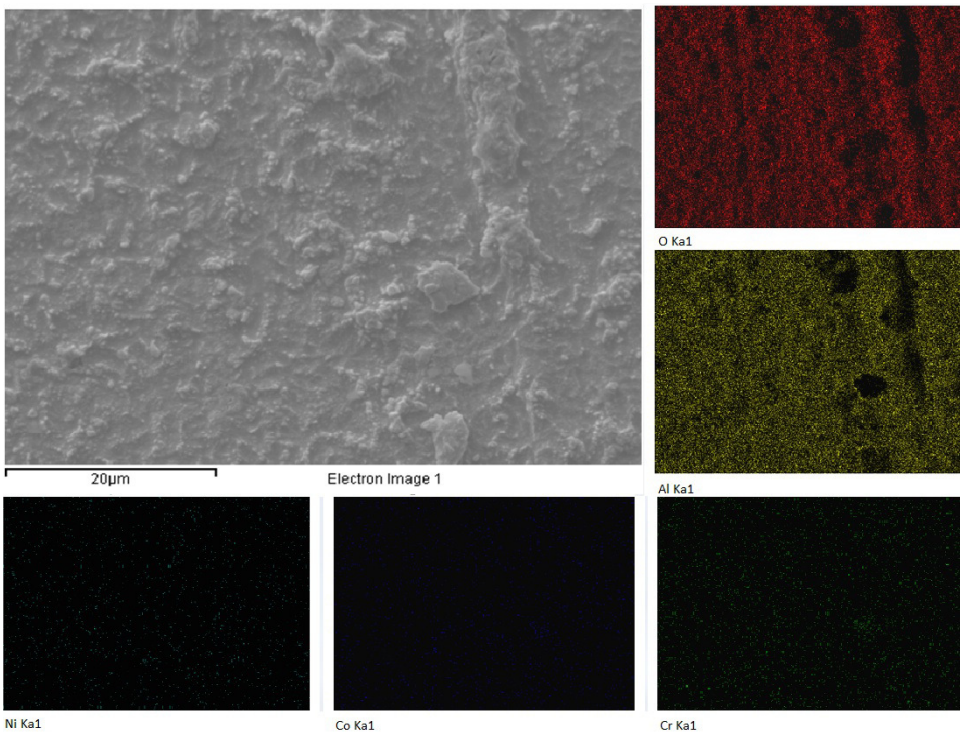

Figure 9.40: SEM image and EDS elemental mapping showing the surface oxide morphology of a CoNiCrAlY HVOF coating following 500h of oxidation at 1100°C

After 1000h the surface is smooth and uniform with indications of surface oxide formation. The EDS analysis indicates the surface is composed mostly of oxygen and aluminum with some traces of chromium, cobalt and nickel. There appears to be an increase of chromium content on the surface between 500h and 1000h indicating the coating may be reaching the end of its Al-rich lifecycle.

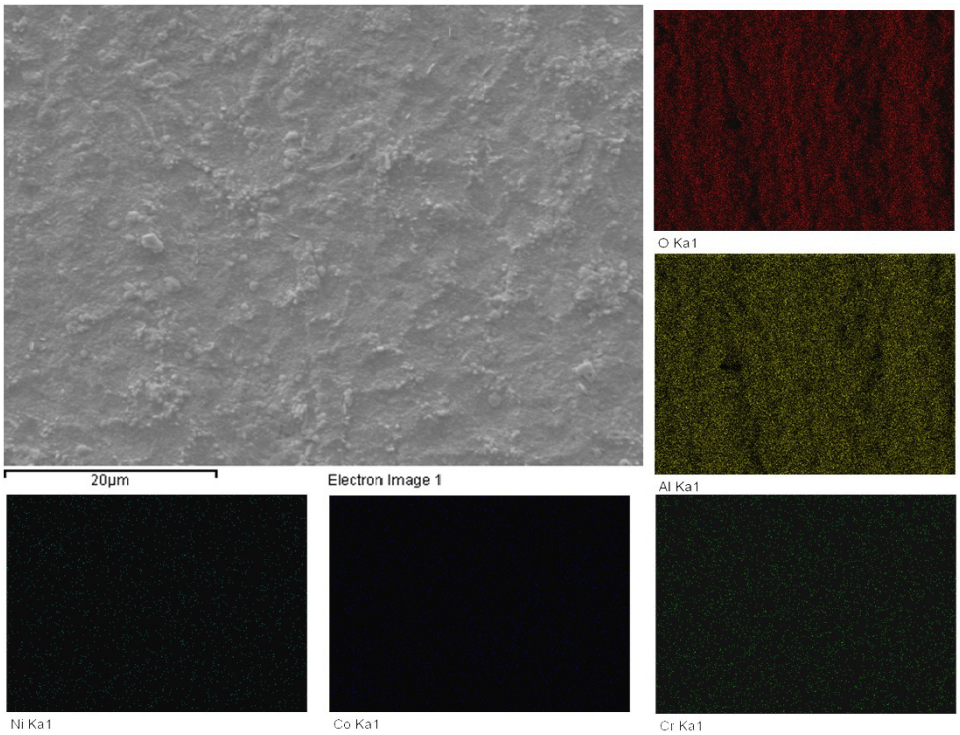

Figure 9.41: SEM image and EDS elemental mapping showing the surface oxide morphology of a CoNiCrAlY HVOF coating following 1000h of oxidation at 1100°C

9.3.2.2. APS Samples

The SEM surface profile of the APS sample varies throughout. Two different regions were selected for SEM and EDS analysis. The first area of interest exhibits a whisker-like morphology indicating that θ-alumina was formed on the surface. EDS analysis reveals the surface composition is mostly oxygen and aluminum with traces of chromium, cobalt and nickel. From this analysis it appears that the surface consists mostly of θ and α-alumina that was previously in the θ state and retained its whisker-like morphology.

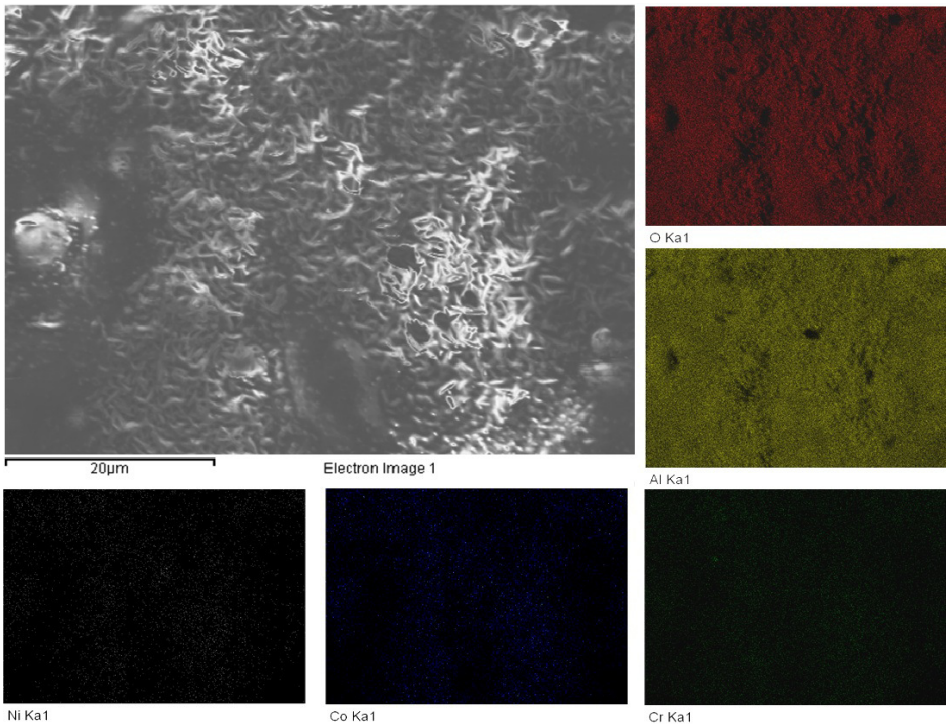

Figure 9.42: SEM image and EDS elemental mapping showing the surface oxide morphology of a CoNiCrAlY APS coating following 500h of oxidation at 1100°C – Area of Interest 1

The second area of interest, exhibits a uniform surface layer with oxide protrusions. EDS analysis indicates the surface layer is composed of oxygen and aluminum and areas of high chromium concentration while the protrusions are composed of oxygen, cobalt, nickel and traces of chromium.

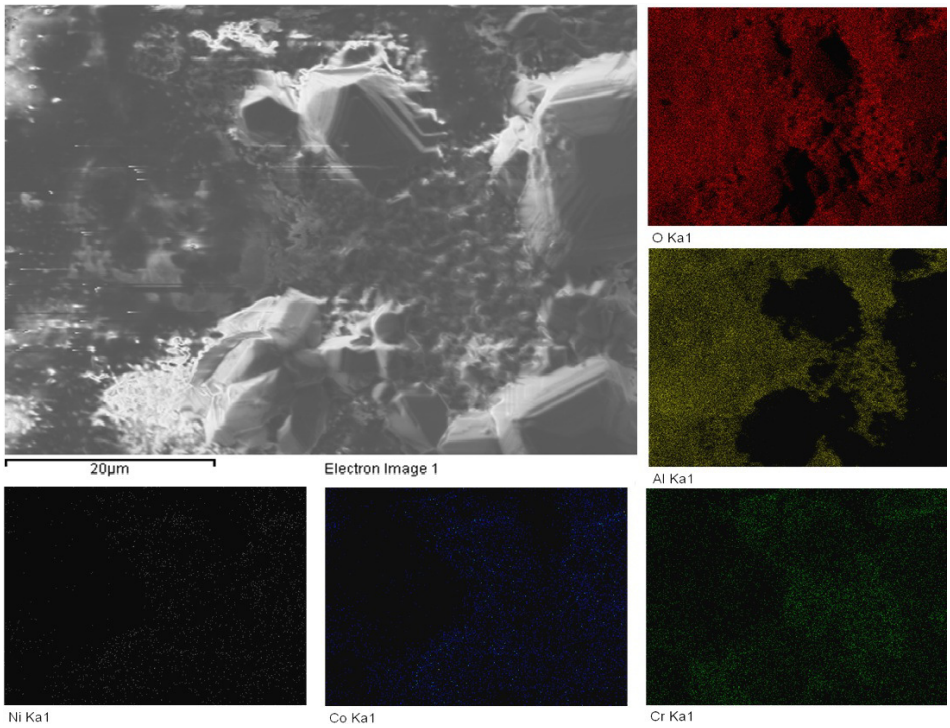

Figure 9.43: SEM image and EDS elemental mapping showing the surface oxide morphology of a CoNiCrAlY APS coating following 500h of oxidation at 1100°C – Area of Interest 2

The surface profile of the APS sample oxidised for 1000h consists of a base oxide layer with oxide protrusions. EDS analysis indicates the base layer consists of oxygen, aluminum and traces of chromium while the oxide protrusions consist of oxygen, nickel, cobalt and traces of chromium. When compared to the samples oxidised for 500h, there appears to be more protrusions indicating the coating is likely past its al-rich lifecycle.

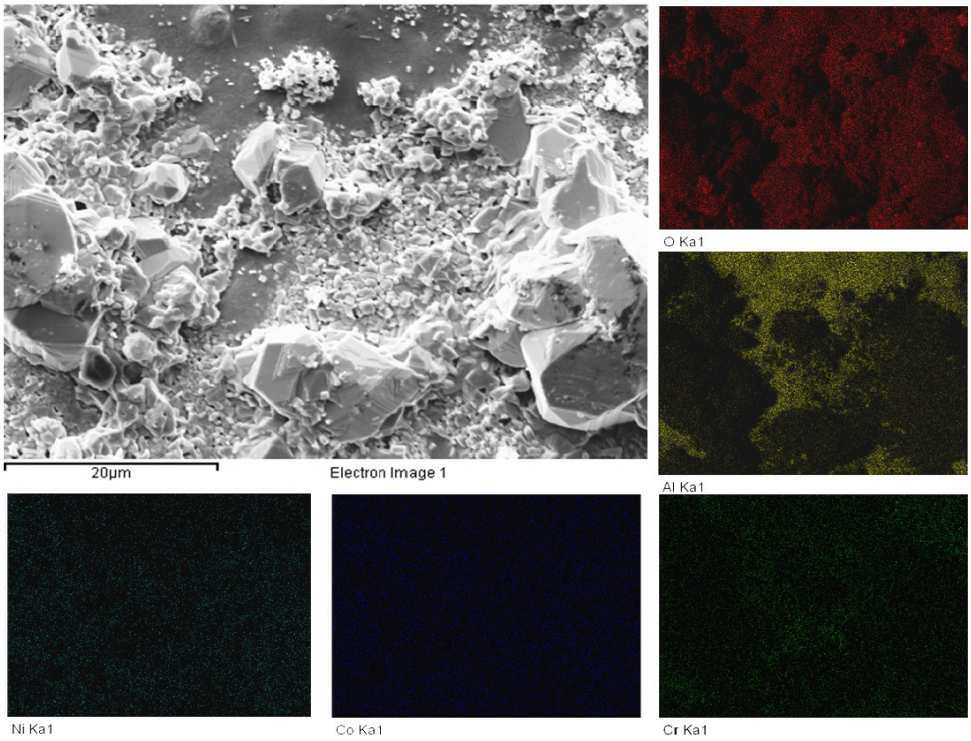

Figure 9.44: SEM image and EDS elemental mapping showing the surface oxide morphology of a CoNiCrAlY APS coating following 1000h of oxidation at 1100°C

9.4. Summary

The oxidation process of CGDS, HVOF and APS samples was investigated at 1100°C and compared with results at 1000°C. The oxidation performance of the samples was analysed using mass gain measurements, SEM and BSE images, as well as EDS and XRD analysis. From this analysis, it appears that the oxidation performance is significantly enhanced at 1100°C when compared to 1000°C in the case of CGDS, HVOF and APS coatings due to the early formation of protective α-Al_2O_3. HVOF coatings also appear to offer the best oxidation performance followed closely by CGDS while the APS coatings offer poor oxidation performance. Samples oxidised in the non-grinded state (with surface oxides due to the spraying process) showed a decrease in oxidation resistance when compared to their grinded counterparts. This decrease is extremely large for the APS coatings while it is noticeable for the HVOF coatings. It is interesting to note that, non-grinded HVOF coatings oxidised at 1100°C outperformed grinded HVOF samples oxidised at 1000°C. Long term oxidation of the samples indicates the lifetime of the non-grinded

samples is approximately 500 to 1000h while the grinded APS samples have a lifetime between 1000 and 1500h and the grinded HVOF samples have a lifetime above 2000h. Oxidation should therefore be conducted at a temperature of 1100°C in order to quickly form a protective α-Al2O3 layer. Additionally, the surface should be grinded to remove oxides formed during the spraying process as well as reduce roughness and increase coating lifetime.

Conclusions

The purpose of this research work was to develop a nozzle capable of depositing dense CoNiCrAlY coatings via CGDS as well as compare the oxidation performance of bond coats manufactured by various processes at temperatures of 1000°C and 1100°C. The work was therefore divided in two sections, the design and manufacturing of a CGDS nozzle with an optimal profile for the deposition of CoNiCrAlY powders and the comparison of the oxidation performance of CoNiCrAlY bond coats.

In order to design an optimal CGDS nozzle, the optimal nozzle expansion ratio was first determined mathematically. A nozzle with this optimal expansion ratio was then modelled and analysed using computational fluid dynamics software and compared with other nozzle profiles. Various CFD models were then developed to conduct further analysis on the effect of nozzle stand-off distance, driving gas stagnation temperature, driving gas stagnation pressure, various gas mixes, heating of feed gas and heating of powder prior to injection in the nozzle. Results indicated the stand-off distance at which the maximum particle velocity is reached varies with gas type and gas stagnation properties. Furthermore, increasing driving gas stagnation temperature yielded faster particle velocities due to the increased speed of sound of the driving gas. Similarly, increase driving gas stagnation pressure yielded faster particle velocities due to the increase in driving gas density. The use of Helium as driving gas yielded the highest particle velocities due to its high speed of sound. Heating of the feed gas and powder was found to increase particle impact temperatures by up to 230K which would reduce the critical velocity by up to 92 m/s and could lead to a significant increase in coating quality and deposition efficiency.

After the nozzle with the optimal profile was determined, it was manufactured using a computer numerically controlled mill. The completed nozzle was then used to deposit CoNiCrAlY bond coats. CoNiCrAlY coatings with less than 0.6% porosity were successfully deposited with the nozzle at travel speeds ranging from 1mm/s to 12mm/s. This is an improvement over the previous nozzle which was limited to low travel speeds in order to maintain acceptable coating porosity. However, after repeated use of the nozzle, internal clogging reduced the nozzle efficiency. A second nozzle of identical profile was

manufactured and its interior coated with tungsten-carbide. The hard coating was added to reduce the possibility of clogging inside the nozzle.

To adequately compare CoNiCrAlY bond coats, stand-alone coatings were oxidised without the presence of a superalloy substrate or ceramic top coat. Coatings produced via CGDS, HVOF and APS were then placed in an air furnace for isothermal oxidation tests at a temperature of 1100°C for up to 100h. Mass gain measurement were taken to asses oxide growth rates while SEM, EDS and XRD analyses were conducted to verify oxide scale composition. Results of these experiments were then compared with previous results obtained at an oxidation temperature of 1000°C. This comparison indicated oxidation at 1100°C yielded slower oxide growth and better resulting oxide composition. This was attributed to the early formation of a protective and dense α-Al_2O_3 oxide scale due to the higher oxidation temperature. HVOF coatings were also found to have a slightly better oxidation performance than CGDS coatings due to the presence of beneficial oxides in the HVOF coating while APS coatings performed poorly. Additional experiments were conducted with samples which were non-grinded on one side in order to retain oxides created during the spraying process. These oxides were found to reduce the oxidation performance of coatings as they facilitated the formation of unwanted mixed oxides. Finally, long-term oxidation tests were conducted in order to compare the lifetime of each bond coat up to 2000h. HVOF coatings were found to retain their protective properties after this extensive oxidation experiment while APS coatings had lost their protective properties.

This work has shown that the quality of coatings deposited via CGDS can be increased by the use of a nozzle of optimal profile. The oxidation temperature of bond coats was also found to have a significant influence on the oxidation performance of the free-standing coatings. Early formation of protective α-Al_2O_3 due to an oxidation temperature of 1100°C as opposed to 1000°C is beneficial to the overall oxidation performance of CoNiCrAlY coatings. Grinding of coating surfaces after deposition should also be conducted to maximise bond coat lifetime. It should be noted however that the oxidation behaviour of a full TBC system including the superalloy substrate and the ceramic top coat will differ from the free-standing coatings in this study.

Future Work

The following section outlines various topics which could be of interest for subsequent studies to advance the work carried out in this thesis. The topics are presented in two subsections: Coating Deposition Techniques and CGDS Development and Bond Coat Oxidation Research.

Coating Deposition Techniques and CGDS Development

1. Although the CGDS nozzle designed and manufactured in this study has been successfully used to deposit dense CoNiCrAlY coatings, the reliability of the nozzle is not adequate for large-scale operations. This could be due to the manufacturing process or the material used and has been addressed by manufacturing a coated nozzle as outlined in section 6.4. However this coated nozzle solution needs to be tested for performance and reliability. Furthermore, the validation of the nozzle design should be done not only via coating quality assessment but also through particle image velocimetry to ensure that the Fluent CFD model adequately represents the manufactured nozzle.

2. The current nozzle design injects particles perpendicular to the driving gas flow. According to simulations and physical testing, this leads to the particles impacting on the nozzle walls and leads to premature wear and clogging of the nozzle. The injection of particles could be conducted at an angle in order to minimise the non-axial particle velocity and reduce the possibility of impact with the nozzle wall as well as reduce any flow disturbance caused by the feed gas injection.

3. The CFD nozzle simulations in this study indicated that an increased nozzle stand-off distance will yield higher particle velocities as well as reduce the bow shock strength. The model used for these simulations however needs refinement and evaluation of the particle velocities should be conducted for a wider range of particle sizes. Furthermore, experimental tests should be conducted with a larger stand-off

distance in order to validate this finding via coating quality analysis or particle image velocimetry.

4. Simulations in which the feed gas and particles were heated prior to injection in the driving gas stream indicated that a significant reduction in particle critical velocity could be achieved due to the elevated particle temperature. Heating of the feed gas only yielded a particle temperature increase of 150K while heating both the particles and the feed gas yielded an increase of 230K. This rise in temperature represents a reduction in critical velocity of approximately 92 m/s. Physical experiments representing these conditions should be conducted in order to investigate the impact of heating the feed gas and particles. Furthermore, increasing the gas temperatures via insulation or heating of the nozzle could have significant influence on the particle impact temperature and velocity and should be investigated.

5. During this study, physical tests were conducted using nitrogen as a driving gas in an effort to reduce manufacturing costs. A thin CoNiCrAlY layer was successfully deposited with a driving gas pressure of 3.5MPa and a gas temperature of 900K which was the maximum pressure and temperature the current CGDS system could achieve. Further tests should be conducted with an increased pressure and driving gas temperature to properly assess the coating quality which can be obtained with this nozzle when using nitrogen as the driving gas.

6. The deposition of CoNiCrAlY particles via a new coating technique, briefly presented in section 2.1.4, was investigated during this study. Successful coating deposition was achieved with driving gas temperature of 550°C, driving gas pressure of 5MPa when the powder was heated to 1100°C. Subsequent tests where the powder was heated to 1000°C yielded no coating. Further testing should be conducted with increased driving gas temperature and powder heating temperatures to assess the potential of this new coating technique.

7. As outlined in section 2.2.3.2, Hydrogen is the gas which features the highest speed of sound. This makes it an interesting candidate as a driving gas as it is more affordable than helium and can provide higher particle velocities. However, there is a significant safety consideration which must be made prior to using this gas due to its volatile and highly flammable nature. Furthermore, the use of hydrogen in the process could lead to hydrogen embrittlement of some materials. However the use of Hydrogen as driving gas should be investigated as it has the potential to drastically reduce CGDS manufacturing costs while increasing coating quality.

Bond Coat Oxidation Research

1. Due to the manufacturing difficulties of CGDS CoNiCrAlY coatings, no XRD analysis or as-sprayed oxidation was conducted. The XRD analysis should be conducted and compared with HVOF to better understand the mass gain differences between the two coating techniques. Oxidation of as-sprayed CGDS coatings should also be conducted as it is believed very little oxides will be formed on the coating surface. This would lead to similar mass gains and oxide formations as the grinded CGDS coatings removing the need for a grinding step and reducing manufacturing costs.

2. The mass gain difference between the HVOF and CGDS coatings is attributed to oxides present in the HVOF coating which act as seed particles and accelerate formation of α-Al_2O_3. Oxidation of the powders prior to deposition or addition of α-Al_2O_3 particles in the powder could further accelerate the formation of an α-Al_2O_3 protective oxide layer. Experiments should therefore be conducted by depositing pre-oxidised or α-Al_2O_3 enriched powders via CGDS and measuring the effect of these seed particles on the mass gain and oxide formation of the coating during oxidation.

3. Long-term oxidation experiments with HVOF and APS samples were halted at 2000h. The HVOF samples however did not show any signs of spallation after this prolonged oxidation. Further tests should be conducted to determine the lifetime of these samples under these conditions. Additional long-term testing should be

conducted with CGDS samples in order to compare their long-term oxidation resistance with other coating techniques. Furthermore, long-term oxidation of as-sprayed samples should be conducted where samples are gradually cooled to room temperature (as opposed to air quenched) in order to reduce the stresses induced by the different coefficients of thermal expansion on each side of the sample. This rapid cooling is thought to have led to premature spalling of the oxide layer as well as deformation of the samples as seen in section 9.3.1.

4. The formation temperature of α-Al_2O_3 is approximately 1050°C. Further oxidation experiments should be conducted between 1050°C and 1200°C and compared with existing data at 1000°C and 1100°C to determine which oxidation temperature yields the best oxidation performance. Testing of nanocrystalline CoNiCrAlY should also be conducted at this optimal oxidation temperature to determine its advantages when compared to conventional coatings.

5. While the oxidation temperature used in this study was 1100°C, current material limitations prevent turbine blades from operating at this temperature. Oxidation at 1100°C is considered a pre-oxidation treatment to initiate the formation of an α-Al_2O_3 protective oxide layer. The optimal time of this pre-oxidation treatment should be determined by conducting the initial oxidation at 1100°C followed by long-term oxidation at the operating temperature expected in a gas turbine.

6. Although oxidation performance is enhanced at 1100°C when compared to 1000°C, no investigation has been done so far to compare the hot corrosion performance at these temperatures. In certain operating environments, hot corrosion resistance could be the limiting factor to turbine blade lifetime. As such, hot corrosion testing should be conducted at these two temperatures and compared.

7. The experiments in this study were focused on determining the optimal oxidation temperature of a stand-alone bond coat. The oxidation performance will however be different when the whole TBC system is considered. As such, further experiments

should be conducted with a superalloy substrate as well as a ceramic top coat to characterise the entire TBC system performance.

8. Finally, as was identified in section 2.4.5.7, the addition of Dysprosium has been shown to be beneficial to both the bond coat and top coat performance. Experiments should be conducted with Dy enriched CoNiCrAlY powder to assess if the oxidation resistance can be further enhanced.

References

[1] R. K. Bhargava, M. Bianchi, A. De Pascale, G. Negri di Montenegro, and A. Peretto, "Gas Turbine Based Power Cycles - A State-of-the-Art Review," *International Conference on Power Engineering 2007*, pp. 309-319, October 2007.

[2] O. Younossi et al., "Military Jet Engine Acquisition," United States Air Force, 2002.

[3] L. S. Langston. [Online]. http://www.memagazine.org/contents/current/features/fahrenheit/fahrenheit.html

[4] J. D. Mattingly, *Elements of Gas Turbine Propulsion*.: McGraw-Hill, 1996.

[5] Y. Tamarin, *Protective Coatings for Turbine Blades*.: ASM International, 2002.

[6] M. R. Dorfman, *Thermal Spray*.: ASM International, 2002.

[7] G. Langer, "The Diversity of Thermal Spray," 2010.

[8] J. R. Davis, *Handbook of Thermal Spray Technology*.: ASM International, 2004.

[9] U. Schulz et al., "Some recent trends in research and technology of advanced thermal barrier coatings," *Aerospace Science and Technology*, vol. 7, pp. 73-80, 2003.

[10] A. P. Alkhimov, A. N. Papyrin, V. F. Kosarev, N. I. Nesterovich, and M. M. Shushpanov, "Gas-dynamic sprayhing method for applying a coating," 5302414, April 1994.

[11] P. Richer, M. Yandouzi, L. Beauvais, and B. Jodoin, "Oxidation behaviour of CoNiCrAlY bond coats produced by plasma, HVOF and cold gas dynamic spraying," *Surface & Coatings Technology*, vol. 204, pp. 3962-3974, 2010.

[12] P. Fauchais, "Understanding Plasma Spraying," *Journal of Physics D: Applied Physics*, vol. 37, pp. R86-R108, 2004.

[13] M. L. Thorpe and H. J. Richter, "A Pragmatic Analysis and Comparison of HVOF Processes," *Journal of Thermal Spray Technology*, vol. 1 (2), pp. 161-170, 1992.

[14] International Thermal Spray Association, "What is Thermal Spray?," International Thermal Spray Association, Fairport Harbor,.

[15] J.-S. Baik and Y.-J. Kim, "Effect of nozzle shape on the performance of high velocity oxygen-fuel thermal spray system," *Surface and Coatings Technology*, vol. 202, pp. 5457-5462, 2008.

[16] Sulzer Metco. [Online]. www.sulzermetco.com

[17] T. Schmidt et al., "From Particle Acceleration to Impact and Bonding in Cold Spraying," *Journal of Thermal Spray Technology*, vol. 18 (5-6), pp. 794-808, 2009.

[18] Plasma Giken. Plasma Giken Co. [Online]. www.plasma.co.jp

[19] Cold Gas Technology. (2011) Cold Gas Technology. [Online]. www.cgt-gmbh.com

[20] M. Yandouzi et al., "Microstructure and mechanical properties of B4C reinforced Al-based matrix composite coatings deposited by CGDS and PGDS processes," *Surface & Coatings Technology*, vol. 205, pp. 2234-2246, 2010.

[21] B. Jodoin et al., "Pulsed-Gas Dynamic Spraying: Process analysis, development and selected coating examples," *Surface & Coatings Technology*, vol. 201, pp. 7544-7551, 2007.

[22] J. Villafuerte, D. Vanderzwet, M. Yandouzi, and B. Jodoin, "Shockwave Induced Spraying," Advanced Materials & Processes magazine, 2009.

[23] S. Kuroda, J. Kawakita, M. Watanabe, and H. Katanoda, "Warm spraying - a novel coating process based on high velocity impact of solid particles," *Science and Technology of Advanced Materials*, vol. 9, pp. 1-17, 2008.

[24] M. Bray, A. Cockburn, and W. O'Neill, "The Laser-assisted Cold Spray process and deposit characterisation," *Surface & Coatings Technology*, vol. 203, pp. 2851-2857, 2009.

[25] R Lupoi, A. Cockburn, M. Sparkes, and W. O'Neill. University of Cambridge, Institute for Manufacturing. [Online]. http://www.ifm.eng.cam.ac.uk/pp/projects/lcs.html

[26] W. Tillmann et al., "Manufacturing Diamond Impregnated Tools for Stone Machining through Thermal Spraying," in *International Thermal Spray Conference*, 2004.

[27] S. Sampath et al., "Role of thermal spray processing method on the microstructure, residual stress and properties of coatings: an integrated study for Ni-5 wt% Al bond coats," *Materials Science and Engineering A*, vol. 364, pp. 216-230, 2004.

[28] H. Herman, S. Sampath, and R. McCune, "Thermal Spray: Current Status and Future Trends," *Materials Research Society Bulletin*, vol. 25 (7), pp. 17-25, 2000.

[29] L. Pawlowski, *The Science and Engineering of Thermal Spray Coatings*.: John Wiley & Sons, 1995.

[30] Victor K. Champagne, *The cold spray materials deposition process*. Cambridge, England: Woodhead Publishing Limited, 2007.

[31] E. Irissou, J.-G. Legoux, A. N. Ryabinin, B. Jodoin, and C. Moreau, "Review on Cold Spray Process and Technology: Part I - Intellectual Property," *Journal of Thermal Spray Technology*, vol. 17(4), pp. 495-515, 2008.

[32] A. H. Shapiro, *The Dynamics and Thermodynamics of Compressible Fluid Flow*., 1953.

[33] E. Sansoucy, "Development of Aluminum-Based Coatings Produced by Cold Gas Dynamic Spraying," University of Ottawa, 2008.

[34] J.-J. Park et al., "Supersonic Nozzle Flow Simulations for Particle Coating

Applications: Effects of Shockwaves, Nozzle Geometry, Ambient Pressure, and Substrate Location upon Flow Characteristics," *Journal of Thermal Spray Technology*, vol. 20 (3), pp. 514-522, 2011.

[35] J.-G. Legoux et al., "Characterization and Performance Evaluation of a Helium Recovery System Designed for Cold Spraying," 2010.

[36] A. P. Alkhimov, V. F. Kosarev, and S. V. Klinkov, "The Features of Cold Spray Nozzle Design," *Journal of Thermal Spray Technology*, vol. 10 (2), pp. 375-381, 2001.

[37] B. Jodoin, "Cold Spray Nozzle Mach Number Limitation," *Journal of Thermal Spray Technology*, vol. 11 (4), pp. 496-507, 2001.

[38] F. Gartner, T. Schmidt, T. Stoltenhoff, and H. Kreye, "Recent Developments and Potential Applications of Cold Spraying," *Advanced Engineering Materials*, vol. 8, no. 7, pp. 611-618, 2006.

[39] B. Jodoin et al., "Effect of particle size, morphology, and hardness on cold gas dynamic sprayed aluminum alloy coatings," *Surface & Coatings Technology*, vol. 201, pp. 3422-3429, 2006.

[40] R. C. Dykhuizen and M. F. Smith, "Gas Dynamic Principles of Cold Spray," *Journal of Thermal Spray Technology*, vol. 7 (2), pp. 205-212, 1998.

[41] T. Klassen et al., "Basic principles and application potentials of cold gas spraying," *Mat.-wiss. u. Werkstofftech*, vol. 41, no. 7, pp. 575-584, 2010.

[42] T. H. Van Steenkiste, J. R. Smith, and R. E. Teets, "Aluminum coatings via kinetic spray with relatively large powder particles," *Surface and Coatings Technology*, vol. 154, pp. 237-252, 2002.

[43] H. Assadi, F. Gartner, T. Stoltenhoff, and H. Kreye, "Bonding mechanism in cold gas spraying," *Acta Materialia*, vol. 51, pp. 4379-4394, 2003.

[44] C.-J. Li, W.-Y. Li, and H. Liao, "Examination of the Critical Velocity for Deposition of Particles in Cold Spraying," *Journal of Thermal Spray Technology*, vol. 15 (2), pp. 212-222, 2006.

[45] T. Stoltenhoff, H. Kreye, and H. J. Richter, "An Analysis of the Cold Spray Process and Its Coatings," *Journal of Thermal Spray Technology*, vol. 11 (4), pp. 542-550, 2002.

[46] M. Grujicic, J. R. Saylor, D. E. Beasley, W. S. DeRosset, and D. Helfritch, "Computational analysis of the interfacial bonding between feed-powder particles and the substrate in the cold-gas dynamic-spray process," *Applied Surface Science*, vol. 219, pp. 211-227, 2003.

[47] T. Schmidt, F. Gartner, H. Assadi, and H. Kreye, "Development of a generalized parameter window for cold spray deposition," *Acta Materialia*, vol. 54, pp. 729-742, 2006.

[48] F. Gartner, T. Stoltenhoff, T. Schmidt, and H. Kreye, "The Cold Spray Process and Its Potential for Industrial Applications," *Journal of Thermal Spray Technology*, vol. 15 (2), pp. 223-232, 2006.

[49] P. C. King, S. H. Zahiri, and M. Jahedi, "Focused ion beam micro-dissection of cold-sprayed particles," *Acta Materialia*, vol. 56, pp. 5617-5626, 2008.

[50] S. Yin, X.-F. Wang, W. Y. Li, and H.-E. Jie, "Effect of substrate hardness on the deformation behavior of subsequently incident particles in cold spraying," *Applied Surface Science*, vol. 257, pp. 7560-7565, 2011.

[51] C.-J. Li et al., "Influence of Spray Materials and Their Surface Oxidation on the Critical Velocity in Cold Spraying," *Journal of Thermal Spray Technology*, vol. 19 (1-2), pp. 95-101, 2010.

[52] W.-Y. Li, C.-J. Li, and H. Liao, "Significant influence of particle surface oxidation on deposition efficiency, interface microstructure and adhesive strength of cold-sprayed

copper coatings," *Applied Surface Science*, vol. 256, pp. 4953-4958, 2010.

[53] T. Schmidt, F. Gartner, and H. Kreye, "New Developments in Cold Spray Based on Higher Gas and Particle Temperatures," *Journal of Thermal Spray Technology*, vol. 15 (4), pp. 488-494, 2006.

[54] D. Zhang, P. H. Shipway, and D. G. McCartney, "Cold Gas Dynamic Spraying of Aluminum: The Role of Substrate Characteristics in Deposit Formation," *Journal of Thermal Spray Technology*, vol. 14(1), pp. 106-116, 3006.

[55] R. C. Dykhuizen et al., "Impact of High Velocity Cold Spray Particles," *Journal of Thermal Spray Technology*, vol. 8 (4), pp. 559-564, 1999.

[56] M. Grujicic, C. L. Zhao, W. S. DeRosset, and D. Helfritch, "Adiabatic shear instability based mechanism for particles/substrate bonding in the cold-gas dynamic-spray process," *Materials and Design*, vol. 25, pp. 681-688, 2004.

[57] Q. Wang, N. Birbilis, and M.-X. Zhang, "Interfacial structure between particles in an aluminum deposit produced by cold spray," *Materials Letters*, vol. 65, pp. 1576-1578, 2011.

[58] T. Hussain, D. G. McCartney, P. H. Shipway, and D. Zhang, "Bonding Mechanisms in Cold Spraying: The Contributions of Metallurgical and Mechanical Components," *Journal of Thermal Spray Technology*, vol. 18(3), pp. 364-379, 2009.

[59] P. C. King. and M. Jahedi, "Relationship between particle size and deformation in the cold spray process," *Applied Surface Science* , vol. 256, pp. 1735-1738, 2010.

[60] L. Ajdelsztajn, B. Jodoin, and J. M. Schoenung, "Synthesis and mechanical properties of nanocrystalline Ni coatings produced by cold gas dynamic spraying," *Surface & Coatings Technology* , vol. 201, pp. 1166-1172, 2006.

[61] T. W. Wright, "Shear band susceptibility: work hardening materials," *International Journal of Plasticity*, vol. 8 (5), pp. 583-602, 1992.

[62] L. Ajdelsztajn, A. Zuniga, B. Jodoin, and E. J. Lavernia, "Cold gas dynamic spraying of a high temperature Al alloy," *Surface & Coatings Technology*, vol. 201, pp. 2109-2116, 2006.

[63] L. Ajdelsztajn, B. Jodoin, P. Richer, E. Sansoucy, and E. J. Lavernia, "Cold Gas Dynamic Spraying of Iron-Base Amorphous Alloy," *Journal of Thermal Spray Technology*, vol. 15 (4), pp. 495-500, 2006.

[64] L. Ajdelsztajn, B. Jodoin, G. E. Kim, and J. M. Schoenung, "Cold Spray Deposition of Nanocrystalline Aluminum Alloys," *Metallurgical and materials transactions A*, vol. 36A, pp. 657-666, 2005.

[65] C.-J. Li et al., "Characterization of Nanostrucutred WC-Co Deposited by Cold Spraying," *Journal of Thermal Spray Technology*, vol. 16 (5-6), pp. 1011-1020, 2007.

[66] E. Sansoucy, P. Marcoux, L. Ajdelsztajn, and B. Jodoin, "Properties of SiC-reinforced aluminum alloy coatings produced by the cold gas dynamic spraying process," *Surface & Coatings Technology*, vol. 202, pp. 3988-3996, 2008.

[67] A. C. Hall, L. N. Brewer, and T. J. Roemer, "Preparation of Aluminum Coatings Containing Homogenous Nanocrystalline Microstructures Using the Cold Spray Process," *Journal of Thermal Spray Technology*, vol. 17 (3), pp. 352-359, 2008.

[68] L. Ajdelsztajn, A. Zuniga, B. Jodoin, and E. J. Lavernia, "Cold-Spray Processing of a Nanocrystalline Al-Cu-Mg-Fe-Ni Alloy with Sc," *Journal of Thermal Spray Technology*, vol. 15 (2), pp. 184-190, 2006.

[69] P. Richer, B. Jodoin, L. Ajdelsztajn, and E. J. Laverni, "Substrate Roughness and Thickness Effects on Cold Spray Nanocrystalline Al-Mg Coatings," *Journal of Thermal Spray Technology*, vol. 15 (2), pp. 246-254, 2006.

[70] P. Richer, A. Zuniga, M. Yandouzi, and B. Jodoin, "CoNiCrAlY microstructural changes induced during Cold Gas Dynamic Spraying," *Surface & Coatings*

Technology, vol. 203, pp. 364-371, 2008.

[71] S. Cadney, M. Brochu, P. Richer, and B. Jodoin, "Cold gas dynamic spraying as a method for freeforming and joining materials," *Surface & Coatings Tecyhnology*, vol. 202, pp. 2801-2806, 2008.

[72] J. Pattison, S. Celotto, R. Morgan, M. Bray, and W. O'Neill, "Cold gas dynamic manufacturing: A non-thermal approach to freeform fabrication," *International Journal of Machine Tools & Manufacture*, vol. 47, pp. 627-634, 2007.

[73] U.S. Army Research Laboratory, "Materials Deposition, Cold Spray," Department of Defense, MIL-STD-3021, 2008.

[74] C. Borchers, F. Gartner, T. Stoltenhoff, and H. Kreye, "Formation of persistent dislocation loops by ultra-high strain-rate deformation during cold spraying," *Acta Materialia*, vol. 53, pp. 2991-3000, 2005.

[75] E. Sansoucy, G. E. Kim, A. L. Moran, and B. Jodoin, "Mechanical Characteristics of Al-Co-Ce Coatings Produced by the Cold Spray Process," *Journal of Thermal Spray Technology*, vol. 16 (5-6), pp. 651-660, 2007.

[76] V. Luzin, K. Spencer, and M.-X. Zhang, "Residual stress and thermo-mechanical properties of cold spray metal coatings," *Acta Materialia*, vol. 59, pp. 1259-1270, 2011.

[77] J. Vlcek, L. Gimeno, H. Huber, and E. Lugscheider, "A Systematic Approach to material Eligibility for the Cold-Spray Process," *Journal of Thermal Spray Technology*, vol. 14 (1), pp. 125-133, 2005.

[78] S. V. Raj, C. Barrett, J. Karthikeyan, and R. Garlick, "Comparison of the cyclic oxidation behaviour of cold sprayed CuCrAl-coated and uncoated GRCop-84 substrates for space launch vehicles," *Surface & Coatings Technology*, vol. 201, pp. 7222-7234, 2007.

[79] K. Taylor, B. Jodoin, and J. Karov, "Particle Loading Effect in Cold Spray," *Journal of Thermal Spray Technology*, vol. 15 (2), pp. 273-279, 2006.

[80] U.S. Army Research Lab, "Economics of Cold Spray Cost-Analysis," U.S. Army Research Lab,.

[81] Y. Xiong, X. Xiong, S. Yoon, G. Bae, and C. Lee, "Dependence of Bonding Mechanisms of Cold Sprayed Coatings on Strain-Rate-Induced Non-Equilibrium Phase Transformation," *Journal of Thermal Spray Technology*, vol. 20(4), pp. 860-865, 2011.

[82] J. Pattison, S. Celotto, A. Khan, and W. O'Neill, "Standoff distance and bow shock phenomena in the Cold Spray process," *Surface & Coatings Technology*, vol. 202, pp. 1443-1454, 2008.

[83] S. Yin, X.-F. Wang, W.-Y. Li, and X.-P. Guo, "Examination on Substrate Preheating Process in Cold Gas Dynamic Spraying," *Journal of Thermal Spray Technology*, vol. 20 (4), pp. 852-859, 2011.

[84] S. Lange et al., "Velocity Diagnostics for Gas Velocity Distributions in Cold Gas and Plasma Spraying using Non-Resonant Laser Scattering," *Journal of Thermal Spray Technology*, vol. 20 (1-2), pp. 12-20, 2011.

[85] P. Fauchais and M. Vardelle, "Sensors in Spray Processes," *Journal of Thermal Spray Technology*, vol. 19 (4), pp. 668-694, 2010.

[86] B. Jodoin, F. Raletz, and M. Vardelle, "Cold spray modeling and validation using an optical diagnostic method," *Surface and Coatings Technology*, vol. 200, pp. 4424-4432, 2006.

[87] P. Fauchais, G. Montavon, and G. Bertrand, "From Powders to Thermally Sprayed Coatings," *Journal of Thermal Spray Technology*, vol. 19 (1-2), pp. 56-80, 2010.

[88] M. K. Stanford and C. DellaCorte, "Water Atomization of Barium Fluoride-Calcium Fluoride for Enhanced Flow Characteristics of PS304 Feedstock Powder Blend,"

NASA, 2003-212125, 2003.

[89] S. Gu and S. Kamnis, "Numerical modelling of in-flight particle dynamics of non-spherical powder," *Surface and Coatings Technology*, vol. 203, pp. 3485-3490, 2009.

[90] ASM International, "Hot Corrosion in Gas Turbines," in *High Temperature Corrosion and Materials Application*., 2007, ch. 9, pp. 249-258.

[91] D. D. Hass, "Directed Vapor Deposition of Thermal Barrier Coatings," University of Virginia, Ph.D. Dissertation 2000.

[92] D. Stöver, H. B. Guo, and R. Vaßen, "Thermophysical properties and thermal cycling behavior of plasma sprayed thick thermal barrier coatings," *Surface and Coatings Technology*, 2005.

[93] I. O. Golosnoy, S. A. Tsipas, and T. W. Clyne, "An Analytical Model for Simulation of Heat Flow in Plasma-Sprayed Thermal Barrier Coatings," *Journal of Thermal Spray Technology*, vol. 14 (2), pp. 205-214, 2005.

[94] S. Stecura, "Effects of Compositional Changes on the Performance of a Thermal Barrier Coating System," National Aeronautics and Space Administration, 1978.

[95] Z. Li, S. Qian, W. Wang, and J. Liu, "Microstructure and oxidation resistance of magnetron-sputtered nanocrystalline NiCoCrAlY coatings on nickel-based superalloy," *Journal of Alloys and Compounds*, vol. 505, pp. 675-679, 2010.

[96] L. He et al., "Substrate Effects on the High-Temperature Oxidation Behavior of Thermal Barrier Coatings," *Journal of Materials Sciences and Technology*, vol. 25 (6), pp. 799-802, 2009.

[97] A. G. Evans, D. R. Mumm, J. W. Hutchinson, G. H. Meier, and F. S. Pettit, "Mechanisms controlling the durability of thermal barrier coatings," *Progress in Materials Science*, vol. 46, pp. 505-533, 2001.

[98] K. Messaoudi, A. M. Huntz, and B. Lesage, "Diffusion and growth mechanism of Al2O3 scales on ferritic Fe-Cr-Al alloys," *Materials Science and Engineering*, vol. A247, pp. 248-262, 1998.

[99] L. Ajdelsztajn, F. Tang, G. E. Kim, V. Provenzano, and J. M. Schoenung, "Synthesis and Oxidation Behavior of Nanocrystalline MCrAlY Bond Coatings," *Journal of Thermal Spray Technology*, vol. 14 (1), pp. 23-30, 2005.

[100] J. Stringer, "Hot Corrosion of High-Temperature Alloys," *Annual Review of Materials Science*, vol. 7, pp. 477-509, 1977.

[101] T. Sourmail. Coatings for Turbine Blades. [Online]. http://www.msm.cam.ac.uk/phase-trans/2003/Superalloys/coatings/index.html

[102] I.-H. Shin et al., "Estimation of spallation life of thermal barrier coatings of gas turbine blade by thermal fatigue test," *Surface & Coatings Technology*, 2011.

[103] N. Curry, N. Markocsan, X.-H. Li, A. Tricoire, and M. Dorfman, "Next Generation Thermal Barrier Coatings for the Gas Turbine Industry," *Journal of Thermal Spray Technology*, vol. 20 (1-2), pp. 108-115, 2011.

[104] R. Eriksson, H. Brodin, S. Johansson, L. Östergren, and X.-H. Li, "Influence of isothermal and cyclic heat treatments on the adhesion of plasma sprayed thermal barrier coatings," *Surface & Coatings Technology*, 2011.

[105] H.-X. Deng, H.-J. Shi, H.-C. Yu, and B. Zhong, "Effect of heat treatment at 900C on microstructural and mechanical properties of thermal barrier coatings," *Surface & Coatings Technology*, 2011.

[106] U. Schulz et al., "Some recent trends in research and technology of advanced thermal barrier coatings," *Aerospace Science and Technology*, vol. 7, pp. 73-80, 2003.

[107] W. Beele, G. Maijnissen, and A. Van Lieshout, "The evolution of thermal barrier coatings - status and upcoming solutions for today's key issues," *Surface & Coatings*

Technology, vol. 120-121, pp. 61-67, 1999.

[108] ALD Vacuum Technologies. ALD Vacuum Technologies. [Online]. http://web.ald-vt.de/cms/?id=68

[109] A. Tricoire et al., "New concepts for plasma sprayed zirconia TBCs for aeronautical applications," in *International Thermal Spray Conference*, Bassel, Switzerland, 2005.

[110] M. Madhwal, E.H. Jordan, and M. Gell, "Failure mechanisms of dense vertically-cracked thermal barrier coatings," *Materials Science and Engineering A*, vol. 384, pp. 151-161, 2004.

[111] A. Hospach, G. Mauer, R. Vaβen, and D. Stöver, "Columnar-Structured Thermal Berrier Coatings (TBCs) by Thin Film Low-Pressure Plasma Spraying (LPPS-TF)," *Journal of Thermal Spray Technology*, vol. 20 (1-2), pp. 116-120, 2011.

[112] M. Shibata et al., "Comparison of Microstructure and Oxidation Behavior of CoNiCrAlY Vond Coatings Prepared by Different Thermal Spray Processes," *Material Transactions*, vol. 47 (7), pp. 1638-1642, 2006.

[113] V. Higuera, F. J. Belzunce, and J. Riba, "Influence of the thermal-spray procedure on the properties of a CoNiCrAlY coating," *Surface & Coatings Technology*, vol. 200, pp. 5550-5556, 2006.

[114] M. Y. Ali, X. Chen, and G. M. Newaz, "Oxide Layer Develpment Under Thermal Cycling and Its Role on Damage Evolution and Spallation in TBC System," *Journall of Material Science*, vol. 36, pp. 4535-4542, 2001.

[115] H. Kazempour-Liacy, S. Abouali, and M. Akbari-Garakani, "Failure analysis of a first stage gas turbine blade," *Engineering Failure Analysis*, vol. 18, pp. 517-522, 2011.

[116] I. McCreary, "The economic cost of FOD to airlines," Insight SRI, 2008.

[117] P.K Wright and A.G. Evans, "Mechanisms Governing the Performance of Thermal

Barrier Coatings," *Current Opinion in Solid State & Material Science*, vol. 4, pp. 255-265, 1999.

[118] Y. H. Sohn, J. H. Kim, E. H. Jordan, and M. Gell, "Thermal cycling of EB-PVD/MCrAlY thermal barrier coatings: I Microstructural development and spallation mechanisms," *Surface & Coatings Technology*, vol. 146-147, pp. 70-78, 2001.

[119] L. Ajdelsztajn et al., "Oxidation Behavior of HVOF Sprayed Nanocrystalline NiCrAlY Powder," *Material Science and Engineering A*, vol. 338, pp. 33-43, 2002.

[120] F. Tang, L. Ajdelsztajn, G. E. Kim, V. Provenzano, and J. M. Schoenung, "Effects of surface oxidation during HVOF processing on the primary stage oxidation of a CoNiCrAlY coating," *Surface & Coatings Technology*, vol. 185, pp. 228-233, 2004.

[121] P. Richer, "Development of Convetional and Nanocrystalline Bond Coats by Cold Gas Dynamic Spraying for Aerospace Thermal Barrier Coatings," University of Ottawa, 2010.

[122] C. Kaplin and M. Brochu, "Effects of water vapor on high temperature oxidation of cryomilled NiCoCrAlY coatings in air and low-SO2 environments," *Surface and Coatings Technology*, vol. 205, pp. 4221-4227, 2011.

[123] R. Mobarra, A. H. Jafari, and M. Karaminezhaad, "Hot corrosion behavior of MCrAlY coatings on IN738LC," *Surface and Coatings Technology*, vol. 201, pp. 2202-2207, 2006.

[124] Z. Zhou, H. Guo, J. Wang, M. Abbas, and S. Gong, "Microstructure of oxides in thermal barrier coatings grown under dry/humid atmosphere," *Corrosion Science*, vol. 53, pp. 2630-2635, 2011.

[125] W. R. Chen, E. Irissou, X. Wu, J.-G. Legoux, and B. R. Marple, "The Oxidation Behavior of TBC with Cold Spray CoNiCrAlY BondCoat," *Journal of Thermal Spray Technology*, vol. 20 (1-2), pp. 132-138, 2011.

[126] Y. Li, C.-J. Li, G.-J. Yang, and L.-K. Xing, "Thermal fatigue behavior of thermal barrier coatings with the MCrAlY bond coats by cold spraying and low-pressure plasma spraying," *Surface & Coatings Technology*, vol. 205, pp. 2225-2233, 2010.

[127] Y. Li, C.-J. Li, Q. Zhang, G.-J. Yang, and C.-X. Li, "Influence of TGO Composition on the Thermal Shock Lifetime of Thermal Barrier Coatings with Cold-sprayed MCrAlY Bond Coat," *Journal of Thermal Spray Technology*, vol. 19 (1-2), pp. 168-177, 2010.

[128] Q. Zhang, C.J. Li, C.X. Li, G.J. Yang, and S.C. Lui, "Study of Oxidation Behavior of Nanostructured NiCrAlY Bond Coatings Deposited by Cold Spraying," *Surface and Coatings Technology*, vol. 202, pp. 3378-3384, 2008.

[129] Z. Li, S. Qian, and W. Wang, "Characterization and oxidation behavior of NiCoCrAlY coating fabricated by electrophoretic deposition and vacuum heat treatment," *Applied Surface Science*, vol. 257, pp. 4616-4620, 2011.

[130] J. Lu, S. Zhu, and F. Wang, "High temperature corrosion behavior of an AIP NiCoCrAlY coating modified by aluminizing," *Surface & Coatings Technology*, vol. 205, pp. 5053-5058, 2011.

[131] T. Liang, H. Guo, H. Peng, and S. Gong, "Microstructural evolution of CoCrAlY bond coat on Ni-based superalloy DZ 125 at 1050C," *Surface and Coatings Technology*, vol. 205, pp. 4374-4379, 2011.

[132] D. Toma, W. Brandl, and U. Köster, "Studies on the transient stage of oxidation of VVPS and HVOF sprayed MCrAlY coatings," *Surface and Coatings Technology*, vol. 120-121, pp. 8-15, 1999.

[133] S. Saeidi, K. T. Voisey, and D. G. McCartney, "The Effect of Heat Treatment on the oxidation Behavior of HVOF and VPS CoNiCrAlY Coatings," *Journal of Thermal Spray Technology*, vol. 18 (2), pp. 209-216, 2009.

[134] M. Di Ferdinando et al., "Isothermal oxidation resistance comparison between air plasma sprayed, vacuum plasma sprayed and high velocity oxygen fuel sprayed CoNiCrAlY bond coats," *Surface and Coatings Technology*, vol. 204, pp. 2499-2503, 2010.

[135] P. Souza Santos, H. Souza Santos, and S.P. Toledo, "Standard Transition Aluminas, Electron Microscopy Studies," *Materials Research*, vol. 3, no. 4, pp. 104-114, 2000.

[136] L. Y. Ni, C. Liu, H. Huang, and C. G. Zhou, "Thermal Cycling Behavior of Thermal Barrier Coatings with HVOF NiCrAlY Bond Coat," *Journal of Thermal Spray Technology*, 2011.

[137] P. K. Kiyohara, H. Souza Santos, A. C. Vieira Coelho, and P. Souza Santos, "Structure, Surface Area and Morphology of Aluminas from Thermal Decomposition of AL(OH)(CH3COO)2 Crystals," *Anais da Academia Brasileira Ciências*, vol. 72, no. 004, pp. 471-495, 2000.

[138] A. Boumaza et al., "Transition alumina phases induced by heat treatment of boehmite: An X-ray diffraction and infrared spectroscopy study," *Journal of Solid State Chemistry*, vol. 182, pp. 1171-1176, 2009.

[139] J.-P. Ahn, J.-K. Park, and H.-W. Lee, "Effect of compact structures on the phase transition, subsequent densification and microstructure evolution during sintering of ultrafine gamma alumina powder," *NanoStructured Materials*, vol. 11, no. 1, pp. 133-140, 1999.

[140] V. Edlmayr, M. Moser, C. Walter, and C. Mitterer, "Thermal stability of sputtered Al2O3 coatings," *Surface & Coatings Technology*, vol. 204, pp. 1576-1581, 2010.

[141] K I Rybakov, A G Eremeev, S V Egorov, Z Pajkic, and M Willert-Porada, "Effect of Microwave Heating on Phase Transformations in Nanostructured Alumina," *Journal of Physics D: Applied Physics*, vol. 41, 2008.

[142] H. C. Kao, W. J. Wei, and C. Y. Huang, "Two-stage densification of ultrafine transition alumina seeded with alpha-phase particulates," *Journal of Ceramic Processing Research*, vol. 4 (1), pp. 34-41, 2003.

[143] H. Xu, S. Gong, Y. Shang, and C. Zhang, "Experimental and computational study on hot-fatigue process of thermal barrier coatings by EB-PVD," *Intermetallics*, vol. 13, pp. 315-322, 2005.

[144] A. Hesnawi, H. Li, Z. Zhou, S. Gong, and H. Xu, "Effect of Surface Condition During Pre-Oxidation Treatment on isothermal Oxidation behaviour of MCrAlY Bond Coat Prepared by EB-PVD," *Surface and Coatings Technology*, vol. 201, pp. 6793-6796, 2007.

[145] W. R. Chen, X. Wu, B. R. Marple, R. S. Lima, and P. C. Patnaik, "Pre-oxidation and TGO growth behaviour of an air-plasma-sprayed thermal barrier coating," *Surface and Coatings Technology*, vol. 202, pp. 3787-3796, 2008.

[146] D. Mercier, C. Kaplin, G. Goodall, G. E. Kim, and M. Brochu, "Parameters influencing the oxidation behavior of cryomilled CoNiCrAlY," *Surface & Coatings Technology*, vol. 205, pp. 2546-2553, 2010.

[147] Y. Li, C.-J. Li, Q. Zhang, L.-K. Xing, and G.-J. Yang, "Effect of Chemical Compositions and Surface Morphologies of MCrAlY Coating on its Isothermal Oxidation Behavior," *Journal of Thermal Spray Technology*, vol. 20 (1-2), pp. 121-131, 2011.

[148] U. Schulz, O. Bernardi, A. Ebach-Stahl, R. Vassen, and D. Sebold, "Improvement of EB-PVD thermal barrier coatings by reatments of a vacuum plasma-sprayed bond coat.," *Surface and Coatings Technology*, vol. 203, pp. 160-170, 2008.

[149] D. Mercier, B. D. Gauntt, and M. Brochu, "Thermal stability and oxidation behavior of nanostructured NiCoCrAlY coatings," *Surface and Coatings Technology*, vol. 205, pp. 4162-4168, 2011.

[150] C. Suryanarayana and C. C. Koch, "Nanocrystalline Materials - Current research and future directions," *Hyperfine Interactions*, vol. 130, pp. 5-44, 2000.

[151] F. Tang, L. Ajdelsztajn, and J. M. Schoenung, "Influence of Cryomilliong on the Morphology and Composition of the Oxide Scales Formed on HVOF CoNiCrAlY Coatings," *Oxidation of Metals*, vol. 61 (314), pp. 219-238, 2004.

[152] K. Ma and J. M. Schoenung, "Isothermal oxidation behavior of cryomilled NiCrAlY bond coat: Homogeneity and growth rate of TGO," *Surface and Coatings Technology*, vol. 205, pp. 5178-5185, 2011.

[153] F. Wang, "The Effect of Nanocrystallization on the Selective Oxidation andAdhesion of Al2O3 Scales," *Oxidation of Metals*, vol. 48, pp. 215-224, 1997.

[154] X. Huang, "High Temperature Radiation Heat Transfer Performance of Thermal Barrier Coatings with Multiple Layered Structures," *Journal of Engineering for Gas Turbines and Power*, vol. 131, pp. 1-7, 2009.

[155] N. M. Yanar, G. H. Meier, and F. S. Pettit, "The Effects of Oxidation-Induced Failures on Thermal Barrier Coatings with Platinum Aluminide and NiCoCrAlY Bond Coats," Materials Science and Engineering, University of Pittsburgh for the Air Force Office of Scientific Research, 2001.

[156] H. Peng, H. Guo, J. He, and S. Gong, "Oxidation and diffusion barrier behavior of double-layer NiCoCrAlY coatings produced by plasma activated EB-PVD," *Surface & Coatings Technology*, vol. 205, pp. 4659-4664, 2011.

[157] A. Fossati et al., "Improvement of the isothermal oxidation resistance of CoNiCrAlY coating sprayed by High Velocity Oxygen Fuel," *Surface & Coatings Technology*, vol. 204, pp. 3723-3728, 2010.

[158] H. Lan, Z.-G. Yang, Z.-X. Xia, Y.-D. Zhang, and C. Zhang, "Effect of dysprosium addition on the cyclic oxidation behaviour of CoNiCrAlY alloy," *Corrosion Science*,

vol. 53, pp. 1476-1483, 2011.

[159] W. J. Brindley, R. A. Miller, and B. J. M. Aikin, "Method of producing controlled thermal expansion coat for thermal barrier coatings," 6,093,454, July 25, 2000.

[160] N. S. Cheruvu, K. S. Chan, and D. W. Gandy, "Effect of Time and Temperature on Thermal Barrier Coating Failure Mode Under Oxidizing Environment," *Journal of Engineering for Gas Turbines and Power*, vol. 131, pp. 1-7, 2009.

[161] M. Van Dyke, *An Album of Fluid Motion*.: The Parabolic Press, 1982.

[162] Z. Zarei, D. L. Frost, and E. V. Timofeev, "Numerical modelling of the entrainment of particles in invicid supersonic flow," *Shock Waves*, vol. 21, pp. 341-355, 2011.

[163] A. G. Evans, D. R. Mumm, J. W. Hutchison, G. H. Meier, and F. S. Pettit, "Mechanisms controlling the durability of thermal barrier coatings," *Progress in Materials Science*, vol. 46, pp. 505-553, 2001.

[164] P. Richer, A. Zúñiga, M. Yandouzi, and B. Jodoin, "CoNiCrAlY microstructural changes induced during Cold Gas Dynamic Spraying," *Surface & Coatings Technology*, no. 203, pp. 364-371, 2008.

[165] H.C. Kao, W.J. Wei, and C.Y. Huang, "Twostage densification of ultrafine transition alumina seeded with alpha-phase particulates," *Journal of Ceramic Processing Research*, vol. 4, no. 1, pp. 34-41, 2003.

[166] N.S. Cheruvu, K.S. Chan, and D.W. Gandy, "Effect of Time and Temperature on Thermal Barrier Coatign Failure Mode Under Oxidizing Environment," *Jour. Eng. Gas Turb. and Pow.*, vol. 131, pp. 1-7, 2009.

[167] Q. Zhang, C.-J. Li, C.-X. Li, G.-J. Yang, and S.-C. Lui, "Study of oxidation behavior of nanostructured NiCrAlY bond coatings deposited by cold spraying," *Surf. Coat. Technol*, vol. 202, pp. 3378-3384, 2008.

[168] W.R Chen, X. Wu, B.R. Marple, R.S. Lim, and P.C. Patnaik, *Surface & Coatings Technology*, no. 202, pp. 3787-3796, 2008.

APPENDIX A

```
edge create "inlet" straight "vertex.1" "vertex.2"
edge create "conv" straight "vertex.2" "vertex.3"
edge create "1" straight "vertex.3" "vertex.4"
edge create "2" straight "vertex.4" "vertex.5"
edge create "3" straight "vertex.5" "vertex.6"
edge create "4" straight "vertex.6" "vertex.7"
edge create "5" straight "vertex.7" "vertex.8"
edge create "6" straight "vertex.8" "vertex.9"
edge create "7" straight "vertex.9" "vertex.10"
edge create "div1" straight "vertex.10" "vertex.11"
edge create "div2" straight "vertex.11" "vertex.12"
edge create "outlet" straight "vertex.12" "vertex.13"
edge create "nzthick" straight "vertex.12" "vertex.17"
edge create "out1" straight "vertex.17" "vertex.18"
edge create "axis" straight "vertex.1" "vertex.16"
edge create "end" straight "vertex.18" "vertex.16"
edge create "outaxis" straight "vertex.13" "vertex.16"
edge create "convlim" straight "vertex.3" "vertex.14"
edge create "convaxis" straight "vertex.14" "vertex.1"
edge create "moc" straight "vertex.11" "vertex.15"
edge create "mocaxis" straight "vertex.14" "vertex.15"
edge create "divaxis" straight "vertex.15" "vertex.13"
face create "fluid" wireframe "inlet" "conv" "1" "2" "3" "4" "5" "6" "7" "div" "out1" "out2"
"end" "axis" real
face create "Inlet" wireframe "inlet" "conv" "convlim" "convaxis" real
face mesh "Inlet" map intervals 15
face create "MOC" wireframe "convlim" "1" "2" "3" "4" "5" "6" "7" "div1" "moc" "mocaxis"
real
face mesh "MOC" map intervals 30
face create "DIV" wireframe "div2" "outlet" "divaxis" "moc" real
face mesh "DIV" map intervals 60
face create "SOD" wireframe "outlet" "nzthick" "out1"  "end" "outaxis" real
face mesh "SOD" map intervals 100
physics create "wall" btype "WALL" edge "conv" "1" "2" "3" "4" "5" "6" "7" "div1" "div2"
"nzthick"
physics create "substrate" btype "WALL" edge "end"
physics create "Inlet" btype "PRESSURE_INLET" edge "inlet"
physics create "Partinlet" btype "PRESSURE_INLET" edge "partinlet"
physics create "ambient" btype "PRESSURE_OUTLET" edge "out1"
physics create "axis" btype "AXIS" edge "convaxis" "mocaxis" "partaxis" "divaxis"
"outaxis"
export fluent5 "NAME.msh" nozval
save
```

APPENDIX B

```
(cx-gui-do cx-activate-item "MenuBar*ReadSubMenu*Case...")
(cx-gui-do cx-set-text-entry "Select File*Text" "SOD1.msh")
(cx-gui-do cx-activate-item "Select File*OK")
(cx-gui-do cx-activate-item "MenuBar*ModelsSubMenu*Solver...")
(cx-gui-do cx-set-toggle-button
"Solver*Table1*Frame1(Solver)*ToggleBox1(Solver)*Density Based" #f)
(cx-gui-do cx-activate-item "Solver*Table1*Frame1(Solver)*ToggleBox1(Solver)*Density
Based")
(cx-gui-do cx-set-toggle-button
"Solver*Table1*Frame5(Space)*ToggleBox5(Space)*Axisymmetric" #f)
(cx-gui-do cx-activate-item
"Solver*Table1*Frame5(Space)*ToggleBox5(Space)*Axisymmetric")
(cx-gui-do cx-activate-item "Solver*PanelButtons*PushButton1(OK)")
(cx-gui-do cx-activate-item "MenuBar*ModelsSubMenu*Energy...")
(cx-gui-do cx-set-toggle-button
"Energy*Frame1(Energy)*Table1(Energy)*Frame1*ToggleBox1*CheckButton1(Energy
Equation)" #f)
(cx-gui-do cx-activate-item
"Energy*Frame1(Energy)*Table1(Energy)*Frame1*ToggleBox1*CheckButton1(Energy
Equation)")
(cx-gui-do cx-activate-item "Energy*PanelButtons*PushButton1(OK)")
(cx-gui-do cx-activate-item "MenuBar*ModelsSubMenu*Viscous...")
(cx-gui-do cx-set-toggle-button "Viscous
Model*Table1*Frame1(Model)*ToggleBox1(Model)*Inviscid" #f)
(cx-gui-do cx-activate-item "Viscous
Model*Table1*Frame1(Model)*ToggleBox1(Model)*Inviscid")
(cx-gui-do cx-activate-item "Viscous Model*PanelButtons*PushButton1(OK)")
(cx-gui-do cx-activate-item "MenuBar*ModelsSubMenu*Discrete Phase...")
(cx-gui-do cx-set-toggle-button "Discrete Phase
Model*Frame1*Table1*Frame1(Interaction)*CheckButton1(Interaction with Continuous
Phase)" #f)
(cx-gui-do cx-activate-item "Discrete Phase
Model*Frame1*Table1*Frame1(Interaction)*CheckButton1(Interaction with Continuous
Phase)")
(cx-gui-do cx-set-integer-entry "Discrete Phase
Model*Frame2*Frame3(Tracking)*Table1*Frame3*Frame1(  Tracking
Parameters)*IntegerEntry1(Max  Number of Steps)" 2000)
(cx-gui-do cx-activate-item "Discrete Phase Model*PanelButtons*PushButton1(OK)")
(cx-gui-do cx-activate-item "Information*OK")
(cx-gui-do cx-activate-item "MenuBar*DefineMenu*Operating Conditions...")
(cx-gui-do cx-set-real-entry-list "Operating
Conditions*Table1*Frame1(Pressure)*Table1(Pressure)*RealEntry2(Operating Pressure)" '(
101325))
(cx-gui-do cx-activate-item "Operating Conditions*PanelButtons*PushButton1(OK)")
```

```
(cx-gui-do cx-activate-item "MenuBar*DefineMenu*Boundary Conditions...")
(cx-gui-do cx-set-list-selections "Boundary Conditions*Table1*Frame1*List1(Zone)" '( 2))
(cx-gui-do cx-activate-item "Boundary Conditions*Table1*Frame1*List1(Zone)")
(cx-gui-do cx-activate-item "Boundary Conditions*PanelButtons*PushButton1(OK)")
(cx-gui-do cx-activate-item "fluid-2-1*PanelButtons*PushButton2(Cancel)")
(cx-gui-do cx-set-list-selections "Boundary Conditions*Table1*Frame1*List1(Zone)" '( 3))
(cx-gui-do cx-activate-item "Boundary Conditions*Table1*Frame1*List1(Zone)")
(cx-gui-do cx-activate-item "Boundary Conditions*PanelButtons*PushButton1(OK)")
(cx-gui-do cx-set-real-entry-list "pressure-inlet-6-
1*Frame4*Frame3(Momentum)*Table1*Table2*RealEntry2(Gauge Total Pressure)" '(
4000000))
(cx-gui-do cx-set-real-entry-list "pressure-inlet-6-
1*Frame4*Frame3(Momentum)*Table1*Table3*RealEntry2(Supersonic/Initial Gauge
Pressure)" '( 3898675))
(cx-gui-do cx-set-text-entry "pressure-inlet-6-1*TextEntry1(Zone Name)" "inlet")
(cx-gui-do cx-set-real-entry-list "pressure-inlet-6-
1*Frame4*Frame4(Thermal)*Table1*Table1*RealEntry2(Total Temperature)" '( 900))
(cx-gui-do cx-set-real-entry-list "pressure-inlet-6-
1*Frame4*Frame6(Species)*Table1*Frame1(Species Mass Fractions)*Table1(Species Mass
Fractions)*Table2*RealEntry2(he)" '( 1))
(cx-gui-do cx-activate-item "pressure-inlet-6-1*PanelButtons*PushButton1(OK)")
(cx-gui-do cx-set-list-selections "Boundary Conditions*Table1*Frame1*List1(Zone)" '( 4))
(cx-gui-do cx-activate-item "Boundary Conditions*Table1*Frame1*List1(Zone)")
(cx-gui-do cx-activate-item "Boundary Conditions*PanelButtons*PushButton1(OK)")
(cx-gui-do cx-set-real-entry-list "pressure-outlet-4-
1*Frame4*Frame3(Momentum)*Table1*Table2*RealEntry2(Gauge Pressure)" '( 0))
(cx-gui-do cx-set-real-entry-list "pressure-inlet-6-
1*Frame4*Frame6(Species)*Table1*Frame1(Species Mass Fractions)*Table1(Species Mass
Fractions)*Table2*RealEntry2(he)" '( 1))
(cx-gui-do cx-activate-item "pressure-outlet-4-1*PanelButtons*PushButton1(OK)")
(cx-gui-do cx-set-list-selections "Boundary Conditions*Table1*Frame1*List1(Zone)" '( 5))
(cx-gui-do cx-activate-item "Boundary Conditions*Table1*Frame1*List1(Zone)")
(cx-gui-do cx-activate-item "Boundary Conditions*PanelButtons*PushButton1(OK)")
(cx-gui-do cx-set-real-entry-list "pressure-inlet-5-
1*Frame4*Frame3(Momentum)*Table1*Table2*RealEntry2(Gauge Total Pressure)" '(
1100000))
(cx-gui-do cx-set-real-entry-list "pressure-inlet-5-
1*Frame4*Frame3(Momentum)*Table1*Table3*RealEntry2(Supersonic/Initial Gauge
Pressure)" '( 1000000))
(cx-gui-do cx-set-real-entry-list "pressure-inlet-6-
1*Frame4*Frame6(Species)*Table1*Frame1(Species Mass Fractions)*Table1(Species Mass
Fractions)*Table2*RealEntry2(he)" '( 1))
(cx-gui-do cx-activate-item "pressure-inlet-5-1*PanelButtons*PushButton1(OK)")
(cx-gui-do cx-activate-item "Boundary Conditions*PanelButtons*PushButton2(Cancel)")
(cx-gui-do cx-activate-item "MenuBar*DefineMenu*Injections...")
(cx-gui-do cx-activate-item "Injections*Frame2*ButtonBox2*PushButton1(Create)")
```

```
(cx-gui-do cx-set-text-entry "Set Injection Properties*TextEntry1(Injection Name)" "nickel-25")
(cx-gui-do cx-set-list-selections "Set Injection Properties*Frame3*DropDownList3(Material)" '( 30))
(cx-gui-do cx-activate-item "Set Injection Properties*Frame3*DropDownList3(Material)")
(cx-gui-do cx-set-real-entry-list "Set Injection Properties*Frame3*Frame9*Frame3(Point Properties)*Frame1*Frame1*Frame1(First Point)*Table1(First Point)*RealEntry1(X-Position)" '( 0.0035))
(cx-gui-do cx-set-real-entry-list "Set Injection Properties*Frame3*Frame9*Frame3(Point Properties)*Frame1*Frame1*Frame1(First Point)*Table1(First Point)*RealEntry2(Y-Position)" '( 1e-006))
(cx-gui-do cx-set-real-entry-list "Set Injection Properties*Frame3*Frame9*Frame3(Point Properties)*Frame1*Frame1*Frame1(First Point)*Table1(First Point)*RealEntry19(Diameter)" '( 2.5e-005))
(cx-gui-do cx-activate-item "Set Injection Properties*PanelButtons*PushButton1(OK)")
(cx-gui-do cx-activate-item "Injections*Frame2*ButtonBox2*PushButton1(Create)")
(cx-gui-do cx-set-text-entry "Set Injection Properties*TextEntry1(Injection Name)" "nickel-in-25")
(cx-gui-do cx-set-real-entry-list "Set Injection Properties*Frame3*Frame9*Frame3(Point Properties)*Frame1*Frame1*Frame1(First Point)*Table1(First Point)*RealEntry1(X-Position)" '( 0.00367))
(cx-gui-do cx-set-real-entry-list "Set Injection Properties*Frame3*Frame9*Frame3(Point Properties)*Frame1*Frame1*Frame1(First Point)*Table1(First Point)*RealEntry2(Y-Position)" '( 0.0039))
(cx-gui-do cx-set-real-entry-list "Set Injection Properties*Frame3*Frame9*Frame3(Point Properties)*Frame1*Frame1*Frame1(First Point)*Table1(First Point)*RealEntry19(Diameter)" '( 2.5e-005))
(cx-gui-do cx-activate-item "Set Injection Properties*PanelButtons*PushButton1(OK)")
(cx-gui-do cx-activate-item "Injections*PanelButtons*PushButton2(Cancel)")
(cx-gui-do cx-activate-item "MenuBar*MonitorsSubMenu*Residual...")
(cx-gui-do cx-set-real-entry-list "Residual Monitors*Table2*RealEntry11" '( 1e-006))
(cx-gui-do cx-set-real-entry-list "Residual Monitors*Table2*RealEntry17" '( 1e-006))
(cx-gui-do cx-set-real-entry-list "Residual Monitors*Table2*RealEntry23" '( 1e-006))
(cx-gui-do cx-set-real-entry-list "Residual Monitors*Table2*RealEntry29" '( 1e-006))
(cx-gui-do cx-set-real-entry-list "Residual Monitors*Table2*RealEntry35" '( 1e-006))
(cx-gui-do cx-set-real-entry-list "Residual Monitors*Table2*RealEntry41" '( 1e-006))
(cx-gui-do cx-set-toggle-button "Residual Monitors*Table1*Frame1(Options)*ToggleBox1(Options)*CheckButton2(Plot)" #f)
(cx-gui-do cx-activate-item "Residual Monitors*Table1*Frame1(Options)*ToggleBox1(Options)*CheckButton2(Plot)")
(cx-gui-do cx-set-toggle-button "Residual Monitors*Table1*Frame1(Options)*ToggleBox1(Options)*CheckButton1(Print)" #t)
(cx-gui-do cx-activate-item "Residual Monitors*Table1*Frame1(Options)*ToggleBox1(Options)*CheckButton1(Print)")
(cx-gui-do cx-activate-item "Residual Monitors*PanelButtons*PushButton1(OK)")
(cx-gui-do cx-activate-item "MenuBar*InitializeSubMenu*Initialize...")
```

```
(cx-gui-do cx-set-list-selections "Solution Initialization*DropDownList1(Compute From)" '(
1))
(cx-gui-do cx-activate-item "Solution Initialization*DropDownList1(Compute From)")
(cx-gui-do cx-activate-item "Solution Initialization*PanelButtons*PushButton1(OK)")
(cx-gui-do cx-activate-item "Solution Initialization*PanelButtons*PushButton2(Cancel)")
(cx-gui-do cx-activate-item "MenuBar*ControlsSubMenu*Solution...")
(cx-gui-do cx-set-real-entry-list "Solution Controls*Table1*Frame4(Solver
Parameters)*Table4(Solver Parameters)*RealEntry1(Courant Number)" '( 0.025))
(cx-gui-do cx-activate-item "Solution Controls*PanelButtons*PushButton1(OK)")
it 500
(cx-gui-do cx-activate-item "MenuBar*ControlsSubMenu*Solution...")
(cx-gui-do cx-set-real-entry-list "Solution Controls*Table1*Frame4(Solver
Parameters)*Table4(Solver Parameters)*RealEntry1(Courant Number)" '( 0.005))
(cx-gui-do cx-activate-item "Solution Controls*PanelButtons*PushButton1(OK)")
(cx-gui-do cx-activate-item "MenuBar*ModelsSubMenu*Viscous...")
(cx-gui-do cx-set-toggle-button "Viscous
Model*Table1*Frame1(Model)*ToggleBox1(Model)*Laminar" #f)
(cx-gui-do cx-activate-item "Viscous
Model*Table1*Frame1(Model)*ToggleBox1(Model)*Laminar")
(cx-gui-do cx-activate-item "Viscous Model*PanelButtons*PushButton1(OK)")
it 2000
(cx-gui-do cx-activate-item "MenuBar*ControlsSubMenu*Solution...")
(cx-gui-do cx-set-real-entry-list "Solution Controls*Table1*Frame4(Solver
Parameters)*Table4(Solver Parameters)*RealEntry1(Courant Number)" '( 0.001))
(cx-gui-do cx-activate-item "Solution Controls*PanelButtons*PushButton1(OK)")
(cx-gui-do cx-activate-item "MenuBar*ModelsSubMenu*Solver...")
(cx-gui-do cx-activate-item "Solver*PanelButtons*PushButton2(Cancel)")
(cx-gui-do cx-activate-item "MenuBar*ModelsSubMenu*Viscous...")
(cx-gui-do cx-set-toggle-button "Viscous
Model*Table1*Frame1(Model)*ToggleBox1(Model)*k-epsilon   (2 eqn)" #f)
(cx-gui-do cx-activate-item "Viscous
Model*Table1*Frame1(Model)*ToggleBox1(Model)*k-epsilon   (2 eqn)")
(cx-gui-do cx-set-position "Viscous Model" '(x 793 y 428))
(cx-gui-do cx-activate-item "Viscous Model*PanelButtons*PushButton1(OK)")
it 54000
(cx-gui-do cx-activate-item "MenuBar*ControlsSubMenu*Solution...")
(cx-gui-do cx-set-real-entry-list "Solution Controls*Table1*Frame4(Solver
Parameters)*Table4(Solver Parameters)*RealEntry1(Courant Number)" '( 0.0005))
(cx-gui-do cx-activate-item "Solution Controls*PanelButtons*PushButton1(OK)")
it 40000
(cx-gui-do cx-activate-item "MenuBar*WriteSubMenu*Stop Journal")
```

APPENDIX C

-0.005,0,0
-0.005,0.002,0
0,0.0007,0
0.00058169001699558,0.0007465019,0
0.00113667300440735,0.0007822146,0
0.00131530362797998,0.0007907303,0
0.00148557587214192,0.0007972125,0
0.00165624073231614,0.0008019913,0
0.00183142593175372,0.0008050191,0
0.00201377966960713,0.0008060905,0
0.2,0.0025604,0
0.2,0,0

APPENDIX D

/solve/set/flow-warnings no
/solve/set/reporting-interval 100
/define/boundary-conditions/pressure-inlet inlet no 1000000 n 900000 n 1000 n y y n 1 n 1 n
/solve/set/courant-number 0.01
it 200000
/solve/set/courant-number 0.005
it 200000
wcd He-800k-1.00MPa.cas
/define/boundary-conditions/pressure-inlet inlet no 1250000 n 900000 n 800 n y y n 1 n 1 n
/solve/set/courant-number 0.01
it 200000
/solve/set/courant-number 0.005
it 200000
wcd He-800k-1.25MPa.cas
/define/boundary-conditions/pressure-inlet inlet no 1500000 n 900000 n 800 n y y n 1 n 1 n
/solve/set/courant-number 0.01
it 200000
/solve/set/courant-number 0.005
it 200000
wcd He-800k-1.50MPa.cas
/define/boundary-conditions/pressure-inlet inlet no 1750000 n 900000 n 800 n y y n 1 n 1 n
/solve/set/courant-number 0.01
it 200000
/solve/set/courant-number 0.005
it 200000
wcd He-800k-1.75MPa.cas
/define/boundary-conditions/pressure-inlet inlet no 2000000 n 900000 n 800 n y y n 1 n 1 n
/solve/set/courant-number 0.01
it 200000
/solve/set/courant-number 0.005
it 200000
wcd He-800k-2.00MPa.cas
/define/boundary-conditions/pressure-inlet inlet no 2250000 n 900000 n 800 n y y n 1 n 1 n
/solve/set/courant-number 0.01
it 200000
/solve/set/courant-number 0.005
it 200000
wcd He-800k-2.25MPa.cas
/define/boundary-conditions/pressure-inlet inlet no 2500000 n 900000 n 800 n y y n 1 n 1 n
/solve/set/courant-number 0.01
it 200000
/solve/set/courant-number 0.005
it 200000
wcd He-800k-2.50MPa.cas

/define/boundary-conditions/pressure-inlet inlet no 2750000 n 900000 n 800 n y y n 1 n 1 n
/solve/set/courant-number 0.01
it 200000
/solve/set/courant-number 0.005
it 200000
wcd He-800k-2.75MPa.cas
/define/boundary-conditions/pressure-inlet inlet no 3000000 n 900000 n 800 n y y n 1 n 1 n
/solve/set/courant-number 0.01
it 200000
/solve/set/courant-number 0.005
it 200000
wcd He-800k-3.00MPa.cas
/define/boundary-conditions/pressure-inlet inlet no 3250000 n 900000 n 800 n y y n 1 n 1 n
/solve/set/courant-number 0.01
it 200000
/solve/set/courant-number 0.005
it 200000
wcd He-800k-3.25MPa.cas
/define/boundary-conditions/pressure-inlet inlet no 3500000 n 900000 n 800 n y y n 1 n 1 n
/solve/set/courant-number 0.01
it 200000
/solve/set/courant-number 0.005
it 200000
wcd He-800k-3.50MPa.cas
/define/boundary-conditions/pressure-inlet inlet no 3750000 n 900000 n 800 n y y n 1 n 1 n
/solve/set/courant-number 0.01
it 200000
/solve/set/courant-number 0.005
it 200000
wcd He-800k-3.75MPa.cas
/define/boundary-conditions/pressure-inlet inlet no 4000000 n 900000 n 800 n y y n 1 n 1 n
/solve/set/courant-number 0.01
it 200000
/solve/set/courant-number 0.005
it 200000
wcd He-800k-4.00MPa.cas

APPENDIX E

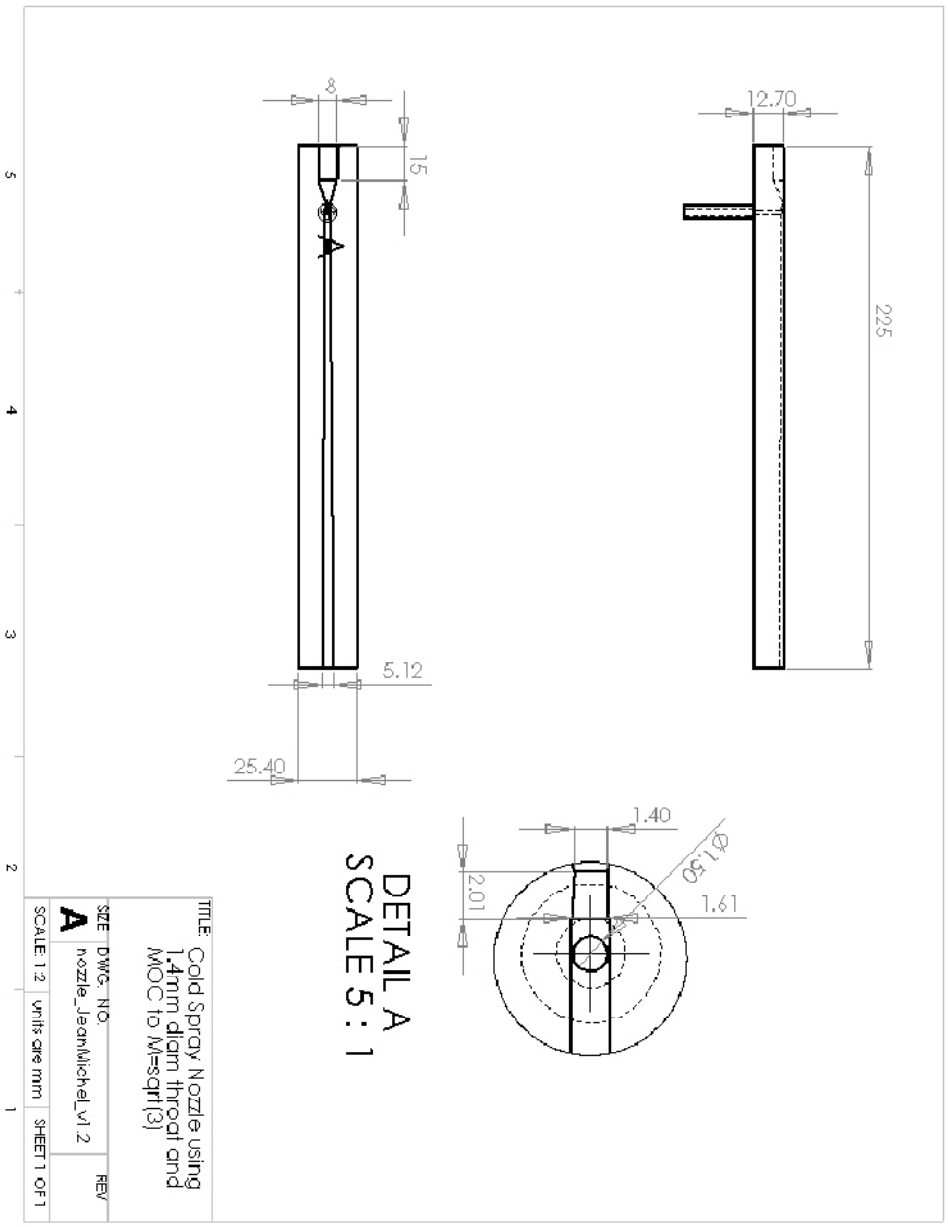
8
15
5.12
25.40
12.70
225
1.40
2.01
1.61
Ø1.50
DETAIL A
SCALE 5 : 1
TITLE:
Cold Spray Nozzle using
1.4mm diam throat and
MOC to M=sqrt(3)
SIZE
A
DWG. NO.
nozzle_JeanMichel_v1.2
REV
SCALE: 1:2
units are mm
SHEET 1 OF 1